KU LEUVEN
ARENBERG DOCTORAL SCHOOL
Faculty of Science

Ground state properties near the $N = 20$ and $N = 40$ islands of inversion

Prof. dr. G. Neyens

Hanne Heylen

2016

Ground state properties near the $N = 20$ and $N = 40$ islands of inversion

Hanne HEYLEN

Examination committee:
Prof. dr. P. Van Duppen, chair
Prof. dr. G. Neyens, supervisor
Prof. dr. N. Severijns
Prof. dr. K. Temst
Prof. dr. T.E. Cocolios
Prof. dr. B. Cheal
(University of Liverpool)
dr. J.C. Thomas
(GANIL)

Dissertation presented in partial fulfillment of the requirements for the degree of Doctor in Science

September 2016

Uitgegeven in eigen beheer, Hanne Heylen, Celestijnenlaan 200D, B-3001 Leuven (Belgium)

Dankwoord

During my PhD, I was incredibly lucky to meet and work with so many smart and passionate scientists. Therefore, I would like to use these first pages to sincerely thank everyone who has introduced me to the fascinating world of experimental nuclear physics and who has made the last four years a fun and enriching experience. A few people deserve a special mention.

Gerda, bedankt voor alle mogelijkheden die ik de laatste vier jaar heb gekregen; door je steun en je vertrouwen kon ik altijd mijn eigen ding doen zonder het gevoel te hebben er alleen voor te staan. Ondanks je drukke agenda, kon ik altijd bij je terecht met mijn vragen, problemen of gewoon voor een toffe babbel. Je enthousiasme voor het kernfysisch onderzoek is aanstekelijk.

I would like to thank all members of the examination committee, for the careful reading of the manuscript, for the stimulating discussions and for asking just those questions which made me dig a little bit deeper.
Bradley, thanks for your patience and guidance, for answering all the questions in my too long e-mails and for the encouragements when I needed them.
Jean-Charles, thanks for all your help and advice during the many weeks at GANIL, for keeping me motivated and sane, and for trying to shift me into a higher gear, even at 5 o'clock in the morning.

I would also like to thank all colleagues who have made the IKS such a pleasant work place, in particular the members of the Nuclear Moments group. Jasna, Marieke, Ivan, Wouter, Ruben, Agi, Ronald, Xiaofei and Xu, thanks for the nice atmosphere in (and outside of) the office. Ook een dikke merci aan de mensen die het IKS achter de schermen draaiende houden. Isabelle, Fabienne en Danielle voor de hulp met de praktische beslommeringen, Bert en Luc voor het oplossen van IT-gerelateerde problemen en Willy voor de technische hulp.

Many thanks to the members of the COLLAPS collaboration, for teaching me everything I needed to know about the set-up and laser spectroscopy and for

making the beam times not only successful but also fun. Special thanks to Carla for the nice collaboration on the Mn results.
The other colleagues at ISOLDE deserve a thank you as well, for the coffee/lunch breaks and the occasional beer which made my visits to CERN so much more enjoyable.

Verder wil ik ook mijn vrienden en familie bedanken voor de broodnodige ontspanning en om me er soms aan te herinneren dat er wel belangrijkere dingen zijn in het leven dan een doctoraat. Bedankt voor de gezellige maaltijden, de spelletjesavonden en alle andere toffe momenten die er voor hebben gezorgd dat ik er de volgende dag op het werk weer kon invliegen.
Een speciale dank gaat naar het thuisfront. Mama en papa, bedankt dat ik steeds mijn dromen heb kunnen nastreven zonder mij ook maar over iets zorgen te moeten maken, bedankt voor de interesse in alles wat ik doe en de niet aflatende steun.
En ten slotte is er nog Christophe. Hoewel onze bioritmes niet helemaal synchroon lopen en onze geografische locaties in de laatste jaren vaak honderden kilometers uit elkaar lagen, was je er altijd als ik je nodig had. Bedankt om de moeilijke momenten zoveel gemakkelijker te maken, ik kan niet wachten om samen aan ons nieuw avontuur te beginnen!

Abstract

In this work, nuclear spins, magnetic moments, quadrupole moments and mean-square charge radii were measured to explore the changing nuclear structure in the islands of inversion around $N = 20$ and $N = 40$. These ground state properties are excellent probes to study the observed structural changes as they are sensitive to the interplay between single-particle and collective effects governing the dynamics in these regions.

Located above the deformed Mg isotopes, the neutron-rich Al ($Z = 13$) isotopes constitute the northern border of the island of inversion around $N = 20$. Their structure is investigated in two β-NMR/NQR experiments at the LISE-GANIL facility.
The quadrupole moment of ^{33}Al is measured with a 5 times higher precision than the previous value. It is only due to this high precision, that it could be unambiguously concluded that there is a significant amount of intruder configurations in the ground state wave function, placing ^{33}Al inside rather than outside of the island of inversion.
Furthermore, the g-factor and quadrupole moment of the recently discovered 1^+ isomer in ^{34}Al is discussed. While so far, 2p-2h (and 4p-4h) excitations are found to dominate the ground and long-lived states in the island of inversion, this low-lying 1^+ isomer is proposed to have a 1p-1h configuration. Its g-factor and quadrupole moment, in comparison with the 1^+ normal ground state of ^{32}Al, enable the verification of this proposed intruder nature and offer the unique opportunity to study the increase in deformation due to these particular 1p-1h excitations.

The region below $^{68}_{28}$Ni$_{40}$ is characterised by a rapid onset of collectivity. The neutron-rich Mn ($Z = 25$) isotopes lie in the middle of this region of collectivity, sometimes also called an island of inversion in view of the parallels with the situation around $N = 20$. Two collinear laser spectroscopy experiments have been performed at ISOLDE-CERN to study the ground state properties along the Mn isotopic chain.

In a first experiment, using the $3d^5 4s^2\ {}^6S_{5/2} \rightarrow 3d^5 4s4p\ {}^6P_{3/2}$ atomic transition, the spins and magnetic moments between $N = 26$ and $N = 39$ were extracted. Previously, all spins beyond $N = 34$ were only tentatively assigned. By our direct measurement we firmly establish a $I = 5/2$ ground state spin for ^{59,61,63}Mn and a $I = 1$ low-spin state and $I = 4$ high-spin state in the ^{58,60,62,64}Mn. Via a comparison of the magnetic moments to large-scale shell model calculations, the significance of neutron excitations across $N = 40$ as well as proton excitations across $Z = 28$ in the structure of the neutron-rich Mn can be established.
In a second experiment, the successful application of optical pumping in ISCOOL enabled the measurement of the quadrupole moments of the odd-even $^{53-63}$Mn isotopes using the $3d^5\ 4s\ {}^5S_2$ (metastable) $\rightarrow 3d^5\ 4p\ {}^5P_3$ ionic transition. The observed rise in quadrupole moments illustrates the development of quadrupole collectivity towards $N = 40$. In particular, it was demonstrated that both the $\nu g_{9/2}$ and $\nu d_{5/2}$ orbitals are necessary to reproduce this collectivity. Additionally, the onset of deformation was confirmed by the mean-square charge radii which show a strong increase towards $N = 40$.
More generally, the results of the two collinear laser spectroscopy experiments in combination with large-scale shell model calculations, enable a systematic investigation of the evolution of nuclear structure between $N = 26$ and $N = 39$ in the Mn isotopic chain.

Beknopte samenvatting

Atoomkernen zijn de bouwstenen van alles rondom ons. Ze bestaan uit een aantal protonen (Z) en neutronen (N) die worden samengehouden door de sterke kernkracht. Ongeveer 300 van deze proton-neutron combinaties vormen stabiele configuraties die voorkomen op aarde, en meer dan 3000 verschillende kernen werden reeds artificieel geproduceerd. De studie van al deze kernen bracht een enorme diversiteit in groottes, vormen en excitatietoestanden aan het licht. Een van de open vragen in de kernfysica is dan "Hoe kunnen we deze rijke fenomenologie beschrijven aan de hand van maar een beperkt aantal ingrediënten: de protonen, neutronen en de onderlinge interacties?".

Hoewel er tot op heden geen universeel kernmodel bestaat, is het schillenmodel bijzonder succesvol in het beschrijven van de kernstructuur van lichte en middel-zware kernen. Historisch gezien is het een belangrijk model omdat het de experimenteel geobserveerde "magische getallen", uitzonderlijk stabiele configuraties met proton- en/of neutrongetal $Z, N=$ 2, 8, 20, 28, 50, 82 en 126, correct kon reproduceren. In analogie met de elektronen in het atomaire schillenmodel worden de protonen en neutronen verondersteld te bewegen in orbitalen die gegroepeerd zijn in schillen. De verhoogde stabiliteit van de magische getallen is dan geassocieerd met grote energiekloven tussen de verschillende schillen, gelijkaardig aan de inerte edelgassen. Ook nu nog is het schillenmodel een van de belangrijkste werktuigen om experimentele observaties te verklaren dicht bij, maar ook ver weg van de stabiliteitsvallei.
Het zijn deze kernen ver weg van stabiliteit, de zogeheten exotische kernen, die momenteel van groot belang zijn in het hedendaags kernfysisch onderzoek. In deze exotische kernen zijn allerlei fenomenen ontdekt die niet stroken met de klassieke verwachtingen. Door hun extreme verhouding van het aantal neutronen tot het aantal protonen worden immers andere aspecten van de kernkracht belicht, vergeleken met de stabiele kernen. Hierdoor zijn het de kernen bij uitstek om de huidige modellen te testen en te verbeteren.

De regio rond $Z \approx 12$ en $N \approx 20$ is een van de eerste voorbeelden waar zulke onverwachte fenomenen zijn waargenomen. Hoewel rond magische getallen zoals $N = 20$ sferische kernen worden verwacht, werden in deze regio indicaties gevonden voor sterk vervormde kernen. Deze vervorming werd al snel gerelateerd aan toestanden waarin n neutronen over de $N = 20$ schillensluiting geëxciteerd worden, de n deeltje - n gat (np-nh[1]) toestanden. Zulke np-nh toestanden worden normaal gezien verhinderd door de hoge energiekost verbonden aan de excitatie van n deeltjes over de grote $N = 20$ energiekloof. Anderzijds kunnen proton-neutroncorrelaties, verantwoordelijk voor vervorming, zich maximaal ontwikkelen in deze np-nh toestanden, wat in bepaalde gevallen tot een grote energiewinst leidt. Als deze energiewinst de energiekost compenseert, kunnen de vervormde np-nh toestanden lager in energie komen dan de sferische 0p-0h toestanden. De kernen waarvoor er zo'n inversie gebeurt, behoren tot het "eiland van inversie".

Oorspronkelijk dacht men dat het eiland van inversie welomlijnd was en gelimiteerd tot de $_{10}$Ne, $_{11}$Na en $_{12}$Mg isotopen met $20 \leq N \leq 22$. Ondertussen is er een uitgebreid onderzoeksprogramma opgezet om de eigenschappen van deze kernen en hun buren in kaart te brengen, met als doel om de achterliggende mechanismes verantwoordelijk voor de veranderende kernstructuur beter te begrijpen. Dit heeft onder andere uitgewezen dat de overgang naar het eiland van inversie gradueel gebeurt, en dat er een variabele hoeveelheid van opmenging is tussen 0p-0h en np-nh toestanden in de kernen gelegen aan de randen. De kernstructuur van deze randkernen hangt in sterke mate af van het delicate evenwicht tussen de grootte van de schillensluiting en de proton-neutroncorrelaties, zodat ze belangrijke input leveren om de accuraatheid van de kernmodellen te toetsen.

Ondertussen werden observaties in andere regio's van de kernkaart ook gelinkt aan dezelfde mechanismen die aan het werk zijn rond $N = 20$. Men spreekt zo van het "eiland van inversie rond $N = 40$" om de regio onder $^{68}_{28}$Ni$_{40}$ te beschrijven, waar eveneens een snelle overgang van sferische naar vervormde kernen aan het licht gekomen is.

In dit doctoraatsonderzoek wordt de kernstructuur in deze eilanden van inversie rond $N = 20$ en $N = 40$ bestudeerd aan de hand van experimenteel gemeten kernspins, magnetische momenten, kwadrupoolmomenten en gemiddelde kwadratische ladingstralen. Deze observabelen spelen een belangrijke rol bij de interpretatie van de eigenschappen in deze regio's, omdat ze gevoelig zijn aan de wisselwerking tussen de een-deeltjes en collectieve aspecten die bepalend zijn voor de veranderende kernstructuur. Omdat de kernen bestudeerd in deze thesis zeer exotisch zijn, met half-waardetijden van een fractie van een seconde, werden de metingen uitgevoerd aan twee radioactieve-ionenbundelfaciliteiten, ISOLDE-CERN in Genève (Zwitserland) en LISE-GANIL in Caen (Frankrijk).

[1] n particle - n hole

Resultaten

De neutronrijke Al ($Z = 13$) isotopen zijn bestudeerd in twee β-NMR/NQR experimenten uitgevoerd aan de LISE-GANIL faciliteit. Deze Al-isotopen zijn gelegen aan de noordgrens van het eiland van inversie rond $N = 20$, net boven de vervormde Mg isotopen.
Het kwadrupoolmoment van de $^{33}Al_{20}$ grondtoestand is opgemeten met een vijf keer betere precisie dan de eerder gemeten waarde. Enkel door deze hoge precisie was het mogelijk om ondubbelzinning te bepalen dat de bijdrage van de 2p-2h configuraties in de golffunctie van de grondtoestand groter is dan 50%. Tot voor onze meting was hier geen sluitend antwoord op. Hoewel state-of-the-art schillenmodelberekeningen over het algemeen de eigenschappen van kernen in en rond het eiland van inversie goed kunnen beschrijven, bleek een correcte reproductie van het experimentele kwadrupoolmoment van ^{33}Al een uitdaging. Dit toont het belang aan van overgangsisotopen zoals ^{33}Al, met een sterke opmenging tussen 0p-0h en 2p-2h configuraties, als kritische test voor de beschikbare modellen.
Verder wordt ook de recent ontdekte 1^+ toestand in $^{34}Al_{21}$ besproken. Tot hiertoe konden de golffuncties van de grond- en isomere toestanden in het eiland van inversie beschreven worden aan de hand van 0p-0h, 2p-2h en in mindere mate ook 4p-4h configuraties. Voor de 1^+ toestand zijn er echter indicaties dat het om een 1p-1h configuratie gaat. De g-factor en het kwadrupoolmoment, in vergelijking met de waardes van de 1^+ toestand in ^{32}Al, laten dan toe om het unieke 1p-1h karakter te verifiëren maar ook om de potentiële vervorming door zulke 1p-1h configuraties te onderzoeken. Omdat dit experiment pas eind mei 2016 plaatsvond is de analyse nog lopende en kunnen er nog geen besluiten worden getrokken.

De neutronrijke Mn ($Z = 25$) isotopen liggen in het midden van het eiland van inversie rond $N = 40$. Deze Mn isotopen werden bestudeerd in twee collineaire laser spectroscopie-experimenten uitgevoerd aan ISOLDE-CERN. In deze metingen werden de spins, kernmomenten en ladingstralen van niet minder dan 13 isotopen gemeten (alsook van drie langlevende isomere toestanden), wat toeliet om de de kernstructuur van Mn systematisch te onderzoeken tussen $N = 26$ en $N = 39$.
In een eerste experiment werd de $3d^5 4s^2\ ^6S_{5/2} \rightarrow 3d^5 4s4p\ ^6P_{3/2}$ atomaire transitie gebruikt om de spins en magnetische momenten op te meten. Eerder waren alle spinbepalingen boven $N = 34$ slechts provisioneel. In onze metingen konden de spins van de $^{61,63}Mn$ en $^{58,60,62,64}Mn$ grondtoestanden en $^{58,60,64}Mn$ isomere toestanden eenduidig worden bepaald, respectievelijk $I = 5/2$, $I = 1$ en $I = 4$. Door een vergelijking van de magnetische momenten met grootschalige schillenmodelberekeningen kon het toenemende belang van zowel neutron excitaties over $N = 40$ als proton excitaties over $Z = 28$ in de nabijheid

van $N = 40$ worden vastgesteld.
In een tweede experiment liet de succesvolle toepassing van optisch pompen in de "cooler/buncher" toe om de kwadrupoolmomenten van $^{53-63}$Mn op te meten via de $3d^5\ 4s\ ^5S_2$ (metastabiel) $\rightarrow 3d^5\ 4p\ ^5P_3$ ionische transitie. De groei in opgemeten kwadrupoolmoment met het neutrongetal illustreert de toename in kwadrupoolvervorming naar $N = 40$. Bijzondere aandacht werd besteed aan de rol van het $\nu d_{5/2}$ orbitaal, in combinatie met het $\nu g_{9/2}$ orbitaal, in de ontwikkeling van deze vervorming. Bovendien toonden de gemiddelde kwadratische landingstralen eveneens een sterke groei, wat het belang van kwadrupoolvervorming in de structuur van de neutronrijke Mn isotopen bevestigt. In het algemeen schetsen de kernmomenten en de ladingsstralen dus een duidelijk en consistent beeld van de kernstructuur van Mn.

Contents

Preface

Together with the electrons, nuclei constitute the atoms which are the basic building blocks of the matter around us. These atomic nuclei are composed of a varying amount of strongly interacting protons (Z) and neutrons (N) which leads to a diversity of nuclear shapes, sizes and excitation modes across the chart of nuclides. The study of nuclear structure has the goal to understand how this rich nuclear phenomenology arises, starting from only a few common ingredients, the nucleons and the nucleon-nucleon interaction[2].
Over recent decades, the availability of intense radioactive beams has opened the door for the exploration of nuclei increasingly far from stability. This has resulted in a number of remarkable discoveries at variance with the classical expectations of an immutable shell structure. These discoveries, and their consequences for our understanding of the nucleus, have caused a "renaissance" in nuclear physics research [Casten, 2000] which moved the research frontier from the stable to the exotic nuclei. The highly asymmetric neutron-to-proton ratios in these exotic nuclei make them very promising to explore new aspects of the nuclear force, while their short half-lives and low production yields make them very challenging to study experimentally.

The goal of this work was to investigate the nuclear structure of the exotic Al and Mn isotopes via the measurement of their spins, magnetic moments, quadrupole moments and mean-square charge radii. Although the isotopic chains are located in two different mass regions, around $N = 20$ and $N = 40$, respectively, the physics motivation is closely linked through the common mechanism responsible for the observed structural changes. Indeed, in both regions deformed intruder states are found to lie below the normally expected spherical configurations, hence they are referred to as *islands of inversion*. This deformation is associated with particle-hole excitations across a reduced shell gap which are energetically

[2] Although nucleons have an internal quark structure, it turns out that not these quarks but rather the nucleons are the relevant degrees of freedom for the description of low-energy nuclear physics.

favourable due to the large quadrupole correlations. As the dynamics in the islands of inversion depend critically on the competition between single-particle and collective effects, the spins, moments and mean-square charge radii provide excellent probes to study them.
The Al and Mn isotopic chains were studied using two different techniques at two different radioactive ion beam facilities: β-NMR/NQR on the Al isotopes at LISE-GANIL and collinear laser spectroscopy on the Mn isotopes at ISOLDE-CERN. This thesis is therefore divided into three parts: an introductory part where the common concepts of the thesis are outlined and two experimental parts in which the specifics of the separate experimental techniques and results are presented. Five scientific papers discussing the results of the experiments form the backbone of this thesis. They are supplemented with background or additional information where appropriate. A summary of the structure of the thesis is given below.

- Chapter 1 and 2 introduce the nuclear shell structure and the experimental observables measured in this work. Special attention is given to the exotic nuclei and what we can learn from them. Both chapters serve to give a general motivation as to why we are interested in measuring ground state properties in the islands of inversion.

- Chapter 3 outlines the measurements of nuclear moments using the β-NMR/NQR technique at GANIL.

- In chapter 4, a motivation is given for the study of the neutron-rich Al isotopes, in particular ^{33}Al and the 1^+ state in ^{34}Al. For the latter only very preliminary results are shown, while the ^{33}Al results are published in Physical Review C.

  Article I: High-precision quadrupole moment reveals significant intruder component in $^{33}_{13}$Al$_{20}$ ground state
  H. Heylen, M. De Rydt, G. Neyens, M.L. Bissell, L. Caceres, R. Chevrier, J.M. Daugas, Y. Ichikawa, Y. Ishibashid, O. Kamalou, T.J. Mertzimekis, P. Morel, T. Otsuka, J. Papuga, A. Poves, M.M. Rajabali, C. Stödel, J.C. Thomas, H. Ueno, Y. Utsuno, N. Yoshida, A. Yoshimi
  Physical Review C 94, 034312 (2016).

- Chapter 5 and 6 focus on the two collinear laser spectroscopy experiments on the neutron-rich Mn isotopes performed at ISOLDE. In chapter 5, an overview of the experimental technique is presented and it is explained how the spins, nuclear moments and mean-square charge radii can be extracted from the measured hyperfine spectra. Chapter 6 starts with a motivation for the investigations of the neutron-rich Mn isotopes. Afterwards, the necessary details of the analysis procedure are given. Finally, the wealth of experimental information extracted in the two experiments is presented in four papers.

Article II: Evidence for Increased Neutron and Proton Excitations in $^{51-63}$Mn
C. Babcock, H. Heylen, J. Billowes, M.L. Bissell, K. Blaum, P. Campbell, B. Cheal, R.F. Garcia Ruiz, C. Geppert, W. Gins, M. Kowalska, K. Kreim, S.M. Lenzi, I.D. Moore, R. Neugart, G. Neyens, W. Nörtershäuser, J. Papuga, D.T. Yordanov
Physics Letters B 750, 176 - 180 (2015).

Article III: Spins and magnetic moments of ^{58,60,62,64}Mn ground states and isomers
H. Heylen, C. Babcock, J. Billowes, M.L. Bissell, K. Blaum, P. Campbell, B. Cheal, R.F. Garcia Ruiz, C. Geppert, W. Gins, M. Kowalska, K. Kreim, S.M. Lenzi, I.D. Moore, R. Neugart, G. Neyens, W. Nörtershäuser, J. Papuga, D.T. Yordanov
Physical Review C 92, 044311 (2015).

Article IV: Quadrupole Moments of odd-A $^{53-63}$Mn : Onset of Collectivity towards $N = 40$
C. Babcock, H. Heylen, M.L. Bissell, K. Blaum, P. Campbell, B. Cheal, D. Fedorov, R.F. Garcia Ruiz, W. Geithner, W. Gins, T. Day Goodacre, L.K. Grob, M. Kowalska, S.M. Lenzi, B. Maass, S. Malbrunot-Etternauer, B. Marsh, R. Neugart, G. Neyens, W. Nörtershäuser, T. Otsuka, R. Rossel, S. Rothe, R. Sánchez, Y. Tsunoda, C. Wraith, L. Xie, X.F. Yang
Physics Letters B 760, 387 - 392 (2016).

Article V: Changes in nuclear structure along the Mn isotopic chain studied via charge radii
H. Heylen, C. Babcock, R. Beerwerth, J. Billowes, M.L. Bissell, K. Blaum, J. Bonnard, P. Campbell, B. Cheal, D. Fedorov, S. Fritzsche, R.F. Garcia Ruiz, W. Geithner, Ch. Geppert, W. Gins, T. Day Goodacre, L.K. Grob, M. Kowalska, K. Kreim, S.M. Lenzi, I.D. Moore, B. Maass, S. Malbrunot-Ettenauer, B. Marsh, R. Neugart, G. Neyens, W. Nörtershäuser, T. Otsuka, J. Papuga, R. Rossel, S. Rothe, R. Sánchez, Y. Tsunoda, C. Wraith, L. Xie, X.F. Yang, and D.T. Yordanov
Submitted to Physical Review C.

- This thesis ends with a conclusion in chapter 7.

Part I

The structure of an atomic nucleus

1 | Nuclear shell structure

Nuclear models provide the frameworks in which we try to understand the structure of atomic nuclei. They should be simple enough to highlight the essential physics and to be mathematically tractable, yet refined enough to describe the rich diversity of nuclear phenomena observed across the nuclear landscape. Furthermore, they should have strong predictive power when going to new and unexplored regions of the chart of nuclides.
This is not a simple task and no universal nuclear theory is currently available. This is not only because of the huge challenges related to solving the quantum many-body problem, but also due to the incomplete knowledge of the strong force and how it acts within the nuclear medium. Despite these difficulties, the nuclear shell model, one of the nuclear models, has proven to be very successful in elucidating the structure of light and medium mass nuclei and continues to play a central role in the interpretation of observations in both stable and exotic nuclei.
In this chapter, the basics of the shell model are introduced and a few modern aspects important for the remainder of this thesis will be outlined. In the next chapter, the focus is shifted towards the experimental observables which are measured in this thesis. Due to the strong connection between experiment and theory, these two chapters go naturally together: a correct interpretation of the experimental results requires an accurate nuclear model, while it is only possible to know how accurate the model is by experimental validation (or maybe more interesting, invalidation).

1.1 The nuclear shell model

Although the nucleus is a complex system of A strongly interacting nucleons, surprisingly simple patterns emerge across the nuclear landscape, most notably the magic numbers associated with particularly stable proton and neutron

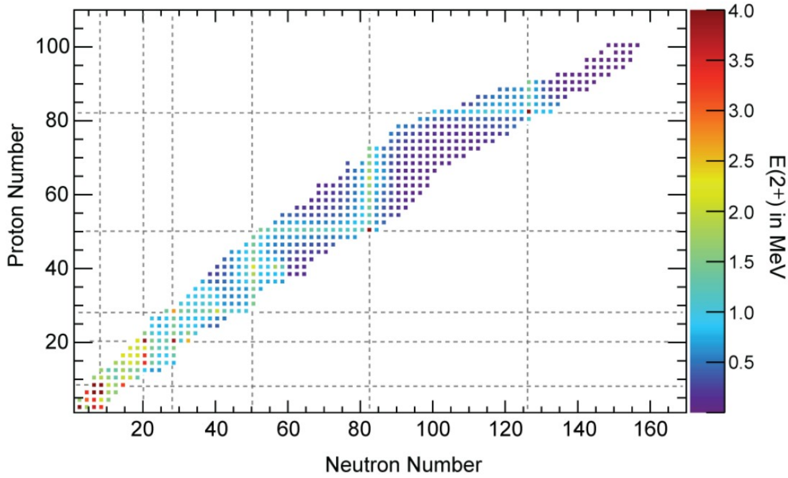

Figure 1.1: Colour-coded $E(2^+)$ systematics of the even-even nuclei across the nuclear chart. Picture taken from [Gade, 2015].

configurations at $N, Z = 2$, 8, 20, 28, 50, 82 and $N = 126$. The magic numbers become immediately visible as regularities in the systematics of many nuclear observables, for example as elevated energies of the first excited 2^+ states in even-even nuclei as shown in Fig. 1.1. In analogy with the shell model of electrons in an atom, these regularities were soon interpreted as evidence for a nuclear shell structure, with the magic numbers corresponding to large energy gaps between the shells.
Here, the basics of the nuclear shell model are outlined. For a more extensive description the reader is referred to the numerous available text books, lecture notes and review papers such as Heyde [1990]; Casten [2000]; Poves and Nowacki [2001]; Caurier et al. [2005]; Otsuka [2009].

1.1.1 The independent particle model

The general nuclear Hamiltonian contains a kinetic energy term and a potential energy term which describes the interactions between the nucleons

$$H = \sum_{i=1}^{A} \frac{\boldsymbol{p}_i^2}{2m_i} + \sum_{i>k=1}^{A} V_{ik}(\boldsymbol{r}_i - \boldsymbol{r}_k). \tag{1.1}$$

This general Hamiltonian can be rewritten as the sum of an independent particle term H_0 plus a term containing the residual interactions H_{res}, by introducing a one-body potential U_i [Casten, 2000]

$$H = \left(\sum_{i=1}^{A} \frac{\boldsymbol{p}_i^2}{2m_i} + U_i(\boldsymbol{r}_i) \right) + \left(\sum_{i>k=1}^{A} V_{ik}(\boldsymbol{r}_i - \boldsymbol{r}_k) - \sum_{i=1}^{A} U_i(\boldsymbol{r}_i) \right) \tag{1.2}$$

$$= H_0 + H_{\text{res}} \tag{1.3}$$

One of the great simplifications and basic concepts of the nuclear shell model is that, in a first approximation, only H_0 needs to be considered: each nucleon is assumed to move independently (non-interacting) in a potential generated by all other nucleons. Or put differently, the main result of the complicated two-body[1] interactions is to generate an average spherical potential.

When this potential is modeled by a harmonic oscillator, the well-known energy eigenvalues $E = \hbar\omega\left(N + \frac{3}{2}\right) = \hbar\omega\left(2n + \ell - \frac{1}{2}\right)$ are obtained, with N the major oscillator quantum number, ℓ the orbital quantum number (taking values between $N, N-2, \ldots 1$ or 0) and $n = (N - \ell + 2)/2$ the radial quantum number, which indicates the number of nodes of the radial wave function [Heyde, 1990]. However, this approach yields shell gaps at 2, 8, 20, 40, 70, ... which only agree with the observed magic numbers up to 20. A decisive step to also get the correct magic numbers at higher nucleon numbers was taken when Goeppert-Mayer [1949] and Haxel et al. [1949] showed the need for the inclusion of a strong spin-orbit potential, as well as an ℓ^2 term to flatten the potential well at large ℓ such that

$$U(r) = \frac{1}{2} m\omega^2 r^2 + D\boldsymbol{\ell}^2 + C\boldsymbol{\ell} \cdot \boldsymbol{s} \tag{1.4}$$

In Fig. 1.2 the calculated single-particle energies using eq. 1.4 are presented. As shown from left to right, the second term lifts the ℓ degeneracy of the harmonic oscillator orbitals while the spin-orbit term lowers the energy of the $j_> = \ell + 1/2$ orbital with respect to the $j_< = \ell - 1/2$ orbital. Since the size of the spin-orbit splitting is proportional to ℓ, it becomes larger for higher ℓ [Otsuka, 2009].
From the above derivation, it is clear that two kinds of magic numbers can be distinguished [Sorlin, 2009]: the harmonic oscillator shell gaps at 8, 20, 40 and the spin-orbit shell gaps at 14, 28, 50, 82 and 126. Since there is a parity change between the orbitals above and below the harmonic oscillator gaps, parity conserving quadrupole excitations across the shell gap are forbidden at the 1 particle-1 hole level (1p-1h), and 2p-2h excitations are needed to generate collectivity. On the other hand, the orbitals above and below the spin-orbit gaps have the same parity and differ by $\Delta\ell = 2$, favouring 1p-1h quadrupole excitations.

[1] Three-body interactions are not explicitly considered here although they are now generally accepted to be important for a successful description of the nuclear structure [Hammer et al., 2013].

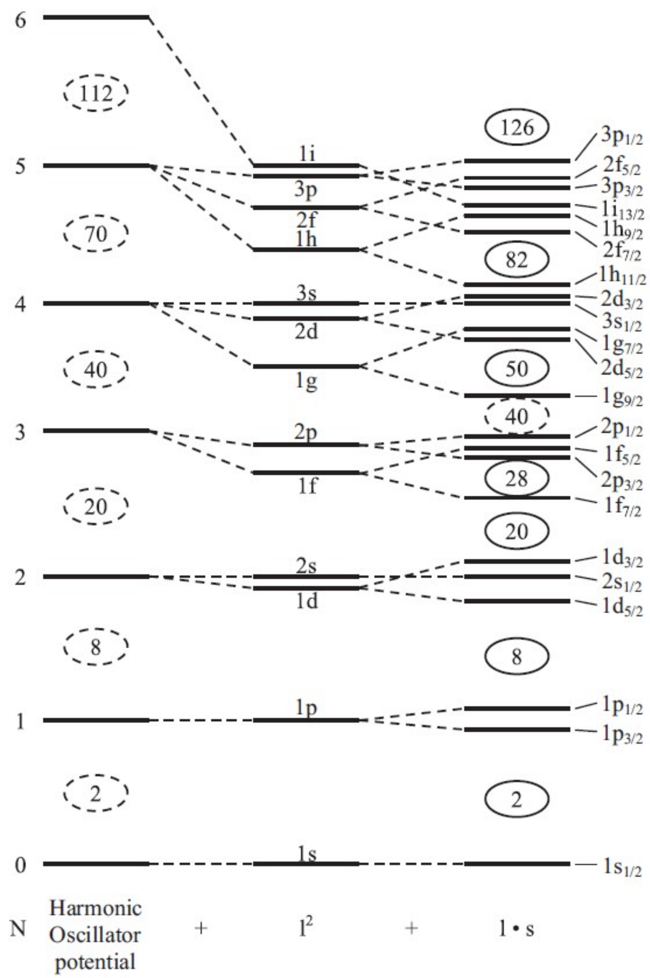

Figure 1.2: Shell structure of the single-particle levels, taken from [Casten, 2000]

The basic idea of the independent particle model is to fill the single-particle orbits sequentially while obeying the Pauli principle such that each orbital can contain $2j + 1$ nucleons. Since the total angular momentum of a filled j-orbital is equal to zero [Casten, 2000], the spins and parities of nuclei with one particle/hole outside a closed core can be predicted. Even more, the spins, magnetic moments and sometimes quadrupole moments of many odd-A ground states can be described correctly using just the independent particle model[2], assuming these properties are determined by the last odd nucleon (see chapter 2). So despite its simplicity, the independent particle model can describe a rather broad range of experimental data. Nevertheless, it is certainly too naive to explain many other aspects of the nuclear structure such as excitation schemes and collective effects. In a next step, the residual interactions between the nucleons outside the closed core therefore need to be included.

1.1.2 The interacting shell model

The interaction between the nucleons and the chosen model space are the basic ingredients of the interacting shell model, schematically shown in Fig. 1.3.
For a nucleus consisting of N neutrons and Z protons, the independent particle model tells us which orbitals are occupied and which are empty. Near the Fermi level however, several orbitals play a role and it is important to include all of these in the calculations. Whereas the best reproduction of experimental results is achieved when the number of orbitals is as large as possible, in practice, this number has to be limited since the dimensions quickly become too large to be handled computationally. Therefore, one defines a closed core of fully occupied orbitals and an external space of empty orbitals which are both excluded from the calculations.
The remaining orbitals constitute the valence space and should be chosen such that they contain all relevant degrees of freedom. A logical choice are valence spaces comprised between the magic numbers as the large energy gaps hinder mixing between different major shells. This is however not always the most appropriate choice for the specific dynamics of the nucleus of interest. Indeed, as we will see in section 2.2, an accurate description of magnetic moments requires that the spin-orbit partners are taken into account, while quadrupole properties are heavily affected by $\Delta\ell = 2$ and $\Delta j = 2$ orbitals.
Starting from the single-particle states in the valence space, all different anti-symmetrized A-particle wave functions ϕ_i or *configurations* can be constructed. The final nuclear wave function is then a linear combination of these configurations [Otsuka, 2009]

$$\Psi = \sum c_i \phi_i \tag{1.5}$$

with c_i the probability amplitudes. The concept of having a combination of several configurations in the wave function is called configuration mixing.

[2] Actually, the available experimental information on the ground state spins and moments of odd-A nuclei in the 1930's provided important evidence for the nuclear independent particle motion which lead to the development of the independent particle model more than a decade later.

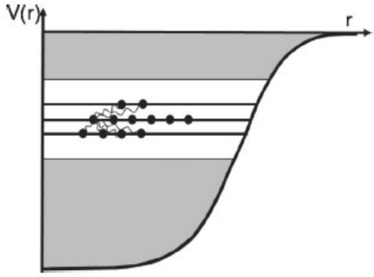

Figure 1.3: Schematic illustration of the inert core, active valence space with effective interactions between the nucleons and external space which constitute the basics of the interacting shell model. Picture taken from [Krücken, 2011].

Whereas in nuclei with only a few nucleons outside a closed shell, wave functions are generally quite pure (i.e. consisting of only a few important configurations), highly fragmented wave functions are found in between shell closures.

Configuration mixing is an important consequence of the introduction of residual interactions and the configuration mixed wave function can be found by solving the Schrödinger equation $H\Psi = E\Psi$. The key components to construct the Hamiltonian H are the single-particle energies ϵ_i (SPE) and the two-body matrix elements (TBME) incorporating the interaction V between the nucleons

$$_n\langle j_i j_j J|V|j_k j_l J\rangle_m. \tag{1.6}$$

Here, $|j_i j_j J\rangle_n$ denotes the state n of two nucleons in the single-particle states j_i and j_j coupled to angular momentum J. For each J, all possible combinations of single-particle orbitals j needs to be considered. The matrix elements of the Hamiltonian are given by

$$H_{nm} = \epsilon_{j_i}\delta_{nm} + \epsilon_{j_j}\delta_{nm} + {}_n\langle j_i j_j J|V|j_k j_l J\rangle_m \tag{1.7}$$

where δ_{nm} the Kronecker delta defined as $\delta_{nm} = 1$ for $n = m$ and $\delta_{nm} =$ for $n \neq m$. ϵ_{j_i} and ϵ_{j_j} denote the single-particle energies of orbital j_i and j_j. The off-diagonal elements are just the two-body matrix elements while the diagonal elements are the single-particle energies corrected by the residual interaction.

The nucleon-nucleon interaction used in the limited shell model valence space is an effective one such that

$$H\Psi = E\Psi \rightarrow H_{\text{Eff}}\Psi_{\text{Eff}} = E\Psi_{\text{Eff}}. \tag{1.8}$$

The effective interaction is therefore derived specifically for the chosen model space. Furthermore, it is assumed that in this procedure excitations from core

orbitals not included in the model space (core-polarization) as well as multiple scattering events via high-lying intermediate states are effectively taken into account via an appropriate renormalization [Otsuka, 2009]. Also the effects of three- or higher-body interactions are renormalised into the effective two-body interactions. Apart from the interaction, also the operators are effective, as discussed in chapter 2.
In general, the determination of the effective interaction is not a straightforward task [Poves and Nowacki, 2001; Caurier et al., 2005; Otsuka, 2009]. While in phenomenological approaches the two-body matrix elements are just left as free parameters to be fit to experiment, also in most microscopic approaches starting from the bare nucleon-nucleon interaction, empirical corrections are required to successfully reproduce experimental data. The empirical tuning of the interactions is a clear weakness of many shell model interactions. Although the interactions work well in the vicinity of the data to which they were adjusted, extrapolations to regions far from stability are often unsuccessful. In a more sound approach, the empirical input should be limited to a few, well-defined and universal parameters.
Recently, important progress has been made to obtain realistic interactions using chiral effective field theory in which the symmetries of the fundamental theory of quantum chromodynamics (QCD) are exploited [Machleidt and Entem, 2011; Tsunoda and Otsuka, 2016]. Since this allows the systematic derivation of nuclear forces based on the low-energy degrees of freedom and explains the hierarchy of the many-body forces, it is a big step towards a more universal theory of the nucleus.

Once the appropriate valence space is chosen with an effective interaction adapted to it, the tremendous task remains to diagonalize the full Hamiltonian for all J. This is nowadays done using large-scale shell model codes as discussed in the next section. This diagonalization yields the energy eigenstates and the nuclear wave functions from which other observables such as Gamow-Teller transition rates, spectroscopic factors, electromagnetic moments etc. can be calculated.

1.1.3 Large-scale shell model calculations

Over the years, increasingly complex computational methods have been developed to deal with the problem of diagonalizing the shell model Hamiltonian in larger and larger model spaces. The main difficulties arise from the combinatorial growth of the dimensionality of the matrices and the accompanying storage of a huge number of matrix elements. The limits on the maximal dimensions of the Hamiltonian are therefore mostly dictated by the available computational power. At present, many shell model calculation codes are available, for example NATHAN [Caurier and Nowacki, 1999], MSHELL [Mizusaki, 2000] and ANTOINE [Caurier and Nowacki, 1999], which differ in how the model space basis is calculated (m-scheme, J coupled scheme or JT coupled scheme) and how the Hamiltonian is diagonalized. For most of the calculations shown in this thesis, the ANTOINE code is employed. Details about the m-scheme and the Lanczos diagonalization method used in ANTOINE can be found elsewhere [Caurier et al., 2005] and are not immediately relevant for this thesis.

Even with the most advanced shell model codes, many regions of the nuclear chart are out of reach due to the large size of the model space necessary to capture all physics. This concerns the heavy mass regions far from closed shells, regions far from stability where mixing between two or more major shells is found to be important or even moderately sized model spaces occupied by a large number of valence nucleons.
To overcome this limit, the Monte Carlo Shell Model (MCSM) has been proposed [Honma et al., 1995]. Instead of doing the full diagonalization, the Monte Carlo method aims at selecting only a few, relevant eigenstates using stochastic methods (Quantum Monte Carlo Diagonalization). This allows for much larger model spaces including more valence particles than in the conventional calculations. While in the latter, dimensions of pf shell calculations increases up to 10^9, the calculation of ^{48}Cr in the Monte Carlo shell model only requires 40 basis states [Otsuka, 2001]. Although the MCSM does not provide an exact diagonalization, the method is found to give results comparable to the full diagonalization [Shimizu et al., 2013].

Currently, large-scale shell model calculations provide the most accurate description for a wide diversity of experimental situations, although the scope is limited to the light and medium mass regions. Irrespective of whether these are performed in the Monte Carlo Shell Model framework or in the ANTOINE shell model code, the quality of the calculations needs to be validated experimentally. In this context, it is important to note that no errors are given on the calculated observables. In general, the phrase "good agreement with experiment" therefore implies that the experimental trend is well reproduced.

1.1.4 Collectivity

While nuclei in the vicinity of shell closures are usually near-spherical, most nuclei across the nuclear chart have a non-spherical or deformed shape. Very common are for example nuclei exhibiting axially symmetric quadrupole deformation [Moller et al., 1995], whose shape can be modeled as an ellipsoid

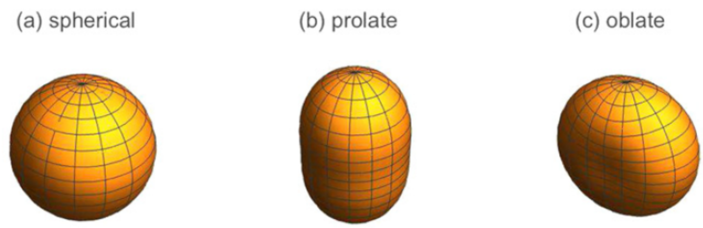

Figure 1.4: Illustration of the main nuclear shapes, pictures taken from [Van Isacker and Pittel, 2016].

described by [Krane, 1987]

$$R(\theta, \phi) = R_{\text{sph}} \left(1 + \beta_2 Y_2^0(\theta, \phi)\right). \tag{1.9}$$

Here R_{sph} is the radius of a sphere with the same volume and $Y_2^0(\theta, \phi)$ does not depend on ϕ (giving rise to cylindrical symmetry). The quadrupole deformation parameter β_2 is defined as

$$\beta_2 = \frac{4}{3}\sqrt{\frac{\pi}{5}}\frac{\Delta R}{R_{\text{sph}}} \tag{1.10}$$

where ΔR is the difference between the long axis and the short axis of the axially symmetric ellipsoid representing the nucleus. Thus, a nucleus with positive β_2 is elongated in a prolate distribution while a negative β_2 indicates a flattened oblate shape, as shown in Fig. 1.4.
In the case that the axial symmetry is broken, the degree of triaxiality is denoted by γ ($\gamma = 0$ for an axially symmetric nucleus).

Although the nuclear shape is not an observable, the notion of shape was for example introduced in the rigid-rotor model since quantum mechanically only non-spherical objects can rotate. In this model, many nucleons are assumed to rotate collectively which gives rise to a typical $I(I+1)$ energy sequence. In literature, the terms "collectivity" and "deformation" are even often used interchangeably.
It is not immediately obvious how shape, defined in the intrinsic frame of the nucleus, can be related to the nuclear wave functions in the laboratory frame. Collectivity, however, is inherently included in the interacting shell model. To explain how collective phenomena emerge from an underlying independent-particle picture, the number of active protons and neutrons and the interactions between them are crucial. In between shell closures, the many available valence particles allow for an efficient build-up of residual interactions which leads to very correlated (i.e. highly fragmented) wave functions [Casten, 2000; Poves,

2011; Heyde, 2013]. However, such highly fragmented wave functions are not easy to interpret in terms of the underlying physics.

An important step to describe nuclear deformation in the laboratory frame was made by Elliott [1958a,b] who showed that the typical $I(I+1)$ rotational band structure could be reproduced by using the fact that SU(3) is a symmetry of the harmonic oscillator shell model wave functions. Despite the somewhat limited applicability of exact SU(3), in which the valence space is restricted to one degenerate harmonic oscillator shell and in which only the quadrupole-quadrupole interaction is important, the approximate quasi-SU(3) and pseudo-SU(3) variants are applicable in many realistic situations [Poves, 2016].
Pseudo-SU(3) [Raju et al., 1973] applies to orbitals with the same j-sequency as the full harmonic oscillator shell with principal quantum number -1 (example: the $p_{3/2}$, $p_{1/2}$ and $f_{5/2}$ orbitals form a pseudo-SU(3) block because their j's correspond to the sd-shell). Quasi-SU(3) [Zuker et al., 1995, 2015] deals with the $j_> = \ell + 1/2$ orbit and its quadrupole partners with $\Delta j = 2$ and $\Delta\ell = 2$ (example: $g_{9/2}$, $d_{5/2}$ and $s_{1/2}$).
Large-scale shell model calculations using valence spaces adapted to these approximate symmetries have been shown to correctly reproduce quadrupole properties of deformed states. As such, they provide interesting truncation strategies to deal with large valence spaces, as for example needed to describe islands of inversion (see section 1.2.3).

1.2 Exotic nuclei

For many decades, nuclear models were constructed based on experiments using stable beams and targets, giving access to nuclei close to the valley of stability. Meanwhile, continuous efforts to improve radioactive beam production and detection systems have enabled studies of increasingly exotic nuclei, with proton-to-neutron ratios which differ significantly from the stable isotopes. As soon as these exotic regions of the nuclear chart could be explored, unexpected phenomena were observed which challenged the conventional views. Due to the new insights which can be gained from their study, a lot of effort is dedicated to rare isotope research, both experimental and theoretical. This has led to a considerable advance in understanding the nucleus in the last few decades, while the prospect of going even more exotic promises many exciting discoveries in the future.

1.2.1 Rare isotope production

For most experimental purposes it is necessary to have pure and intense beams of radioactive ions [Blumenfeld et al., 2013]. The production of exotic species is however hindered by the short half-lives, low production yields and the overwhelming production of unwanted contamination. The production techniques should therefore be fast, efficient and selective. A general description of the two main families of radioactive ion beam facilities is given here, while the GANIL and ISOLDE facilities are described in more detail later.

In the ISOL (isotope separation online) method, a driver beam of light particles impinges on a thick, heavy production target and a variety of isotopes are produced via fragmentation, spallation and fission reactions, amongst others. The reaction products are thermalised in the target, diffuse through the target matrix and effuse towards the ion source via a hot transfer line. To enhance the diffusion and effusion processes, the target is heated to high temperatures of around 2000°C. This diffusion depends strongly on the element-target chemistry and diffusion times range from a few ms to much longer for a few refractory elements. This relatively slow and chemistry-dependent extraction procedure is an important disadvantage of ISOL-facilities as it limits the half-lives and range of isotopes which can be produced. After extraction from the target, the reaction products are ionized in an appropriate ion source and subsequently accelerated electrostatically to several tens of keV. To select the isotope of interest from the cocktail of stable and unstable isotopes produced in the reaction process, the ion beams are mass separated according to their mass-over-charge ratio in one or several bending magnets. The mass separated beams are then directly sent to the low-energy beam lines or post-accelerated for applications which require higher energies up to a few MeV/u.

In the *in-flight* technique, an accelerated heavy-ion beam impinges on a light, thin target which produces radioactive isotopes via fragmentation reactions. The secondary beam is produced at a speed similar to the primary beam and the ions are (fully) stripped of their electrons. The fragments are subsequently selected in a large-acceptance fragment separator consisting of dipole magnets for selection according to the magnetic rigidity in combination with an intermediate energy degrader for additional Z-selection. Afterwards, they are delivered to the experimental set-ups. The main advantages of in-flight facilities are the possibility of producing radioactive isotopes regardless of their chemical properties and the fast extraction times such that isotopes with half-lives down to less than one μs can be studied. Additionally, the beams can be spin-polarized in the reaction process. On the other hand, the yields are usually lower than at ISOL-facilities and the beam quality is often worse.

1.2.2 Structure of exotic nuclei

The shell model and its magic numbers provide a valid starting point for the study of the nuclear structure, as illustrated by the big success of describing properties near the valley of stability. However, when the experimental data on nuclei far from stability started to accumulate, it became clear that the paradigm of immutable magic numbers needed to be modified. The concept of *shell structure evolution* in exotic nuclei is now commonly accepted and an important goal in present-day nuclear structure physics is to identify the drivers of this structural evolution.

To understand how evolution in shell structure comes about, the two-body matrix elements introduced in section 1.1.2 need to be examined more closely. Since the proton-neutron interaction is stronger than the interaction between like particles, it is the main reason for the observed structural changes [Sorlin, 2009].
Dufour and Zuker [1996] pointed out that any effective interaction can be divided in a monopole (m) and a multipole (M) part

$$H = H_m + H_M. \tag{1.11}$$

This representation has the advantage that it allows studying the interplay between the (changing) shell gaps, described by the monopole part, and the strong correlations between the valence nucleons, described by the multipole part.

The monopole matrix element or *centroid* of the interaction between two nucleons in orbitals with angular momentum j and j', is the average of the interaction over all directions, independent of their relative orientation [Otsuka and Tsunoda, 2016]

$$v_m(j,j') = \frac{\sum_J (2J+1)\langle jj'J|V|jj'J\rangle}{\sum_J (2J+1)}. \tag{1.12}$$

This monopole component causes a shift $\Delta\epsilon_j$ in the single-particle energy of the orbit j, when the orbital j' is filled

$$\Delta\epsilon_j = v_m(j,j')n_{j'}. \tag{1.13}$$

In this context, often the term effective single-particle energy is used (ESPE). Since the shift is linear in the occupation of orbital j' ($n_{j'}$), the monopole interaction can cause a significant change in single-particle energy when going from stability towards the exotic nuclei. This explains why it is an important mechanism behind the observed shell evolution.
Note that the monopole shift was already included in the original Hamiltonian

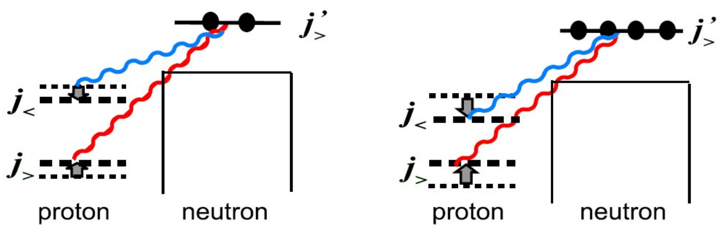

Figure 1.5: Schematic illustration of the effect of the tensor force, picture taken from [Otsuka and Tsunoda, 2016].

in eq. 1.7. Nevertheless, its meaning in terms of the tensor part of the nuclear force was only discussed by Otsuka and collaborators in the beginning of this century [Otsuka et al., 2001, 2005]. The effect of the tensor force is illustrated in Fig. 1.5, where the proton orbitals are spin-orbit partners

$$j_> = \ell + 1/2, \qquad j_< = \ell - 1/2. \tag{1.14}$$

The tensor interaction is attractive between $j_<$ and $j'_>$ orbitals while it is repulsive for $j_>$ and $j'_>$ ($j_<$ and $j'_<$) orbitals. As compared to the situation with two neutrons in the $j'_>$ orbital, the proton $j_<$ orbital is more bound (lower in energy) when four neutrons occupy the $j'_>$ orbital. Conversely, the proton $j_>$ orbital is less bound (higher in energy). This means that the proton spin-orbit energy gap becomes smaller with an increasing number of neutrons in $j'_>$. Not limited to spin-orbit partners, the effect is largest when $\Delta\ell \approx 0$ and $\Delta n \approx 0$, such that a maximal overlap of the radial wave functions is obtained and the nuclear interaction can have maximal effect.
The robust mechanism for shell structure evolution due to the tensor interaction presented above, provides an intuitive framework to explain changes in single-particle energies as a function of the proton or neutron occupation of certain orbits.

The multipole part of the Hamiltonian is dominated by a pairing component plus the quadrupole-quadrupole interaction [Poves, 2011]. Pairing is the most important for like particles and has the far-reaching consequence that most of the nucleons in the nucleus are paired to total angular momentum zero. The quadrupole correlations on the other hand, are strongest between protons and neutrons and drive a system with a sufficiently large number of valence nucleons towards deformation.

The balance between the opposite effects produced by the monopole part (shell gaps) and multipole part (correlations) of the Hamiltonian governs the structure of a nucleus with a particular number of protons and neutrons. This subtle balance will be the key ingredient for the appearance of islands of inversion as discussed next.

1.2.3 Islands of inversion

In the island of inversion, deformed configurations associated with n particle-n hole (np-nh) excitations across a shell gap are found to lie below the spherical configurations obtained by a normal filling of the shell model orbitals. Since the energy cost of promoting n nucleons from the lower to the higher shell is n times the shell gap, np-nh configurations are usually expected at high energies. However in some cases, the loss in energy can be compensated by a huge gain in correlation energy such that the np-nh configurations come down in energy and can even become the ground state. Therefore these np-nh configurations are often referred to as intruder configurations.

Although the reduction of the shell gap under influence of the monopole interaction (shell quenching) facilitates excitations across the shell gap, the most important contribution to lowering the intruder's energy comes from the strong proton-neutron correlations [Heyde and Wood, 2011]. To qualitatively estimate whether ground state deformation could be energetically favourable, several aspects need to be considered. To support the efficient development of quadrupole correlations, the orbitals near the Fermi level need to be adapted to the quadrupole coupling schemes (pseudo/quasi-SU(3)), as discussed in section 1.1.4. In addition, the degree of collectivity is determined by the total size of the proton-neutron valence space. This means that open proton shells are advantageous in order to build highly correlated states by exciting neutrons across the shell gap (and vice versa) while closed (sub)shells stabilise the system in a spherical shape.

Quantitatively, the energies of the normal and intruder configurations are calculated using large-scale shell model interactions including at least 2 major shells. A systematic study of the island of inversion around $N = 20$ was performed using the SDPF-U-MIX interaction [Caurier et al., 2014]. The effect of correlations on the relative energy difference between the 0p-0h and 2p-2h configurations of the $N = 20$ isotones is illustrated in Fig. 1.6. Without correlations, the energy of the 2p-2h intruder state is lowered with respect to the normal 0p-0h state when protons are removed from the $\pi d_{5/2}$-orbital, reflecting the reduction of the $N = 20$ shell gap due to the monopole shift. Although this amounts to a decrease of more than 9 MeV between $Z = 14$ and $Z = 8$, it is not sufficient to make the 2p-2h configurations the ground state. Only when correlations are included, is the experimentally observed inversion of intruder and normal configurations reproduced. The calculated correlation energy gain

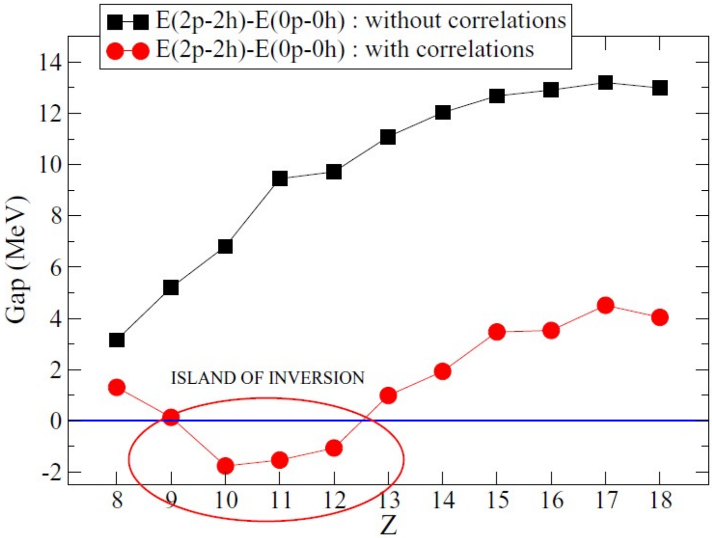

Figure 1.6: Illustration of the effect of correlations on the energy difference between the 0p-0h and 2p-2h configurations, as taken from [Caurier et al., 2014].

is around 10 MeV for the open proton shell nuclei, while at the $Z = 8$ shell closure this decreases to less than 2 MeV.

1.2.4 Side note

From the above discussion, it is clear that exotic nuclei play a crucial role in the development of nuclear models. They provide decisive tests for the predictive power of models when going to new regions of the nuclear chart and they offer the possibility to study previously unknown features of the nucleon-nucleon interaction which are amplified due to their asymmetric proton-to-neutron ratios. Nevertheless, the comprehensive understanding of nuclei far from stability can only succeed when the changing nuclear structure is mapped from the valley of stability up to the most exotic nuclei. Only by performing systematic studies along the isotopic and isotonic chains, can unexpected phenomena be identified and can their origins be characterised.

2 | Ground state properties

Progress in nuclear theory goes hand in hand with the development of experimental techniques. The available theories can be put to a test by comparison to experimental observables, and predictions deviating from experiment can provide guidelines for the improvement of the nuclear models. To obtain a comprehensive picture of the atomic nuclei, a variety of experimental observables need to be known, each giving complementary pieces of information on the nuclear structure. In this work, spins, magnetic dipole moments, electric quadrupole moments and changes in mean-square charge radii of ground states[1] are measured. These ground state properties will be shortly introduced in this chapter along with what we can learn from them.

2.1 Nuclear spins

Each nuclear state can be labeled by its total angular momentum, the nuclear spin I, and parity π. The nuclear spin is the vector sum of the angular momenta of each nucleon, taking into account the intrinsic and orbital angular momentum $\boldsymbol{j} = \boldsymbol{\ell} + \boldsymbol{s}$, while the total parity is the multiplication of the parities of each nucleon. Since the pairing interaction favours coupling of nucleons to anti-parallel pairs of zero angular momentum, in practice one only has to consider the valence nucleons. This lead to the following general observations:

- Without a single exception, all even-even nuclei have ground state spin $I = 0^+$.
- For many odd-A nuclei, especially those near shell closures, the ground state spin and parity is determined by the last valence nucleon in orbital j.

[1] and long-lived isomers

- For many odd-odd nuclei, the ground state spin can be calculated from the vector sum of the proton $\boldsymbol{j}_\pi$ and neutron $\boldsymbol{j}_\nu$ spin which ranges from $I = j_\pi + j_\nu$ to $I = |j_\pi - j_\nu|$. Which possibility comes lowest in energy and thus becomes the ground state can be qualitatively estimated via Paar's rule [Paar, 1979].

The spin therefore gives a first indication of the single-particle orbitals occupied by the valence nucleons and deviations from these general guidelines point to correlations beyond the single-particle picture.
The firm determination of the ground state spins is indispensable in order to build reliable level schemes from experimental decay data.

2.2 Nuclear moments

The motion and configuration of the nucleons inside the nucleus can be probed via its electromagnetic moments. The magnetic dipole moment (commonly referred to as magnetic moment) arises from convection and spin currents in the nucleus while the electric quadrupole moment (commonly referred to as quadrupole moment) is associated with the nuclear charge distribution. The nuclear moments give therefore direct information on the structure of a nucleus, as illustrated with numerous examples in [Neyens, 2003]. Historically, magnetic dipole moments were crucial for the development of the nuclear shell model while evidence for regions of strong deformation between the shell closures were deduced from systematic studies of electric quadrupole moments.

2.2.1 The magnetic dipole moment

Classically, the magnetic moment of an orbiting particle with angular momentum $\boldsymbol{\ell}$ is given by

$$\boldsymbol{\mu} = \frac{q}{2m}\boldsymbol{\ell} \tag{2.1}$$

where q and m are the charge and mass of the particle. In quantum mechanics, the magnetic moment operator originates from both its orbital and intrinsic angular momentum, the spin. The magnetic moment operator of the entire nucleus can be written as the sum of the individual contributions of the nucleons

$$\hat{\mu} = \frac{\mu_\mathrm{N}}{\hbar}\left(\sum_i^A g_\ell^i \hat{\ell}_i + \sum_i^A g_s^i \hat{s}_i\right) \tag{2.2}$$

where the nuclear magneton $\mu_{\mathrm{N}} = \frac{e\hbar}{2m_\pi}$ is the often omitted unit of the nuclear magnetic moment. g_ℓ and g_s are the orbital and spin gyromagnetic ratios which for a free proton and neutron are given by

$$g_\ell^\pi = 1, \quad g_s^\pi = +5.585694700(18) \quad \text{(free proton)} \tag{2.3}$$

$$g_\ell^\nu = 0, \quad g_s^\nu = -3.82608545(90) \quad \text{(free neutron)} \tag{2.4}$$

Alternatively, the magnetic moment can be written in terms of the nuclear spin $\hat{I}$ and the nuclear g-factor

$$\hat{\mu} = \frac{\mu_{\mathrm{N}}}{\hbar} g \hat{I} \tag{2.5}$$

The magnetic moment is then obtained by taking the expectation value of the z-component for a state $|I, m = I\rangle$

$$\mu = \langle I, m = I| \, \hat{\mu}_z \, |I, m = I\rangle \tag{2.6}$$

$$= gI\mu_{\mathrm{N}}. \tag{2.7}$$

This shows that a spin $I = 0$ nucleus has a zero magnetic moment.

Magnetic moments, or specifically the nuclear g-factors, are very sensitive to which orbitals are occupied by the valence nucleons and as such, they give important information on the nuclear wave function. In a pure single-particle picture of an odd-A nucleus, all but one nucleon pairs to spin zero and the magnetic moment is determined by the last valence nucleon in orbital j

$$\mu(\ell + 1/2) = \left[\left(j - \frac{1}{2}\right) g_\ell + \frac{1}{2} g_s\right] \tag{2.8}$$

$$\mu(\ell - 1/2) = \frac{j}{j+1}\left[\left(j + \frac{3}{2}\right) g_\ell - \frac{1}{2} g_s\right] \tag{2.9}$$

These values are referred to as the *Schmidt moments*. Furthermore, the g-factor is not sensitive to the number of particles in a specific orbital since [Heyde, 1990]

$$g(j^n) = g(j) \tag{2.10}$$

This expression is even valid in the case that the final spin of the state does not equal the spin of the occupied orbital, for example $g(\pi f_{7/2}^3)_{7/2^-} = g(\pi f_{7/2}^3)_{5/2^-}$. These two simple relations can already explain a few general observations seen in nuclei not too far from magic numbers:

- Isotopes having their unpaired valence nucleons in the same orbital have very similar g-factors, as for example illustrated for the odd-Z $\pi f_{7/2}$-nuclei in Fig. 6.6. This g-factor is close to the Schmidt value although some general deviations can be seen. Comparison of the measured g-factor to the single-particle estimate then gives information on the configuration of the valence nucleons.

- The g-factors of odd-Z, even-N nuclei are approximately constant along an isotopic chain, since they are only determined by the last unpaired proton[2]. A sudden change in g-factor is then an indication for a changing orbital occupancy as was recently discussed for Cu, Ga [Flanagan et al., 2009; Cheal et al., 2010] and K [Papuga et al., 2013].

The deviation of the experimentally observed g-factors from the Schmidt value has two explanations. Firstly, the pure single-particle picture is too simple and mixing of other configurations into the wave function needs to be taken into account. Hence, the experimental g-factor lies closest to the Schmidt value at neutron or proton shell closures since there the configuration mixing is limited. In particular, g-factors are sensitive to mixing of spin-orbit ($j = \ell \pm 1/2$) partners into the wave function [Arima and Horie, 1954; Noya et al., 1958; Lutter et al., 1974] and even admixtures of a few percent will have significant influence on the total magnetic moment[3]. As can be seen from the near constant trend across the isotopic chain, the g-factor is on the other hand not very sensitive to deformation effects originating from quadrupole (E2) correlations and coupling to vibrations of the core.
Secondly, even if the assumption of a pure-single particle wave function is valid, for example for doubly-magic $\pm$ 1 nuclei, the g-factor is reduced due to the influence of the nuclear medium. A common approach is therefore to replace the free nucleon g-factors by effective ones, typically $g_{s,\mathrm{eff}} \approx 0.7 - 0.9 g_{s,\mathrm{free}}$ and $g^{\pi}_{\ell,\mathrm{eff}} \approx 1.1$, $g^{\nu}_{\ell,\mathrm{eff}} \approx -0.1$. These effective g-factors include corrections due to meson exchange currents (which result in the addition of two-body terms to the magnetic moment operator) and first and second order core-polarization effects [Castel and Towner, 1990].

The magnetic moment of an odd-odd nucleus can be decomposed in the unpaired proton and neutron contribution. For a state with spin I obtained from the

[2] The same would of course be true for even-Z,odd-N nuclei but systematic studies of an isotonic chain are less common.

[3] In a two level mixing picture, $|I\rangle = \alpha|\ell - 1/2\rangle + (1-\alpha)|\ell + 1/2\rangle$ such that $\mu = \alpha^2 \mu_{\ell-1/2} + (1-\alpha)^2 \mu_{\ell+1/2} + \alpha(1-\alpha)\langle \ell - 1/2|\hat{\mu}|\ell + 1/2\rangle$. Since the M1 off-diagonal matrix element is non-vanishing between spin-orbit partners, this gives an important contribution to the total magnetic moment, in addition to the small contribution proportional to $(1-\alpha)^2$. A worked out example can be found e.g. in appendix A.5 of the thesis of Garcia Ruiz [2015].

weak coupling of a proton in orbital j_π and neutron in orbital j_ν, the magnetic moment can be calculated by [Heyde, 1990]

$$\mu(I) = \frac{I}{2}\left[\frac{\mu_\pi}{j_\pi} + \frac{\mu_\nu}{j_\nu} + \left(\frac{\mu_\pi}{j_\pi} - \frac{\mu_\nu}{j_\nu}\right)\frac{j_\pi(j_\pi+1) - j_\nu(j_\nu+1)}{I(I+1)}\right]. \tag{2.11}$$

As an estimate for the proton and neutron magnetic moments μ_π and μ_ν, the empirical values of the neighbouring odd mass nuclei can be used, or when these are not available, the effective Schmidt values. Comparison of the experimental moment of the odd-odd nucleus with the calculated value, assuming a particular configuration for the protons and the neutrons, then allows a test of the purity of the proposed configuration.

Although a few-particle model with configuration mixing can satisfactorily describe the magnetic moment of many nuclei, nuclei far from magic numbers are sometimes also treated in a collective model. In the coupling scheme for strongly deformed nuclei, the magnetic moment of an odd-A nucleus is given by [Villars, 1957]

$$\mu = g_R I + (g_K - g_R)\frac{K^2}{I+1} \tag{2.12}$$

where g_K arises from the single-particle motion in a deformed potential and $g_R \approx Z/A$ is the collective gyromagnetic ratio of a rigid-rotor. It is for example observed that the g-factors of many 2^+ states in even-even nuclei are approximately equal to Z/A. Note that for $K = 1/2$, also the decoupling constant should be taken into account.

2.2.2 The electric quadrupole moment

The electric quadrupole moment is a measure of the non-sphericity of the nuclear charge distribution. This is clear from the definition of the quadrupole moment operator in Cartesian coordinates

$$\hat{Q} = \sum_i^A e_i(3z_i^2 - r_i^2) \tag{2.13}$$

where the e_i are effective charges taking into account core-polarization effects (typical values are $e_\pi \approx 1.1 - 1.5$ and $e_\nu \approx 0.1 - 1$). Since the neutrons have a non-zero effective charge, they can also contribute to the quadrupole moment. Equivalently to eq. 2.13, the quadrupole moment operator can be written in terms of the spherical tensor components

$$\hat{Q} = \sqrt{\frac{16\pi}{5}}\sum_i^A e_i r_i^2 Y_2^0(\theta_i, \phi_i). \tag{2.14}$$

The experimentally measured quadrupole moment is found by taking the expection value of the $\hat{Q}_z$ in the state $|I, m = I\rangle$

$$Q_s = \langle I, m = I|\hat{Q}_z|I, m = I\rangle \tag{2.15}$$

$$= \sqrt{\frac{I(2I-1)}{(2I+1)(2I+3)(I+1)}} \langle I\|\hat{Q}_z\|I\rangle \tag{2.16}$$

Written in terms of the reduced matrix element using the Wigner-Eckhart theorem, it becomes clear that the spectroscopic quadrupole moment of a nuclear state with spin $I < 1$ is zero although this does not imply that the state is not deformed in its intrinsic reference frame.

Similar to the case of the magnetic moment, the quadrupole moment of nuclei not too far from magic numbers is determined by the configuration of the valence particles. Let's first look at the isotopes with an odd number of neutrons (protons) and an even number of protons (neutrons). For a nucleus with a single particle or hole outside a closed shell, the single-particle (sp) quadrupole moment is

$$Q_{\text{sp}} = -e_j \frac{2j-1}{2j+2} \left\langle r_j^2 \right\rangle \tag{2.17}$$

where j denotes the orbital and $\left\langle r_j^2 \right\rangle$ is the mean-square charge radius (see section 2.3). This means that the quadrupole moment of one particle orbiting a closed shell is negative which can be interpreted as the polarization of the spherical core by the particle towards an oblate shape, while the positive quadrupole moment of a single hole reflects the polarization towards a prolate shape.
If an orbital contains more than one particle, all of the n particles in that orbital contribute to the quadrupole moment according to

$$Q(j^n) = Q_{\text{sp}} \left(\frac{2j+1-2n}{2j-1} \right) \tag{2.18}$$

From this relation it can be seen that the quadrupole moment varies linearly between Q_{sp} and $-Q_{\text{sp}}$ and is zero for a half-filled orbital. This means that for a nucleus with an odd number of neutrons and an even number of protons, the filling of the subsequent neutron orbitals along an isotopic chain is reflected in the piecewise straight lines in the quadrupole moments, as for example seen in the Ca isotopes [Garcia Ruiz et al., 2015]. Sometimes the quadrupole moments of an isotopic chain follow a linear trend which is shifted upwards such that the quadrupole moment is not exactly zero for an half-filled orbital [Neyens, 2003]. This is evidence for a core-contribution to the quadrupole moment

$$Q_s = Q_{\text{core}} + Q_{\text{sp}}. \tag{2.19}$$

The single-particle moment of an odd-proton, even-neutron nucleus and how this varies with increasing proton number is similarly given by eq. 2.18. Usually however, we are interested in how the quadrupole moment changes with the addition of neutrons along an isotopic chain. The additional neutrons induce a polarization of the core which is quadratic in the number of valence particles/holes, resulting in a quadrupole moment which changes parabolically between two shell closures, as for example seen in Cu [Vingerhoets et al., 2010].

Similar to the magnetic moment, the quadrupole moment for odd-odd nuclei with spin I arising from a weak coupling between the odd proton (j_π) and the odd-neutron (j_ν), can be decomposed in a proton and neutron component

$$Q_s(I) = \begin{pmatrix} I & 2 & I \\ -I & 0 & I \end{pmatrix} (-1)^{j_\pi + j_\nu + I}(2I+1) \tag{2.20}$$

$$\times \left[\begin{Bmatrix} j_\pi & I & j_\nu \\ I & j_\pi & 2 \end{Bmatrix} \frac{Q_s(j_\pi)}{\begin{pmatrix} j_\pi & 2 & j_\pi \\ -j_\pi & 0 & j_\pi \end{pmatrix}} + \begin{Bmatrix} j_\nu & I & j_\pi \\ I & j_\nu & 2 \end{Bmatrix} \frac{Q_s(j_\nu)}{\begin{pmatrix} j_\nu & 2 & j_\nu \\ -j_\nu & 0 & j_\nu \end{pmatrix}} \right]$$

Moreover, the quadrupole moments are very sensitive to development of deformation in nuclei. For the specific case of a well-deformed axially symmetric nucleus, the spectroscopic quadrupole moment (measured in the laboratory frame) gives access to the intrinsic quadrupole moment Q_0 through

$$Q_s = \frac{3K^2 - I(I+1)}{(I+1)(2I+3)} Q_0 \tag{2.21}$$

where K is the spin-projection on the symmetry axis. This intrinsic quadrupole moment can be related to the quadrupole deformation parameters $\langle\beta_2\rangle$ via

$$Q_0 \approx \frac{3}{\sqrt{5\pi}} Z \langle r^2_{\text{sph}} \rangle \langle\beta_2\rangle (1 + 0.36\langle\beta_2\rangle) \tag{2.22}$$

not taking into account the surface correction which is very small. A change in static deformation is therefore reflected in a change in quadrupole moment.

2.3 Mean-square charge radii

The nuclear size is a fundamental property of the nucleus, often characterised by its radius. When the experimental methods used to probe this size are electromagnetic in nature, only the contribution from the charged protons is measured and one talks about the charge radius of a nucleus. The difference between the mass radius and charge radius $\Delta r_{\nu\pi}$ can be investigated with hadronic probes, showing that $\Delta r_{\nu\pi}$ is small for stable isotopes but increases with $(N - Z)/A$. For very neutron-rich isotopes, larger differences can be expected, notably in halo nuclei [Nörtershäuser and Geppert, 2014]. For the most neutron-rich isotope of which the charge radius is studied in this work (^{64}Mn), a difference of 0.18 fm is predicted [Duflo and Zuker, 2002].

In a first approximation, the nucleus can be considered as a uniformly charged liquid drop with a radius

$$R = 1.2A^{1/3} \text{ fm} \tag{2.23}$$

which has a simple dependence on the atomic mass number A. This implies that the nuclear volume is globally proportional to the number of nucleons inside the nucleus.

More generally, the nuclear charge distribution needs to be described by its different radial moments of which the second, the mean-square charge radius, $\langle r^2 \rangle$

$$\langle r^2 \rangle = \frac{\int \rho_N(\boldsymbol{r}) r^2 d\boldsymbol{r}}{\int \rho_N(\boldsymbol{r}) d\boldsymbol{r}} \tag{2.24}$$

is the one experimentally accessible with the collinear laser technique used in this work. The denominator represents the total charge of the nucleus eZ and ρ_N is the nuclear charge density distribution.

While the global increase in mean-square charge radius with increasing mass number displays a liquid drop behaviour, it is the deviation from this trend which reveals the underlying nuclear structure. An important example is the manifestation of a shell closure by a characteristic kink in the mean-square charge radii, related to the reduced correlations at magic proton or neutron numbers [Angeli et al., 2009]. Deformation on the other hand, results from the strong development of correlations and hence leads to an increase in charge radii compared to the spherical limit. This is described according to

$$\langle r^2 \rangle = \langle r^2 \rangle_{\text{sph}} \left(1 + \frac{5}{4\pi} \sum_i \langle \beta_i^2 \rangle \right) \tag{2.25}$$

where $\langle \beta_i^2 \rangle$ is the mean-square deformation parameter of order i. For an axially symmetric quadrupole deformed nucleus, this becomes

$$\langle r^2 \rangle = \langle r^2 \rangle_{\text{sph}} \left(1 + \frac{5}{4\pi} \langle \beta_2^2 \rangle \right) \tag{2.26}$$

Here $\langle r^2 \rangle_{\text{sph}}$ is the spherical nucleus of identical volume often modeled by the droplet model [Myers and Schmidt, 1983; Berdichevsky and Tondeur, 1985].

The change in quadrupole deformation between two isotopes A and A' can then be estimated from the change in mean-square charge radius

$$\delta\langle r^2\rangle^{A,A'} \approx \delta\langle r^2\rangle^{A,A'}_{\mathrm{sph}} + \langle r^2\rangle_{\mathrm{sph}}\frac{5}{4\pi}\delta\langle\beta_2^2\rangle^{A,A'}. \tag{2.27}$$

Contrary to the quadrupole moment, the nuclear charge radius is not only sensitive to a change in static deformation, but also to dynamical shape fluctuations which have a contribution to $\langle\beta_2^2\rangle$ but average out in $\langle\beta_2\rangle$. A comparison between $\langle\beta_2\rangle^2$ from the quadrupole moments and $\langle\beta_2^2\rangle$ from the charge radii therefore gives information on the dynamic nature of the deformation (i.e. on the steepness of the potential energy well as a function of quadrupole deformation)

$$\langle\beta_2^2\rangle = \langle\beta_2\rangle^2 \qquad \text{(static)}, \tag{2.28}$$

$$- (\langle\beta_2\rangle^2 - \langle\beta_2^2\rangle) \qquad \text{(dynamic)}. \tag{2.29}$$

Across the chart of nuclides, it is observed that the charge radius of an odd-neutron isotope is consistently smaller than the average of its even-neutron neighbours. Although this odd-even staggering (OES) in the mean-square charge radii is ubiquitous, no general microscopic explanation without phenomenological input is available. Qualitatively, the odd-even scattering is associated with the blocking of pair scattering due to the odd neutron.
Sudden changes in the magnitude or even inversions of the odd-even staggering have been interpreted as due to nuclear structure effects such as deformation or reflection-asymmetric shapes, see for example Lievens et al. [1996] and Budinčević et al. [2014].

2.4 Nuclear structure fingerprints

As shown in the previous sections, spins, nuclear moments and mean-square charge radii are sensitive probes to study nuclear structure features such as magicity and collectivity. Beyond these ground state properties, a variety of other fingerprints exist to identify these features, including - but not limited to - masses, low-energy excitation spectra and transition probabilities. None of these observables on its own is sufficient to probe the complex structure of an atomic nucleus, and only by measuring a variety of complementary observables can a comprehensive picture be obtained.

Nuclear masses are often one of the earliest properties which can be measured for exotic nuclei and provide a first insight in the nuclear structure. Similar to the mean-square charge radii, masses are bulk properties embodying all interactions in the nucleus. The global variation in masses along an isotopic chain is smooth while deviations from this smooth behaviour indicate underlying changes in nuclear structure. To highlight these small changes, usually the mass derivative is plotted under the form of the two-neutron separation energies. At closed shells, these two-neutron separation energies show a sudden drop since it costs less energy to remove a pair of neutrons outside a closed shell compared to just before. A sudden increase in two-neutron separation energies on the other hand is then a manifestation of deformation. Note however that a large difference in nuclear deformation is not always accompanied by a large change in binding energy (mass), which is maybe most obvious in the context of shape coexistence where states with very different shapes can be almost degenerate in energy.

In even-even nuclei, a high energy of the first excited 2^+ state in combination with a small reduced transition probability $B(E2; 2^+ \rightarrow 0^+)$ are both evidence for the rigidity against excitations and therefore point to a possible shell closure. Conversely, a low $E(2^+)$ and high $B(E2)$ suggest a collective wave function. Another key observable is the ratio between the energy of the 4^+ and 2^+ state which provides a convenient classification of the shape excitation mode: $E(4^+)/E(2^+)$ is smaller than 2 for a non-collective state, around 2 for spherical-vibrational states[4] and equal to 3.33 for a rigid-rotor. Transitional values around 2.5 are typically observed in γ-soft states.

[4] Recent work, however, questions the existence of spherical-vibrational states below the pairing gap in atomic nuclei [Garrett and Wood, 2010].

Part II

β-NMR on neutron-rich Al

3 | β-NMR at LISE-GANIL

The neutron-rich Al isotopes were studied via β-detected nuclear magnetic and quadrupole resonance at the LISE-GANIL facility. This chapter deals with the experimental aspects of the production of (spin-polarized) radioactive ion beams at LISE, the β-NMR/NQR technique and how the g-factors and quadrupole moments can be extracted from the measured spectra.

3.1 The LISE-GANIL facility

GANIL (Grand Accélérateur National d'Ions Lourds) is a French laboratory which provides intermediate-energy heavy ions beams for fundamental nuclear research as well for nuclear related applications. In the β-NMR experiments, these heavy ions serve as the primary beam for radioactive isotope production via the in-flight technique.

The primary beam with intensities of a few μA is accelerated to 40-100 MeV/u in two consecutive cyclotrons after which it is injected in the LISE beam line (Ligne d'Ions Super-Epluchés[1]). Here the beam impinges on a thin, rotating target, typically 200-2000 μm of ^{9}Be, producing a variety of isotopes in projectile-fragmentation and pick-up reactions. In the process, the reaction products are stripped of their electrons and obtain a velocity close to the primary beam velocity. The secondary beam in then purified in the LISE3 fragment separator consisting of two dipole magnets combined with a wedge degrader in the intermediate plane. The selection of the dipole magnets is determined by the magnetic rigidity

$$B\rho \propto \beta\gamma\frac{A}{q} \tag{3.1}$$

[1] Fully stripped ions beam line.

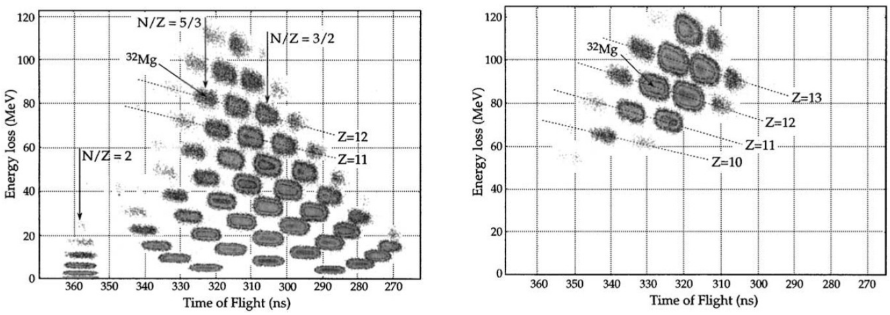

Figure 3.1: Illustration of the purity of the secondary fragment beam obtained with pure magnetic rigidity selection without wedge (left) and with additional energy-loss filtering with a wedge (right). Note that the number of contaminants is reduced significantly by introducing the wedge. The constant Z-lines as well as the constant time of flight lines corresponding to constant N/Z are indicated. Figures taken from [Bazin et al., 2002].

where $\beta = v/c$, $\gamma = 1/\sqrt{1-\beta^2}$ and $q = Z$ for fully stripped fragments. Apart from a dependence on the mass-over-charge ratio, the selection thus also depends on the velocity of the fragments. After the first dipole, the fragments lose energy (and as such lose velocity) in the wedge degrader according to A^3/Z^2 [Anne et al., 1987]. The velocity dependence of the second dipole therefore results in an additional purification and in optimal conditions high-purity beams (>85%) of the fragment of interest can be achieved. The energy loss versus time of flight plots, used for the identification of the fragments, show the large reduction of contaminants in the beam by the introduction of a wedge degrader, as illustrated in Fig. 3.1. If necessary, further purification can be obtained by a Wien filter. The selected fragments are finally guided to the β-NMR apparatus, as shown in Fig. 3.2.

The LISE++ program [Tarasov and Bazin, 2008] can be used to simulate the production of radioactive nuclei and transmission through the ion optics in fragment separators. It is therefore very useful in the preparation of an experiment for the optimisation of the target and wedge thickness, magnetic rigidity etc. in order to obtain the most intense and pure secondary beams of the isotope of interest.

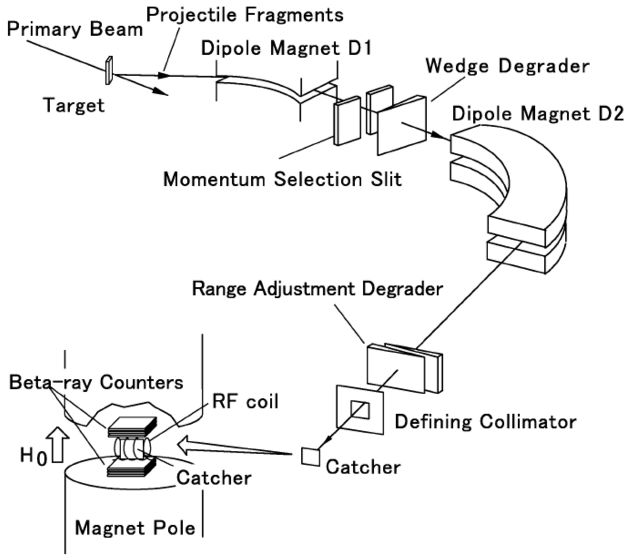

Figure 3.2: Schematic of the important elements for the production and selection of radioactive ions beam for β-NMR at in-flight facilities. Figure taken from [Asahi and Matsuta, 2001].

.

3.1.1 Spin-polarization

An important feature of radioactive beam production at fragment separators is that the secondary beams can be spin-oriented in the projectile-fragmentation or pick-up reactions.

Spin-orientation means that the nuclear spin ensemble has a preferential direction in space. By defining the probability p_m that the spin has a projection $|m\rangle$ on the z-axis, one can distinguish between spin-alignment, in which $p_m = p_{\text{-}m}$ for every m, and spin-polarization, in which $p_m \neq p_{-m}$ for at least one $m \neq 0$. In this thesis, only spin-polarization is considered and the amount of polarization is given by $P = \frac{1}{I} \sum_m m p_m = \frac{\langle I_z \rangle}{I}$.

To qualitatively describe the production of spin-polarized beams in projectile-fragmentation reactions, a simple kinematical model was developed [Asahi et al., 1990; Okuno et al., 1994], which was later extended for pick-up reactions [Turzó et al., 2006]. Although the model is only strictly valid for relativistic energies, also at the intermediate energies of few tens of MeV/u typical for GANIL, the general predictions remain valid.

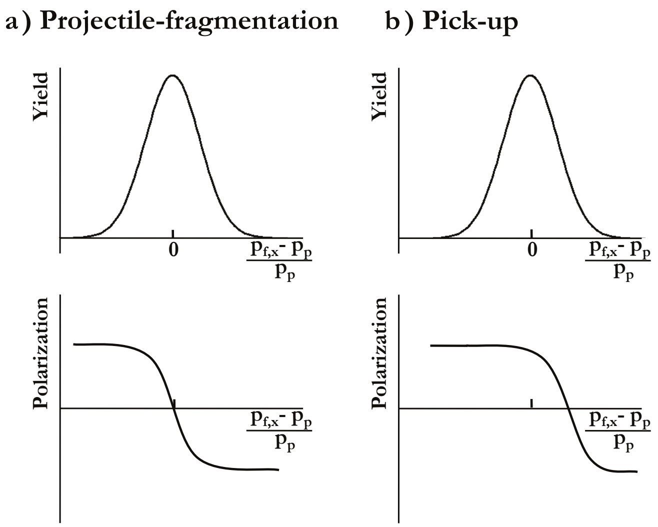

Figure 3.3: Yield and polarization curves as a function of the relative momentum of the fragment, shown for the projectile-fragmentation and pick-up reaction mechanism. Pure far-side collisions are assumed. Picture adapted from [De Rydt, 2010].

The fragmentation (pick-up) reaction is modelled as a peripheral collision in which the projectile loses (absorbs) the nucleons in the geometrical overlapping volume with the target. This 'pre-fragment' then evaporates nucleons isotropically after which the final fragment is formed. It is assumed that the pre-fragment acts as a spectator and that the evaporation happens without changing the angular momentum. In this framework, the spin-polarization of the fragment originates from the momentum transfer in the reaction process. From conservation laws for linear and angular momentum, it is deduced that the spin of the outgoing fragment is related to its linear longitudinal momentum, as illustrated in Fig. 3.3. An appropriate selection in the wing (center) of the momentum distribution then leads to a spin-polarized beam for projectile-fragmentation (pick-up) reactions. This selection is achieved by horizontal slits placed after the first dipole, as illustrated in Fig. 3.2. While selecting only part of the momentum distribution always induces a loss of yield, this is a larger disadvantage for the projectile-fragmentation reactions where the maximal yield corresponds to zero polarization, as can be seen in Fig. 3.3. In the pick-up reactions on the other hand, the maximal yield also corresponds to maximum polarization.

As detailed in [De Rydt, 2010], the sign of the obtained polarization is opposite

for fragments colliding at the right side compared to the left side of the target nucleus, hence mixing of the two leads to a reduction of the total polarization. For low-Z targets such as ^{9}Be, the collisions are mainly of the far-side type where the nuclear attraction dominates the Coulomb repulsion, and a selection of the fragments under a positive angle with respect to the forward direction ensures that mostly projectiles colliding at the right are considered. In practice, the selection under an angle is achieved by putting the primary beam under an angle of $2(1)^\circ$ on target. The polarization curves presented in Fig. 3.3 are calculated assuming pure far-side collisions. This assumption is reasonable for the production of aluminium via projectile-fragmentation and pick-up reactions on a ^{9}Be target, as was shown experimentally by Borremans et al. [2002] and Turzó et al. [2006].
The amount of polarization produced in projectile-fragmentation and pick-up reactions at intermediate energies is in the order of a few percent.

3.2 The β-NMR/NQR technique

β-detected nuclear magnetic or quadrupole resonance is a technique to measure magnetic (β-NMR) and quadrupole moments (β-NQR) of β-decaying nuclei with half-lives in the order of ms to s. The experimental set-up and important aspects of the technique will be outlined in the next paragraphs.

3.2.1 Set-up

The general components of a β-NMR/NQR set-up are presented in Fig. 3.2, while an extensive description of the dedicated β-NMR/NQR set-up used at GANIL, shown schematically in Fig. 3.4, can be found in [De Rydt et al., 2009].

After fragment separation, the spin-polarized fragments are guided to the β-NMR/NQR vacuum chamber ($\sim 10^{-6}$ mbar) where they are stopped in a suitable catcher crystal of 0.5 - 1 mm thick. The crystal holder can contain several crystals which can be moved into the implantation position without breaking the vacuum. Implantation in the center of the crystal is achieved by using several adjustable energy degraders. The degrader material needs to be chosen in order to minimize electron pick-up, as the interaction between the randomly oriented electron spins with the nuclear spins would cause a reduction of the polarization [Vyvey et al., 2000]. For the experiments on neutron-rich Al, Al degraders with variable thicknesses between 1500 μm and 3100 μm were used.

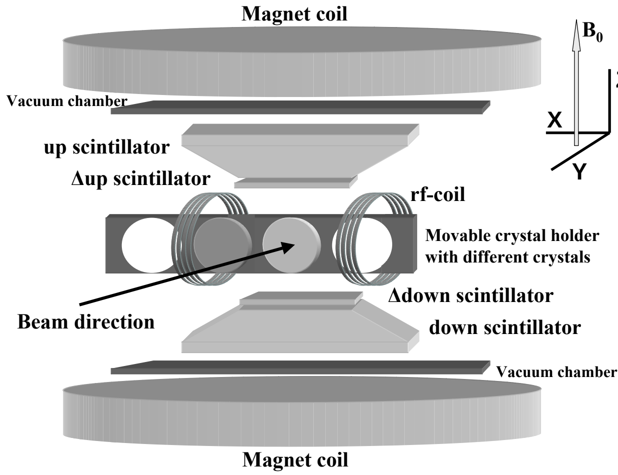

Figure 3.4: Schematic depiction of the β-NMR set-up used at LISE-GANIL. Picture taken from [De Rydt et al., 2009].

The crystal is placed in a static magnetic field B_0 oriented along the spin-polarization axis. Additionally, also a radio frequency (rf) magnetic field B_1 is applied perpendicular to the static field. This rf-field is generated by sending the amplified signals of one or more rf-generators to two Helmholtz coils mounted around the crystal. While the static field is usually around several thousand gauss, the rf-field strength is only in the order of a few gauss.
The last important part of the set-up are the two $\Delta E - E$ pairs of β-detectors placed above and below the implantation crystal, inside of the vacuum chamber. To minimise the influence of random noise and γ-ray background, only events detected in coincidence between the ΔE and E detector are taken into account. Although not necessary for the β-NMR/NQR measurements itself, two γ-ray detectors are placed outside the chamber to detect β-delayed γ-rays for identification purposes.

3.2.2 β-decay asymmetry

The β-NMR/NQR measurements require an initially spin-polarized beam. For these spin-polarized beams, the β-decay pattern is anisotropic in space and the angular distribution for allowed β-decay is given by

$$W(\theta) = 1 + \frac{v_\beta}{c} A_\beta P \cos\theta \tag{3.2}$$

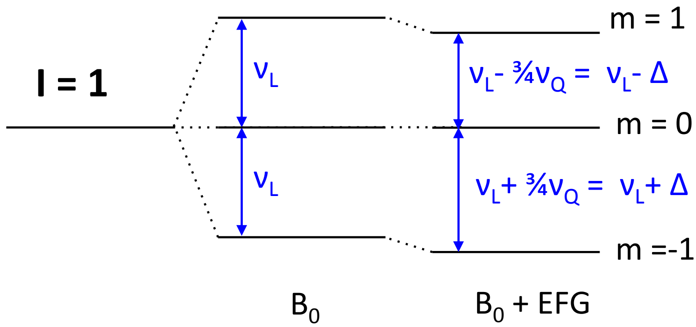

Figure 3.5: Hyperfine splitting of a $I = 1$ nucleus in the absence of hyperfine fields (left), in an external magnetic field B_0 (middle) and in a combination of an electric field gradient (EFG) and an external magnetic field (right). Typical splittings using magnetic fields of a few thousand gauss are in the order of 100 kHz - 5 MHz.

.

For the cases we considered, with Q_β values of a few MeV or more, the velocity of the β-particle relative to the speed of light $\frac{v_\beta}{c}$ is almost equal to one. The β-asymmetry parameter A_β depends on the spins of the initial I_i and final state I_f and is tabulated in [De Rydt, 2010, p. 18]. In general, the β-decay can involve several final states and the total A_β is the sum of the individual branches weighted by their branching ratio.
Experimentally the anisotropy of the β-decay is measured by the two β-telescopes placed at 0° (up) and 180° (down). The asymmetry $\mathcal{A}$ is defined as

$$\mathcal{A} = \frac{N_{\text{up}} - N_{\text{down}}}{N_{\text{up}} + N_{\text{down}}} \approx A_\beta P \tag{3.3}$$

where N_{up} and N_{down} are the counts in the up and the down detectors. The asymmetry is therefore a measure of the polarization in the nuclear ensemble. If the polarization is destroyed, for example as is done in a β-NMR measurement, a change in asymmetry is observed proportional to $A_\beta P$.

3.2.3 Hyperfine interactions in the implantation crystal

Measurements of g-factors and quadrupole moments in β-NMR/NQR depend on the interaction of the implanted nucleus with external electromagnetic fields as well as hyperfine fields in the implantation crystal. In general, the description of these hyperfine interactions is very complex [Cottenier and Rots, 2005] but for specific lattice symmetries, the formalism is greatly simplified. These are the cases which are used in the β-NMR/NQR measurements and will be described below.

For β-NMR measurements, the host crystal is chosen to have a cubic lattice structure. If the isotopes are implanted on a substitutional lattice site, they do not feel a static electric field gradient and thus, the implanted nuclei are only exposed to the external static magnetic field which induces an equidistant Zeeman splitting of the nuclear magnetic substates $|I,m\rangle$ according to

$$E_m - E_{m+1} = h\nu_L = |g|\mu_N B_0 \tag{3.4}$$

Here $g = \mu/I$ is the nuclear g-factor and ν_L is called the Larmor frequency.
For β-NQR measurements on the other hand, a host with a non-cubic lattice structure is selected in which the implanted nuclei are exposed to an axially symmetric electric field gradient V_{zz}. This induces an additional energy shift of the nuclear substates and, on the condition that the magnetic interaction dominates the quadrupole interaction, the energy splitting between two m-states is given by

$$E_m - E_{m+1} = h\nu_L - \frac{3h\nu_Q}{8I(2I-1)}(2m+1)(3\cos^2\theta - 1) \tag{3.5}$$

Here $\nu_Q = e|Q_s|V_{zz}/h$ is the quadrupole coupling constant and θ is the angle between the symmetry axis of the electric field gradient and the external magnetic field. Contrary to the NMR case, the splitting between the different m-states in NQR is not equidistant and $2I$ different transition frequencies exist. In our experiment, θ is set to zero such that expression 3.5 is simplified to

$$E_m - E_{m+1} = h\nu_L - \frac{3h\nu_Q}{4I(2I-1)}(2m+1) \tag{3.6}$$

As an alternative for ν_Q, Δ is sometimes introduced

$$\Delta = \begin{cases} \frac{3\nu_Q}{4I(2I-1)}, & \text{for integer } I \\ \frac{6\nu_Q}{4I(2I-1)}, & \text{for half-integer } I \end{cases} \tag{3.7}$$

Although its definition is slightly different for integer and half-integer spins, it has the advantage that the smallest quadrupole splitting is in both cases equal to Δ.

3.2.4 Measuring nuclear moments via β-NMR/NQR

The basic idea of β-NMR/NQR is that a resonant destruction of polarization can be observed through a change in β-asymmetry. This destruction of polarization

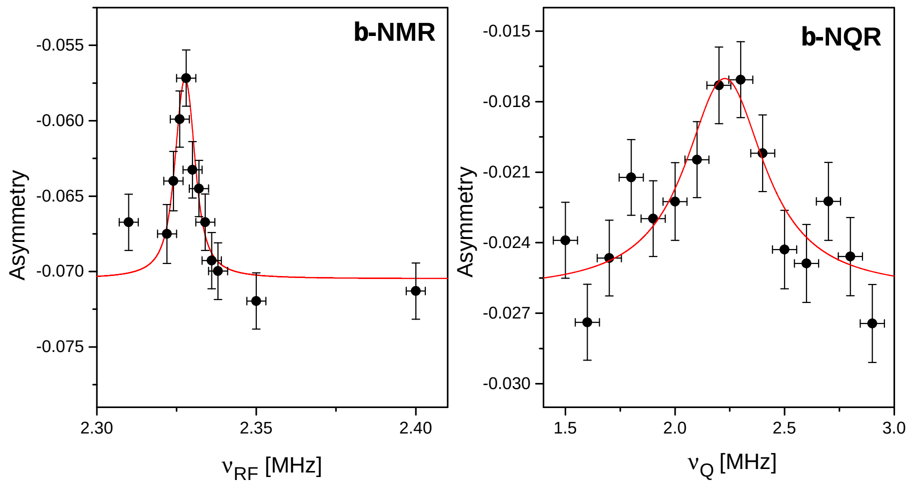

Figure 3.6: Typical β-NMR spectrum (left) and β-NQR spectrum (right) of ^{31}Al measured in the same experiment as ^{33}Al (see section 4.2.3). The frequency modulation is respectively 3 kHz and 55 kHz in the NMR and NQR spectrum.

is achieved by applying an rf-field B_1 with the correct frequency/frequencies, although the details differ between β-NMR and β-NQR.

In a β-NMR measurement, the splitting of the magnetic substates is equidistant and equal to the Larmor frequency. If the rf-frequency ν_{RF} matches this Larmor frequency, the magnetic substates are coupled and their populations are equalised, i.e. the polarization is destroyed. This is then observed as a change in the asymmetry, as shown on the β-NMR spectrum in Fig. 3.6. The resonant change in asymmetry can be a "peak" or a "dip" depending on the sign of the polarization (determined by which part of the momentum distribution is selected) and the β-asymmetry parameter. From the position of the resonance in the spectrum and the known external static magnetic field, the g-factor can be extracted using relation 3.4.
For a β-NQR measurement, the situation is a bit more complicated because in this case the hyperfine splitting of the magnetic substates is not equidistant. When only one rf-frequency is applied, only one of the $2I$ transition frequencies can be matched and the polarization can only be partially destroyed. This is reflected in a small change in asymmetry. To maximise the signal, $2I$ frequencies need to be applied simultaneously in a technique referred to as multi-rf NQR [Borremans et al., 2005]. Since the transition frequencies are correlated through the common quadrupole coupling constant, in practice this quadrupole coupling constant or Δ is scanned. When the resonance condition is

met, the polarization is fully destroyed and the change in asymmetry is maximal. To ensure all applied frequencies are on resonance simultaneously, prior to the β-NQR measurements, ν_L is precisely determined in a β-NMR measurement. A typical β-NQR spectrum can be seen in Fig. 3.6. The quadrupole moment can be extracted from the measured ν_Q resonance position and the known electric field gradient via relation 3.5.
Note that β-NMR/NQR experiments only yield the absolute value of the g-factor and quadrupole moment but not their sign.

During the β-NMR/NQR measurements, the rf-frequency is scanned in a number of discrete steps. In order not to miss an intermediate resonance frequency, a frequency modulation is applied around the central frequency. To search for the resonance, initially a broad frequency scan is performed with large frequency steps and corresponding large modulation. Step-by-step, the frequency range and stepsize are reduced to get a precise determination of the resonance position.
The frequency modulation has an influence on the line shape of the NMR resonance. Although several descriptions exist, in article I (see section 4.2.3) the resonance peaks are fitted according to [De Rydt, 2010]

$$\mathcal{A}(\nu) = \text{baseline } + \mathcal{I}\left(\frac{1}{2\nu}\int_{\nu-\Delta\nu}^{\nu+\Delta\nu}\frac{\nu_0-\nu}{\sqrt{(\nu_0-\nu)^2+\nu_1^2}}d\nu\right)^2 \tag{3.8}$$

where $\mathcal{I}$ is the peak amplitude, ν_0 is the resonance position, $\Delta\nu$ is the frequency modulation and ν_1 is a term related to power broadening due to the power of the rf-field.

In the discussion in section 3.2.3, it was assumed that the nucleus is implanted at a substitutional lattice position. However, in reality some of the nuclei are implanted at other lattice sites with other symmetries, where they experience different hyperfine fields. These nuclei do not contribute to the resonance signal. Furthermore, also defects or crystal imperfections might generate small electric field gradients such that not all nuclei are at resonance at exactly the same rf-frequency. The use of frequency modulation is therefore also beneficial to compensate for this spread in resonance frequencies, maximising the nuclei which are at resonance simultaneously and hence maximising the signal amplitude.
In general, the implantation of nuclei in a crystal is a complicated process, and although the Hume-Rothery [Sood, 1978] rules provide a general rule of thumb to estimate the probability for substitutional implantation, the suitability of a particular nucleus-host combination for β-NMR needs to be verified experimentally.

Spin-lattice relaxation

In the β-NMR/NQR measurements, the destruction of polarization happens resonantly. However, also non-resonant destruction of the spin-polarization takes place due to random spin-lattice interactions. If these spin-lattice relaxation processes occur faster than the nuclear lifetime, the polarization will be destroyed before the nucleus decays and consequently no resonant change of asymmetry can be observed. Spin-lattice relaxation therefore puts an upper limit on the half-life of the studied nucleus and typical half-lives of isotopes studies via β-NMR are shorter than a few s.

The spin-lattice relaxation time is measured experimentally by implanting the beam for a period t_{imp} after which the beam is switched off and the evolution of the asymmetry is measured as a function of time. This time evolution is described via [Hossain et al., 2009]

$$\mathcal{A}(t) = \mathcal{A}_0 \frac{T_1}{\tau + T_1} \frac{1 - \exp[-t(\tau + T_1)/(\tau T_1)]}{1 - \exp[-t/\tau]} \qquad \text{for } t < t_{\mathrm{imp}} \tag{3.9}$$

$$\mathcal{A}(t) = \mathcal{A}_0 \frac{T_1}{\tau + T_1} \frac{1 - \exp[-t_{\mathrm{imp}}(\tau + T_1)/(\tau T_1)]}{1 - \exp[-t_{\mathrm{imp}}/\tau]} \times \exp[-(t - t_{\mathrm{imp}})/T_1] \qquad \text{for } t > t_{\mathrm{imp}} \tag{3.10}$$

where τ is the nuclear lifetime and T_1 the spin-lattice relaxation time. In the case of a continous beam such as the one employed in our β-NMR experiments, $t_{\mathrm{imp}} \to \infty$ and the asymmetry in eq. 3.9 reaches its equilibrium value

$$\mathcal{A}_{\mathrm{cont}} = \mathcal{A}_0 T_1/(\tau + T_1) \tag{3.11}$$

$$= \mathcal{A}_0/(1 + \tau/T_1) \tag{3.12}$$

Hence, for the same initial parameters (A_β, polarization produced in the reaction process, Q_β, etc.) the experimentally observed asymmetry will be reduced for isotopes with long half-lives or for implantation crystals with short spin-lattice relaxation times.

The specific spin-lattice relaxation mechanism depends on the chosen implantation host. In metals, the conduction electrons induce fast changing fields which cause magnetic relaxation, while in insulators, quadrupolar relaxation is caused by fluctuating electric field gradients due to lattice vibrations. Often the relaxation in insulators is much slower than in metals. In general, the relaxation process is slower at low temperatures than at high temperatures.
Once T_1 is known for one isotope-host combination at a specific temperature, it

can be estimated for other isotopes of the same element, implanted in the same host, via [Korringa, 1950; Mieher, 1960]

$$\frac{T_1^A}{T_1^{A'}} = \left(\frac{g^{A'}}{g^A}\right)^2 \qquad \text{in metals}$$

$$\frac{T_1^A}{T_1^{A'}} = \left(\frac{Q^{A'}}{Q^A}\right)^2 \qquad \text{in insulators}$$

Apart from determining T_1, spin-lattice relaxation time measurements can be performed before the β-NMR measurements to verify whether there is any polarization at all.

4 Nuclear moments of ^{33}Al and ^{34}Al

The island of inversion around $N = 20$ has been attracting the attention of the nuclear structure community since the first discovery of anomalous binding energies in the neutron-rich $_{11}$Na isotopes in 1975. In this chapter, a motivation is given as to why specifically we want to study the neutron-rich Al isotopes, located at the northern border of this island of inversion. Then, the experimental quadrupole moment of ^{33}Al is discussed which was measured in a β-NQR experiment in 2011. Furthermore, also the interest of studying a newly discovered isomer in ^{34}Al is outlined, as well as the very preliminary results from the experiment to measure its g-factor and quadrupole moment performed at the end of May 2016.

4.1 The island of inversion around $N = 20$

The interest in the region centered around $^{32}_{12}$Mg$_{20}$ started by the mass measurement of the neutron-rich Na isotopes [Thibault et al., 1975]. Although $N = 20$ is a strong shell closure near the valley of stability, the experiment showed that $^{31}_{11}$Na$_{20}$ and $^{32}_{11}$Na$_{21}$ were significantly more bound than expected for a closed $N = 20$ shell. Also the increase in mean-square charge radii of ^{29,30,31}Na [Huber et al., 1978] and the low energy of the first excited 2^+ state in ^{32}Mg [Détraz et al., 1979] were inconsistent with the conventional $N = 20$ magic number view.
Theoretically, these anomalies were soon interpreted as due to ground state deformation [Campi et al., 1975], associated with neutron excitations across $N = 20$, from the (normal) sd shell into the (intruder) pf orbitals [Wildenthal and Chung, 1980; Watt et al., 1981; Warburton et al., 1990] (see Fig. 4.1 for the

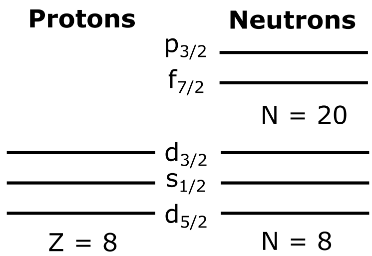

Figure 4.1: Relevant shell model orbitals in the island of inversion around $N = 20$.

relevant shell model orbitals in this region). Specifically, configurations where two neutrons are excited across $N = 20$, the so-called 2 particle - 2 hole (2p-2h) excitations, were considered to be important. Originally, it was predicted that for the $_{10}$Ne, $_{11}$Na and $_{12}$Mg isotopes with $20 \leq N \leq 22$, the energy needed to promote two nucleons across the shell gap was compensated by a large gain in quadrupole correlation energy. For these isotopes, the order of the normal 0p-0h configurations and intruder 2p-2h configurations would therefore be inverted, giving rise to an *island of inversion*. As discussed in section 1.2.3, the energy balance in favour of the intruder configurations partly arises because of the reduction of the $N = 20$ gap when protons are removed from the $\pi d_{5/2}$ orbital below $Z = 14$. However, the energy cost for exciting neutrons across $N = 20$ remains significant and it is only when the enormous correlation energy is taken into account that the 2p-2h configurations can become the ground state [Caurier et al., 2014]. Here also the importance of the open proton $d_{5/2}$ orbital needs to be stressed, as it brings the possibility of additional proton-neutron correlations [Sorlin, 2014] while the relatively large gap between the $\pi d_{5/2}$ and $\pi s_{1/2}$ orbitals plays a stabilizing role for isotopes with $Z \geq 14$.

To better understand the drivers of the structural changes in the island of inversion, an extensive research programme has been performed determining the low-energy properties in this region of the nuclear chart (see [Himpe, 2006] for an overview up to 2006). A summary of the current status can be found in Fig. 4.2. In this effort, measurements of nuclear spins, moments and mean-square charge radii have been crucial, as discussed in detail in for example [Utsuno et al., 2004; De Rydt, 2010; Neyens, 2016]. Along the way, it has been realised that the limits of the island of inversion are not sharply defined and that the amount of intruder configurations changes gradually as a function of N and Z. Nevertheless, the exact extent of the island is still an open question, both from the experimental and from the theoretical point of view. Since the nuclear observables of isotopes at the shores of the island of inversion depend critically on the balance between the shell gaps and the correlations, they are

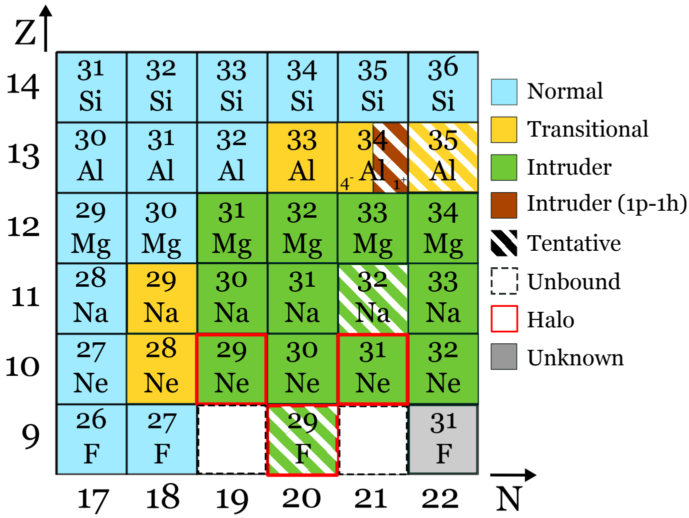

Figure 4.2: Current status of the intruder nature of the ground or long-lived states in the island of inversion around $N = 20$. The term normal (intruder) is used to denote configurations dominated by normal (intruder) configurations.

excellent probes to test the available nuclear models and their parametrisations. Due to their sensitivity to the wave function composition and deformation, nuclear moments play an important role in this context.

4.1.1 The $Z = 13$ isotopes

The neutron-rich Al isotopes ($Z = 13$) are located at the northern border of the island of inversion. Lying in between the deformed $_{12}$Mg and spherical $_{14}$Si isotopes, they provide a unique opportunity to study the transition from normal to intruder configurations. The transitional character of the Al isotopes was investigated in several β-NMR/NQR experiments [Borremans et al., 2005; Himpe et al., 2006; Kameda et al., 2007; Nagae et al., 2009; De Rydt et al., 2009]. The experimental g-factors and quadrupole moments of $^{31,32}\text{Al}_{18,19}$ have demonstrated that their ground state structure can be well reproduced in a normal sd-picture in which neutron excitations across $N = 20$ are excluded. On the other hand, an accurate description of the g-factors of ^{33}Al and ^{34}Al requires a model space including the neutron pf-orbitals and an admixture with at least 25% and 50% intruder configurations in the ground state wave function of ^{33}Al and ^{34}Al were suggested, respectively [Himpe et al., 2006, 2008]. Since the proposed mixed intruder nature of the ^{33}Al ground state was based on a

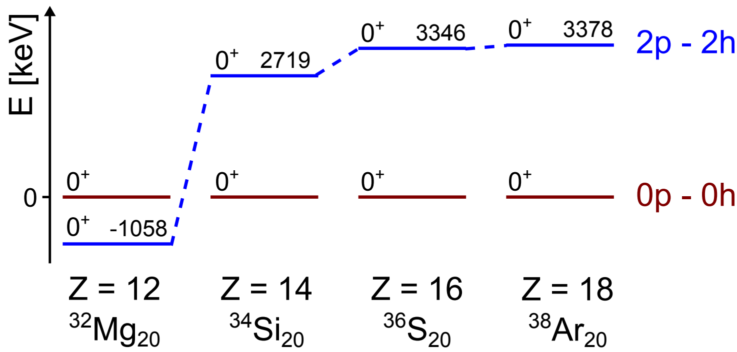

Figure 4.3: Evolution of the first and second excited 0^+ states along the $N = 20$ isotopes. Data taken from [Flynn et al., 1975; Hogenbirk et al., 1990; Wimmer et al., 2010; Rotaru et al., 2012].

deviation of only a few percent between the theoretical *sd* calculation and the experimental g-factor, its validity was sometimes questioned (see e.g. [Tripathi et al., 2008]). Although the quadrupole moment is much more sensitive to the effects of 2p-2h excitations, the low precision on the experimental value determined prior to this work, precluded clarification of the situation [Shimada et al., 2012]. Up to now, attempts to measure the quadrupole moment of the 4^- ground state in ^{34}Al have been unsuccessful.
Recently, a second long-lived state in ^{34}Al has been discovered, suggested to have 1^+ spin-parity and a 1p-1h intruder configuration [Rotaru et al., 2012]. A motivation to measure the g-factor and quadrupole moment of this state can be found in section 4.3.

4.2 The intruder component in the ground state wave function of ^{33}Al

4.2.1 The $N = 20$ isotones

Over the last few years, a lot of progress has been made to follow the development of the intruder configurations along the $N = 20$ isotones [Gade and Liddick, 2016]. Especially, the second 0_2^+ states in ^{30,32}Mg and ^{34}Si have only recently been identified experimentally [Schwerdtfeger et al., 2009; Wimmer et al., 2010; Rotaru et al., 2012]. Fig. 4.3 depicts the systematics of the $0_{1,2}^+$ states along the $N = 20$ isotopes. This shows that between $^{34}_{14}$Si and $^{32}_{12}$Mg a particularly rapid change in nuclear structure is observed. Whereas in ^{34}Si the ground state is thought to be dominated by normal configurations[1] and a 2p-2h intruder state is found at 2.7 MeV, in $^{32}_{12}$Mg this intruder state comes down by almost 4 MeV, becoming the ground state more than 1 MeV below the normal 0p-0h state. Shell model calculations using the SDPF-U-MIX interaction however suggest that the above picture of nearly pure 0p-0h and 2p-2h states is too simple [Caurier et al., 2014]. The ground state of ^{32}Mg is indeed calculated to be dominated by intruder configurations (54% 2p-2h, 35% 4p-4h) but the excited state 0^+ state is strongly mixed with only 33% 0p-0h configurations.

$^{33}_{13}$Al$_{20}$ is a clear transitional isotope into the island of inversion, both along the $Z = 13$ and $N = 20$ line. As discussed in the next section, experimental efforts to determine the normal, intruder or mixed nature of its ground state have previously led to contradicting results and also theoretically no consensus is reached. The high-precision quadrupole moment will provide a sensitive probe to clarify the situation.

4.2.2 Large-scale shell model interactions

Several shell model interactions are employed for calculations in the island of inversion around $N = 20$. All these interactions start from the USD interaction for the *sd* shell developed by Brown and Wildenthal [1988], while different cross-shell interactions are used. Also their monopole matrix elements have been tuned differently, leading to other effective single particle energies and shell gaps.

- SDPF-U-MIX [Caurier et al., 2014]
  - Valence space: ^{16}O core, *sd* shell for protons and full $sd + pf$ shell for neutrons.
  - Remark: Cannot reproduce the quadrupole moment of ^{33}Al (see 4.2.3). Probably the size of the $N = 20$ shell gap is overestimated in this interaction which results in a too small intruder component.
  - Full Lanczos diagonalisation in ANTOINE
- SDPF-NR [Nummela et al., 2001], SDPF-U [Nowacki and Poves, 2009]
  - Valence space: ^{16}O core, *sd* shell for protons and full $sd + pf$ shell for neutrons.

[1] Recent shell model calculations by Otsuka and collaborators shed doubt on this conclusion [Private communication].

- Remark: Predecessors of SDPF-U-MIX, have become obsolete since they cannot mix different np-nh configurations.
- Full Lanczos diagonalisation in ANTOINE

- SDPF-M [Utsuno et al., 1999]
  - Valence space: ^{16}O core, sd shell for protons and $sd + \nu f_{7/2}p_{3/2}$ shell for neutrons.
  - Remark: Reproduces the quadrupole moment of ^{33}Al very well. From the g-factor measurement of ^{34g}Al it was deduced that the size of $N = 28$ is overestimated [Himpe et al., 2008]. This means that mixing with $\nu p_{3/2}$ configurations is not well reproduced.
  - Originally used in the Monte Carlo Shell framework, while recently full Lanczos diagonalisation using the MSHELL64 code have become available.

4.2.3 Article I: High-precision ^{33}Al quadrupole moment reveals intruder dominated ground state

This article reports on the results of the β-NQR experiment on ^{33}Al performed in July 2011 at LISE-GANIL. The precision on the previously known quadrupole moment of ^{33}Al was improved by a factor of 5. Due to this high precision, a pure sd picture without neutron excitations across $N = 20$ could be firmly excluded. In order to assess the intruder component in the ground state wave function, the experimental result is compared to state-of-the-art shell model calculations. This demonstrated that the wave function is mixed with at least 50% of intruder configurations, illustrating the transitional nature of ^{33}Al.

As a master student at the time of the experiment, I participated in the β-NQR experiment which was led by Marieke De Rydt. She performed a first data analysis and prepared a first draft of the paper in 2012. With newly available theoretical calculations, I've finalised the paper for submission. This involved an independent data analysis, shell model calculations with the USD interaction, several discussions with our collaborators and completely reworking the initial draft.

PHYSICAL REVIEW C **94**, 034312 (2016)

High-precision quadrupole moment reveals significant intruder component in $^{33}_{13}Al_{20}$ ground state

H. Heylen,[1] M. De Rydt,[1] G. Neyens,[1,*] M. L. Bissell,[1] L. Caceres,[2] R. Chevrier,[3] J. M. Daugas,[3] Y. Ichikawa,[4,†] Y. Ishibashi,[4,5] O. Kamalou,[2] T. J. Mertzimekis,[6] P. Morel,[3] J. Papuga,[1] A. Poves,[7] M. M. Rajabali,[1] C. Stödel,[2] J. C. Thomas,[2] H. Ueno,[4] Y. Utsuno,[8,9] N. Yoshida,[10] and A. Yoshimi[4,‡]

[1]*KU Leuven, Instituut voor Kern- en Stralingsfysica, 3001 Leuven, Belgium*
[2]*Grand Accélérateur National d'Ions Lourds (GANIL), CEA/DRF-CNRS/IN2P3, B.P. 55027, F-14076 Caen Cedex 5, France*
[3]*CEA, DAM, DIF, F-91297 Arpajon Cedex, France*
[4]*RIKEN Nishina Center, 2-1 Hirosawa, Wako, Saitama 351-0198, Japan*
[5]*Institute of Physics, University of Tsukuba, 1-1-1 Tennodai, Tsukuba, Ibaraki 305-8577, Japan*
[6]*Department of Physics, University of Athens, Zografou Campus, GR-15784, Athens, Greece*
[7]*Departamento de Física Teórica and IFT-UAM/CSIC, Universidad Autónoma de Madrid, E-28049 Madrid, Spain*
[8]*Advanced Science Research Center, Japan Atomic Energy Agency, Tokai, Ibaraki 319-1195, Japan*
[9]*Center for Nuclear Study, University of Tokyo, Hongo, Bunkyo-ku, Tokyo 113-0033, Japan*
[10]*Department of Physics, Tokyo Institute of Technology, 2-12-1 Oh-okayama, Meguro-ku, Tokyo 152-8551, Japan*

(Received 5 July 2016; published 12 September 2016)

The electric quadrupole moment of the $^{33}_{13}Al_{20}$ ground state, located at the border of the island of inversion, was obtained using continuous-beam β-detected nuclear quadrupole resonance (β-NQR). From the measured quadrupole coupling constant $\nu_Q = 2.31(4)$ MHz in an α-Al_2O_3 crystal, a precise value for the electric quadrupole moment is extracted: $|Q_s(^{33}\mathrm{Al})| = 141(3)$ mb. A comparison with large-scale shell model calculations shows that ^{33}Al has at least 50% intruder configurations in the ground state wave function, favoring the excitation of two neutrons across the $N = 20$ shell gap. ^{33}Al therefore clearly marks the gradual transition north of the deformed Na and Mg nuclei towards the normal $Z \geqslant 14$ isotopes.

DOI: 10.1103/PhysRevC.94.034312

I. INTRODUCTION

In recent decades, the study of isotopes far from β stability has decisively altered our understanding of the nuclear shell structure through the observation of many phenomena at variance with conventional expectations. One of the oldest examples is the region of deformation around the classic magic number $N = 20$, which was first discovered through anomalies in the properties of neutron-rich Na and Mg isotopes [1–3]. This deformation is associated with two-particle–two-hole (2p-2h) neutron excitations across $N = 20$, from the sd orbitals to the fp orbitals. Due to the combination of a reduced $N = 20$ shell gap and a large gain in quadrupole correlation energy, the energy for such particle-hole configurations is lowered drastically and, at specific N,Z combinations, these so-called intruder configurations can even become the ground state, below the normal sd configurations. The isotopes for which this inversion of normal and intruder configurations occurs are referred to as belonging to the island of inversion.

Warburton *et al.* [4] originally predicted that the island of inversion around $N = 20$ contains the $_{10}$Ne, $_{11}$Na, and $_{12}$Mg isotopes with $20 \leqslant N \leqslant 22$. Since then, an extensive research program has focused on the characterization of the low-energy properties of these isotopes and their neighbors, in order to understand the origin of the changing nuclear structure [5–10]. Moreover, it is recognized that the development of deformation happens gradually as a function of N and Z [11]. Since nuclei at the edge of the island of inversion have a transitional character with a varying amount of normal and intruder configurations, their study is imperative to understand the drivers of the sudden structural changes in the region.

The neutron-rich Al isotopes ($Z = 13$) constitute the northern border of the island of inversion, between the spherical Si isotopes and the deformed Mg isotopes. $^{33}_{13}Al_{20}$ is thought to be a key isotope as the transition into the island is particularly rapid in the $N = 20$ isotones. In $^{34}_{14}Si_{20}$ a 2p-2h intruder state was recently found at 2719 keV [12], which comes down almost 4 MeV in $^{32}_{12}Mg_{20}$, where it becomes the ground state, lying 1058 keV below the normal configuration [13]. ^{33}Al is therefore expected to have a transitional nature, with potentially a significant amount of intruder admixtures in its ground state. Experimental measurements to determine this intruder component have led to conflicting results. Whereas mass measurements [14] and the $^{33}\mathrm{Al} \rightarrow {}^{33}\mathrm{Si}$ β-decay study [15] place ^{33}Al outside the island of inversion, the g factor [16] and the (debated) $^{33}\mathrm{Mg} \rightarrow {}^{33}\mathrm{Al}$ β-decay scheme [17–19] suggest a sizable intruder component in the ^{33}Al ground state, while also one-neutron removal cross sections and longitudinal momentum distributions do not exclude the presence of intruder configurations [20]. The quadrupole moment is a particularly well-suited observable to shed light on this issue due to its sensitivity to $E2$ collectivity and 2p-2h excitations in the wave function. However, as the precision on the previous measurement was low (12%), no firm conclusion could be drawn [21].

*gerda.neyens@kuleuven.be

†Present address: Department of Physics, Tokyo Institute of Technology, 2-12-1 Oh-okayama, Meguro-ku, Tokyo 152-8551, Japan.

‡Present address: Research Core for Extreme Quantum World, Okayama University, Okayama 700-8530, Japan.

Here, we present the first high-precision quadrupole moment measurement of the ^{33}Al ground state ($I = 5/2^+$, $t_{1/2}$ = 41.7 ms) via continuous-beam β-NQR at LISE-GANIL. Via a comparison with large-scale shell model calculations, the mixing of intruder configurations in the ground state wave function of ^{33}Al is investigated.

II. EXPERIMENTAL DETAILS

The β-detected nuclear quadrupole resonance (β-NQR) measurements were performed at the LISE-GANIL facility. Neutron-rich ^{33}Al nuclei were produced and spin polarized in a projectile fragmentation reaction induced by a $^{36}S^{16+}$ primary beam (77 MeV/u and 1.8 μA) on a 1018-μm thick ^{9}Be target. After selection in the LISE3 fragment separator, a 94% pure beam of ^{33}Al (8×10^3 particles per second) was guided to the β-NMR/NQR setup [22]. Here the beam was implanted into a α-Al_2O_3 single crystal at room temperature. The crystal was placed in a static external magnetic field ($B_0 = 2002(7)$ gauss) along the spin direction in order to maintain the spin polarization and induce a Zeeman splitting. Perpendicular to the static field, a radio-frequency field with frequency $\nu_{\rm rf}$ was applied, generated by the amplified rf generator signals sent to two Helmholtz coils mounted around the crystal. The β decay of the radioactive ^{33}Al isotopes was detected in two sets of ΔE-E plastic scintillator telescopes placed above and below the implantation crystal. To reduce the influence of scattering and noise events, ΔE-E scintillator coincidences were required. For a spin-polarized ensemble, the β decay is anisotropic in space and the asymmetry $\mathcal{A}$ is defined as

$$\mathcal{A} = \frac{N_{\rm up} - N_{\rm down}}{N_{\rm up} + N_{\rm down}} \approx A_\beta P$$

with A_β being a parameter determined by the β-decay properties and P being the amount of spin polarization. $N_{\rm up}$ and $N_{\rm down}$ are the number of counts detected in the upper and lower detectors, respectively.

The implanted ^{33}Al nuclei are exposed to an axially symmetric electric field gradient V_{zz} in the hexagonal α-Al_2O_3. In addition to the Zeeman splitting due to the external magnetic field, this field gradient induces a shift due to the quadrupole interaction. In a field of ~2000 gauss, the magnetic interaction dominates the electric quadrupole interaction and the splitting of the $|I,m\rangle$ states is in first order given by [23]

$$\nu_m - \nu_{m+1} = \nu_L - \frac{3\nu_Q}{8I(2I-1)}(2m+1)(3\cos^2\theta - 1).$$

Here θ is the angle between the external field and the symmetry axis of the electric field gradient in the crystal, which was put to zero in the experiment. From a precise measurement of the transition frequencies, the nuclear g factor and spectroscopic quadrupole moment Q_s can be extracted via the relations for the Larmor frequency $\nu_L = |g|\mu_N B_0/h$ and the quadrupole coupling constant $\nu_Q = e|Q_s|V_{zz}/h$.

For a $I = 5/2^+$ nucleus such as ^{33}Al, there exist five transition frequencies between the $|I,m\rangle$ states ($m = -5/2, -3/2, \ldots, 5/2$). When the applied rf field has a frequency that matches one of these frequencies, the population of the two magnetic substates is equalized, which induces only a partial destruction of the ensemble polarization, reflected as a small change in the asymmetry $\mathcal{A}$ [24]. In order to enhance this change in asymmetry and thus the resonance signal, the polarization needs to be fully destroyed. As the five transition frequencies are correlated through the common coupling constant ν_Q, they can be scanned simultaneously by varying this ν_Q. When the resonance condition for ν_Q is met, the population of all $|I,m\rangle$ states is equalized, and a full change in asymmetry is observed. To guarantee all five frequencies are at resonance simultaneously, precise knowledge of ν_L is required. Therefore, prior to the β-NQR measurement, a β-NMR measurement in a cubic Si crystal was performed, yielding ν_L in the applied B_0. During the β-NMR and NQR measurements, the rf frequencies were scanned in discrete steps and for each frequency, a frequency modulation of more than 50% of the step size was applied to cover the full frequency range. A detailed description of the methodology of continuous-beam β-NQR can be found in Ref. [22].

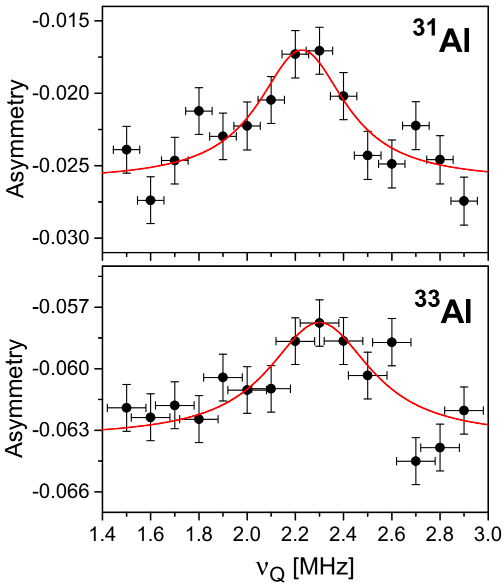

FIG. 1. Experimental β-NQR spectra for the ^{31}Al and ^{33}Al ground states with a frequency modulation of respectively 55 and 80 kHz.

The setup was first tested using the well-known ^{31}Al isotope after which the ^{33}Al measurements were performed in similar conditions. Typical spectra are shown in Fig. 1 and an overview of the results can be found in Table I. The quadrupole moments of ^{31}Al and ^{33}Al have been extracted from the measured quadrupole coupling constant, relative to that of ^{27}Al

$$|Q_s(^{A}\mathrm{Al})| = \frac{|Q_s(^{27}\mathrm{Al})|\nu_Q(^{A}\mathrm{Al})}{\nu_Q(^{27}\mathrm{Al})}.$$

The ^{31,33}Al results are in good agreement with the previously known literature values, and the precision on $|Q_s(^{33}\mathrm{Al})|$ is

TABLE I. The quadrupole coupling constant of the ^{31,33}Al ground state extracted during the β-NQR measurements in an α-Al_2O_3 crystal at room temperature. The results are compared to the literature values and for completeness also the ^{27}Al reference values are presented.

	N	I^π	$t_{1/2}$	ν_Q (MHz)	Q_s (mb)	Ref.
^{27}Al	14	$5/2^+$	Stable	2.4031(2)	+146.6(10)	[25,26]
^{31}Al	18	$5/2^+$	644 ms	2.24(3)	136.5(23)	This work
				2.19(2)	134.0(16)	[27]
^{33}Al	20	$5/2^+$	41.7 ms	2.31(4)	141(3)	This work
				2.2(3)	132(16)	[21]

improved with more than a factor of 5, from 12% in the previous measurement [21] to 2% in this work. This precision allows a detailed discussion of the intruder components in the ^{33}Al ground state.

III. RESULTS AND DISCUSSION

The experimental ground state quadrupole moment of $^{33}Al_{20}$ is very similar to that of $^{27}Al_{14}$ and $^{31}Al_{18}$, as shown in Fig. 2. This is inconsistent with a picture in which no particle-hole excitations occur: for a closed-shell isotope like $^{33}Al_{20}$ the quadrupole moment should decrease with respect to the open-neutron shell isotopes ^{27,31}Al. That is illustrated in the shell model calculations using the USD shell model interaction [28] with a ^{16}O core and protons and neutrons restricted to the sd-shell model space, the triangles in Fig. 2. Indeed, the ^{33}Al quadrupole moment would then be entirely due to the proton configuration because the $N = 20$ shell closure inhibits all neutron contributions. The open neutron shell in ^{27}Al and ^{31}Al on the other hand allows for additional proton-neutron correlations, resulting in an increase in quadrupole moment.

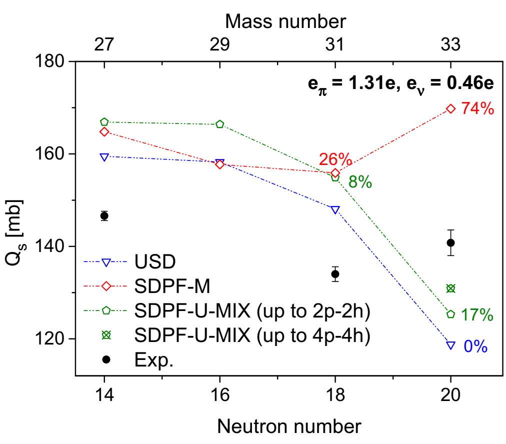

FIG. 2. The experimental quadrupole moments compared to shell model calculations using various interactions and the universal effective charges [32]. The predicted amount of intruder configurations in the wave functions are indicated in brackets.

The fact the ^{27,31}Al and ^{33}Al quadrupole moments are similar in size therefore suggests that this pure sd picture is too limited and that neutron excitations across $N = 20$ are necessary to reproduce $Q_s(^{33}\mathrm{Al})$.

Therefore, large-scale shell model calculations have been performed in different model spaces, using different effective interactions. The results are presented in Fig. 2. The ANTOINE shell model code has been used with SDPF-U-MIX [29], the most recent effective interaction for this region, which builds upon a ^{16}O core and comprises the full sd and pf shell for neutrons. This allows excitations of neutrons across $N = 20$ and mixing between np-nh configurations. The calculations are truncated to maximum 2p-2h neutron excitations across $N = 20$ for Al isotopes up to ^{31}Al, and up to 4p-4h for ^{33}Al. As an alternative, the SDPF-M effective interaction [30] is used including excitations from the neutron sd shell to the two lowest levels of the pf shell ($f_{7/2}p_{3/2}$). Previously, calculations with this interaction were performed in the Monte Carlo shell model framework [21], while recently full Lanczos diagonalizations (calculated using the MSHELL64 code [31]) have become available, truncated to maximally 4p-4h excitations. Since both diagonalization approaches yield similar results, only the results from the full diagonalization are shown here.

In Fig. 2, all quadrupole moments have been calculated using the theoretically derived universal effective charges $e_\pi = 1.31e$ and $e_\nu = 0.46e$ [32]. The calculations consistently overestimate the experimental quadrupole moments for all three interactions, which is related to the choice of effective charges, as discussed later. At this point, however, it is more important to note that only the SDPF-M interaction is able to reproduce the experimental trend, which goes up at $N = 20$. The USD and SDPF-U-MIX interaction on the other hand predict a sizable decrease. Allowing also 4p-4h excitations for ^{33}Al in the SDPF-U-MIX interaction does not really improve the agreement with experiment. An inspection of the intruder admixtures in the ^{33}Al ground state (indicated in Fig. 2) reveals that 74% of intruders are predicted using SDPF-M while only 17% are predicted using SDPF-U-MIX. The discrepancy between the SDPF-U-MIX calculations and the experimental value at $N = 20$ is therefore suggested to at least partly arise from an underestimation of intruder configurations. To obtain a theoretical ^{33}Al quadrupole moment in better agreement with the experimental trend, the intruder component would need to be doubled, requiring a reduction of the $N = 20$ shell gap by 0.5 MeV. However, since the (unmodified) SDPF-U-MIX calculations have been shown to give good results for $E(2^+)$'s, $B(E2)$'s, and binding energies in the neighboring isotopic chains [14,29], simply decreasing the $N = 20$ shell gap will have detrimental effects on the predictions for these neighboring isotopes and a more careful analysis of the problem is necessary. The observed discrepancy at ^{33}Al emphasizes the need for high-precision quadrupole moments as a complementary test for state-of-the-art interactions.

To further illustrate the significance of the high-precision result we have obtained in this work, our value is presented in Fig. 3 along with the old, low-precision value [21] and the results from the USD and the SDPF-M shell model calculations using $e_\pi = 1.1e$, $e_\nu = 0.5e$. The use of these

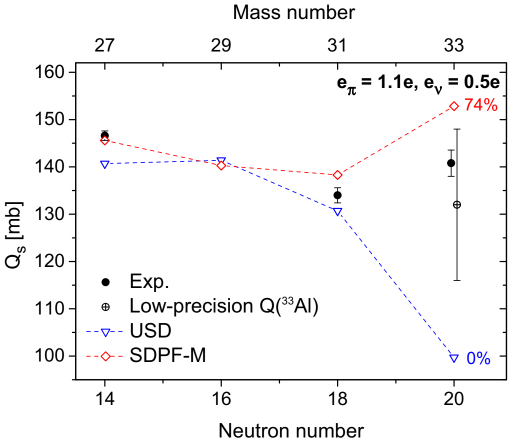

FIG. 3. Experimental quadrupole moments of ^{27}Al, ^{31}Al, and ^{33}Al where for ^{33}Al both the high-precision value obtained in this work and the low-precision value [21] are shown. These are compared to shell model calculations with the USD and SDPF-M effective interactions using constant effective charges $e_\pi = 1.1e$, $e_\nu = 0.5e$.

effective charges is justified based on the analysis of the quadrupole moments and $B(E2)$ values of the odd-Z even-N πsd isotopes by De Rydt *et al.* [27,33], which showed that a reduction of the proton effective charge gives a better reproduction of the experimental data.

Both USD and SDPF-M can reproduce the experimental quadrupole moments of ^{27,31}Al, suggesting a structure dominated by normal configurations. For ^{33}Al, the old low-precision quadrupole moment agrees best with the SDPF-M calculations, even though its large uncertainty prevents firmly ruling out the USD prediction. Due the high precision obtained in this work, it can be unambiguously concluded that the quadrupole moment of the ^{33}Al ground state is inconsistent with the USD calculation without intruder configurations. The SDPF-M value on the other hand compares much more favorably to the experimental value, although it is somewhat too high. This suggests that the predicted 74% intruder configurations is somewhat overestimated.

The influence of the exact amount of intruder components on the quadrupole moment is therefore investigated through a variation of the size of the $N = 20$ shell gap, obtained by shifting the $\nu f_{7/2}$ and $\nu p_{3/2}$ orbitals simultaneously by ΔE. The results are shown in Fig. 4. A good agreement between the experimental and theoretical quadrupole moment is already obtained at 62% intruder configurations, subdivided in 55% 2p-2h and 7% 4p-4h components. Immediately, also the clear correlation between the total intruder component in the wave function (in the top panel) and the predicted quadrupole moment (in the bottom panel) becomes evident. Furthermore, the strong dependence of the amount of intruder admixtures on the size of the $N = 20$ shell gap is illustrated. Indeed,

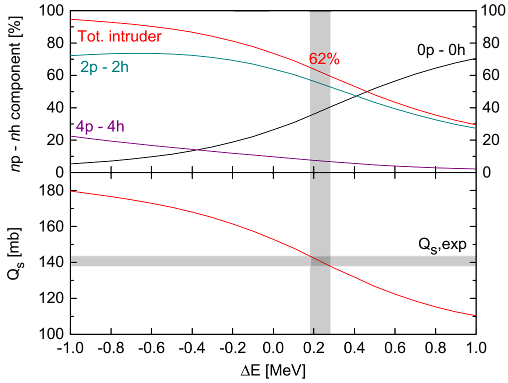

FIG. 4. Variation of 0p-0h, 2p-2h, and 4p-4h component in the SDPF-M wave function (top) and quadrupole moments (bottom) when the $N = 20$ shell gap is changed by ΔE. Quadrupole moments were calculated using the $e_\pi = 1.1e$, $e_\nu = 0.5e$ effective charges. The gray bands indicate the interval around the experimental value.

increasing the shell gap by 1 MeV already reduces the amount intruder configurations by 40%.

While the above analysis is instructive to study the sensitivity of the quadrupole moment to the intruder composition of the wave function, it is not meant as a quantitative determination of the optimal $N = 20$ shell gap in the SDPF-M interaction, which would require a much more elaborate investigation.

Note that the exact amount of intruder admixtures also depends on the choice of effective charges, for example, with the isospin-dependent effective charges used previously in [21,34] 76% of intruder admixtures would be required to reproduce the experimental quadrupole moment. Whichever effective charges are the most appropriate, it is clear that the main conclusion of this work is solid: To reproduce the quadrupole moment of the ^{33}Al ground state, a significant admixture of intruder configurations is necessary. This confirms and strengthens the conclusion of the ^{33}Al g factor measurement [16]. However, for a consistent interpretation of the low-energy structure of ^{33}Al, it would be interesting to investigate how the ground state moments can be consolidated with the apparent contradictory experimental information from the mass and β-decay measurements [14,15].

IV. CONCLUSION

In conclusion, the ground state quadrupole moment of ^{33}Al has been measured using the β-NQR technique at LISE-GANIL. The high-precision experimental value, $|Q_s(^{33}\text{Al})| = 141(3)$ mb, is inconsistent with a picture in which mixing with neutron intruder configurations beyond $N = 20$ is excluded. Furthermore, a comparison with large-scale shell model calculations has demonstrated the sensitivity of the ^{33}Al quadrupole moment to intruder components. The SDPF-U-MIX interaction predicts only 17% mixing with intruder configurations but cannot capture the observed rise in quadrupole moment.

On the other hand, good agreement between the SDPF-M calculations and the experimental ^{27,31,33}Al quadrupole moments is obtained, and for ^{33}Al a ground state configuration mixed with more than 50% intruders is suggested. Hence, ^{33}Al cannot be placed outside of the island of inversion but should be considered as an important transitional isotope.

ACKNOWLEDGMENTS

The authors thank the GANIL staff for their support during the preparation and running of the experiment. This work was partly supported by the European Community FP6—Structuring the ERA—Integrated Infrastructure Initiative Contract EURONS No. RII3-CT-2004-506065, by the FWO-Vlaanderen, by the IAP programme of the Belgium Science Policy under Grants No. P6/23 and No. P7/12, by a grant of the MICINN (Spain) (FPA2011-29854), by the Nupnet network SARFEN (PRI-PIMMNUP-2011-1361), by MINECO (Spain) Centro de Excelencia Severo Ochoa Programme under Grant No. SEV-2012-0249, and by JSPS KAKENHI (Japan) Grants No. 21740204 and No. 15K05094. The experiment was carried out under Experimental Program E437b.

[1] C. Thibault, R. Klapisch, C. Rigaud, A. M. Poskanzer, R. Prieels, L. Lessard, and W. Reisdorf, Phys. Rev. C **12**, 644 (1975).
[2] G. Huber, F. Touchard, S. Büttgenbach, C. Thibault, R. Klapisch, H. T. Duong, S. Liberman, J. Pinard, J. L. Vialle, P. Juncar *et al.*, Phys. Rev. C **18**, 2342 (1978).
[3] C. Détraz, D. Guillemaud, G. Huber, R. Klapisch, M. Langevin, F. Naulin, C. Thibault, L. C. Carraz, and F. Touchard, Phys. Rev. C **19**, 164 (1979).
[4] E. K. Warburton, J. A. Becker, and B. A. Brown, Phys. Rev. C **41**, 1147 (1990).
[5] Y. Utsuno, T. Otsuka, T. Glasmacher, T. Mizusaki, and M. Honma, Phys. Rev. C **70**, 044307 (2004).
[6] G. Neyens, M. Kowalska, D. Yordanov, K. Blaum, P. Himpe, P. Lievens, S. Mallion, R. Neugart, N. Vermeulen, Y. Utsuno *et al.*, Phys. Rev. Lett. **94**, 022501 (2005).
[7] D. T. Yordanov, M. Kowalska, K. Blaum, M. De Rydt, K. T. Flanagan, P. Lievens, R. Neugart, G. Neyens, and H. H. Stroke, Phys. Rev. Lett. **99**, 212501 (2007).
[8] P. Himpe, G. Neyens, D. L. Balabanski, G. Bélier, J. M. Daugas, F. de Oliveira Santos, M. De Rydt, K. T. Flanagan, I. Matea, P. Morel *et al.*, Phys. Lett. B **658**, 203 (2008).
[9] D. T. Yordanov, M. L. Bissell, K. Blaum, M. De Rydt, C. Geppert, M. Kowalska, J. Krämer, K. Kreim, A. Krieger, P. Lievens *et al.*, Phys. Rev. Lett. **108**, 042504 (2012).
[10] A. Chaudhuri, C. Andreoiu, T. Brunner, U. Chowdhury, S. Ettenauer, A. T. Gallant, G. Gwinner, A. A. Kwiatkowski, A. Lennarz, D. Lunney *et al.*, Phys. Rev. C **88**, 054317 (2013).
[11] G. Neyens, P. Himpe, L. D. Balabanski, P. Morel, L. Perrot, M. De Rydt, I. Stefan, C. Stodel, J. C. Thomas, N. Vermeulen *et al.*, Eur. Phys. J. Spec. Topics **150**, 149 (2007).
[12] F. Rotaru, F. Negoita, S. Grévy, J. Mrazek, S. Lukyanov, F. Nowacki, A. Poves, O. Sorlin, C. Borcea, R. Borcea *et al.*, Phys. Rev. Lett. **109**, 092503 (2012).
[13] K. Wimmer, T. Kröll, R. Krücken, V. Bildstein, R. Gernhäuser, B. Bastin, N. Bree, J. Diriken, P. Van Duppen, M. Huyse *et al.*, Phys. Rev. Lett. **105**, 252501 (2010).
[14] A. A. Kwiatkowski, C. Andreoiu, J. C. Bale, A. Chaudhuri, U. Chowdhury, S. Malbrunot-Ettenauer, A. T. Gallant, A. Grossheim, G. Gwinner, A. Lennarz *et al.*, Phys. Rev. C **92**, 061301 (2015).
[15] A. Morton, P. Mantica, B. Brown, A. Davies, D. Groh, P. Hosmer, S. Liddick, J. Prisciandaro, H. Schatz, M. Steiner *et al.*, Phys. Lett. B **544**, 274 (2002).
[16] P. Himpe, G. Neyens, D. L. Balabanski, G. Bélier, D. Borremans, J. M. Daugas, F. de Oliveira Santos, M. De Rydt, K. Flanagan, G. Georgiev *et al.*, Phys. Lett. B **643**, 257 (2006).
[17] V. Tripathi, S. L. Tabor, P. F. Mantica, Y. Utsuno, P. Bender, J. Cook, C. R. Hoffman, S. Lee, T. Otsuka, J. Pereira *et al.*, Phys. Rev. Lett. **101**, 142504 (2008).
[18] D. T. Yordanov, K. Blaum, M. De Rydt, M. Kowalska, R. Neugart, G. Neyens, and I. Hamamoto, Phys. Rev. Lett. **104**, 129201 (2010).
[19] V. Tripathi, S. L. Tabor, P. F. Mantica, Y. Utsuno, P. Bender, J. Cook, C. R. Hoffman, S. Lee, T. Otsuka, J. Pereira *et al.*, Phys. Rev. Lett. **104**, 129202 (2010).
[20] C. Nociforo, A. Prochazka, R. Kanungo, T. Aumann, D. Boutin, D. Cortina-Gil, B. Davids, M. Diakaki, F. Farinon, H. Geissel *et al.*, Phys. Rev. C **85**, 044312 (2012).
[21] K. Shimada, H. Ueno, G. Neyens, K. Asahi, D. L. Balabanski, J. M. Daugas, M. Depuydt, M. De Rydt, L. Gaudefroy, S. Grévy *et al.*, Phys. Lett. B **714**, 246 (2012).
[22] M. De Rydt, R. Lozeva, N. Vermeulen, F. de Oliveira Santos, S. Grévy, P. Himpe, C. Stdel, J. C. Thomas, P. Vingerhoets, and G. Neyens, Nucl. Instrum. Methods Phys. Res., Sect. A **612**, 112 (2009).
[23] A. Abragam, *Principles of Nuclear Magnetism* (Oxford University Press, Oxford, UK, 1961).
[24] D. Borremans, D. L. Balabanski, K. Blaum, W. Geithner, S. Gheysen, P. Himpe, M. Kowalska, J. Lassen, P. Lievens, S. Mallion *et al.*, Phys. Rev. C **72**, 044309 (2005).
[25] M. De Rydt, M. Depuydt, and G. Neyens, At. Data Nucl. Data Tables **99**, 391 (2013).
[26] V. Kellö, A. J. Sadlej, P. Pyykkö, D. Sundholm, and M. Tokman, Chem. Phys. Lett. **304**, 414 (1999).
[27] M. De Rydt, G. Neyens, K. Asahi, D. L. Balabanski, J. M. Daugas, M. Depuydt, L. Gaudefroy, S. Grévy, Y. Hasama, Y. Ichikawa *et al.*, Phys. Lett. B **678**, 344 (2009).
[28] B. A. Brown and B. H. Wildenthal, Annu. Rev. Nucl. Part. Sci. **38**, 29 (1988).
[29] E. Caurier, F. Nowacki, and A. Poves, Phys. Rev. C **90**, 014302 (2014).
[30] Y. Utsuno, T. Otsuka, T. Mizusaki, and M. Honma, Phys. Rev. C **60**, 054315 (1999).
[31] T. Mizusaki, N. Shimizu, Y. Utsuno, and M. Honma (unpublished).
[32] M. Dufour and A. P. Zuker, Phys. Rev. C **54**, 1641 (1996).
[33] M. De Rydt, Ph.D. thesis, KU Leuven, Leuven, Belgium, 2010 (unpublished).
[34] D. Nagae, H. Ueno, D. Kameda, M. Takemura, K. Asahi, K. Takase, A. Yoshimi, T. Sugimoto, K. Shimada, T. Nagatomo *et al.*, Phys. Rev. C **79**, 027301 (2009).

4.3 The unique nature of the 1^+ isomer in ^{34}Al

In May 2016, a β-NMR/NQR experiment (E650) was performed to determine the g-factor and quadrupole moment of the newly discovered 1^+ isomer in $^{34}Al_{21}$. Due to the low production yield and the large number of β's originating from the daughter decay, this experiment was very challenging. In a first part of the experiment, the set-up was therefore tested and optimised using the well-known ^{32}Al isotope.
For this experiment, I was in charge of the experimental preparation and setting up of the β-NMR/NQR apparatus at GANIL.

4.3.1 Physics case

Recently, the 0_2^+ state in ^{34}Si was discovered following the β-decay of ^{34}Al [Rotaru et al., 2012] at GANIL. From the absence of γ-rays in coincidence with the 511 keV γ-rays produced in the $0_2^+ \rightarrow 0_1^+$ internal pair creation decay, it could be concluded that the 0_2^+ state was fed directly in the ^{34}Al β-decay. In this experiment, the existence of two β-decaying states in ^{34}Al was surmised based on the observation of two distinctly different half-lives in the timed β-γ-spectra: the 4^- state with the known 56 ms half-life and a new isomer with a 26 ms half-life.
From shell-model calculations, a 1^+ isomeric state is predicted in ^{34}Al at a few 100 keV [Himpe et al., 2008]. As shown in Fig. 4.4, this 1^+ state is suggested to arise from the excitation of one neutron from the sd shell to the pf-shell, i.e. a 1p-1h intruder. Following these predictions, the β-decay from the 1^+ state would then proceed mainly through the $\nu d_{3/2} \rightarrow \pi d_{5/2}$ Gamow-Teller decay,

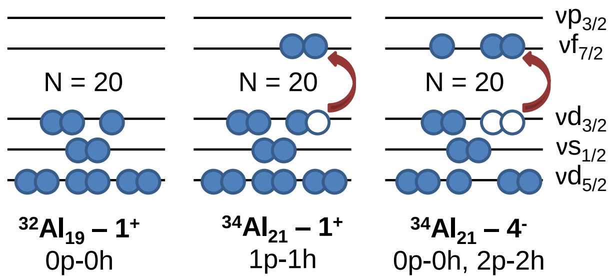

Figure 4.4: The proposed neutron configurations of the 1^+ ground state in ^{32}Al, the 1^+ state in ^{34}Al and the 4^- state in ^{34}Al.

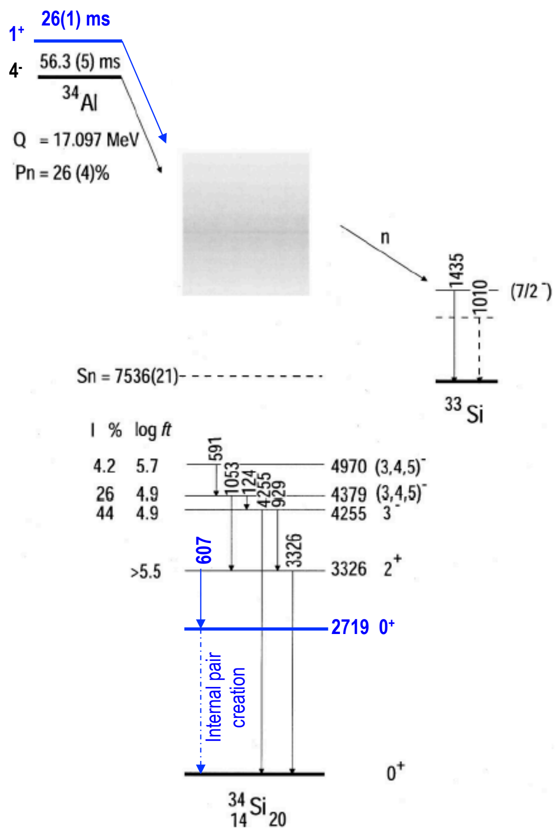

Figure 4.5: Updated ^{34}Al β-decay scheme, adapted from [Nummela et al., 2001].

populating the 2p-2h 0_2^+ state in ^{34}Si. An updated β-decay scheme of ^{34}Al is shown in Fig. 4.5.
Note that the relative energy difference between the 4^- and the 1^+ state in ^{34}Al could not yet be determined, giving rise to the question which of them is the actual ground state. As pointed out by Ascher et al. [2013], if the 1^+ state would be the ground state, the two-neutron separation energies would be altered, washing out the cross-over observed by Kwiatkowski et al. [2015]. Although the naming is ambiguous, in this thesis the 4^- state will be referred to as the ground state while the term isomer is reserved for the 1^+ state.

So far, the ground and long-lived states of isotopes inside the island of inversion have been described in terms of an even number of neutron excitations across

Table 4.1: Shell model calculations for the nuclear moments of ^{32,34}Al. Free g-factors and $e_\pi = 1.31e, e_\nu = 0.46e$ effective charges are used in the calculations. Because of the small size of the quadrupole moments, the choice of effective charges has little influence on the absolute quadrupole moment.

			Exp.	SDPF-U-MIX	SDPF-M
g-factor	^{32}Al	1^+	1.9516(22)	1.80	1.83
	^{34m}Al	1^+	-	1.76	1.73
	^{34g}Al	4^-	0.539(2)	0.54	0.37
Q_s [mb]	^{32}Al	1^+	24(2)	26.9	29.6
	^{34m}Al	1^+	-	44.6	42.9

$N = 20$ (2p-2h, 4p-4h and to a lesser extend also 6p-6h excitations). From a β-decay study, the ground state of ^{33}Mg was interpreted as having a 1p-1h nature [Tripathi et al., 2008] but this was not supported by other experimental evidence [Neyens, 2011]. The proposed 1p-1h nature of the 1^+ state in ^{34}Al offers therefore a first opportunity to study the deformation associated with such exceptional intruder wave functions.
Comparing the g-factor of the 1^+ state in ^{34}Al with the one of the ^{32}Al ground state will allow verification of the proposed 1p-1h configuration. Indeed, the unpaired nucleon configuration of the 1^+ state of ^{34}Al ($\pi d_{5/2}^{-1} \otimes \nu d_{3/2}^{-1} (f_{7/2}^2)_{J=0^+}$) would be similar to the 1^+ state of ^{32}Al (see Fig. 4.4) and hence their g-factors would be similar as well. However, the intruder nature in ^{34}Al might induce a significant amount of deformation which would be manifested in a larger quadrupole moment. Shell model calculations using various effective interactions indeed predict an almost doubling of the quadrupole moment for a pure 1p-1h wave function compared to the normal ^{32}Al ground state, as can be seen in table 4.1.

^{34m}Al is a unique case where the increase in deformation due to a 1p-1h excitation can be experimentally verified. As such, a g-factor and quadrupole moment measurement are indispensable to establish a unified picture of the nuclear structure in the island of inversion.

4.3.2 Overview

The ^{32}Al and ^{34}Al fragments were produced in projectile-fragmentation and pick-up reactions induced by a $^{36}S^{16+}$ primary beam (3.5 μA, 77.7 MeV/u) on a ^{9}Be target (1043.6 μm). In order to obtain a spin-polarized beam, the primary beam was put on target under an angle of 1.5°. A 1053.4 μm thick

^{9}Be wedge was placed in the dispersive plane between the two magnets of the LISE3 fragment separator.
For ^{34}Al, both the ground state and the isomer are produced simultaneously and inseparable. An isomeric ratio of $\sim 30\%$ was estimated based on the experiment in which the isomer was discovered [Rotaru et al., 2012], which was performed under similar conditions as ours.
An overview of the spectrometer settings, corresponding yields and additional useful information, can be found in table 4.2.

During beam tuning, the fragments were identified by means of their energy loss in a Si-detector and time of flight referenced to the radio frequency of the cyclotrons. The transmission, yield and purity was determined at three places along the beam line: after the fragment separator, just before the vacuum chamber and just before the implantation crystal. Additionally, a dedicated measurement of the yield as a function of the linear momentum was made by changing the position of the F31 slits after the first separator dipole magnet. As explained in section 3.1.1, an appropriate selection in the momentum distribution, taking into account the different reaction mechanisms for the production of ^{32}Al and ^{34}Al, gives rise to a polarized beam. As shown in the top of Fig. 4.6, a selection in the right wing of the momentum distribution was made for ^{32}Al while a selection around the center was made for ^{34}Al.
The energy loss versus time of flight plots with the spectrometer settings for ^{32}Al and ^{34}Al can be seen in Fig. 4.6. After beam-tuning, the Si-detectors were removed to avoid electron pick-up which would reduce the polarization in the β-NMR/NQR measurements.
To cross-check the identification of the fragments made via the energy loss time of flight plots, two HPGe detectors (Canberra GC7023 (γ_H) and Ortec EGCN 20-18-R (γ_G)) were placed outside the β-NMR chamber to detect β-delayed γ-rays.

The data were collected on an event-by-event basis on two separate data-acquisitions. Our own e650-acquisition was the main acquisition during the β-NMR/NQR measurements, using β-coincidences as trigger. The standard LISE-acquisition was used during the beam-tuning. Additionally, also the γ-signals and β-coincidences were copied and sent to the LISE-acquisition. This allowed optimisation of the final beam-tuning to the set-up via the β-coincidence rate, and offered the possibility to collect γ-triggered γ-spectra in the LISE-acquisition simultaneously with the β-triggered spectra in our acquisition.

Table 4.2: Spectrometer settings for production of ^{32}Al and ^{34}Al (numbers taken from run 266 and run 275 of the LISE-acquisition, respectively). Note that for ^{34}Al the total $(g + m)$ numbers are shown. The β-coincidences also include the β-decay of the contaminants and the daughters.

	^{32}Al	**^{34}Al**
	Production	
Reaction:	Projectile-fragmentation	Neutron pick-up
Target angle:	35°	35°
Dipoles:	$B\rho_1 = 2.9504$ Tm	$B\rho_1 = 3.0423$ Tm
	$B\rho_2 = 2.7494$ Tm	$B\rho_2 = 2.8212$ Tm
Slits:	F31: [+15, +40] mm	F31: [−15, +10] mm
	F43: [−10,10] mm	F43: [−10,10] mm
Production:	4700 pps/μA	125 pps/μA
Purity:	90%	85%
Contaminants:	^{30}Mg (5%)	^{36}Si (4%)
	^{31}Mg (0.3%)	^{35}Si (3%)
	^{29}Na (2%)	^{33}Al (1%)
		^{32}Mg (5%)
	Properties	
Spin:	1^+	4^- (g)
		1^+ (m)
Half-life:	33 ms	56 ms (g)
		26 ms (m)
Q_β:	13.02 MeV	12 - 14 MeV
	β-NMR (0.5 mm Si at 30°)	
Degraders:	1500 + 1157 μm	1500 + 518 μm
β-coincidences:	1450/s/μA[1]	100/s/μA[2]
Hours of data-taking:	6h	44h30
	β-NQR (1 mm Al_2O_3 at 25°)	
Degraders:	1500 + 700 μm	1500 + 0 μm
β-coincidences:	1050/s/μA[3]	70/s/μA[4]
Hours of data-taking:	1h30	15h40

[1] Not corrected for the dead time of 39%.
[2] Not corrected for the dead time of 3%.
[3] Not corrected for the dead time of 35%.
[4] Not corrected for the dead time of 3%.

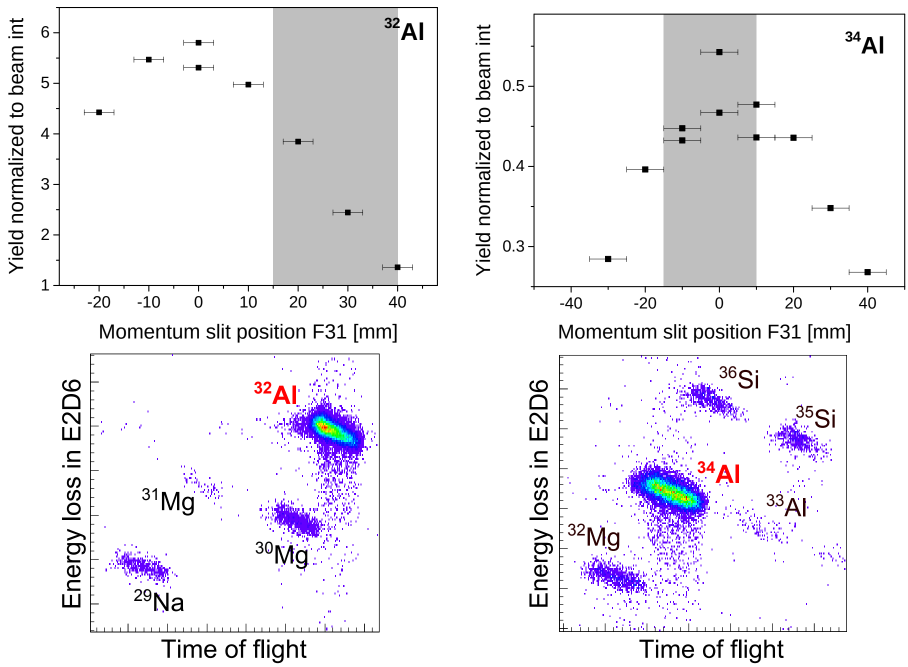

Figure 4.6: (top) Experimental momentum distribution on which the selection used during the experiment is indicated by a gray band. (bottom) Energy loss versus time of flight plots for the identification of ^{32}Al and ^{34}Al.

4.3.3 β-NMR/NQR measurements

Conditioned β-spectra

Since the data is collected on an event-by-event basis, software conditions on the β-spectra can be placed in the analysis of the data. This might be advantageous in case there are a lot of background β's with much higher or lower end-point energies. Since the purity of the beam is very high in our case, this background originates mostly from the daughter decay in the decay chain from the isotope of interest. Note that the β-spectra are not energy calibrated.

The β-spectrum of ^{32}Al collected in the E_{up} and E_{down} detectors is shown along with the β-decay scheme in Fig. 4.7. This spectrum is almost purely determined by the $Q_\beta = 13.02$ MeV ground state to ground state branch, since the ^{32}Si daughter has a very low $Q_\beta = 0.22$ MeV and a very long half-life ($T_{1/2} = 153$ year). The bump in the spectrum around channel 7000 corresponds to a ΔE

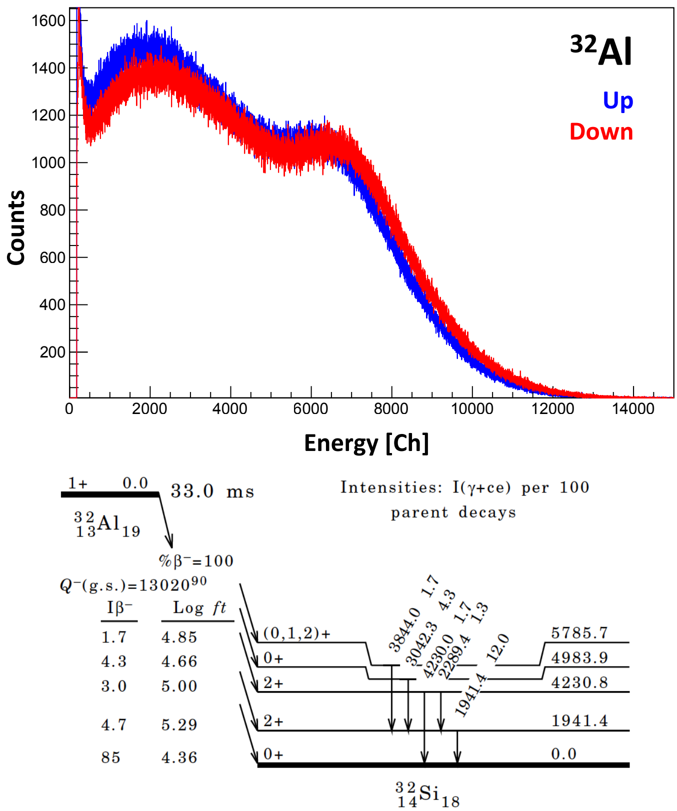

Figure 4.7: Experimental β-spectrum and β-decay scheme [Ouellet and Singh, 2011] of ^{32}Al.

peak of the high-energy β's which fly through the 28 mm thick E-detectors. According to GEANT4 simulations [De Rydt et al., 2009], this peak occurs at approximately 5.5 MeV.

The ^{34}Al case is a bit more complicated. First of all, it is estimated that only $\sim 30\%$ of the β's in the ^{34}Al decay originates from the 1^{+} isomer while the remaining 70% comes from the ground state. The exact decay scheme of the isomer is not well-known but the energies of the β's will be very similar to those of the ground state, between 12 - 14 MeV. This means that it is impossible to distinguish between the two states based on their β-energies. Furthermore, the decay chain of ^{34}Al is much longer than for ^{32}Al, with a significant βn branch

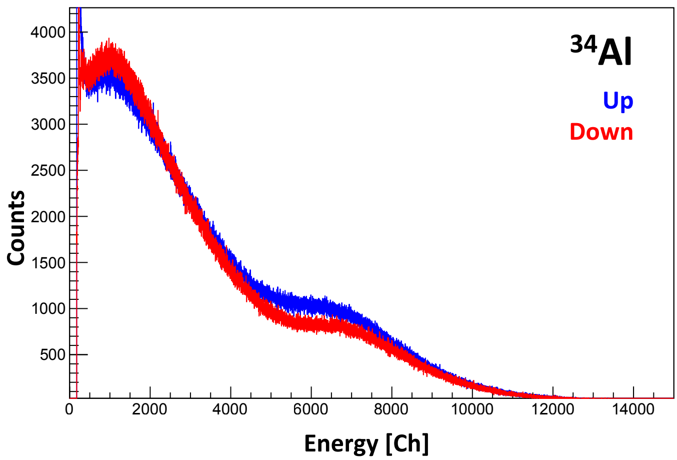

Figure 4.8: Experimental β-spectrum of ^{34}Al.

of 26%

$$
\begin{aligned}
{}^{34m,g}\text{Al}\ (\beta) &\rightarrow {}^{34}\text{Si (2.77 s, 4.59 MeV)} \\
&\rightarrow {}^{34}\text{P (12.43 s, 5.38 MeV)} \\
&\rightarrow {}^{34}\text{S (stable)} \\
{}^{34m,g}\text{Al}\ (\beta n) &\rightarrow {}^{33}\text{Si (6.11 s, 5.85 MeV)} \\
&\rightarrow {}^{33}\text{P (25.35 days, 0.25 MeV)}
\end{aligned}
$$

For every β that is emitted, only approximately one in three belongs to ^{34}Al and only 30% of those belong to the isomer. This results in an experimental spectrum as shown in Fig.4.8, where the ΔE bump is much less pronounced than in ^{32}Al due the low-energy contribution of the daughter decay.
As shown in appendix A.1, the effect of the β's of the daughter and the ground state is to reduce the experimental asymmetry, defined as the difference between the asymmetry on and off resonance

$$\mathcal{A}_{\text{exp}} = \mathcal{A}_{\text{on}} - \mathcal{A}_{\text{off}}. \tag{4.1}$$

Compared with a situation in which only the isomer ^{34m}Al would be present, the asymmetry is reduced by a factor of 9

$$\frac{\mathcal{A}_{\text{exp}}}{\mathcal{A}^{34m}} = \frac{N^{34m}_{\text{tot}}}{N^{34m}_{\text{tot}} + N^{bg}_{\text{tot}}} \approx \frac{1}{9} \tag{4.2}$$

In principle, the influence of the low-energy daughter β's can be reduced by placing energy cuts in the spectrum. However, this also means cutting out part of the good β's. A careful analysis of the loss in statistics versus gain in experimental signal amplitude needs to be performed.
The reduced β-asymmetry in combination with the low production yield, make the measurements very challenging.

Very preliminary results

No in-depth analysis of the available data has been performed at the time of writing. To give an idea of the quality of the data, part of the online results is presented here. Note that the experimental asymmetry resonance is a peak for ^{32}Al, while it is a dip for ^{34m}Al. This is a consequence of the opposite spin-polarization of the beam, in combination with the same sign of the A_β parameter[2]. Due to the different reaction mechanisms to produce ^{32}Al and ^{34}Al, the opposite polarization arises from the chosen selection in the momentum distribution (see Fig. 4.6).

At the start of the experiment, the set-up was optimised using ^{32}Al. A selection of the ^{32}Al β-NMR and β-NQR spectra can be seen in Fig. 4.9. For simplicity, the spectra are fitted with a Gaussian line shape.
Furthermore, in order to have an idea of what to expect for ^{34m}Al, a β-NMR and β-NQR spectrum of ^{32}Al was taken with exactly the same stepsize and modulation as used in ^{34m}Al. In the β-NMR runs with stepsize of 60 kHz and modulation of 45 kHz, one or two frequency points are at resonance, depending on whether the real resonance frequency lies in the overlapping part of two neighbouring modulation intervals or not. Note that this implies that the resonance position can be determined more precisely than the applied modulation: if one point is in resonance, the real resonance frequency can be found in the 15 kHz interval around the central value of the modulation range. If two points are in resonance on the other hand, the real resonance frequency should lie in the 15 kHz interval around the central value of the overlapping modulation ranges. With this uncertainty of 15 kHz on the ν_L extracted from the β-NMR spectra in mind, the effect of using a ν_L which differs 15 kHz from the real value in a β-NQR measurement is tested. It turns out that the resonance amplitude is only slightly reduced, while the extracted ν_Q is shifted by 15 kHz.

The ^{32}Al spectra and ^{34m}Al spectra taken under the same conditions are shown in Fig. 4.10. In the case of ^{32}Al, no cuts are made in the β-spectra while for

[2] Although the full β-decay scheme and thus the A_β of ^{34m}Al is not known, it is assumed that the ^{34m}Al β-decay proceeds mostly via $1^+ \rightarrow 0^+$ branches.

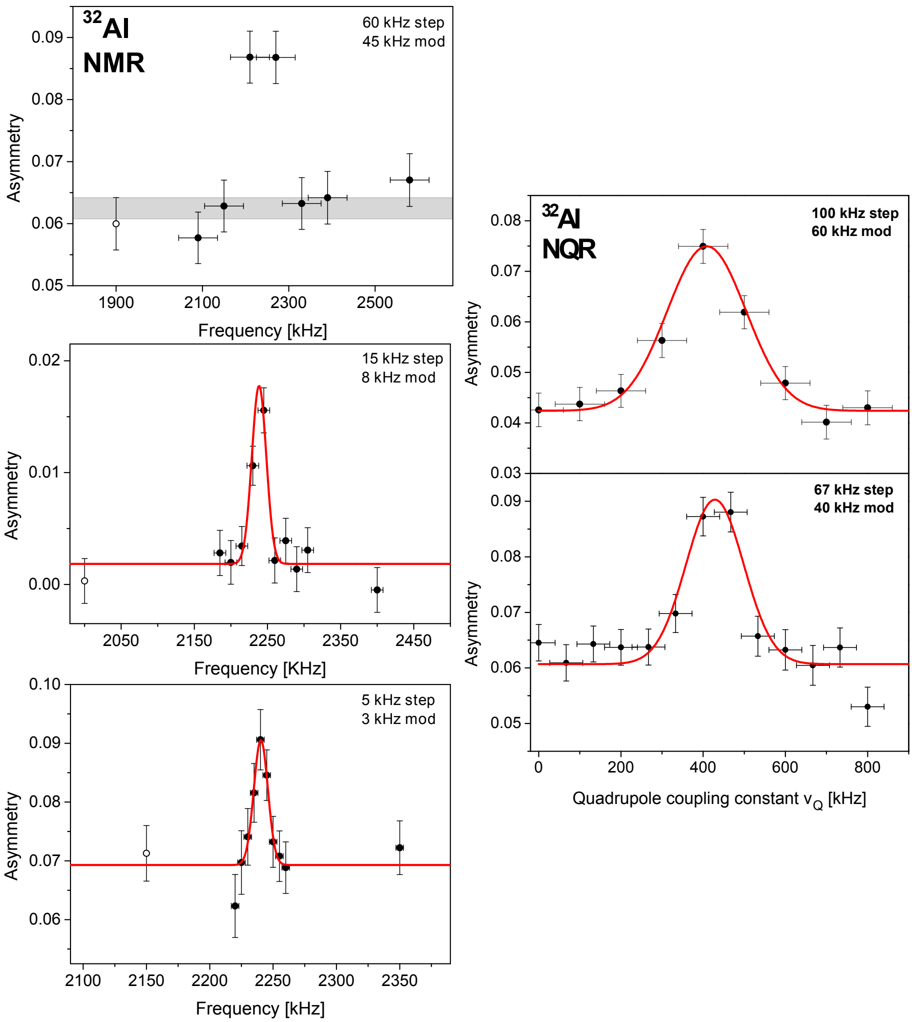

Figure 4.9: β-NMR and β-NQR spectra of ^{32}Al. The stepsize and modulation range is reduced from top to bottom. From these spectra, the preliminary results $\nu_L = 2240.6(6)$ kHz and $\nu_Q = 408(9)$ kHz are obtained although a more careful analysis is required to estimate the uncertainties on these values.

^{34m}Al only β's with an energy above 3000 Ch in the E-spectra are considered. In the β-NMR spectra, the average of the points in the base line are indicated by a gray band. Although the ^{34m}Al spectrum shows all statistics collected for this frequency range ($\sim$ 18h), the statistical significance is only 2.3σ. Since

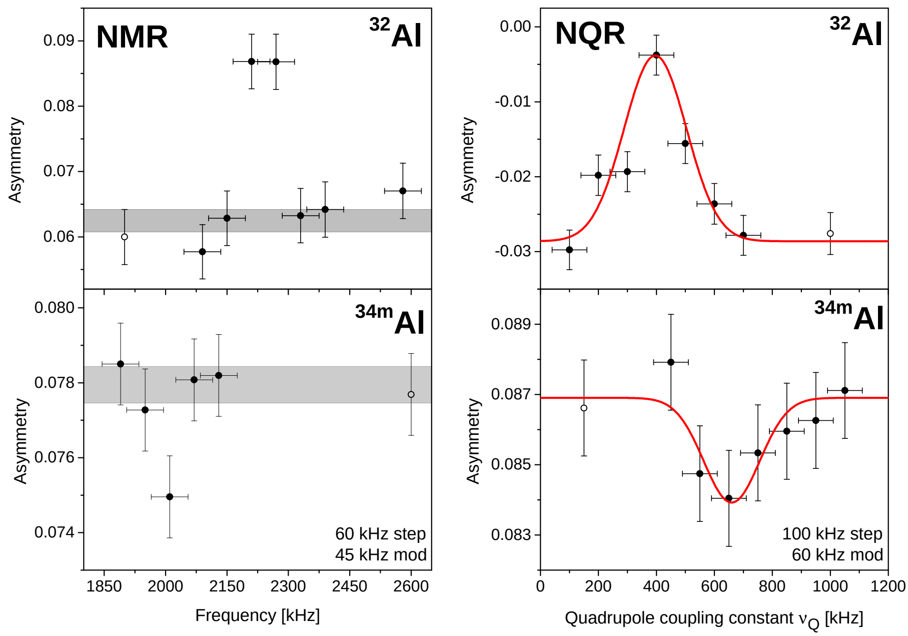

Figure 4.10: Comparison of the β-NMR and β-NQR spectra of ^{32}Al and ^{34m}Al, taken with the same stepsize and modulation range.

other β-NMR spectra taken with a smaller stepsize or different frequency range show a hint for a resonance at the same position, albeit similarly insignificant on their own, it was decided to start a β-NQR measurement.
The total statistics of the β-NQR measurement on ^{34m}Al is shown on the right side of Fig. 4.10. Although the statistics is again limited, the fact that the obtained width for ^{32}Al (0.25(3) MHz) and ^{34}Al (0.23(8) MHz) are very similar, gives some confidence in the observed resonance for ^{34m}Al. In principle, a successful β-NQR measurement confirms that the ν_L determined in the β-NMR measurement must be correct (within the measured uncertainty).

It is clear that a thorough analysis of the data is required before any solid conclusions can be drawn. Therefore, no attempt is made to discuss the results in Fig. 4.10 in detail. Nevertheless, from the preliminary resonance positions of ^{34m}Al with respect to ^{32}Al, it is suggested that the g-factor of ^{34m}Al is a little bit smaller than the one of ^{32}Al while its quadrupole moment is significantly larger, in good agreement with the shell model calculations.

4.4 Concluding remarks

Although it is already 40 years ago that the first indications for the changing nuclear structure around $N = 20$ were observed, research in this region of the nuclear chart is still highly relevant today. Only in recent years have the most exotic species become available for detailed experimental investigation and have the computational capabilities reached a level which enables the treatment of the huge model spaces necessary for a theoretical description of the observed structural changes.

In this chapter, the focus was on the ^{33,34}Al isotopes at the northern border of the island of inversion.
The quadrupole moment of the ^{33}Al ground state was measured with a 5 times higher precision than previously. Due to this high precision, the importance of 2p-2h and 4p-4h intruder configurations in the ground state wave function could unambiguously be demonstrated. This confirms ^{33}Al$_{20}$ as the transition point into the island of inversion, both in the Z-direction between Si and Mg, as in the N-direction along the Al isotopic chain[3].
Additionally, an experiment was performed to determine the g-factor and quadrupole moment of the 1^+ isomer in ^{34}Al, which is suggested to have a 1p-1h intruder dominated wave function. The characterisation of this isomer is very exciting since so far, it is the first case for which the nuclear moments of a long-lived 1p-1h intruder state can be studied in the island of inversion. The experiment was performed close to the submission of this manuscript and a careful analysis of the low-statistics data is still underway.

One of the major challenges in the $N = 20$ region is to theoretically describe the wealth of experimental information currently available, and in particular to explain how several apparently contradicting results can be reconciled with each other. Nuclear moments of the neutron-rich Al isotopes have shown to be excellent test cases for the available state-of-the-art models, see for example section 4.2.3 and [Himpe et al., 2008]. As such, the g-factor and quadrupole moment measurements of ^{33}Al and ^{34m,g}Al are essential to obtain a complete picture of the nuclear structure in the island of inversion and to improve its theoretical understanding.

[3]The intruder dominance in the wave function of the 4^- ground state in ^{34}Al$_{21}$ was already established from a g-factor measurement [Himpe et al., 2008].

Part III

Collinear laser spectroscopy on neutron-rich Mn

5 Collinear laser spectroscopy at ISOLDE-CERN

The neutron-rich Mn were studied using collinear laser spectroscopy at ISOLDE in CERN. In this chapter, an overview is given of the production of radioactive ion beams at the ISOLDE facility. Then it is introduced how hyperfine spectra give information on spins, magnetic moments, quadrupole moments and changes in mean-square charge radii. Finally, the collinear laser spectroscopy technique is explained and the specific lay-out of the collinear laser spectroscopy beam line at ISOLDE is discussed.

5.1 The ISOLDE facility

Since its first commissioning in 1967, ISOLDE (Isotope Separation Online DEvice) has been one of the leading radioactive beam facilities in the world, producing more than 700 different isotopic beams used for research in nuclear physics, solid state physics and life sciences.
The facility is located at the CERN accelerator complex where it receives a 1.4 GeV pulsed proton beam from the Proton Synchrotron Booster. The pulses contain approximately $3 \cdot 10^{13}$ protons/pulse and are organised in a supercycle which consists of 30 - 40 pulses separated 1.2 s apart. Throughout the supercycle typically 30 - 50 % of the proton pulses is delivered to ISOLDE. Impact of the high-energy protons on a hot, thick target produces a variety of radioactive nuclides via a range of nuclear reactions such as fission, spallation and fragmentation. For the production of isotopes at the neutron-rich side of the chart of nuclides, often uranium carbide targets are selected.
After diffusing from the target, the reaction products are ionized in an appropriate ion source and accelerated to 30 - 60 keV. The primary ion sources

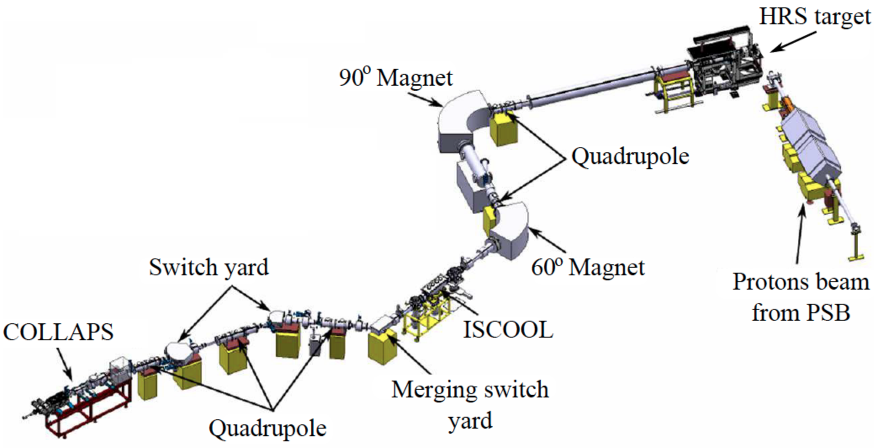

Figure 5.1: Schematic depiction of the subsequent stages from radioactive beam production in the HRS target up to the COLLAPS beam line.

at ISOLDE are a surface ion source, plasma ion source and resonance ionization laser ion source (RILIS), the most suitable option depending on the physical and chemical properties of the species of interest. Due to the efficiency and selectivity of the element-specific stepwise photo-ionization process, RILIS is currently the principal ion source at ISOLDE [Rothe et al., 2016]. In order to get an isotopically pure beam, the singly-charged ion beams are mass separated using dipole magnets, although in general, it is not possible to eliminate all unwanted isobars which are produced and ionized along with the beam of interest. At ISOLDE two mass separators connected to two independent target stations are available: the general purpose separator (GPS) and the high-resolution separator (HRS). An important advantage of the HRS is its superior mass resolving power which is obtained by a 60° and a 90° bending magnet and an elaborate ion-optics system. Furthermore, a radio frequency quadrupole trap ISCOOL [Mané et al., 2009] is installed in the focal plane of the HRS to cool and bunch the ion beams. Since the availability of bunched beams is essential for collinear laser spectroscopy on exotic beams, the experiments in this work were performed on HRS-beams. Finally, the mass separated beams are guided to one of the low-energy experimental beam lines or, when higher energies are needed, post-accelerated to several MeV/u using REX/HIE-ISOLDE [Van Duppen and Riisager, 2011]

The subsequent stages from production in the HRS target to the collinear laser spectroscopy set-up COLLAPS are schematically shown in Fig. 5.1.

Table 5.1: Overview of the spins, half-lives, masses [Wang et al., 2012; Naimi et al., 2012] and yields of the Mn isotopes studied in this thesis. The spin assignments for $^{61-64}$Mn were made in this work. The yields were extracted from the ISOLDE yield database and should only be considered as a rough estimate.

	N	I^π	$T_{1/2}$	Mass [u]	Yield [ions/μC]
^{51}Mn	26	$5/2^-$	46.2 m	50.9482085	$6.0 \cdot 10^4$[1]
^{53}Mn	28	$7/2^-$	$3.74 \cdot 10^6$ y	52.9412889	$3.0 \cdot 10^7$
^{54}Mn	29	3^+	312.1 d	53.9403576	$9.0 \cdot 10^7$
^{55}Mn	30	$5/2^-$	stable	54.9380439	-
^{56}Mn	31	3^+	2.58 h	55.9389037	$4.0 \cdot 10^8$
^{57}Mn	32	$5/2^-$	85.4 s	56.9382861	$1.5 \cdot 10^8$
^{58g}Mn	33	1^+	3.0 s	57.940067	$1.7 \cdot 10^7$[1]
^{58m}Mn	33	4^+	65.4 s	57.940144	-[2],
^{59}Mn	34	$5/2^-$	4.6 s	58.9403911	$1.5 \cdot 10^8$
^{60g}Mn	35	1^+	0.28 s	59.943137	-[2]
^{60m}Mn	35	4^+	1.77 s	59.943429	-[2]
^{61}Mn	36	$5/2^-$	0.67 s	60.9444525	$1.7 \cdot 10^6$
^{62g}Mn	37	1^+	92 ms	61.947904	-[2]
^{62m}Mn	37	4^+	671 ms	61.948276	-[2]
^{63}Mn	38	$5/2^-$	275 ms	62.949665	$2 \cdot 10^5$
^{64}Mn	39	1^+	90 ms	63.953849	$7 \cdot 10^3$

[1] SC yield with 0.6 GeV protons
[2] Not tabulated for UC_x

5.1.1 Manganese production

The manganese isotopes were produced by the bombardment of a 1.4 GeV proton beam on a uranium carbide target and selectively ionized in a three-step ionization scheme with a 19% ionization efficiency [Marsh et al., 2010]. In table 5.1, the ISOLDE yields for the Mn isotopes studied in this work are shown along with the nuclear spins, masses and half-lives. These yields were determined in 2000 with a 1 GeV proton beam and a less efficient RILIS scheme [Oinonen et al., 2000] and should be considered as a rough guideline which differs from the online conditions. The exact yields varied between the two runs discussed in this work and were particularly bad in the second run due to problems with the target.

5.2 Nuclear properties from atomic spectra

Although the nucleus is approximately four orders of magnitude smaller than the average radius of its surrounding atomic electrons, the properties of the nucleus have a small but non-negligible effect on the atomic energy levels. Very precise measurements of these atomic levels therefore enable the extraction of nuclear spins, magnetic dipole moments,electric quadrupole moments and changes in mean-square charge radii.

5.2.1 Hyperfine splitting

In a first approximation, the energy of an atom can be calculated by considering the movement of the electrons in the Coulomb field of a point-nucleus with charge eZ, combined with the electron-electron interaction including a spin-orbit term. This describes the atomic energy levels up to the fine structure.
Taking into account the internal structure of the nucleus results in an additional splitting of the atomic levels due to the electromagnetic interaction between the nuclear moments and the surrounding electron cloud. Since the size of the so-called hyperfine splitting is very small compared to the fine structure splitting (μeV vs meV), it can be calculated in first order perturbation theory. When considering the hyperfine interaction, the appropriate quantum number to label a state is the total angular momentum $\boldsymbol{F}$ which is the vector sum of the nuclear spin $\boldsymbol{I}$ and the electronic spin $\boldsymbol{J}$. From angular momentum coupling rules, F can range from $|I-J|$ to $I+J$.

For a nucleus with $I > 0$ and an electronic state with $J > 0$, there is an interaction between the nuclear magnetic dipole moment μ and the magnetic field generated by the electrons at the center of the nucleus B_J. This magnetic dipole interaction results in an energy shift of the atomic level F

$$\Delta E_{\text{dip}}/h = \frac{A_J}{2}\left[(F(F+1) - I(I+1) - J(J+1)\right] \tag{5.1}$$

where the (magnetic) hyperfine coupling constant

$$A_J = \frac{\mu B_J}{IJ} \tag{5.2}$$

is introduced. When $I, J > 1/2$, also the orientation of the nuclear electric quadrupole moment Q_s with respect to the electric field gradient V_{zz} produced by the electrons is important. The quadrupole interaction induces an additional energy shift

$$\Delta E_{\text{quad}}/h = B_J \frac{3C(C+1) - 4I(I+1)J(J+1)}{8I(2I-1)J(2J-1)} \tag{5.3}$$

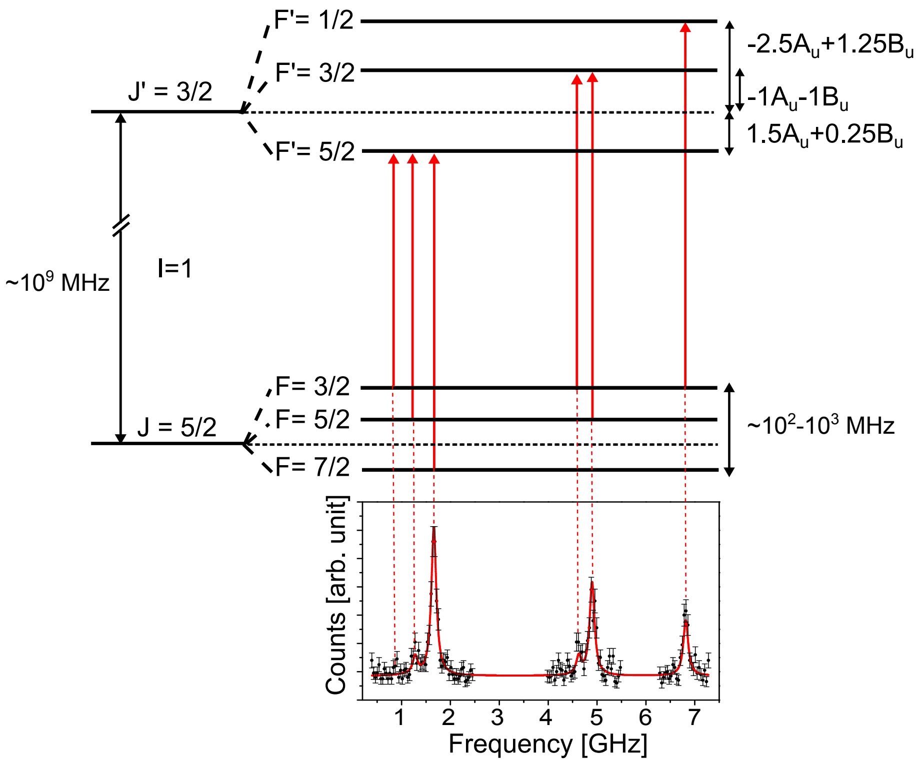

Figure 5.2: Hyperfine structure of the $J = 5/2 \rightarrow J' = 3/2$ atomic transition in ^{64}Mn ($I = 1$). The corresponding experimental hyperfine spectrum is shown underneath.

using the shorthand notation $C = F(F+1) - I(I+1) - J(J+1)$. The (quadrupole) hyperfine parameter is defined as

$$B_J = eQ_sV_{zz}. \tag{5.4}$$

Since the contribution of higher order electromagnetic multipoles to the hyperfine splitting become increasingly small, for most practical purposes it is sufficient to consider only the magnetic dipole interaction and electric quadrupole interaction. A realistic depiction of the hyperfine structure of the ^{64}Mn atom is shown in top of Fig. 5.2.

Once A and B are measured for a reference isotope with a known magnetic and quadrupole moment, unknown nuclear moments can be extracted using

$$\mu = \mu_{\text{ref}} \frac{AI}{A_{\text{ref}} I_{\text{ref}}} \tag{5.5}$$

$$Q_s = Q_{s,\text{ref}} \frac{B}{B_{\text{ref}}}. \tag{5.6}$$

Eq. 5.5 however neglects finite-size contributions of the nucleus and is therefore only strictly valid for a point-nucleus. Taking into account the distribution of the magnetisation over the nuclear volume gives rise to a correction

$$\mu = \mu_{\text{ref}} \frac{AI}{A_{\text{ref}} I_{\text{ref}}} \left(1 + {}^{1}\Delta^{2}\right) \tag{5.7}$$

where ${}^{1}\Delta^{2}$ is the differential hyperfine anomaly which depends on the atomic states and nuclei under consideration. In general, the hyperfine anomaly is very small, on the 10^{-4} level, but for specific cases it might be on the order of a few percent. A compilation of the known hyperfine anomalies can be found in [Persson, 2013].

5.2.2 Isotope shift

The isotope shift is a shift in the transition frequency observed when going from one isotope A to another isotope A' of the same element:

$$\delta\nu^{A,A'} = \nu_0^{A'} - \nu_0^{A} \tag{5.8}$$

Here, ν_0^A is the centroid frequency of the hyperfine structure for an isotope A which equals the unperturbed fine structure transition frequency. The isotope shift is in general decomposed in two components

$$\delta\nu^{A,A'} = \delta\nu_{\text{MS}}^{A,A'} + \delta\nu_{\text{FS}}^{A,A'}, \tag{5.9}$$

the mass shift (MS) and the field shift (FS), which are related to the finite mass and finite size of the atomic nucleus, respectively.

Field shift

The field shift arises from the change in electrostatic potential felt by the electrons due to the different nuclear charge distribution of different isotopes. For a transition between two atomic states, it is proportional to the change in electron probability density $\Delta|\psi_e(0)|^2$ at the nucleus and the change in nuclear charge radius between two isotopes

$$\delta\nu_{\mathrm{FS}}^{A,A'} = \frac{\pi a_0^3}{Z}\Delta|\psi_e(0)|^2 f(Z)\delta\langle r^2\rangle^{A,A'} \tag{5.10}$$

$$= F\delta\langle r^2\rangle^{A,A'}. \tag{5.11}$$

Here a_0 is the Bohr radius, $f(Z)$ is a relativistic correction factor and F is the field shift factor. For heavy nuclei $\delta\langle r^2\rangle^{A,A'}$ is replaced by the Seltzer moment $\lambda^{A,A'} = K(Z)\delta\langle r^2\rangle^{A,A'}$ [Seltzer, 1969; Torbohm et al., 1985] which depends on higher-order radial moments.

Mass shift

The mass shift arises from the recoil motion of a nucleus with finite mass and is written as

$$\delta\nu_{\mathrm{MS}}^{A,A'} = M\frac{m_{A'} - m_A}{m_{A'}m_A} \tag{5.12}$$

where M is the mass shift factor. Although the mass shift is uninteresting for our purpose, its effect needs to be known in order to reliably extract the field shift, from which the mean-square charge radius can be deduced.
The mass shift factor M contains two components: the normal mass shift factor and the specific mass shift factor ($M = M_{\mathrm{NMS}} + M_{\mathrm{SMS}}$). The normal mass shift factor is given by $M_{\mathrm{NMS}} = \frac{\nu_0}{1822.9}$ with $m_{\mathrm{proton}}/m_{\mathrm{electron}} = 1822.9$. The specific mass shift factor on the other hand is due to correlations between the electron momenta which are complicated to evaluate.

The mass shift overwhelmingly dominates the isotope shift in light elements, while the field shift has the largest contribution in the heavier systems. The small contribution of the field shift to the total isotope shift makes a precise determination of mean-square charge radii of light elements very challenging [Nörtershäuser and Geppert, 2014].

Calibration of *F* and *M*

The change in mean-square charge radii between two isotopes can be extracted from the measured isotope shift

$$\delta\nu_i^{A,A'} = M_i\frac{m_{A'} - m_A}{m_{A'}m_A} + F_i\delta\langle r^2\rangle^{A,A'} \tag{5.13}$$

only if the mass shift parameter M_i and field shift parameter F_i are known. Note that these M_i and F_i are element specific, i.e. constant along an isotopic chain, but need to be evaluated for each transition i separately.

A common method to extract these mass and field shift parameters is the King plot method [King, 1984] in which eq. 5.13 is multiplied by a scaling factor

$$\mu^{A,A'} = \frac{m_{A'} m_A}{m_{A'} - m_A} \tag{5.14}$$

for two different transitions i and j of the same element, giving

$$\mu^{A,A'} \delta\nu_i^{A,A'} = M_i + F_i \mu^{A,A'} \delta\langle r^2 \rangle^{A,A'} \tag{5.15}$$

$$\mu^{A,A'} \delta\nu_j^{A,A'} = M_j + F_j \mu^{A,A'} \delta\langle r^2 \rangle^{A,A'}. \tag{5.16}$$

Since $\delta\langle r^2 \rangle^{A,A'}$ is the same for both transitions, it can be eliminated in the combined relation

$$\mu^{A,A'} \delta\nu_j^{A,A'} = \frac{F_j}{F_i} \mu^{A,A'} \delta\nu_i^{A,A'} + M_j - \frac{F_j}{F_i} M_i. \tag{5.17}$$

Hence, when the scaled isotope shift j is plotted with respect to the scaled isotope shift i, a linear relation is obtained with slope $\frac{F_j}{F_i}$ and offset $M_j - \frac{F_j}{F_i} M_i$. This relates the atomic factors of both transitions and enables the determination of the unknown factors of one transition, if the mass and field shift factors of the other transition are known. In particular, if $\delta\langle r^2 \rangle$ is determined for more than two isotopes via absolute charge radii measurements, the mass and field shift factors can be extracted from a comparison between the modified isotope shifts and the modified changes in mean-square charge radii. Since so far those absolute charge radii measurement techniques require a large amount of sample material, they have only been performed on stable isotopes.
In many isotopic chains, one therefore needs to rely on atomic calculations such as the multi-configurational Dirac-Fock calculations [Fritzsche, 2002]. Because the level of precision of these calculations is usually quoted to be only around 10 - 15%, there are large uncertainties on the absolute $\delta\langle r^2 \rangle$ values. Luckily, this does not prevent the extraction of nuclear structure effects, as these appear as local irregularities of $\delta\langle r^2 \rangle$ which are unaffected by the uncertainties on M and F. An overview of the role and limitations of the atomic factor calculations has recently been given by Cheal et al. [2012].

It is interesting to note that although optical isotope shifts provide the most precise way of determining changes in mean-square charge radii along an isotopic chain, they cannot provide absolute charge radii. To extract absolute mean-square charge radii, non-optical techniques, such as muonic atom spectroscopy and high-energy elastic electron scattering, need to be employed for at least one (stable) reference isotope.

5.2.3 Hyperfine spectra

The hyperfine structure of an atom can be studied via laser spectroscopy in which laser light is used to resonantly induce optical transitions from a lower (l) hyperfine level $|IJF\rangle$ to an upper (u) hyperfine level $|IJ'F'\rangle$. The resonant excitation process can be detected by measuring the spontaneous fluorescence decay or by further ionizing the atom, after which the ion can be detected.

When the laser frequency is scanned over the hyperfine structure, a hyperfine spectrum is obtained as shown in Fig. 5.2. The positions of the hyperfine peaks in the spectrum are given by

$$\nu^{F,F'} = \nu_0 + \frac{C'}{2}A_u + \frac{3C'(C'+1) - 4I(I+1)J'(J'+1)}{8I(2I-1)J'(2J'-1)}B_u \tag{5.18}$$

$$- \frac{C}{2}A_l - \frac{3C(C+1) - 4I(I+1)J(J+1)}{8I(2I-1)J(2J-1)}B_l. \tag{5.19}$$

Fitting all peaks in the hyperfine spectrum using this equation allows the extraction of the centroid frequency and hyperfine A and B parameters, under the assumption of a particular nuclear spin. However, for nuclei far from stability the spins are often unknown or only tentatively assigned. In this case, the spin can be extracted from the analysis of the hyperfine spectrum.
The number of allowed transitions between the hyperfine levels is determined by the electric dipole selection rules

$$\Delta F = 0,\ \pm 1 \text{ and } F = 0 \nrightarrow F' = 0 \tag{5.20}$$

and in the case that $I < J$, there is a unique relation between the number of peaks in the spectrum and the nuclear spin. Alternatively, a spin assignment can be made based on the ratio of the hyperfine A parameters of the upper and lower states

$$\frac{A_u}{A_l} = \frac{B_{J'}}{B_J}\frac{J}{J'} \tag{5.21}$$

This ratio only depends on electronic properties and should therefore be constant along the isotopic chain[1]. If, for a particular spin assumption, the obtained ratio deviates significantly from the constant trend, then this is a clear indication that this assumed spin is incorrect. Moreover, since the ratio should be constant for all isotopes along the isotopic chain, it can be fixed in the fitting of low-statistics spectra to reduce the number of fit variables. The same is true for the ratio of the B-parameters.

[1] in the absence of a sizeable hyperfine anomaly

In general, the relative spacings between the peaks and the relative intensities [Magnante and Stroke, 1969]

$$I_{F,F'} \propto (2F+1)(2F'+1)\left\{ \begin{array}{ccc} F & F' & 1 \\ J' & J & I \end{array} \right\}^2 \tag{5.22}$$

depend on the nuclear spin, and an incorrect spin assignment might yield a structure incompatible with the observed spectrum.
Note that the spin determination using above techniques gets more difficult for higher spin-values.

5.3 Collinear laser spectroscopy

The advent of laser spectroscopy has introduced a powerful tool to study nuclear structure across the chart of nuclides [Campbell et al., 2016]. In particular, the application of high-resolution collinear laser spectroscopy at radioactive ion beam facilities has enabled the systematic study of ground state properties from the valley of stability up to exotic regions of the nuclear chart.

In collinear laser spectroscopy, an accelerated ion beam is collinearly overlapped with a co- or contra-propagating laser. The use of such an accelerated beam minimises the resolution limit set by the Doppler broadening of the spectral lines, caused by the thermal motions of the ions. Since the thermal energy spread

$$\delta E = \delta\left(\frac{1}{2}mv^2\right) = mv\delta v \tag{5.23}$$

is constant under acceleration, a higher velocity results in a decrease of the longitudinal velocity spread and hence a reduction of the Doppler width. With a kinetic energy spread of $\delta E \approx 1$ eV of the ions leaving the ion source[2], an acceleration voltage of 30 kV reduces the Doppler width to near the natural line width (see eq. 5.28). In fast beam collinear laser spectroscopy, the reduction of the Doppler broadening of the line width results in the high-resolution necessary to resolve the hyperfine structure.

In the reference frame of the accelerated ions, the laser frequency ν_L is Doppler shifted according to

$$\nu = \nu_L \frac{1 \pm \beta}{\sqrt{1-\beta^2}} \tag{5.24}$$

[2]For HRS beams, the kinetic energy spread of the beam is determined by ISCOOL instead of the ion source but the same numbers apply.

for a collinear (−) or anti-collinear (+) geometry. Here β is the relativistic Lorentz factor

$$\beta = \frac{v}{c} = \sqrt{1 - \frac{m^2c^4}{\left(eV + mc^2\right)^2}}. \tag{5.25}$$

with V the acceleration voltage. In this way, the laser frequency in the laboratory frame can be locked to a precise reference frequency while the Doppler-shifted frequency is scanned across the hyperfine structure by applying a tuneable acceleration voltage. This is beneficial since it is easier to stabilise a laser to a fixed frequency than to vary its frequency across the scanning range.

5.3.1 Spectral line shape

The observed width and shape of a peak in the hyperfine spectrum is influenced by several broadening mechanisms.
Due to Heisenberg's uncertainty principle, the limited lifetime τ of an excited atomic state gives rise to a minimal linewidth, called the natural linewidth

$$\Delta\nu_0 = \frac{\Delta E}{h} = \frac{1}{2\pi\tau} \tag{5.26}$$

Furthermore, the atomic linewidth increases due to power broadening effects

$$\Delta\nu_P = \Delta\nu\sqrt{1 + \frac{I}{I_S}} \tag{5.27}$$

where I is the applied laser intensity and I_S is the saturation intensity. This can be understood because the laser photons induce stimulated emission which decreases the lifetime of the excited state compared to the situation in which only spontaneous decay would be present. With increasing laser power, the stimulated emission rate is increased which in turn leads to shorter lifetimes and hence an increased linewidth. Both natural line broadening and power broadening are described by a Lorentzian line shape.
Additionally, the motion of the atoms causes a Doppler broadening of the linewidth which, for an accelerated beam, is given by

$$\Delta\nu_D = \nu_0\frac{\delta E}{\sqrt{2eVmc^2}} \tag{5.28}$$

This gives rise to a Gaussian line profile.

In collinear laser spectroscopy, the Doppler broadening is greatly reduced and in first approximation the line profile can be described by a pure Lorentzian

$$L(\nu) = \frac{\mathcal{I}}{4}\frac{\Gamma^2}{(\nu - \nu_0)^2 + (\Gamma/2)^2} \tag{5.29}$$

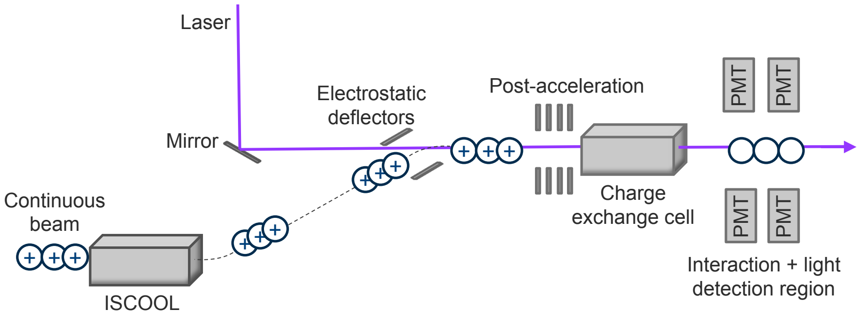

Figure 5.3: A schematic depiction of the COLLAPS set-up for optical spectroscopy on atoms. To perform spectroscopy on ionic beams, the charge exchange cell is replaced by a tube. Picture adapted from [Papuga et al., 2013]. For details see text.

where $\mathcal{I}$ is the peak intensity, Γ is the full width at half maximum and ν_0 is the centroid frequency.
Taking into account the Gaussian component to the line shape gives rise to a Voigt profile, which is the convolution of a Gaussian and a Lorentzian profile [NIST, 2016].

5.3.2 The COLLAPS beam line

A schematic depiction of the collinear laser spectroscopy beam line (COLLAPS) [Neugart, 1981] at ISOLDE is shown in Fig. 5.3.
The mass separated ion beams are cooled and bunched in ISCOOL and reaccelerated to 30 or 40 keV before they are guided to the COLLAPS beam line. Here, the ion bunches are overlapped with a co-propagating narrowband laser via a 10° electrostatic deflector. In the post-acceleration region, an acceleration voltage is applied additionally to the ISCOOL voltage such that the total voltage the ions experience is

$$V_{\rm tot} = V_{\rm ISCOOL} - V_{\rm offset} - k \cdot V_{\rm scan} \tag{5.30}$$

The offset voltage between -10 and 10 kV is used to shift the laser frequency close to the resonance frequency in the rest frame of the ions, taking into account the mass dependent Doppler shift factor and the isotope shift. A second voltage is then applied to scan the laser frequency across the hyperfine spectrum. The scanning voltage ranges between -10 and $+10$ V and is amplified by an amplification factor (called kepco factor) $k \sim 50$ giving a total scanning voltage of ± 500 V. The total post-acceleration voltage is applied gradually by four ring

electrodes at $\frac{1}{4}$, $\frac{1}{2}$, $\frac{3}{4}$ and full $V_{\text{post-acc.}}$ respectively.
Due to constraints on the wavelengths which can be efficiently produced by narrowband lasers, it is often necessary to perform laser spectroscopy on the atom instead of the ion. In this case, the ions (X) are neutralised in a charge exchange cell filled with an alkali vapour (Y), usually Na or K heated to $\sim 200°$C. The cross section of the charge exchange reaction

$$X^+ + Y \rightarrow X + Y^+ + \Delta E \tag{5.31}$$

is largest when $\Delta E \approx 0$, i.e. when the process happens quasi-resonantly. This means that often the direct charge exchange doesn't populate the atomic ground state but rather a (set of) excited states with a more favourable energy match. This can be disadvantageous because it can spread the population over a large number of atomic states. Since these states do not necessarily decay promptly to the state selected for spectroscopy, this process reduces the overall efficiency. Furthermore, also inelastic processes with or without charge exchange can take place in the charge exchange cell. These inelastic collisions take away energy from the incident beam and result in satellite peaks/tails at the low-frequency side of the resonances in the hyperfine spectrum. To avoid these problems, ionic transitions are preferred if technically possible.
The fluorescence decay subsequent to the laser-induced excitations is detected in four photomultiplier tubes (PMTs) positioned perpendicular to the beam line. In front of each PMT a set of two aspherical lenses is placed to focus the photons onto the PMT.

To reduce beam losses and photon background due to collisions with residual gas, the set-up is kept under vacuum ($< 10^{-6}$ mbar).

5.3.3 Background reduction

At COLLAPS, the main mode of operation is optically detected collinear laser spectroscopy where hyperfine spectra are recorded as fluorescence counts as a function of the Doppler-tuning voltage. However, the efficiency of fluorescence detection using photomultiplier tubes is low and its sensitivity is limited due to background originating from dark counts in the PMTs and scattered laser light. This low sensitivity and high background count rate is a serious disadvantage when working with exotic nuclei which have low yields and short half-lives. To deal with these limitations, two improvements have been implemented which enhance the signal-to-background ratio.

Bunched beams By performing spectroscopy on bunched beams produced in ISCOOL, the fluorescence signal can be gated to only accept photons when

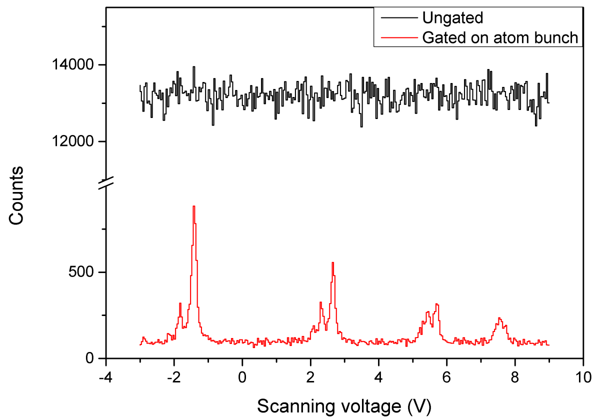

Figure 5.4: Hyperfine spectrum of ^{55}Mn measured on the atomic $3d^5 4s^2\ ^6S_{5/2} \rightarrow 3d^2 54s4p\ ^6P_{3/2}$ transition measured with (red) and without (black) gating the fluorescence signal to when the atom bunch passes in front of the PMTs.

the ion bunch passes in front of the PMTs. With a typical bunch width of a few μs and a bunch separation around 100 ms, the sensitivity for bunched beams is improved by a factor of 10^4 (= bunch separation/bunch width) compared to the continuous case. Bunched beams are therefore essential to go to isotopes far from stability. An example of the significant background reduction is shown in Fig. 5.4 for ^{55}Mn using a 6 μs bunch separated 43 ms apart.

Proton triggering Due to the fast radioactive decay, short-lived isotopes can only be studied in a limited period after each proton pulse. Therefore, only ion bunches arriving within approximately one half-life after proton impact are considered in the measurements, which reduces collecting background when most of the isotope of interest has decayed already. This is especially advantageous to clean the spectrum of a short-lived isomeric state when two states are present with sufficiently different half-lives. This is illustrated for the odd-odd Mn isotopes in section 6.3.3. The same technique needs to be used when the release from the target is very fast.

Even using these improvements, typically around 1000 - 10 000 ions/s are realistically necessary to perform optically detected collinear laser spectroscopy at COLLAPS. To push the limits to more exotic species, new techniques based on particle detection have been developed, such as ROC [Vermeeren et al., 1992; Garcia Ruiz, 2015] and CRIS [Flanagan et al., 2013].

6 Ground state properties of the neutron-rich Mn isotopes

The neutron-rich Mn isotopes are located in a region of deformation which is sometimes called the island of inversion around $N = 40$ due to its resemblance with the situation around $N = 20$. In this chapter, an overview of the experimental evidence for an $N = 40$ island of inversion is given, along with a comparison between the regions around $N = 20$ and $N = 40$. Afterwards, the details of the experimental campaign and data analysis are presented. Finally, the outcome of the experiments is discussed on the basis of four articles.

6.1 Motivation

6.1.1 The island of inversion around $N = 40$?

The region around $N \approx 40$ and $Z < 28$, shown in Fig. 6.1, has been studied extensively due to the similarity with the island of inversion around $N = 20$. An overview of the relevant shell model orbitals in this region can be found in Fig. 4 of article III (section 6.3.3).

Although $N = 40$ occurs naturally as a shell gap using a harmonic oscillator potential, its size is reduced when the spin-orbit interaction is included and as such it is not considered a magic number in the classical shell model picture. Nevertheless, its magicity was first proposed based on the $^{68}_{20}Ni_{40}$ nucleus in which the second 0_2^+ state appears below the first excited 2_1^+ state and this 2_1^+ is found at relatively high energy [Bernas et al., 1982; Broda et al., 1995],

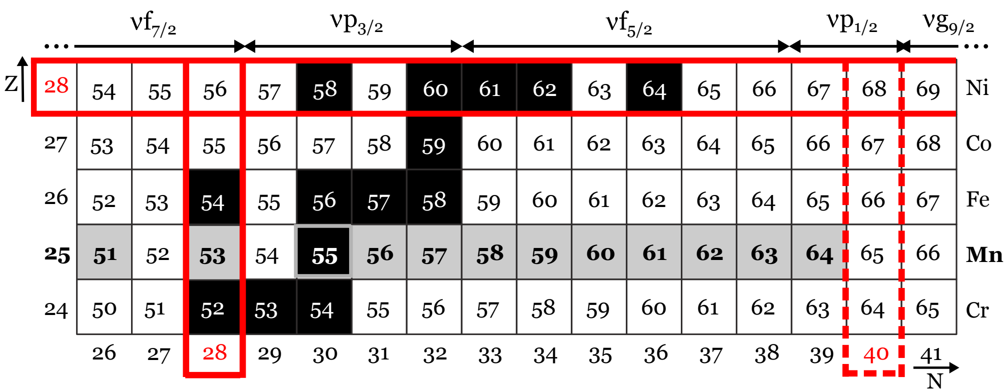

Figure 6.1: The region of the nuclear chart around the neutron-rich Mn isotopes, with shell gaps and subshell gaps indicated in red. The normal filling of the shell model orbitals by the neutrons is shown on top. The Mn isotopes indicated in gray were measured, analysed and discussed in this work.

both signatures of a doubly magic nucleus. Later also the low $B(E2; 2^+ \rightarrow 0^+)$ transition probability seemed to support this conclusion, although it was pointed out that neutron pair scattering counteracts the $N = 40$ magicity [Sorlin et al., 2002]. Furthermore, the two-neutron separation energies vary rather smoothly through $N = 40$, showing only a small effect of the $N = 40$ shell gap in the Ni isotopes [Guénaut et al., 2007], as can be seen in Fig. 8 in article V (see section 6.5). It is therefore generally thought that $N = 40$ is only a weak subshell gap and that the semi-magic features occur locally in ^{68}Ni due to the stabilising effect of the $Z = 28$ magic number.

For open proton shell nuclei below $Z = 28$, the weak $N = 40$ subshell gap is not sufficiently large to stabilise the nuclei in a spherical shape and a strong increase in deformation is observed. First evidence for this deformation came from a β-decay experiment on the neutron-rich $_{25}$Mn isotopes [Hannawald et al., 1999] in which a low $E(2^+)$ in $^{66}_{26}$Fe and almost three times longer half-lives than calculated were measured. These observations were associated with deformation and in particular with a change in neutron occupancy of the $\nu f_{5/2}$ orbital in favour of the $\nu g_{9/2}$ orbital. Since the β-decay predominantly proceeds via a $\nu f_{5/2} \rightarrow \pi f_{7/2}$ Gamow-Teller transition, this reduced occupancy of $\nu f_{5/2}$ therefore leads to a retardation of the β-decay. Similar conclusions where drawn in the half-life measurements of the neutron-rich $_{21}$Sc, $_{22}$Ti, $_{23}$V and $_{24}$Cr isotopes [Gaudefroy et al., 2005].

The quadrupole collectivity was further inferred from the $E(2^+)$, $E(4^+)/E(2^+)$-ratio and $B(E2)$ systematics of the $_{26}$Fe and $_{24}$Cr isotopes [Aoi et al., 2009; Gade et al., 2010; Ljungvall et al., 2010; Baugher et al., 2012; Crawford et al.,

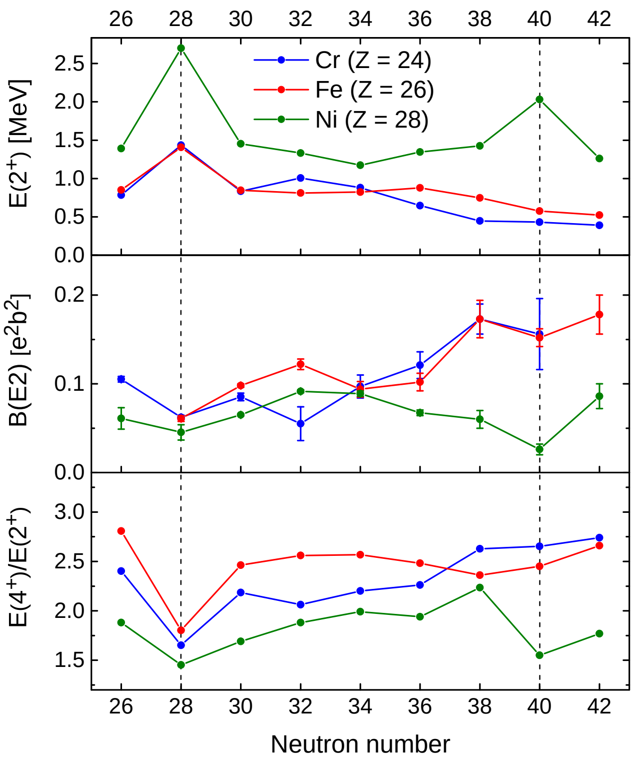

Figure 6.2: Systematics of the even-even nuclei in ${}_{28}$Ni, ${}_{26}$Fe and ${}_{24}$Cr between $N = 26$ and $N = 42$: (top) Energy of the first excited 2^+ state, (middle) $E2$ transition probabilities (bottom) Ratio of the energy of the first excited 4^+ and 2^+ states. Data taken from [Pritychenko et al., 2016] and NNDC.

2013], shown in Fig. 6.2. Whereas at the $N = 28$ magic number the typical peak in $E(2^+)$, the minimum in $E(4^+)/E(2^+)$-ratio and the $B(E2)$ appear in the systematics of Ni as well as Fe and Cr, at $N = 40$, these features are only observed in the Ni chain. In the Fe and Cr isotopes on the other hand, the low $E(2^+)$ and high $B(E2)$ and $E(2^+)/E(4^+)$ are interpreted in terms of collectivity. Along these isotopic chains, the onset of this collectivity seems rather gradual starting at $N = 38$ in Fe and $N = 36$ in Cr. Nevertheless, the $E(4^+)/E(2^+)$-ratio always remains smaller than the 3.3 value expected in the rigid-rotor limit.

Evidence for deformation is also found in the odd-mass neighbours, for example in the low-lying positive (unnatural) parity states in ^{65}Fe [Block et al., 2008; Olaizola et al., 2013] or the coexistence of spherical and deformed structures at low excitations energy in ^{67}Co [Pauwels et al., 2008; Recchia et al., 2012].

The observed deformation is understood in terms of np-nh excitations across $Z = 28$ and $N = 40$. As explained in section 1.2.3, the cost for promoting n particles across the (sub)shell gaps is compensated by a large energy gain associated with quadrupole correlations which are strongly supported due to the quasi- and pseudo-SU(3) nature of the neutron and proton orbitals near the Fermi-level.
The development of collectivity is further enhanced due to the narrowing of the $N = 40$ shell gap going from $_{28}$Ni to $_{20}$Ca. When protons are removed from the $\pi f_{7/2}$ orbital the attractive (repulsive) $\pi f_{7/2} - \nu f_{5/2}$ ($\pi f_{7/2} - \nu g_{9/2}$) tensor interaction decreases, resulting in less (more) binding of the $\nu f_{5/2}$ ($\nu g_{9/2}$) orbital and hence a smaller subshell gap which facilitates neutron excitations across $N = 40$. Similarly, an increased occupancy of the $\nu g_{9/2}$ orbital causes a decrease of the $Z = 28$ shell closure because of the change in repulsive (attractive) $\pi f_{7/2} - \nu g_{9/2}$ ($\pi f_{5/2} - \nu g_{9/2}$) interaction, which in turn causes more proton excitations across $Z = 28$. Since the quadrupole collectivity depends on the total dimension of the proton-neutron valence space, the combination of both proton and neutron excitations additionally boosts the collectivity in the $Z < 28$ and $N \approx 40$ region.

Although the observations in the $N \approx 40$ and $Z < 28$ region are qualitatively understood, a correct quantitative interpretation depends critically on the parametrisation of the model to reproduce the subtle interplay between single-particle and collective effects. Measuring the ground state properties of the neutron-rich Mn isotopes will provide a sensitive test for the predictive power of the available interactions.

6.1.2 $N = 20$ vs $N = 40$

A comparison between section 4.1 about $N = 20$ and the previous section dealing with $N = 40$, reveals many similarities. In both regions, the observed deformation can be related to neutron excitations across a harmonic oscillator shell gap to orbitals enhancing the quadrupole collectivity due to their quasi-SU(3) nature. Around $N = 20$ this concerns the $\nu f_{7/2}$ and $\nu p_{3/2}$ quadrupole partners, while replacing the orbital angular momentum ℓ by $\ell + 1$ gives the corresponding $\nu g_{9/2}$ and $\nu d_{5/2}$ orbitals around $N = 40$. Additionally, the active proton orbitals, $\pi d_{5/2}$ and $\pi s_{1/2}$ around $N = 20$ and $\pi f_{7/2}$ and $\pi p_{3/2}$ around $N = 40$, have a pseudo-SU(3) nature.
Furthermore, a reduction of the $N = 20$ and $N = 40$ harmonic oscillator gaps takes place due to the tensor interaction. In the $N = 20$ case, the gap between $\nu f_{7/2}$ and $\nu d_{3/2}$ decreases when protons are removed from the $\pi d_{5/2}$ orbital,

while similarly in the $N = 40$ case, the gap between $\nu g_{9/2}$ and $\nu f_{5/2}$ is reduced with the removal of protons from $\pi f_{7/2}$. The similarity is illustrated in Fig. 6.3 which shows the theoretical effective single particle energies of the neutron orbits around $N = 20$ and $N = 40$ calculated with the LNPS and SDPF-U interactions, respectively. Here, also one of the major differences become clear: the size of the $N = 40$ subshell gap is never comparable to the $N = 20$ shell gap. So whereas the large $N = 20$ shell gap results in a picture which is generally consistent with a $N = 20$ magic number for isotopes with $Z \geq 14$, around $N = 40$ only ${}^{68}_{28}\mathrm{Ni}_{40}$ shows some signatures for a (doubly)-magic nucleus while all other $N = 40$ isotones develop collectivity.

6.1.3 The neutron-rich Mn isotopes

In between the proton-magic ${}_{20}\mathrm{Ca}$ and ${}_{28}\mathrm{Ni}$ isotopes, the Mn ($Z = 25$) isotopes lie in an interesting region of the nuclear chart, characterised by a rich variety in nuclear structure. Nevertheless, before the start of our experimental campaign the available information on the Mn isotopic chain was rather limited. A short overview is given below.

Spins Beyond ${}^{59}\mathrm{Mn}_{34}$ spins were only tentatively assigned and as it turned out, especially the assignment of the odd-odd isotopes was ambiguous.
In ${}^{58,60,62,64}\mathrm{Mn}$ two long-lived states are known with a large spin difference between them. For a long time, the spin assignments were based on β-decay studies from the 1980s [Runte et al., 1983, 1985; Bosch et al., 1988] in which the low-spin state in ${}^{58,60}\mathrm{Mn}$ was assigned $I = (0^+)$ and the high-spin state was assigned $I = (3^+)$. In ${}^{62}\mathrm{Mn}$ only the high-spin state was observed and similarly assigned $I = (3^+)$. The $\Delta I = 3$ difference in ${}^{58,60}\mathrm{Mn}$ was further confirmed by the observation of an M3 transition in an electron conversion spectroscopy experiment [Schmidt-Ott et al., 1993]. Only 20 years later, the spin issue was revised when Liddick et al. [2006] questioned the validity of the previous conclusions and proposed a $I = (1^+)$ and $I = (4^+)$ assignment for ${}^{58,60}\mathrm{Mn}$ instead. Evidence for a low-spin state in ${}^{62}\mathrm{Mn}$ was first seen in GANIL [Gaudefroy et al., 2005] where $I = (1^+)$ was tentatively suggested. Based on this assignment for the low-spin state, the $I = (3^+)$ for the high-spin state was deemed unlikely and $I = (4^+)$ was proposed. However, this was not adapted in the NNDC chart of nuclides which still quotes $I = 3^+$ (without brackets!) up to the date of writing. In the same GANIL campaign, also the spins of the long-lived states in ${}^{64}\mathrm{Mn}$ were investigated, suggesting $I = (1^+)$ and $I = (4^+)$ [Gaudefroy, 2005]. Later, Liddick et al. [2011] confirmed these suggestions in a β-decay measurement at NSCL.

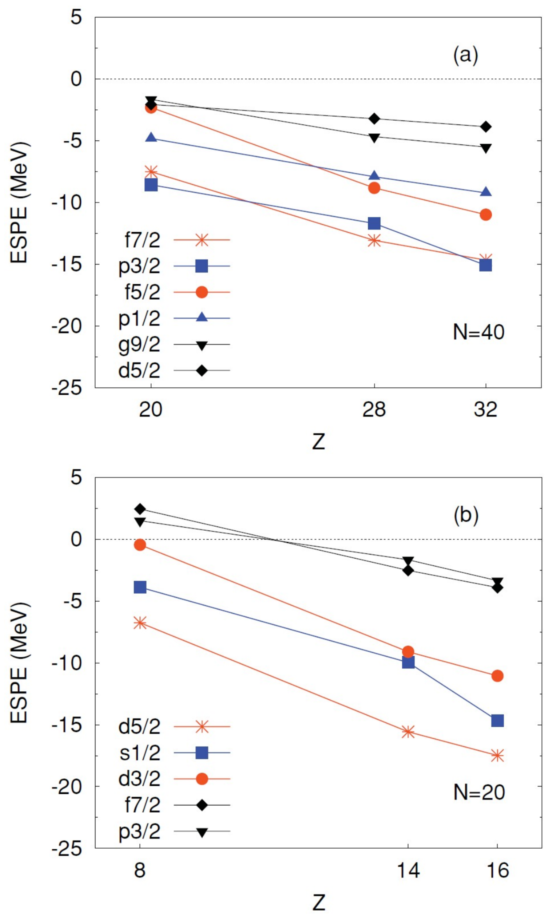

Figure 6.3: Neutron effective single-particle energies calculated with (a) the LNPS interaction around $N = 40$ and (b) the SDPF-U interaction around $N = 20$. Pictures taken from [Lenzi et al., 2010].

Masses In 2012, high-precision masses of $^{57-66}$Mn were published by the ISOLTRAP collaboration [Naimi et al., 2012]. For ^{62}Mn, only the mass of the 4^+ state could be measured and at that time it was not clear whether it was the ground state of the isomer. Although it was assumed that the mass belonged to the isomer, it was still used to calculate the two-neutron separation energies.

Since then, a Coulomb excitation experiment has tentatively proposed that the 4^+ state lies 346 keV above the 1^+ ground state [Gaffney et al., 2015]. With this new value, the two-neutron separation energies at ^{62}Mn and ^{64}Mn are slightly altered, as discussed in article V (see section 6.5).

Moments and charge radii The magnetic dipole moment, electric quadrupole moment and changes in mean-square charge radii of $^{50-56}$Mn$_{25-31}$ were measured in a collinear laser spectroscopy experiment at the JYFL facility [Charlwood et al., 2010]. No moments or radii information was known for more neutron-rich isotopes, beyond $N = 31$.
Between $Z = 20$ and $Z = 28$, the knowledge on charge radii and nuclear moments is in general very scarce due to the refractory nature of these elements which makes the production at ISOL-facilities challenging.

Level schemes Valiente-Dobón et al. [2008] studied the low-energy structure of $^{59-63}$Mn via multi-nucleon transfer reactions. More elaborate level schemes were obtained using fusion-evaporation reactions [Steppenbeck et al., 2010] for $^{57-60}$Mn and using deep-inelastic reactions for ^{61,62}Mn [Chiara et al., 2010]. These level schemes show evidence for quasi-rotational bands.

6.2 The experimental campaign

The ground state properties of the neutron-rich Mn isotopes were measured in two collinear laser spectroscopy experiments performed at the COLLAPS beam line.
In November 2012, laser spectroscopy of $^{51,53-64}$Mn was performed using the $3d^5 4s^2\ {}^6S_{5/2} \rightarrow 3d^5 4s4p\ {}^6P_{3/2}$ ground state transition in atomic manganese. Although originally a different transition starting from a metastable state in the ion was proposed [Cheal et al., 2010], this spectroscopy scheme required optical pumping in a cooler/buncher which was found to be impossible at that time due to a misalignment of ISCOOL. While the experiment on atomic manganese was very successful in measuring the spins and magnetic moments, the atomic transition lacked sensitivity to the quadrupole moments.
The alignment of ISCOOL was optimised during the long shutdown of ISOLDE in 2013 and 2014, as described in Carla Babcock's PhD thesis [Babcock, 2015]. In June 2015, optical pumping in ISCOOL could therefore be applied successfully during a second Mn laser spectroscopy experiment, performed on the $3d^5\ 4s\ {}^5S_2$ (metastable) $\rightarrow 3d^5\ 4p\ {}^5P_3$ ionic transition. This experiment yielded the desired quadrupole moments of the odd-even $^{53-63}$Mn isotopes. Furthermore, using this ionic transition, the total experimental efficiency was approximately 10 times higher than with the atomic transition in 2012. Although this should have enabled the extension of the measurements to $N = 40$, one

isotope more neutron-rich than was obtained in 2012, target problems resulted in low Mn yields which prevented measurements beyond $N = 38$.

6.2.1 The need for optical pumping in ISCOOL

Laser spectroscopy on atomic manganese has the disadvantage that the quadrupole moment sensitivity of the ground state transitions is low. Indeed, for the $3d^5 4s^2\ ^6S_{5/2} \rightarrow 3d^5 4s4p\ ^6P_{3/2}$ transition used in 2012, the lower state quadrupole splitting is zero within our experimental precision ($B(S_{5/2}) = -0.019031(17)$ MHz for ^{55}Mn) and the upper state splitting is only around 15 MHz (see table 1 in article II, section 6.3.2). This results in relative errors of 50% or larger on the obtained B-parameters.
From a previous experiment in Jyväskylä, it was known that the ionic $3d^5\ 4s\ ^5S_2$ (metastable) $\rightarrow 3d^5\ 4p\ ^5P_3$ transition is much more suitable for the extraction of quadrupole moments [Charlwood et al., 2010]. However, since the natural population of the metastable state is low, its population needs to be enhanced to perform efficient optical spectroscopy. This is achieved by employing optical pumping in ISCOOL.
In the optical pumping scheme presented in Fig. 2 in paper IV, section 6.4.2, the ion is excited from the ground state to an excited state at 43370.5 cm^{-1} which subsequently decays to the metastable state at 9473 cm^{-1}. The decay from the metastable state back to the ground state is forbidden such that the population is accumulated in the metastable state. Since the excitation step is spectroscopically weak, a long laser-ion interaction time is necessary to ensure efficient optical pumping. Instead of in-flight optical pumping, the optical pumping is therefore performed in the trapping region of ISCOOL, where the ions can be kept up to a few seconds. Using a 200 ms accumulation time, a significant increase in population of the metastable state is established, as illustrated in Fig. 3 in paper IV, section 6.4.2 which shows the difference in intensity of the hyperfine peaks with and without optical pumping.
Due to the Doppler broadened velocity profile of the ions in the cooler-buncher, the resolution constraints on the excitation step are less stringent and a pulsed broadband laser can be used to produce the 230.5 nm laser light (frequency-quadrupled Ti:Sa) instead of narrowband cw laser for which higher-order harmonics generation is more difficult to achieve.

Apart from the manganese case, optical pumping might be useful for several isotopic chains across the nuclear chart: it is specifically applicable when "ground state transitions are inefficient, inaccessible with the available lasers, or insensitive to nuclear properties" [Babcock, 2015].

6.2.2 Conversion of raw data

The raw hyperfine spectra are recorded as counts versus the scanning voltage V_{scan}. To convert these raw spectra to frequency spectra via eq. 5.25, an accurate knowledge of the laser frequency and all voltages in eq. 5.30 is required.

Kepco amplification factor

To determine the kepco amplification factor k in eq. 5.30, several calibration scans are performed during the run. In these calibration scans, the amplified scanning voltage $k \cdot V_{\text{scan}}$ is measured as a function of V_{scan} which gives a linear relation with slope k. In general, the fluctuations between the different calibration scans are small and an average of all scans is employed in the final conversion:

$$k_{2012} = 50.427(2)$$

$$k_{2015} = 50.430(1)$$

The uncertainty on the frequency due to the uncertainty on k is negligible compared to other contributions discussed further.

ISCOOL stability and correction factor

The stability of V_{ISCOOL} over time is shown in Fig. 6.4. Over the course of several days of experiment, the variation is small, 1 V in 2012 and 2 V in 2015, respectively. Apart from this drift over time, which is taken into account, the read-out value of the ISCOOL voltage divider is known to have a time and voltage dependent offset. Therefore, a correction voltage needs to be added to this read-out value to get the real acceleration voltage

$$V_{\text{ISCOOL}} = V_{\text{ISCOOL, read-out}} + V_{\text{corr}}. \tag{6.1}$$

The correction voltage is known to lie around $\pm$15V and needs to be calibrated for each experiment separately. This calibration is achieved by comparing the measured isotope shifts with literature values, as the isotope shifts are particularly sensitive to a small change in acceleration voltage. No isotope shifts for the atomic transition used in 2012 were known in literature and therefore a general uncertainty of 15 V is assumed in the analysis. To obtain a good agreement between the $\delta\nu^{55,53}$ isotope shift measured in 2015 and the Jyväskylä value [Charlwood et al., 2010], a correction voltage of +8 V is applied.

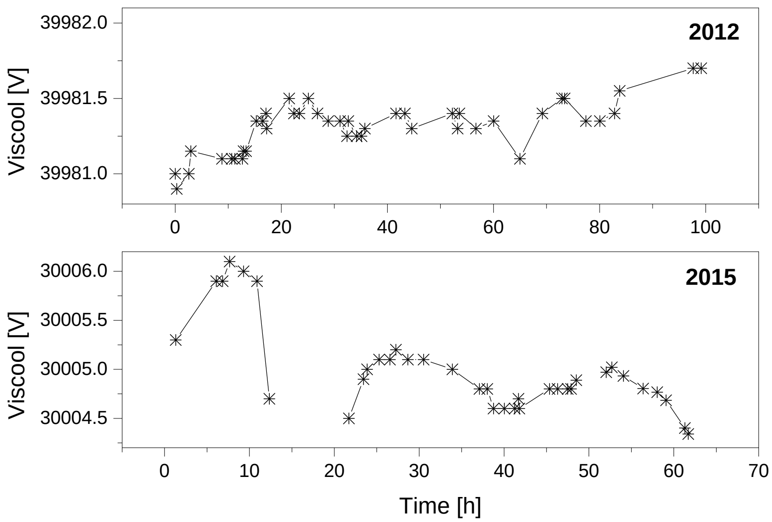

Figure 6.4: Stability of the ISCOOL voltage during the 2012 and 2015 experiments.

Laser stability

The laser stability is monitored by recording the wave number $\lambda^{-1} = \nu/c$. As shown in Fig. 6.5, the laser frequency was not very stable during the 2012 experiment. Apart from a continuous drift, there is a jump in frequency at around time 4600 min, which corresponds to the moment where the laser needed to be relocked. To obtain the laser frequency for each run, the duration of the experiment is divided in three regions and a linear fit of each region is performed.

During the 2015 experiment, the undoubled laser frequency was fixed at 16967.13200 cm^{-1}. Since this time the laser was stabilised with respect to the wavemeter itself, no long term drifts could be detected.

The final frequency of the laser is obtained from the wavenumber $\nu = 2c\lambda^{-1}$ where the factor 2 originates from the frequency doubling process. Since the absolute frequencies obtained after the conversion are in the order of 10^9 MHz, the frequencies in the final hyperfine spectra are shown relative to the absolute transition frequency of ^{55}Mn in order to get more convenient numbers on the

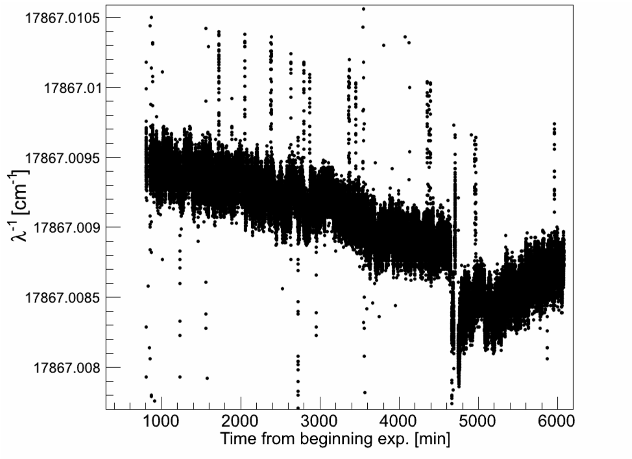

Figure 6.5: Stability of the laser frequency during the 2012 experiment.

x-axis

$$\lambda_{\text{ref}}^{-1} = 33897.54\ \text{cm}^{-1} \qquad (S_{5/2} \to P_{3/2})$$

$$\lambda_{\text{ref}}^{-1} = 35689.98\ \text{cm}^{-1} \qquad (S_2 \to P_3)$$

This does not alter the extracted hyperfine parameters which only depend on the relative frequencies.

The isotope shifts are very sensitive to drifts in laser frequency and acceleration voltage. To minimise the effects of these drifts, a reference run of ^{55}Mn was taken in between runs of different masses, and isotope shifts are calculated relative to the nearest (or average of two) ^{55}Mn centroids.

6.2.3 Data analysis

The peak positions in the hyperfine spectra (given by eq. 5.19) were fitted using the standard χ^2 minimisation method in the MINUIT package in ROOT. A simultaneous fit of all hyperfine spectra of one isotope was performed in which the hyperfine A and B parameters were common for all spectra, while the parameters which change from one run to another (centroid frequency, background, intensity etc.) were determined for each run individually.

If the reduced chi-square χ^2_{red} obtained in the fit-procedure was larger than one, the fit errors were multiplied with $\sqrt{\chi^2_{\mathrm{red}}}$ to obtain the final statistical errors.

2012 - atomic $S_{5/2} \rightarrow P_{3/2}$ transition

The hyperfine peaks were fitted with a Lorentzian line profile. Although a small Gaussian component could be present, no significant difference was seen when a Voigt profile was used.
To account for inelastic processes in the charge exchange cell which resulted in a slightly asymmetric peak shape, a Lorentzian side peak was included at the left side of each peak. The frequency offset of the side peak with respect to the main peak was fixed to the average offset of ^{55}Mn (78(2) MHz), which corresponds to an energy offset of 4.61(10) eV. This suggests that an important inelastic channel in the charge exchange cell involves excitation to the ^6P triplet at 4.4 eV. The energy offset of ^{55}Mn was used to scale the frequency offset for the other masses. The relative side peak-to-main peak intensity was kept the same for all peaks in one spectrum, but left free from one spectrum to another. Although the asymmetry of the line shape is not obvious by eye, the introduction of a side peak resulted in a consistent reduction of the χ^2_{red} value and changed the ^{55}Mn reference value from $A(^{55}\mathrm{Mn}, S_{5/2}) = -71.9(2)$ MHz to $A(^{55}\mathrm{Mn}, S_{5/2}) = -72.4(2)$ MHz, in better agreement with the high-precision literature value $A(^{55}\mathrm{Mn}, S_{5/2}) = -72.430836(15)$ MHz [Davis et al., 1971].
To aid the fitting of partially unresolved peaks, the relative intensities were fixed to the Racah intensities given by eq. 5.22. Since the quadrupole splitting of the lower state is zero within our precision ($B(^{55}\mathrm{Mn}, S_{5/2}) = -0.019031(17)$ MHz), $B(S_{5/2})$ was fixed to zero in the fitting procedure. Additionally, the ratio of $A(P_{3/2})/A(S_{5/2})$ of the radioactive isotopes was constrained to the ^{55}Mn value of 13.3.

2015 - ionic $S_2 \rightarrow P_3$ transition

The hyperfine peaks were fitted with a (symmetric[1]) Voigt profile. In this case, all hyperfine peaks were well resolved and the relative intensities were left free. No constraints were placed on the A-ratio or B-values.

[1]Due to the absence of a charge exchange cell no asymmetric line shape was necessary.

6.3 Spins and magnetic moments

6.3.1 Spins and g-factors between $Z = 20$ and $Z = 28$

Manganese has 25 protons, giving rise to 3 protons holes in the $\pi f_{7/2}$ orbital. In a pure single-particle picture, the odd-A Mn isotopes, with an even number of neutrons, are expected to have a ground state spin $I = 7/2^-$. However, this is only true for ^{53}Mn at the $N = 28$ shell closure, while all other odd-A Mn isotopes are found to have ground state spin $I = 5/2^-$.
Despite their different spins, the g-factors are very similar, as shown in Fig. 6.6. In fact, the g-factors of all odd-proton even-neutron isotopes between $Z = 20$ and $Z = 28$ are very similar. This is an excellent illustration of equation 2.10 which states that the g-factor is just determined by the orbital occupied by the last unpaired valence nucleon, the $\pi f_{7/2}$ orbital in this case, irrespective of the number of valence nucleons in this orbital or the final spin. Indeed, the experimental values are in reasonable agreement with the theoretical single-particle estimate (Schmidt value) for a $\pi f_{7/2}$ orbital, indicated by the dashed line. This tells us that the $I = 5/2^-$ spin for the odd-A Mn isotopes is not related to the excitation of a proton from the $\pi f_{7/2}$ to the $\pi f_{5/2}$ orbital, as could naively be assumed, but that it needs to be understood in terms of a more complicated wave function, involving couplings with neutron excitations. For example, Paar [1973] discussed the observed $I = j - 1$ anomaly in terms of a three-proton-hole cluster coupled to quadrupole vibrations of the Ni isotopes. More generally, the correct ground state spins can be predicted using large-scale shell model calculations including both proton and neutrons excitations across $N = Z = 28$.

Although the g-factor is in first approximation determined by the proton configuration, also the neutrons will have a small but important influence, as will be discussed in article II and III. Due to the high precision of the experimentally obtained g-factors, the clear role of neutron excitations across $N = 40$ in the Mn structure approaching $N = 40$ could be deduced. Whether the observed changes in g-factors are directly related to the coupling with neutron configurations which are not paired to angular momentum zero, or indirectly, due to an increased mixing with $\pi f_{5/2}$ configurations, is not immediately clear.

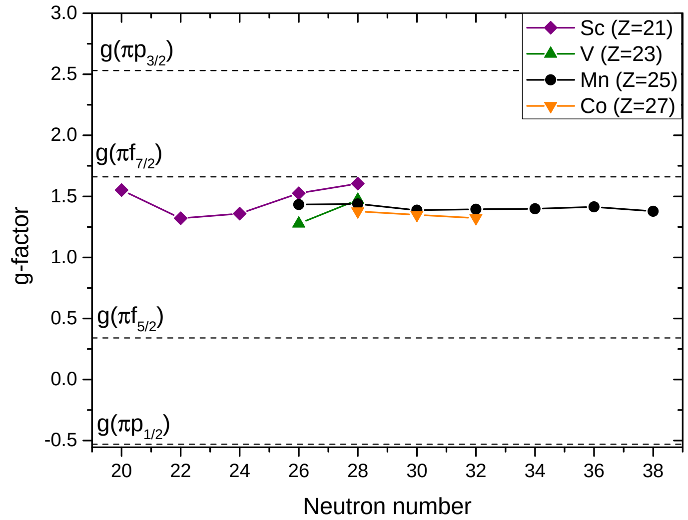

Figure 6.6: Experimentally known g-factors of the odd-proton isotopes between $Z = 20$ and $Z = 28$. The experimental values are compared to the single-particle estimates (Schmidt values) using free g-factors.

6.3.2 Article II: Evidence for increased neutron and proton excitations between $^{51-63}$Mn

The following articles deal with the results of the odd-even (Article II) and odd-odd (Article III) $^{51-64}$Mn isotopes obtained in the atomic collinear laser spectroscopy experiment. The previously tentative ground state spins of ^{61,63}Mn and ^{60,62,64}Mn are firmly established along with the isomeric state spins in ^{60,62}Mn. Furthermore, also a positive parity for the studied ground and isomeric state in the odd-odd isotopes was proposed based on the sign of the magnetic moment. The obtained magnetic moments are compared to large-scale shell model calculations using different model spaces. This shows that a model space without neutron excitations across $N = 40$ (GXPF1A), is too limited to reproduce the magnetic moments of the neutron-rich Mn isotopes, while calculations in a larger model space including neutron excitations (LNPS), agree excellently with the experimental observations. In addition to neutron excitations across $N = 40$, also the importance of proton excitations across $Z = 28$ is illustrated by a detailed analysis of the predicted wave functions.

As the second author on paper II and the first author on paper III, I contributed to each stage to get these final publications. This means that I participated in the experiment, I performed a full and independent data-analysis and I was actively involved in the writing of the manuscript, from the first draft up to submission. In particular, the physics discussion in both papers is largely based on my input, for which I was in contact with theoreticians and I performed shell model calculations using the GXPF1A interaction.

Physics Letters B 750 (2015) 176–180

Contents lists available at ScienceDirect

Physics Letters B

www.elsevier.com/locate/physletb

Evidence for Increased neutron and proton excitations between $^{51-63}$Mn

C. Babcock [a,b,*], H. Heylen [c,**], J. Billowes [d], M.L. Bissell [c], K. Blaum [e], P. Campbell [d], B. Cheal [a], R.F. Garcia Ruiz [c], C. Geppert [f,i], W. Gins [c], M. Kowalska [b], K. Kreim [e], S.M. Lenzi [g], I.D. Moore [h], R. Neugart [e,f], G. Neyens [c], W. Nörtershäuser [i], J. Papuga [c], D.T. Yordanov [e]

[a] Oliver Lodge Laboratory, Oxford Street, University of Liverpool, L69 7ZE, UK
[b] ISOLDE, CERN, CH-1211 Geneva 23, Switzerland
[c] KU Leuven, Instituut voor Kern- en Stralingsfysica, 3001 Leuven, Belgium
[d] School of Physics and Astronomy, University of Manchester, M13 9PL, UK
[e] Max-Planck-Institut für Kernphysik, D-69117 Heidelberg, Germany
[f] Institut für Kernchemie, Johannes Gutenberg-Universität Mainz, D-55128, Germany
[g] Dipartimento di Fisica e Astronomia dell'Università and INFN, Sezione di Padova, I-35131 Padova, Italy
[h] Department of Physics, University of Jyväskylä, PB 35 (YFL) Jyväskylä, Finland
[i] Institut für Kernphysik, TU Darmstadt, D-64289 Darmstadt, Germany

ARTICLE INFO

Article history:
Received 3 July 2015
Received in revised form 12 August 2015
Accepted 5 September 2015
Available online 10 September 2015
Editor: V. Metag

Keywords:
Magnetic dipole moment
Manganese
Spin determination

ABSTRACT

The hyperfine structures of the odd-even $^{51-63}$Mn atoms ($N = 26 - 38$) were measured using bunched beam collinear laser spectroscopy at ISOLDE, CERN. The extracted spins and magnetic dipole moments have been compared to large-scale shell-model calculations using different model spaces and effective interactions. In the case of ^{61,63}Mn, the results show the increasing importance of neutron excitations across the $N = 40$ subshell closure, and of proton excitations across the $Z = 28$ shell gap. These measurements provide the first direct proof that proton and neutron excitations across shell gaps are playing an important role in the ground state wave functions of the neutron-rich Mn isotopes.

1. Introduction

The complexity of nuclear interactions has made it difficult to define a single model that describes the variety of nuclear properties observed. The nuclear-shell model has been successful in characterizing many of these properties, however predicting phenomena such as the migration of single-particle levels and the disappearance of magic numbers has proven challenging due to the large model spaces needed. Comparisons of shell-model calculations with experimental results, such as electric and magnetic properties, provide a powerful tool to understand nuclear structure evolution and improve its description within the shell model.

Collinear laser spectroscopy is a technique that is used to measure the atomic hyperfine structure, resulting from the interplay between the nucleus and the magnetic and electric fields generated by the electrons. The HFS spectrum allows the magnetic dipole moments and electric quadrupole moments of a nucleus to be derived, as well as a model-independent determination of the nuclear spin [1,2].

Neutron-rich manganese isotopes ($Z = 25$) provide an opportunity for studying shell structure evolution towards the suspected subshell closure at $N = 40$ [3,4]. This appears as a possible subshell closure for ^{68}Ni, observed through a low quadrupole transition probability and a high lying 2_1^+ state [5], however mass measurements of neutron-rich Ni indicate that the closure is a weak one [6]. An increase in collectivity and deformation measured for Fe and Cr in this region [7,8], as well as a lack of significant discontinuities in the 2-neutron separation energies for Fe [9] and Mn [10], also suggests that $N = 40$ is a very weak subshell gap, which decreases quickly as protons are removed from the $1f_{7/2}$ shell. For elements above $Z = 28$, such as Cu and Ga, no magicity is suggested for $N = 40$ from mass measurements [11]. Though the

* Primary corresponding author at: ISOLDE, CERN, CH-1211 Geneva 23, Switzerland.
** Corresponding author.
E-mail addresses: cbabcock@cern.ch (C. Babcock), hanne.heylen@fys.kuleuven.be (H. Heylen).

http://dx.doi.org/10.1016/j.physletb.2015.09.012

measured nuclear moments of Cu could be interpreted as having a shell gap at $N = 40$, the parity change between the pf and g orbitals could also explain this behavior [12]. In Ga isotopes, strong shape changes have been observed from $N = 40$ to $N = 50$ [13].

Theory suggests that the weakening of the $N = 40$ subshell gap results from the reduction of the proton–neutron interaction as protons are removed from the $1f_{7/2}$ orbital. This results in a reduced binding of the $\nu 1f_{5/2}$ level, and an increased binding of the $\nu 1g_{9/2}$ and $\nu 2d_{5/2}$ levels, thus a reduction of the $N = 40$ gap [8,14]. This is supported by the results of deep-inelastic reaction studies which show that the excited states in heavier odd–odd Mn isotopes occur at energies similar to those of the intruder $\nu 1g_{9/2}$ isomers in the Fe isotones [15].

As a result, quadrupole correlations are enhanced by the excitation of neutrons from the $\nu p_{1/2}$ and $\nu f_{5/2}$ orbitals into the $\nu g_{9/2}$ and $\nu d_{5/2}$ orbitals, making collectivity energetically favorable in these nuclei. The development of quadrupole collectivity also favors the excitation of protons across the $Z = 28$ gap.

This has been observed in the odd Co isotopes at $N = 40$, where ^{67}Co is suggested to have a low lying $1/2^-$ isomer resulting from a proton intruder state coexisting with the ground state [16,17]. In the Mn isotopes, the effect of these proton excitations may be observed in the magnetic moments of the odd-Z ground states.

There have been theoretical attempts to describe this region of the nuclear chart using a variety of effective shell-model interactions, one of the most used being the GXPF1A interaction, which models the full pf space [18,19]. This interaction has been very successful in describing nuclei with particles in the mid-pf shell, however for isotopes approaching $N = 40$, the exclusion of the $\nu 1g_{9/2}$ orbital from the model space limits its effectiveness [4,20]. The model space has therefore been extended to the $pfg_{9/2}$ orbitals and the isotopes $^{57-63}$Mn have been investigated with various interactions [4,21]. Good agreement with published excitation energy data has been found for most of the isotopes, but information on the electromagnetic properties is required to fully test the interactions. In order to reproduce the observed quadrupole collectivity, it has been argued that it is also necessary to take into account the $\nu 2d_{5/2}$ level [22]. This has been incorporated into the LNPS interaction [22], using a ^{48}Ca core and allowing excitations to $\nu 1g_{9/2}$ and $\nu 2d_{5/2}$. It greatly expands the computational domain as compared to the previously discussed models, and has been used successfully to describe energies and transition probabilities in the elements Fe [3,23], Cr [8,24], Co [17] and Cu [25].

In view of the theoretical challenges, and the need for data to better characterize the nuclear structure changes and test the effective nucleon–nucleon interactions in this region, we present here measurements of the spins, A and B hyperfine coefficients, and the deduced magnetic dipole moments of the odd isotopes in $^{51-63}$Mn, as well as a comparison with theory.

2. Experimental setup

Manganese ions were produced by the impact of a 1.4-GeV proton beam produced by the PS Booster at CERN on a thick uranium carbide target. The yield of Mn ions was increased, and isobaric contaminants minimized, through the use of ISOLDE's resonant laser ion source (RILIS) [26]. After passage through a mass separator, the ions were trapped in a radio-frequency quadrupole cooler and buncher [27] for approximately 50 ms before being released in 6 μs bunches to the collinear laser spectroscopy beamline (COLLAPS, see [28]).

At the COLLAPS setup, the ion beam entered a charge-exchange cell filled with sodium vapor which was floating on the Doppler tuning potential. The ion beam emerged from the charge-exchange cell as an atomic beam and was overlapped with a co-propagating COLLAPS laser used to probe the transition of interest. Up to four photomultiplier tubes positioned around the interaction region detected the emitted fluorescence. Background suppression was accomplished by gating the photomultipliers to accept only photons which arrived during the time the atom bunch was traversing the interaction region, thus reducing the background due to randomly scattered photons and dark counts by a factor of approximately 10^4 [1]. The atomic transition from the $3d^5\,4s^2\ ^6S_{5/2}$ (ground state) to the $3d^5\,4s4p\ ^6P_{3/2}$ excited state at 35 689.98 cm^{-1} was probed using a narrow band dye laser providing approximately 1–3 mW of light at 280.2 nm. The 40 keV ion beam energy was tuned using the potential of the charge-exchange cell, so that the laser frequency (as seen by the fast atom beam) was Doppler shifted over the range corresponding to the hyperfine splitting.

Fitting the spectra with a least-squares minimization procedure and Lorentzian profiles yields the hyperfine structure coefficients A and B, for the upper and lower states, as well as the nuclear spins. Because of the low laser power density, the relative intensities of the hyperfine structure components were fixed to the Racah intensities to further constrain the fit.

In the fitting routine, parameters to describe the multi-component resonance profile were included. Processes such as collisional excitation and non-resonant charge-exchange result in the formation of some atoms in an excited state, the energy for which is transferred from the kinetic energy of the beam. When these excited atoms decay back to the atomic ground state, they require a higher acceleration voltage to reach the Doppler-shifted resonance frequency. The additional peaks produced by these atoms are located at a slightly lower frequency, very close to the main resonance peak [29]. This was taken into account in the fitting procedure by the inclusion of a second Lorentzian profile associated with each line. Each of these secondary peaks was given a fixed energy offset of 4.43 eV, corresponding to the energy of the populated state (determined through the fit of the high-statistics ^{55}Mn data), and a fitted relative intensity. The fits to the relative intensities indicate that the atoms affected by these inelastic processes during charge-exchange constitute approximately 20% of the total measured beam.

In the case of ^{63}Mn, which has a shorter half life than the other isotopes (250 ms), a proton triggering technique was used which consists of accepting photons only during a time window after each proton impact corresponding to one half life of the isotope. This enhanced the signal to noise ratio on the observed hyperfine structure by further suppressing the stray light background.

3. Results

Table 1 shows the hyperfine coefficients A and B of the upper state. Literature values for the coefficients of the lower state of ^{55}Mn are $A_l = -72.420836(15)$ MHz and $B_l = -0.019031(17)$ MHz, obtained in spin-exchange optical pumping experiments [30]. Good agreement is shown between the A_l value from this work ($A_l = -72.4(7)$ MHz) and the literature value. In this analysis, the ratio A_l/A_u was constrained to be 0.0752, as determined from the high statistics data for ^{55}Mn. A negligible hyperfine anomaly is assumed at this level of accuracy. The A values have been used to calculate the magnetic moments of the isotopes using [1],

$$\mu = \mu_{\text{ref}} \frac{I\,A}{I_{\text{ref}}\,A_{\text{ref}}}$$

with the value of $\mu_{\text{ref}} = +3.46871790(9)$ taken from [31]. Since the value of B_l is much less than 1 MHz, it has been constrained to zero. Sensitivity to the quadrupole moment in the upper state is also very weak, resulting in a large relative uncertainty for

Table 1
The measured nuclear spins, and A and B hyperfine coefficients for the $^6P_{3/2}$ excited state. Magnetic dipole moments are determined as described in Section 3. Values are compared to shell-model calculations using the GXPF1A and the LNPS effective interactions with free nuclear g-factors. All moments are given in units of μ_N.

Isotope	A (MHz)	B (MHz)	Spin	μ	μ [GXPF1A]	μ [LNPS]
^{51}Mn	−993.7(12)	17(9)	5/2	+3.577(4)	+3.46	–
^{53}Mn	−996.8(8)	3(8)	7/2	+5.024(4)	+4.76	–
^{55}Mn	−963.1(3)	14(1)	5/2	–	+3.35	–
^{57}Mn	−967.4(5)	9(4)	5/2	+3.483(2)	+3.44	+3.60
^{59}Mn	−970.3(5)	7(4)	5/2	+3.493(2)	+3.48	+3.56
^{61}Mn	−981.6(4)	16(3)	5/2	+3.534(1)	+3.62	+3.56
^{63}Mn	−954.3(11)	10(8)	5/2	+3.435(4)	+3.77	+3.48

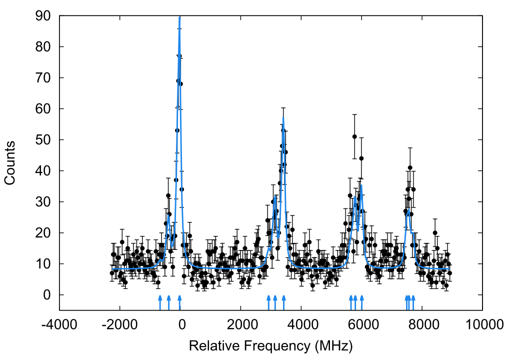

Fig. 1. HFS data from ^{63}Mn with fit for spin 5/2 overlaid, frequencies shown relative to the ^{55}Mn center of gravity. The arrows indicate the predicted positions of the peaks (color online).

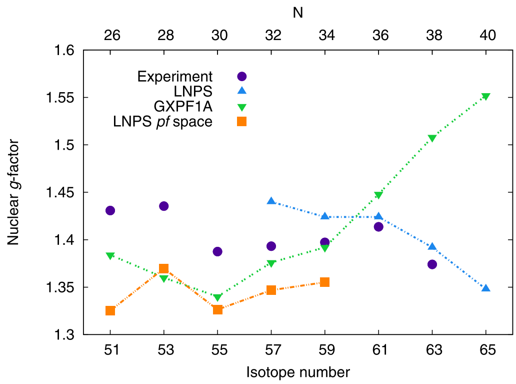

Fig. 2. Comparison of experimental data from this study to calculations using the GXPF1A interaction, the LNPS interaction, and the LNPS interaction in the pf shell but instead using a ^{40}Ca core and blocking excitations to the neutron $g_{9/2}$ and $d_{5/2}$ orbitals. All calculations were performed with free g-factors. Error bars are within the symbols (color online).

B_u, therefore quadrupole moments have not been extracted. Spectroscopy on the isotopes $^{50-56}$Mn has already been described and compiled elsewhere [30–32], and the reported magnetic moments for ^{51,53}Mn are in agreement with our results.

An advantage of laser spectroscopy is the possibility of making an unambiguous determination of nuclear spins. The spins of all odd–even isotopes for $A = 51 - 63$ have been measured here by analyzing the pattern of the HFS peaks, as shown in Fig. 1.

Table 1 shows the spin values derived from the least-squares fit to the spectra. Where uncertainties existed, the spin was confirmed by the observation that the use of an alternative value for the spin in the fitting procedure produces a B coefficient that is unphysically large. For example, assuming $I = 7/2$ for ^{63}Mn gives $B = -229(8)$ MHz which would yield the unrealistically large quadrupole moment $Q_s = -5.8(9)$ b. For ^{59}Mn and ^{61}Mn, the quadrupole moments would be similarly large, $Q_{s,59} = -5.9(9)$ b and $Q_{s,61} = -5.6(8)$ b.

In an independent particle shell-model interpretation, the odd manganese isotopes with 3 holes in the $\pi f_{7/2}$ shell would have a spin 7/2 ground state. However, except for ^{53}Mn (with 28 neutrons), all isotopes have been found to have spin 5/2.

4. Discussion

Shell-model calculations of the energy levels and moments of neutron-rich isotopes in the region $Z = 20$ to $Z = 28$ have sought to characterize the rapid structure evolution and lack of a robust sub-shell closure near $N = 40$. Using the code ANTOINE [33] and the GXPF1A effective interaction [19], calculations of the magnetic moments of neutron-rich Mn have been performed in the pf model space, allowing up to eight particles (maximum 2 protons and 6 neutrons) to be excited from the $1f_{7/2}$ to the $2p_{3/2}$, $1f_{5/2}$ and $2p_{1/2}$ orbitals.

Magnetic moments and their associated g-factors are highly sensitive to the nuclear wave function, and provide a stringent test of the models. Shell-model results obtained with free g-factors ($g = \mu_I/I\mu_N$) are shown in Fig. 2 and compared to the experimental results. Calculations using the GXPF1A interaction do not reproduce the observed trend very well, but given the scale, the absolute values are reproduced within a 1–10% range up to ^{61}Mn. Using effective g-factors does not significantly improve the overall agreement. From $N = 36$ onwards, the GXPF1A calculations predict an increase in the g-factors towards the Schmidt value, as would be expected if $N = 40$ were a magic number. Instead, the experimental data shows a decrease after $N = 36$.

The widening discrepancy between the measured magnetic moments and the GXPF1A calculations suggests that the model space is insufficient to describe the structural changes in the heavier isotopes. If the $\nu 1g_{9/2}$ and $\nu 2d_{5/2}$ orbitals play a crucial role, as has been proposed to reproduce the level scheme of ^{66}Fe [3,23] and in Cr [24], then the model space must be expanded. These orbitals are taken into account by the LNPS interaction, which includes the entire pf shell for protons and the levels $1f_{5/2}$, $2p_{3/2}$, $2p_{1/2}$, $1g_{9/2}$ and $2d_{5/2}$ for neutrons [22]. Calculations done with this interaction reproduce very well the decreasing trend in the g-factors from ^{61}Mn ($N = 36$) onwards, as shown in Fig. 2. The calculated free g-factors agree with the observed values for ^{61,63}Mn to within 1%. This confirms the importance of neutron excitations across $N = 40$ for isotopes with neutron numbers $N = 36$ and higher. For the sake of completeness, the results of LNPS calculations for the lighter Mn

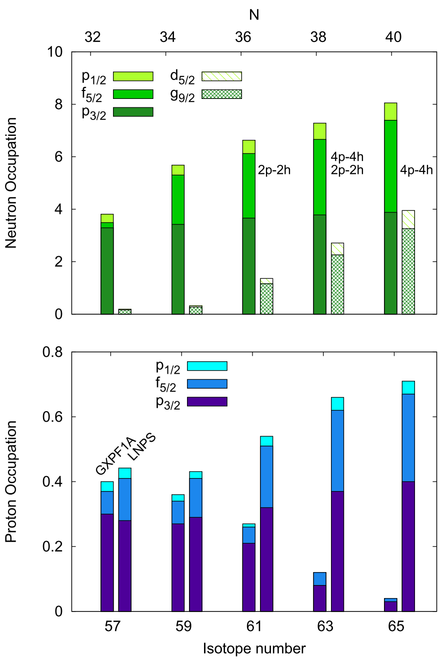

Fig. 3. Top: Orbital occupation numbers for neutrons calculated using the LNPS interaction. Occupation levels are grouped into the pf group ($\nu p_{3/2}$, $\nu f_{5/2}$, $\nu p_{1/2}$) and the gd group ($\nu g_{9/2}$, $\nu d_{5/2}$). Bottom: Orbital occupation numbers for protons excited across $Z = 28$ calculated using the GXPF1A and LNPS interactions (color online).

isotopes, using the full pf space with a ^{40}Ca core and blocking excitations to the $\nu 1g_{9/2}$ and $\nu 2d_{5/2}$ orbitals are also shown in Fig. 2. As expected, these results are similar to those of GXPF1A.

Since the observed magnetic moments of ^{57,59}Mn are better reproduced by the GXPF1A calculations, and the trend in the heavier isotopes can only be reproduced by the LNPS calculations, these results can be used to investigate changes in the ground state wave functions of odd-A Mn isotopes with increasing neutron number from ^{57}Mn ($N = 32$) onwards. Fig. 3 shows the predicted occupation of the relevant orbitals for the ground state wave function.

As expected, the level occupations calculated with LNPS show that additional neutrons are preferentially excited into the $1g_{9/2}$ orbital, with a marked augmentation of the $2d_{5/2}$ level occupation as well. The LNPS predicted ground state configuration for ^{65}Mn ($N = 40$) is dominated by 4p-4h neutron excitations, as is the case for Fe, Cr, Ti and Ca [22], indicating the strong contribution of these configurations to the wave function.

In the case of the protons, a comparison between the level occupation predicted with the LNPS and GXPF1A interactions shows that LNPS predicts increasing numbers of proton excitations in the upper pf shell while GXPF1A predicts decreasing numbers, and far fewer excited protons in total, as one moves towards $N = 40$. The accuracy of the LNPS interaction in predicting the measured g-factors at higher neutron number, along with the predicted increase in proton excitations across $Z = 28$, suggest that proton excitations play a pivotal role in the structural evolution observed in this mass region. The removal of protons from the $f_{7/2}$ orbital as one moves away from ^{68}Ni induces a stronger binding of the orbits $\nu 1g_{9/2}$ and $\nu 2d_{5/2}$, allowing neutron promotion across $N = 40$. The promotion of these neutrons then results in a repulsive potential with the $\pi 1f_{7/2}$ orbital and an attractive potential with the $\pi 1f_{5/2}$ orbital, contributing to the reduction of the $Z = 28$ shell gap and thus enhancing the probability for the excitation of protons across it. A similar explanation has been put forth to describe the Type-II shell evolution seen in the $0^+_{1,2,3}$ states of ^{68}Ni, calculated using the advanced Monte Carlo shell-model [34], and to describe the level structure in neutron-rich Cu [25]. The resulting increase in deformation is reflected in the ground state spins, shown in Table 1, where spin 5/2 is favored over the expected spin 7/2 [20,35]. The ground state spins are correctly predicted to be 5/2 by both GXPF1A [4,36] and LNPS, with the 7/2 states in ^{57,59,61,63}Mn at less than 300 keV for both interactions.

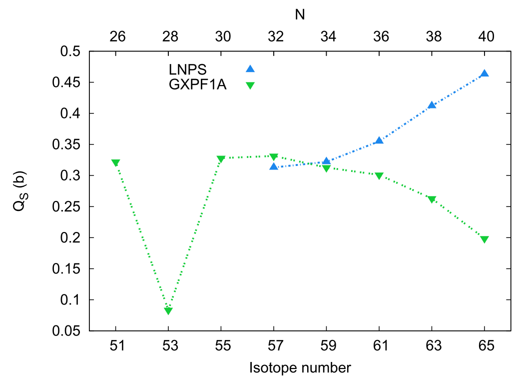

Fig. 4. The electric quadrupole moments as predicted by the GXPF1A and LNPS effective interactions (color online).

There are two abrupt decreases in the g-factors visible in Fig. 2, after $N = 28$ and after $N = 36$. The first discontinuity can be explained by the occupation of the higher νpf orbitals beyond $N = 28$, which allows for more proton–neutron correlations. A similar effect was seen in Cu isotopes near $N = 28$ [12,37]. The discontinuity between $N = 36$ and $N = 38$ is induced by the increase in proton occupation of the higher pf orbitals, as shown in the LNPS calculations. The increased occupation of the $\pi f_{5/2}$ orbital from $N = 36$ onwards leads to small admixtures of the spin-orbit partner $\pi 1f_{5/2}$ into the wave function dominated by the $\pi 1f_{7/2}$ configuration, and this has a significant effect on the calculated magnetic moments [38].

As demonstrated, the magnetic moments are sensitive probes of the nuclear wave function and have provided the first evidence for the influence of intruder orbitals on the ground states of isotopes with $N < 40$. However, the magnetic dipole moment is only indirectly sensitive to collectivity, whereas the electric quadrupole moment provides a direct probe of the quadrupole correlations between nucleons. Fig. 4 shows the GXPF1A and LNPS predictions for the quadrupole moments of Mn isotopes, in which the two predictions can be seen to deviate significantly starting at ^{61}Mn. This deviation can be attributed to increased correlations resulting from excitations across $N = 40$ and $Z = 28$, which are only included in the LNPS calculation. In this region of the nuclear chart, where the onset of collectivity has been observed in Fe and Cr [3,39], comparison of experimentally determined quadrupole moments to the GXPF1A and LNPS predictions will provide valuable information on the degree of collectivity in manganese isotopes.

180 C. Babcock et al. / Physics Letters B 750 (2015) 176–180

5. Conclusions

Nuclear spins as well as magnetic dipole moments have been reported for the odd–even isotopes $^{51-63}$Mn. The magnetic moments have been compared to shell-model calculations based on the GXPF1A and LNPS interactions. As a result of this comparison, it is found that the neutron $1g_{9/2}$ and $2d_{5/2}$ orbitals are required in the model space in order to reproduce the dipole moments for ^{61}Mn and heavier isotopes. This highlights the importance of neutron excitations, which lead to an increase of proton excitations across the $Z = 28$ shell gap from $N = 36$ onwards. The larger proton population in the higher pf orbitals, as well as the weakening of the $N = 40$ closure in manganese (and other neighboring isotope chains), produce an increase in quadrupole correlations, as shown by the LNPS predicted quadrupole moments. A future measurement of the quadrupole moments of these isotopes, using a laser transition with greater sensitivity to the hyperfine B coefficient, will shed more light on this.

Acknowledgements

This work was supported by the Belgian Research Initiative on Exotic Nuclei (IAP-project P7/12), the FWO-Vlaanderen, GOA grant 10/010 from KU Leuven, BMBF (05 P12 RDCIC), the Max-Planck Society, the Science and Technology Facilities Council, a Marie Curie ITN Fellowship of the European Community's FP7 Programme (PITN-GA-2010-264330-CATHI), and EU FP7 via ENSAR (No. 262010). We would like to thank the ISOLDE technical group for their support and assistance.

References

[1] B. Cheal, K. Flanagan, J. Phys. G, Nucl. Part. Phys. 37 (2010) 113101.
[2] K. Blaum, J. Dilling, W. Nörtershäuser, Phys. Scr. 2013 (2013) 014017.
[3] J. Ljungvall, et al., Phys. Rev. C 81 (2010) 061301.
[4] J.J. Valiente-Dobón, et al., Phys. Rev. C 78 (2008) 024302.
[5] O. Sorlin, et al., Phys. Rev. Lett. 88 (2002) 092501.
[6] S. Rahaman, et al., Eur. Phys. J. A 34 (2007) 5.
[7] O. Sorlin, et al., Eur. Phys. J. A 16 (2003) 55.
[8] H.L. Crawford, et al., Phys. Rev. Lett. 110 (2013) 242701.
[9] R. Ferrer, et al., Phys. Rev. C 81 (2010) 044318.
[10] S. Naimi, et al., Phys. Rev. C 86 (2012) 014325.
[11] C. Guénaut, et al., Phys. Rev. C 75 (2007) 044303.
[12] P. Vingerhoets, et al., Phys. Rev. C 82 (2010) 064311.
[13] B. Cheal, et al., Phys. Rev. Lett. 104 (2010) 252502.
[14] T. Otsuka, et al., Phys. Rev. Lett. 95 (2005) 232502.
[15] C.J. Chiara, et al., Phys. Rev. C 82 (2010) 054313.
[16] D. Pauwels, et al., Phys. Rev. C 78 (2008) 041307.
[17] F. Recchia, et al., Phys. Rev. C 85 (2012) 064305.
[18] M. Honma, T. Otsuka, B.A. Brown, T. Mizusaki, Phys. Rev. C 69 (2004) 034335.
[19] M. Honma, T. Otsuka, B.A. Brown, T. Mizusaki, Eur. Phys. J. A 25 (2005) 499.
[20] D. Radulov, et al., Phys. Rev. C 88 (2013) 014307.
[21] H. Jin, Y. Sun, K. Kaneko, S. Tazaki, Phys. Rev. C 87 (2013) 044327.
[22] S.M. Lenzi, F. Nowacki, A. Poves, K. Sieja, Phys. Rev. C 82 (2010) 054301.
[23] W. Rother, et al., Phys. Rev. Lett. 106 (2011) 022502.
[24] T. Baugher, et al., Phys. Rev. C 86 (2012) 011305.
[25] E. Sahin, et al., Phys. Rev. C 91 (2015) 034302.
[26] B. Marsh, et al., Hyperfine Interact. 196 (2010) 129.
[27] H. Frånberg, et al., Nucl. Instrum. Methods Phys. Res., Sect. B, Beam Interact. Mater. Atoms 266 (2008) 4502.
[28] J. Papuga, et al., Phys. Rev. C 90 (2014) 034321.
[29] K.R. Anton, et al., Phys. Rev. Lett. 40 (1978) 642.
[30] S. Davis, J. Wright, L. Balling, Phys. Rev. A 3 (1971) 1220.
[31] N. Stone, At. Data Nucl. Data Tables 90 (2005) 75.
[32] F. Charlwood, et al., Phys. Lett. B 690 (2010) 346.
[33] E. Caurier, F. Nowacki, Acta Phys. Pol. B 30 (1999) 705.
[34] Y. Tsunoda, et al., Phys. Rev. C 89 (2014) 031301.
[35] J. Comfort, P. Wasielewski, F. Malik, W. Scholz, Nucl. Phys. A 160 (1971) 385.
[36] D. Steppenbeck, et al., Phys. Rev. C 81 (2010) 014305.
[37] T.E. Cocolios, et al., Phys. Rev. Lett. 103 (2009) 102501.
[38] H. Noya, A. Arima, H. Horie, Prog. Theor. Phys. Suppl. 8 (1958) 33.
[39] N. Aoi, et al., in: INPC 2007 Proceedings of the 23rd International Nuclear Physics Conference, Nucl. Phys. A 805 (2008) 400c.

6.3.3 Article III: Spins and magnetic moments of ^{58,60,62,64}Mn ground states and isomers

PHYSICAL REVIEW C **92**, 044311 (2015)

Spins and magnetic moments of ^{58,60,62,64}Mn ground states and isomers

H. Heylen,[1,*] C. Babcock,[2,3,†] J. Billowes,[4] M. L. Bissell,[1] K. Blaum,[5] P. Campbell,[4] B. Cheal,[2] R. F. Garcia Ruiz,[1] Ch. Geppert,[6,7] W. Gins,[1] M. Kowalska,[3] K. Kreim,[5] S. M. Lenzi,[8] I. D. Moore,[9,10] R. Neugart,[5,6] G. Neyens,[1] W. Nörtershäuser,[7] J. Papuga,[1] and D. T. Yordanov[5,‡]

[1]*KU Leuven, Instituut voor Kern- en Stralingsfysica, 3001 Leuven, Belgium*
[2]*Oliver Lodge Laboratory, Oxford Street, University of Liverpool, Liverpool L69 7ZE, United Kingdom*
[3]*ISOLDE, Physics Department, CERN, CH-1211 Geneva 23, Switzerland*
[4]*School of Physics and Astronomy, The University of Manchester, Manchester M13 9PL, United Kingdom*
[5]*Max-Plank-Institut für Kernphysik, D-69117 Heidelberg, Germany*
[6]*Johannes Gutenberg-Universität Mainz, Institut für Kernchemie, D-55128, Germany*
[7]*Institut für Kernphysik, TU Darmstadt, D-64289 Darmstadt, Germany*
[8]*Dipartimento di Fisica e Astronomia dell'Università and INFN, Sezione di Padova, Padova, Italy*
[9]*Department of Physics, University of Jyväskylä, PB 35 (YFL) Jyväskylä, Finland*
[10]*Helsinki Institute of Physics, FI-00014, University of Helsinki, Finland*

(Received 26 August 2015; published 13 October 2015)

The odd-odd ^{54,56,58,60,62,64}Mn isotopes ($Z = 25$) were studied using bunched-beam collinear laser spectroscopy at ISOLDE, CERN. From the measured hyperfine spectra the spins and magnetic moments of Mn isotopes up to $N = 39$ were extracted. The previous tentative ground state spin assignments of ^{58,60,62,64}Mn are now firmly determined to be $I = 1$ along with an $I = 4$ assignment for the isomeric states in ^{58,60,62}Mn. The $I = 1$ magnetic moments show a decreasing trend with increasing neutron number while the $I = 4$ moments remain quite constant between $N = 33$ and $N = 37$. The results are compared to large-scale shell-model calculations using the GXPF1A and LNPS effective interactions. The excellent agreement of the ground state moments with the predictions from the LNPS calculations illustrates the need for an increasing amount of proton excitations across $Z = 28$ and neutron excitations across $N = 40$ in the ground state wave functions from $N = 37$ onwards.

DOI: 10.1103/PhysRevC.92.044311 PACS number(s): 21.10.Hw, 21.10.Ky, 21.60.Cs, 42.62.Fi

I. INTRODUCTION

Ongoing developments in radioactive beam production provide the opportunity to study increasingly exotic nuclei. In recent years, a substantial effort has been devoted to understanding the nuclear structure of these exotic nuclei, in particular the often drastic variations in shell structure when moving from β stability towards the drip lines. The neutron-rich pf-shell nuclei are of considerable interest because of the rapid structure evolution in the $Z < 28$ and $N \approx 40$ region. Due to the stabilizing effect of the $Z = 28$ shell closure, the $^{68}_{28}$Ni$_{40}$ ground state remains spherical whereas removal of only a few protons from this $Z = 28$ shell results in an onset of deformation in $_{26}$Fe [1–3] and $_{24}$Cr [4,5]. This deformation is associated with the development of quadrupole correlations arising when neutrons are promoted across $N = 40$. These neutron excitations are facilitated for open $\pi f_{7/2}$ nuclei due to the weakening of the $N = 40$ subshell, suggested to result from the reduced proton-neutron interaction between protons in $\pi f_{7/2}$ and neutrons in $\nu f_{5/2}$ and $\nu g_{9/2}$ orbitals [6].

Nuclear spins and moments are powerful probes to identify and understand such modifications of the nuclear structure due to their sensitivity to the composition of the wave function and deformation. These observables can be precisely extracted from high-resolution hyperfine spectra measured by collinear laser spectroscopy [7,8].

At Jyväskylä, this method was applied to measure hyperfine structures of Mn ($Z = 25$) isotopes near the $N = 28$ shell closure [9]. At CERN-ISOLDE, this work has recently been extended to the odd-even Mn isotopes up to $N = 38$ [10]. The magnetic moments beyond $N = 31$ were determined and the $I = 5/2$ spins of ^{59,61,63}Mn could be firmly established for the first time. From the systematic trend of the g factors, $g = \mu/(I\mu_N)$, a structural change between $N = 36$ and $N = 38$ is inferred. The results were compared to large-scale shell-model calculations using the LNPS [11] and GXPF1A [12,13] effective interactions. The failure of the GXPF1A calculations to reproduce the neutron-rich g factors, and the very good agreement of the LNPS predictions demonstrates the need for a model space including the $\nu g_{9/2}$ and $\nu d_{5/2}$ orbitals from $N = 36$ onwards. Along with a gradual rise in the number of neutron excitations across $N = 40$ with increasing N, an increase in proton excitations across $Z = 28$ indicates that both proton and neutron excitations are important in the ground state wave function of Mn isotopes towards $N = 40$.

In the current article, the odd-odd ^{54,56,58,60,62,64}Mn results obtained in the ISOLDE experiment are presented. In the

*hanne.heylen@fys.kuleuven.be
†carla.babcock@cern.ch
‡Present address: Institut de Physique Nucléaire d'Orsay, CNRS/IN2P3, Université Paris-Sud, F-91406 Orsay Cedex, France.

low-energy structure of ^{58,60,62,64}Mn two long-lived states are known with tentatively assigned $I^\pi = (1^+)$ and $I^\pi = (4^+)$ spin-parity. Although firm spin-parity assignments are indispensable for the construction of reliable level schemes, prior to this work only indirect assignments based on β-decay measurements, shell-model calculations, and regional systematics have been presented [14–17]. Furthermore, the nuclear configuration and degree of collectivity of these states is still unknown. Recently, Liddick *et al.* suggested shape coexistence between a deformed (1^+) state and spherical (4^+) state in ^{64}Mn [17]. These conclusions were based on the available information on neighboring nuclei and require verification by direct experimental evidence. For the lighter $^{58-62}$Mn isotopes only theoretical attempts to describe the nature of these states have been made. Sun *et al.* described ^{58}Mn and ^{60}Mn in the projected shell-model framework using prolate deformed basis states [18]. Alternatively, shell-model calculations of $^{57-62}$Mn were performed using an extended pairing-plus-quadrupole interaction with monopole corrections in the $fpg_{9/2}$ model space [19]. In the latter study the significance of neutron excitations to the $\nu g_{9/2}$ intruder orbital has been pointed out. Although magnetic and quadrupole moments are key probes to investigate the nuclear structure of odd-odd Mn isotopes, no electromagnetic moments were published in these theoretical studies.

Here we present the direct measurement of spins and magnetic moments of the odd-odd Mn ground states from $N = 29$ up to $N = 39$ including the ^{58m,60m,62m}Mn isomers. We compare our results to large-scale shell-model calculations using the GXPF1A interaction with protons and neutrons restricted to the pf orbits only, as well as to the LNPS interaction where neutron excitations into the positive-parity $\nu g_{9/2}$ and $\nu d_{5/2}$ orbitals are allowed.

II. EXPERIMENTAL METHOD AND DATA ANALYSIS

Radioactive manganese isotopes were produced at ISOLDE, CERN by bombarding a thick UC$_x$ target with a 1.4 GeV proton beam. After the Mn atoms diffused out of the hot target, they were selectively ionized using the RILIS laser ion source [20]. Next, the 40 keV ion beam was mass separated in the high-resolution separator (HRS) and sent to the ISCOOL cooler-buncher [21] where, after each proton pulse, several 6 μs ion bunches were produced by a successive 43 ms accumulation and fast release. These ion bunches were guided to the dedicated collinear laser spectroscopy beam line COLLAPS, schematically shown in Ref. [22], and overlapped with a copropagating laser. Following neutralization in a sodium vapor-filled charge exchange cell, the created atoms interact with the laser light and resonance fluorescence is observed in the subsequent interaction region. Laser light was obtained from a frequency-doubled narrow-band dye laser to probe the $3d^54s^2\ {}^6S_{5/2} \rightarrow 3d^54s4p\ {}^6P_{3/2}$ ground state atomic transition (transition wave number: 35689.980 cm^{-1}) in manganese. The laser frequency was scanned across the hyperfine structure by applying a Doppler-tuning voltage to the ions prior to neutralization.

Laser-induced fluorescence was detected by three PMTs in the light collection region. Since this fluorescence signal was only accepted when the atom bunch passed in front of the PMTs, the continuous laser background was reduced by a factor of 10^4 (ratio of bunch period and bunch length). Additional background suppression for short-lived states in ^{60,62,64}Mn was achieved by considering only atom bunches which arrived within one half-life after proton impact. This proton gating eliminates background collection for bunches in which the short-lived state has already decayed. As a result, the features of the short-lived state in the spectrum are enhanced with respect to the long-lived state, facilitating their identification. This effect is illustrated for ^{62}Mn in Fig. 1, where spectra taken with and without proton-gating are compared. Taking into account the half-lives (Table I) and relative intensities of the two states in the hyperfine spectra, the isomeric ratio $N(1^+)/N(4^+)$ is estimated to be around 30%.

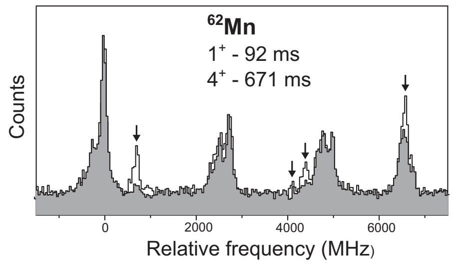

FIG. 1. Hyperfine spectra of ^{62}Mn taken without (shaded spectrum) and with (plain spectrum) proton gating. With proton gating photons are accepted only during one half-life of the shortest-lived isomer after proton impact. This clearly enhances the hyperfine structure of the short-lived state (indicated with arrows) with respect to the long-lived state. For visual comparison, the nongated spectrum is scaled to match the background intensity. The frequency is shown relative to the ${}^6S_{5/2} \rightarrow {}^6P_{3/2}$ literature transition frequency of ^{55}Mn [23].

Typical experimental spectra for ^{58,60,62,64}Mn can be found in Fig. 2. The centroid frequency and hyperfine parameters A and B were extracted from the hyperfine structures via a χ^2 minimization routine using the expression for hyperfine splitting energies (see, e.g., Ref. [7]). $A(P_{3/2})$ and $B(P_{3/2})$ were left as free fit parameters while $B(S_{5/2})$ was set to 0 MHz considering our experimental uncertainty is not better than 0.2 MHz and the ^{55}Mn literature value is $B(S_{5/2}) = 0.019031(15)$ MHz [24]. The hyperfine ratio was fixed to the value $A(P_{3/2})/A(S_{5/2}) = 13.3$ established for ^{55}Mn [10]. In order to correctly fit the partially unresolved peaks, the relative peak intensities were constrained to spin-dependent Racah values [25]. It was verified that such constrained relative intensities do not significantly change the fit results as compared to fits with free intensities, which were only possible for isotopes without isomers. The peaks were fitted with Lorentzian line profiles with common widths for all peaks in the spectrum. To account for inelastic processes in the charge exchange cell [26,27] which result in a small asymmetric line shape, a Lorentzian satellite peak at a fixed energy offset [4.61(10) eV] was

TABLE I. Extracted spins, hyperfine structure parameters $A(P_{3/2})$ and $B(P_{3/2})$, and corresponding magnetic moments and quadrupole moments for ^{54,56,58,60,62,64}Mn ground states and isomers. The ratio of hyperfine parameters is constrained to $A(P_{3/2})/A(S_{5/2}) = 13.3$ found in the odd Mn isotopes [10]. No hyperfine anomaly correction is taken into account for the calculation of the magnetic moments.

A	I^{π}	$T_{1/2}$	$A(P_{3/2})$ (MHz)	$B(P_{3/2})$ (MHz)	$\mu_{\rm exp}$ ($\mu_{\rm N}$)	$\mu_{\rm lit}$ ($\mu_{\rm N}$)	$Q_{s,\rm exp}$ (eb)	$Q_{s,\rm lit}$ (eb)
54	3^+	312 d	−763.2 (7)	+15 (6)	+3.299 (3)	+3.2966 (2)[a]	+0.37 (14)	+0.33 (3)[a]
						+3.306 (1)[b]		+0.37 (3)[b]
56	3^+	2.59 h	−750.2 (4)	+10 (3)	+3.242 (2)	+3.24121 (13)[c]	+0.24 (8)	+0.47(15)[b]
58	1^+	3.0 s	−1821.5 (16)	+1 (3)	+2.624 (2)		+0.03 (8)	
	4^+	65.4 s	−531.7 (3)	+20 (4)	+3.064 (2)		+0.47 (9)	
60	1^+	0.28 s	−1728 (5)	+4 (9)	+2.489 (7)		+0.1 (2)	
	4^+	1.77 s	−590.3 (3)	+14 (4)	+3.402 (2)		+0.33 (10)	
62	1^+	92 ms	−1656 (5)	+4 (9)	+2.385 (7)		+0.1 (2)	
	4^+	671 ms	−550.4 (4)	+25 (5)	+3.172 (3)		+0.59 (13)	
64	1^+	90 ms	−1448 (3)	+9 (5)	+2.086 (3)		+0.21 (11)	
	(4^+)	0.50 ms	–	–	–		–	
55	*5/2*	*stable*	*−963.1(3)*	*+13.4(8)*	*Ref.*	*+3.4687179(9)*[d]	*Ref.*	*0.33(1)*[e]

[a]Nuclear magnetic resonance on oriented nuclei data [36] recalculated with current ^{55}Mn reference values.
[b]Collinear laser spectroscopy experiment on the $S_2 \rightarrow P_3$ ionic transition [9].
[c]Atomic beam magnetic resonance data [37] recalculated with current ^{55}Mn reference values.
[d]Nuclear magnetic resonance data [38] corrected for diamagnetic shielding.
[e]Atomic beam magnetic resonance experiment [39].

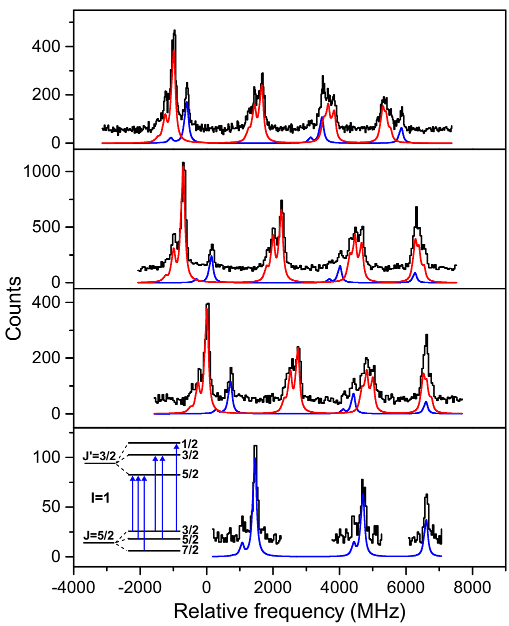

FIG. 2. (Color online) Hyperfine spectra of the ^{58,60,62,64}Mn 1^+ states (blue) and ^{58,60,62}Mn 4^+ states (red) obtained by bunched-beam collinear laser spectroscopy on the atomic $^6S_{5/2} \rightarrow {}^6P_{3/2}$ line. For ^{60,62,64}Mn proton gating was used. The inset shows a schematic depiction of the hyperfine structure of an $I = 1$ state along with the allowed hyperfine transitions. The frequency is shown relative to the $^6S_{5/2} \rightarrow {}^6P_{3/2}$ literature centroid of ^{55}Mn [23].

included. Due to the complex nature of the nonresonant Mn^+–Na charge exchange and the various atomic multiplets available, this energy offset was determined empirically.

III. RESULTS

In the literature the spins of $^{58–64}$Mn were previously only tentatively assigned; $I = (1^+)$ and $I = (4^+)$ for the ground and isomeric states were adopted in the most recent data compilations [28–31] while earlier publications also reported $I = (0^+,2^+)$ and $I = (3^+)$ [32–35]. As a result of our hyperfine spectra analysis, the spins can now be firmly established but no information on the relative energies of the states is obtained. In addition, from the hyperfine A and B parameters the magnetic and quadrupole moments are extracted. The sign and value of the deduced g factor enable parity assignments.

A. Low-spin state: $I = 1$

Despite the predominant high-spin state, multiple peaks corresponding to the low-spin state can be clearly identified in the hyperfine spectra of Fig. 2. These multiple peaks are in contradiction with the absence of hyperfine splitting in the case of $I = 0$ which would yield only one peak. An $I = 0$ spin assignment can therefore be ruled out unambiguously. To definitely decide between $I = 1$ and $I = 2$, both spin assignments were considered in the initial analysis. From the hyperfine transition selection rules, three hyperfine multiplets are expected in the case of $I = 1$ while four multiplets should appear for $I = 2$. Although no evidence for a fourth multiplet is seen on the wide frequency scans, the possibility cannot be disregarded considering the rather low statistics. Therefore, for $I = 2$, the spectra are fitted assuming one multiplet is unaccounted for on the high frequency side of our measuring

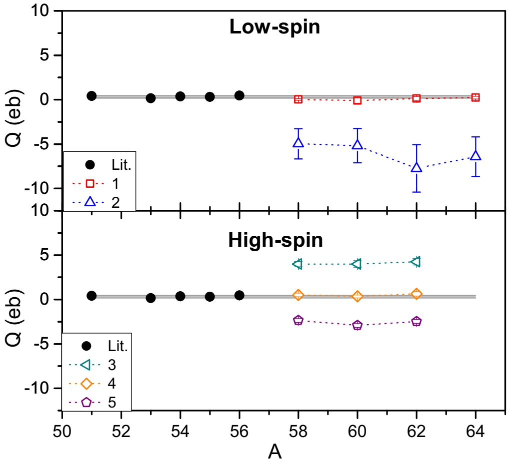

FIG. 3. (Color online) Extracted quadrupole moments assuming different spins for the low-spin state and high-spin state in ^{58,60,62,64}Mn. Note that the error bars are in most cases smaller than the symbols on this scale. These are compared with the known literature quadrupole moments. The shaded area represents the minimum and maximum literature value in the Mn chain.

range. An unobserved multiplet on the left can be ruled out, as this would severely violate the smoothly increasing trend in centroid frequency seen in the Mn chain.

As shown in Fig. 3, the extracted quadrupole moments assuming an $I = 2$ in the fitting procedure are an order of magnitude larger than the known values in the Mn chain and such large quadrupole moments are found only occasionally in much heavier mass regions (details on Q determination are given in Sec. III C). These extraordinarily large quadrupole moments combined with a worse fit quality (reflected in a higher χ^2_{red}) exclude a possible $I = 2$ spin assignment. Based on the presented evidence, we firmly assign $I = 1$ for all low-spin states in ^{58,60,62,64}Mn.

B. High-spin state: $I = 4$

The different $I = 3$,4, and 5 spin possibilities all yield the same number of multiplets in the hyperfine spectrum, hence it is impossible to discriminate between the spins based on this criterion. From fitting the high-spin structures in ^{58,60,62}Mn with the alternative spins, quadrupole moments can be extracted as shown in Fig. 3. Analogous to the low-spin case, the unrealistically large moments in the case of $I = 3$ and 5 exclude these spins, establishing $I = 4$ in ^{58,60,62}Mn. The high-spin state in ^{64}Mn could not be measured because of its short 0.50 ms half-life. This $I = 4$ spin in combination with the $I = 1$ low-spin assignment agrees with the earlier suggested $M3$ multipolarity of the isomeric transitions in ^{58,60}Mn, measured via electron conversion spectroscopy [40].

C. Hyperfine parameters

The experimental hyperfine parameters obtained with the above established spins, along with the corresponding nuclear moments are presented in Table I. The nuclear moments were extracted by comparison with the precise ^{55}Mn reference moments [38,39] and hyperfine parameters [10] using

$$\mu = \mu_{\text{ref}} \frac{IA}{I_{\text{ref}} A_{\text{ref}}} \quad \text{and} \quad Q_s = Q_{s,\text{ref}} \frac{B}{B_{\text{ref}}}.$$

The hyperfine anomaly is assumed to be negligible. For ^{54,56}Mn there is a satisfactory agreement between our results and the previously known literature values [9,36,37].

Since the quadrupole splitting of both the lower and the upper atomic state is small, the quadrupole moment sensitivity is low, resulting in large relative uncertainties. Due to this low precision, a detailed discussion on the quadrupole moments is not presented. It should be noted however that the consistently smaller quadrupole moment of the $I = 1$ state compared to the $I = 4$ state does not imply that the latter is intrinsically more deformed. Under the assumption that the nuclear deformation is axially symmetric, the intrinsic quadrupole moment Q_0 can be related to the measured moment Q_s using

$$Q_s = \frac{3K^2 - I(I+1)}{(I+1)(2I+3)} Q_0,$$

where K is the projection of the total spin I on the symmetry axis [41]. In the case that the spin is along the symmetry axis ($K = I$), an identical intrinsic quadrupole moment results in a spectroscopic quadrupole moment which is 5 times smaller for $I = 1$ than for $I = 4$. With the current experimental precision, the smaller quadrupole moment for $I = 1$ compared to $I = 4$ can therefore be fully explained by this spin-factor. Furthermore, the presence of a large ground state deformation in ^{64}Mn, as suggested by Liddick *et al.* [17], cannot be confirmed nor refuted. A more precise measurement of the 1^+ ground state quadrupole moments is needed to draw such a conclusion.

D. Parity

At present, a positive parity for the $I = 1$ state in ^{58,60,62,64}Mn is proposed based on log ft values found in β decay from the 0^+ state in Cr [14,17] or β decay to the 0^+ state in Fe [15,42]. Together with the observed $M3$ transitions, this suggests also a positive parity of the $I = 4$ state in ^{58,60}Mn. However for ^{62,64}Mn, the multipolarity of the isomeric transition is not measured experimentally and little β-decay data are available. Although the parity cannot be extracted from the hyperfine spectra directly, the sign and magnitude of the extracted g factor $g = \mu/(I\mu_N)$, can help its determination. Considering the relevant shell-model orbitals in Fig. 4, the natural parity for an odd-odd nucleus is positive, a result of the coupling between protons and neutrons occupying the pf orbitals. On the other hand, a negative parity state can only come from the coupling to an unpaired neutron in the $\nu g_{9/2}$ or $\nu d_{5/2}$ orbitals. For pure configurations arising from a weak coupling between the unpaired protons and neutrons, the g factor can be estimated via the g factor additivity rule [43]. For neutron-rich Mn this assumption is too simple

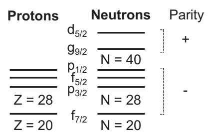

FIG. 4. The single-particle orbitals and their parity relevant in the discussion of neutron-rich Mn isotopes. In a simple shell-model picture the five valence protons reside in $\pi f_{7/2}$ and the valence neutrons occupy the pf orbitals.

and configuration mixing needs to be taken into account. Nevertheless, the estimated g factor can be an indication of the sign and magnitude of the g factor to be expected. For the calculations, shown in Table II, empirical g factors are taken from ^{55}Mn ($\pi f_{7/2}^{-3}$), ^{69}Cu ($\pi p_{3/2}$), ^{75}Cu ($\pi f_{5/2}$) for protons and ^{57}Ni ($\nu p_{3/2}$), ^{65}Ni ($\nu f_{5/2}$), ^{67}Ni ($\nu p_{1/2}$), ^{69}Zn ($\nu g_{9/2}$), ^{91}Zr ($\nu d_{5/2}$) for neutrons. As found in the odd Mn isotopes [10], the leading proton configuration along the isotopic chain are three proton holes in $\pi f_{7/2}$ coupled to $I^\pi = 5/2^-$, while for isotopes near $N = 40$ also a contribution of the $\pi p_{3/2}$ and $\pi f_{5/2}$ orbitals cannot be disregarded.

The calculated g factor for all negative parity states is negative with the exception of the $\pi f_{7/2}^{-3} \otimes \nu d_{5/2}$ configuration where it is marginally positive with a value of +0.04. The experimental g factors for both the $I = 1$ ($+2.087 < g < +2.624$) and $I = 4$ ($+0.766 < g < +0.850$) states are however positive and much larger than the calculated negative parity values. This strongly supports a positive parity assignment for the $I = 1$ and $I = 4$ states in ^{58,60,62,64}Mn.

TABLE II. Summary of g factors calculated with the additivity rule using empirical g factors. The configurations not yielding the spin of interest are indicated by a hyphen.

Protons	Neutrons	$I = 1$	$I = 4$
	Positive parity		
$\pi (f_{7/2}^{-3})_{5/2}$	$\nu p_{3/2}$	+2.79	+0.68
	$\nu f_{5/2}$	+0.83	+0.83
	$\nu p_{1/2}$	–	–
$\pi p_{3/2}$	$\nu p_{3/2}$	+0.70	+0.70
	$\nu f_{5/2}$	−0.93	+0.89
	$\nu p_{1/2}$	+2.07	–
$\pi f_{5/2}$	$\nu p_{3/2}$	+1.08	+0.06
	$\nu f_{5/2}$	+0.34	+0.34
	$\nu p_{1/2}$	–	–
	Negative parity		
$\pi (f_{7/2}^{-3})_{5/2}$	$\nu g_{9/2}$	–	−0.09
	$\nu d_{5/2}$	+0.04	+0.04
$\pi p_{3/2}$	$\nu g_{9/2}$	–	−0.31
	$\nu d_{5/2}$	−3.70	−0.10
$\pi f_{5/2}$	$\nu g_{9/2}$	–	−0.16
	$\nu d_{5/2}$	−0.04	−0.04

IV. DISCUSSION

Shell-model calculations using two different effective interactions and model spaces have been performed to obtain energy levels, spins, and magnetic moments. The single-particle orbitals relevant for the discussion below are schematically shown in Fig. 4.

The GXPF1A [12,13] and LNPS [11] effective interactions have been used with the ANTOINE shell-model code [45]. The GXPF1A model space comprises the full pf shell for protons and neutrons with ^{40}Ca as a core. Since the neutron $\nu g_{9/2}$ and $\nu d_{5/2}$ orbitals are not included, no excitations across $N = 40$ are allowed. The model space in the LNPS calculations consists of the full pf-shell for protons and the $p_{3/2}, f_{5/2}, p_{1/2}, g_{9/2}$ and $d_{5/2}$ orbitals for neutrons. This model space is unsuited for isotopes below $N = 35$ due to the absence of cross-shell excitations across $N = 28$ using a ^{48}Ca core. Due to the large dimensions of the model space, the Mn calculations require truncations. In the GXPF1A calculations up to two protons and six neutrons have been allowed to excite from $f_{7/2}$ to the higher orbitals while in the LNPS calculations a maximum of $11p - 11h$ excitations across $Z = 28$ and $N = 40$ are allowed.

The currently available spectroscopic information below 1 MeV is compared to the shell-model predictions in Fig. 5. Due to the lengthy computation time, only a few relevant low-spin states in ^{60,62,64}Mn were calculated with LNPS.

The GXPF1A calculations reproduce the high level density in ^{58}Mn, but the agreement for the heavier isotopes is poor. The inversion of the 4^+ and 1^+ state at ^{58}Mn is not significant considering the 119 keV rms energy deviation [46]. Note that the spin-parity assignments of excited states in ^{58,60}Mn are mostly based on the good correspondence between calculated and experimental level energies [46]. Taking into account a typical 100–200 keV rms energy deviation, LNPS correctly reproduces the positive parity level sequence in ^{60,62,64}Mn, while the energy of the isomeric 4^+ state is predicted slightly lower than the experimental value. The energy of the low-lying (2^-) negative parity state in ^{64}Mn, arising due to the coupling with a neutron in the positive parity gd orbits, is calculated almost 500 keV too high.

In Fig. 6, the experimental and predicted g factors are presented. The calculations have been performed using free-nucleon spin and orbital g factors for the LNPS interaction and mildly quenched values for GXPF1A ($g_{s,\mathrm{eff}} = 0.9 g_{s,\mathrm{free}}$, $g_{l,\mathrm{eff}}^{\pi} = 1.1, g_{l,\mathrm{eff}}^{\nu} = -0.1$) as in Ref. [12]. The 1^+ g factors are excellently described by LNPS for ^{60,62,64}Mn, whereas GXPF1A is unable to reproduce the downward slope, although there is a good agreement for ^{58}Mn and ^{62}Mn. For the 4^+ state, GXPF1A correctly calculates the value for ^{58}Mn, but fails to predict the nearly constant trend towards the more neutron-rich isotopes. On the other hand, the LNPS calculations do reproduce the rather constant g factor although the actual value is about 20% higher than the experimental value.

Using the empirically calculated g factors from Table II, an attempt can be made to at least qualitatively explain the experimentally observed trends. The $g(1^+)$ at ^{58}Mn could correspond to a configuration dominated by $\pi f_{7/2}^{-3} \otimes \nu p_{3/2}$

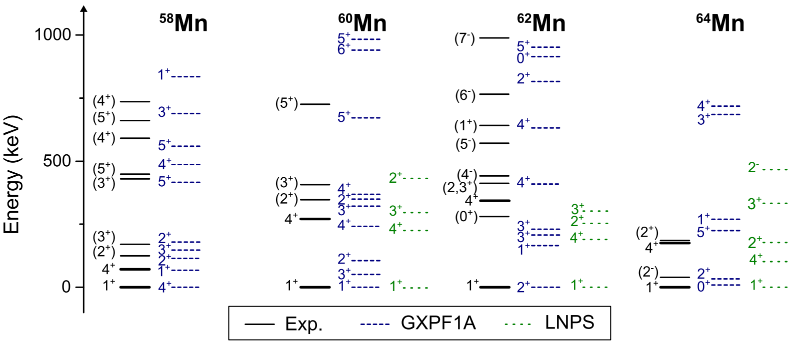

FIG. 5. (Color online) ^{58,60,62,64}Mn energy levels below 1 MeV compared to GXPF1A and LNPS calculations. The long-lived 1^+ and 4^+ states are highlighted with a bold line. Experimental levels taken from the most recent Nuclear Data Sheets [28–31] and [17,44].

while the decreasing g factor with increasing neutron number is then evidence for increased configuration mixing with other

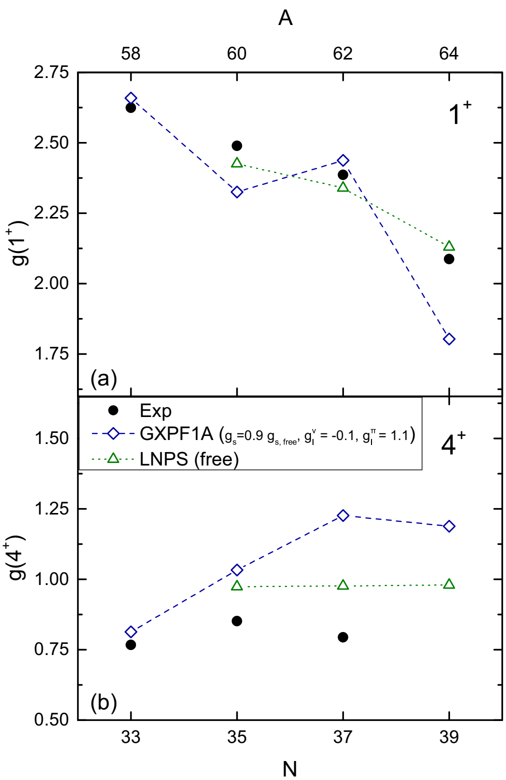

FIG. 6. (Color online) ^{58,60,62,64}Mn g factors of the 1^+ (a) and 4^+ states (b). Comparison of experimental values with shell-model calculations performed with GXPF1A (dashed line) and LNPS (dotted line).

neutron orbitals in the pf shell or admixtures with proton intruder states. Since all of these configurations would yield a smaller g factor (see Table II), it is difficult to identify which of them are the main contributors. Note that although the g factors clearly suggest a changing configuration, the spin remains 1^+ for all four isotopes between $N = 33$ and $N = 39$. The g factors of the 4^+ states are not very sensitive to the wave function configuration, as can be seen from the very similar g factors for all configurations in Table II. This means that the nearly constant g factor measured experimentally does not imply that also the nuclear configuration remains unchanged.

Although the empirical calculations in Table II are valuable to build an intuitive interpretation of the g factors, they are too simple to provide a quantitative description of the wave function. Therefore it is more instructive to look at the average proton and neutron occupation numbers that come out of the large-scale shell model calculations. In Fig. 7, these occupation numbers predicted by the LNPS interaction are shown for the 1^+ state. Because of the sensitivity of g factors to the wave function composition, the excellent correspondence between the experimental $g(1^+)$ of $^{60–64}$Mn suggests that the leading configurations of these 1^+ states are calculated correctly. In the top panel, the increase in neutron occupation of the $\nu g_{9/2}$ and $\nu d_{5/2}$ orbitals (in red) towards $N = 40$ can be seen while the occupation of the $\nu p_{3/2}\, f_{5/2}\, p_{1/2}$ orbitals (in black) remains almost constant at 7–8, well below the maximum of 12 neutrons. This shows that from $N = 37$ onwards the wave function is dominated by $2p - 2h$ and $4p - 4h$ neutron excitations across $N = 40$, analogous to the odd Mn case [10]. The importance of neutron excitations to the $\nu g_{9/2}$ and $\nu d_{5/2}$ orbitals is further visible in the energy spectrum of ^{64}Mn where a negative parity 2^- state appears between the natural parity 1^+ and 4^+ states. As a consequence of this intermediate 2^- state, an $M2$-$E1$ isomeric cascade is favored over the much slower β decay, resulting in a half-life significantly shorter than those of the other studied 4^+ states [17].

In addition to neutron excitations, proton excitations across $Z = 28$ become increasingly important towards $N = 40$ as illustrated by the rising $\pi p_{3/2}\, f_{5/2}\, p_{1/2}$ occupation numbers in the bottom panel of Fig. 7. Such a parallel rise of proton and

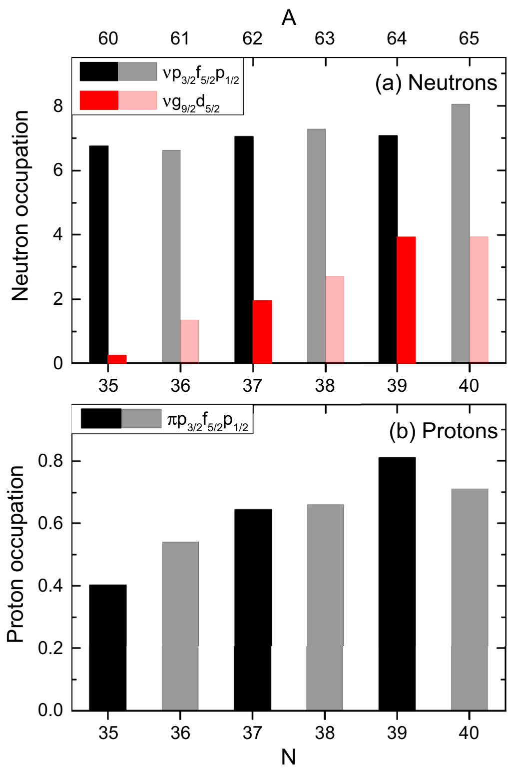

FIG. 7. (Color online) Neutron (a) and proton (b) occupation numbers of the 1^+ state calculated with the LNPS effective interaction. There is a large similarity between the odd-even Mn (shaded) and odd-odd Mn (solid) occupations.

neutron excitations is also seen in the odd Mn chain [10] and is understood as arising from the complex interplay between the protons in the pf shell and neutrons in the pf and gd shells. More neutrons in the $\nu g_{9/2}$ and $\nu d_{5/2}$ orbitals result in a less bound proton $\pi f_{7/2}$ and more bound proton $\pi f_{5/2}$ orbital due to the proton-neutron tensor force [6]. This effectively reduces the $Z = 28$ shell gap, facilitating particle-hole excitations which lead to stronger deformation and, in turn, to more neutrons in $\nu g_{9/2}$ and $\nu d_{5/2}$. In contrast to the odd Mn case however, the trend in g factors is smooth and no discontinuity related to a sudden structural change is seen [10].

For the 4^+ states, LNPS predicts a similar increase in proton and neutron cross shell excitations as for the 1^+ states. However, taking into account the 20% overestimation of the calculated g factor, other observables are desired to support this interpretation.

V. CONCLUSION

The hyperfine spectra of odd-odd Mn from $A = 54$ up to $A = 64$ were measured using collinear laser spectroscopy yielding direct information on spins and magnetic moments. The previously suggested $I = 1$ and $I = 4$ spins for the long-lived states in ^{58,60,62,64}Mn were firmly determined, except for the high-spin state in ^{64}Mn which could not be observed due to its short half-life.

The experimental results are compared with shell-model calculations using two different effective interactions in a model space restricted to the pf shell (GXPF1A), and in a model space including the $\nu g_{9/2}$ and $\nu d_{5/2}$ orbitals (allowing excitations across $N = 40$) but excluding the $\nu f_{7/2}$ (LNPS). A comparison of energy levels, spins, and g factors shows that a model space without neutron excitations across $N = 40$ is too limited to accurately predict observables of the neutron-rich Mn isotopes. On the other hand, calculations with the LNPS interaction, including such excitations, give an excellent description of the 1^+ g factors. In addition, the flat trend of the g factors as a function of the neutron number of the 4^+ states is correctly reproduced although the actual value is overestimated by about 20%. From the average occupation numbers in LNPS, the importance of both neutron excitations across $N = 40$ as well as proton excitations across $Z = 28$ is established.

The determination of spins and magnetic moments is an important first step in understanding the changing nuclear structure in the neutron-rich Mn isotopes near $N = 40$ but for direct information on possible shape transitions, a more precise knowledge of the quadrupole moments is required, while also the mean square charge radii will provide complementary information.

ACKNOWLEDGMENTS

We would like to thank the ISOLDE technical group for their support and assistance. This work was supported by the Belgian Research Initiative on Exotic Nuclei (IAP-project P7/12), the FWO-Vlaanderen, GOA Grant nos. 10/010 and 10/015 from KU Leuven, BMBF (05P12RDCIC), the Max-Planck Society, the Science and Technology Facilities Council, and EU FP7 via ENSAR (No. 262010).

[1] M. Hannawald, T. Kautzsch, A. Wöhr, W. B. Walters, K.-L. Kratz, V. N. Fedoseyev, V. I. Mishin, W. Böhmer, B. Pfeiffer, V. Sebastian, Y. Jading, U. Köster, J. Lettry, H. L. Ravn, and the ISOLDE Collaboration, Phys. Rev. Lett. **82**, 1391 (1999).

[2] J. Ljungvall, A. Görgen, A. Obertelli, W. Korten, E. Clément, G. de France, A. Bürger, J.-P. Delaroche, A. Dewald, A. Gadea, L. Gaudefroy, M. Girod, M. Hackstein, J. Libert, D. Mengoni, F. Nowacki, T. Pissulla, A. Poves, F. Recchia, M. Rejmund, W. Rother, E. Sahin, C. Schmitt, A. Shrivastava, K. Sieja, J. J.

Valiente-Dobón, K. O. Zell, and M. Zielińska, Phys. Rev. C **81**, 061301(R) (2010).

[3] W. Rother, A. Dewald, H. Iwasaki, S. M. Lenzi, K. Starosta, D. Bazin, T. Baugher, B. A. Brown, H. L. Crawford, C. Fransen, A. Gade, T. N. Ginter, T. Glasmacher, G. F. Grinyer, M. Hackstein, G. Ilie, J. Jolie, S. McDaniel, D. Miller, P. Petkov, T. Pissulla, A. Ratkiewicz, C. A. Ur, P. Voss, K. A. Walsh, D. Weisshaar, and K.-O. Zell, Phys. Rev. Lett. **106**, 022502 (2011).

[4] T. Baugher, A. Gade, R. V. F. Janssens, S. M. Lenzi, D. Bazin, B. A. Brown, M. P. Carpenter, A. N. Deacon, S. J. Freeman, T. Glasmacher, G. F. Grinyer, F. G. Kondev, S. McDaniel, A. Poves, A. Ratkiewicz, E. A. McCutchan, D. K. Sharp, I. Stefanescu, K. A. Walsh, D. Weisshaar, and S. Zhu, Phys. Rev. C **86**, 011305(R) (2012).

[5] H. L. Crawford, R. M. Clark, P. Fallon, A. O. Macchiavelli, T. Baugher, D. Bazin, C. W. Beausang, J. S. Berryman, D. L. Bleuel, C. M. Campbell, M. Cromaz, G. de Angelis, A. Gade, R. O. Hughes, I. Y. Lee, S. M. Lenzi, F. Nowacki, S. Paschalis, M. Petri, A. Poves, A. Ratkiewicz, T. J. Ross, E. Sahin, D. Weisshaar, K. Wimmer, and R. Winkler, Phys. Rev. Lett. **110**, 242701 (2013).

[6] T. Otsuka, T. Suzuki, R. Fujimoto, H. Grawe, and Y. Akaishi, Phys. Rev. Lett. **95**, 232502 (2005).

[7] B. Cheal and K. T. Flanagan, J. Phys. G **37**, 113101 (2010).

[8] K. Blaum, J. Dilling, and W. Nörtershäuser, Phys. Scr. **2013**, 014017 (2013).

[9] F. Charlwood, J. Billowes, P. Campbell, B. Cheal, T. Eronen, D. Forest, S. Fritzsche, M. Honma, A. Jokinen, I. Moore, H. Penttilä, R. Powis, A. Saastamoinen, G. Tungate, and J. Äystö, Phys. Lett. B **690**, 346 (2010).

[10] C. Babcock, H. Heylen, J. Billowes, M. Bissell, K. Blaum, P. Campbell, B. Cheal, R. G. Ruiz, C. Geppert, W. Gins, M. Kowalska, K. Kreim, S. Lenzi, I. Moore, R. Neugart, G. Neyens, W. Nörtershäuser, J. Papuga, and D. T. Yordanov, Phys. Lett. B **750**, 176 (2015).

[11] S. M. Lenzi, F. Nowacki, A. Poves, and K. Sieja, Phys. Rev. C **82**, 054301 (2010).

[12] M. Honma, T. Otsuka, B. A. Brown, and T. Mizusaki, Phys. Rev. C **69**, 034335 (2004).

[13] M. Honma, T. Otsuka, B. Brown, and T. Mizusaki, Eur. Phys. J. A **25**, 499 (2005).

[14] L. Gaudefroy, O. Sorlin, C. Donzaud, J. Angélique, F. Azaiez, C. Bourgeois, V. Chiste, Z. Dlouhy, S. Grévy, D. Guillemaud-Mueller, F. Ibrahim, K.-L. Kratz, M. Lewitowicz, S. Lukyanov, I. Matea, J. Mrasek, F. Nowacki, F. de Oliveira Santos, Y.-E. Penionzhkevich, B. Pfeiffer, F. Pougheon, M. Saint-Laurent, and M. Stanoiu, Eur. Phys. J. A **23**, 41 (2005).

[15] S. N. Liddick, P. F. Mantica, B. A. Brown, M. P. Carpenter, A. D. Davies, M. Horoi, R. V. F. Janssens, A. C. Morton, W. F. Mueller, J. Pavan, H. Schatz, A. Stolz, S. L. Tabor, B. E. Tomlin, and M. Wiedeking, Phys. Rev. C **73**, 044322 (2006).

[16] C. J. Chiara, I. Stefanescu, N. Hoteling, W. B. Walters, R. V. F. Janssens, R. Broda, M. P. Carpenter, B. Fornal, A. A. Hecht, W. Królas, T. Lauritsen, T. Pawłat, D. Seweryniak, X. Wang, A. Wöhr, J. Wrzesiński, and S. Zhu, Phys. Rev. C **82**, 054313 (2010).

[17] S. N. Liddick, S. Suchyta, B. Abromeit, A. Ayres, A. Bey, C. R. Bingham, M. Bolla, M. P. Carpenter, L. Cartegni, C. J. Chiara, H. L. Crawford, I. G. Darby, R. Grzywacz, G. Gürdal, S. Ilyushkin, N. Larson, M. Madurga, E. A. McCutchan, D. Miller, S. Padgett, S. V. Paulauskas, J. Pereira, M. M. Rajabali, K. Rykaczewski, S. Vinnikova, W. B. Walters, and S. Zhu, Phys. Rev. C **84**, 061305(R) (2011).

[18] Y. Sun, Y.-C. Yang, H. Jin, K. Kaneko, and S. Tazaki, Phys. Rev. C **85**, 054307 (2012).

[19] H. Jin, Y. Sun, K. Kaneko, and S. Tazaki, Phys. Rev. C **87**, 044327 (2013).

[20] V. N. Fedosseev, L.-E. Berg, D. V. Fedorov, D. Fink, O. J. Launila, R. Losito, B. A. Marsh, R. E. Rossel, S. Rothe, M. D. Seliverstov, A. M. Sjödin, and K. D. A. Wendt, Rev. Sci. Instrum. **83**, 02A903 (2012).

[21] E. Mané, J. Billowes, K. Blaum, P. Campbell, B. Cheal, P. Delahaye, K. Flanagan, D. Forest, H. Franberg, C. Geppert, T. Giles, A. Jokinen, M. Kowalska, R. Neugart, G. Neyens, W. Nörtershäuser, I. Podadera, G. Tungate, P. Vingerhoets, and D. T. Yordanov, Eur. Phys. J. A **42**, 503 (2009).

[22] J. Papuga, M. L. Bissell, K. Kreim, C. Barbieri, K. Blaum, M. De Rydt, T. Duguet, R. F. Garcia Ruiz, H. Heylen, M. Kowalska, R. Neugart, G. Neyens, W. Nörtershäuser, M. M. Rajabali, R. Sánchez, N. Smirnova, V. Somà, and D. T. Yordanov, Phys. Rev. C **90**, 034321 (2014).

[23] G. Başar, G. Başar, G. Acar, I. K. Öztürk, and S. Kröger, Phys. Scr. **67**, 476 (2003).

[24] S. J. Davis, J. J. Wright, and L. C. Balling, Phys. Rev. A **3**, 1220 (1971).

[25] P. C. Magnante and H. H. Stroke, J. Opt. Soc. Am. **59**, 836 (1969).

[26] N. Bendali, H. T. Duong, P. Juncar, J. M. Saint Jalm, and J. Vialle, J. Phys. B **19**, 233 (1986).

[27] K. Kreim, M. L. Bissell, J. Papuga, K. Blaum, M. De Rydt, R. G. Ruiz, S. Goriely, H. Heylen, M. Kowalska, R. Neugart, G. Neyens, W. Nörtershäuser, M. Rajabali, R. S. Alarcón, H. H. Stroke, and D. T. Yordanov, Phys. Lett. B **731**, 97 (2014).

[28] C. D. Nesaraja, S. D. Geraedts, and B. Singh, Nucl. Data Sheets **111**, 897 (2010).

[29] E. Browne and J. Tuli, Nucl. Data Sheets **114**, 1849 (2013).

[30] A. L. Nichols, B. Singh, and J. K. Tuli, Nucl. Data Sheets **113**, 973 (2012).

[31] B. Singh, Nucl. Data Sheets **108**, 197 (2007).

[32] F. Ajzenberg-Selove, R. E. Brown, E. R. Flynn, and J. W. Sunier, Phys. Rev. C **31**, 777 (1985).

[33] L. Peker, Nucl. Data Sheets **61**, 189 (1990).

[34] J. Tuli, Nucl. Data Sheets **100**, 347 (2003).

[35] H. Junde and B. Singh, Nucl. Data Sheets **91**, 317 (2000).

[36] L. Niesen and W. Huiskamp, Physica **50**, 259 (1970).

[37] W. J. Childs, L. S. Goodman, and L. J. Kieffer, Phys. Rev. **122**, 891 (1961).

[38] O. Lutz and W. Steinkilberg, Z. Naturforsch. **29a**, 1467 (1974).

[39] J. Dembczyski, W. Ertmer, U. Johann, S. Penselin, and P. Stinner, Z. Phys. A **291**, 207 (1979).

[40] W.-D. Schmidt-Ott, K. Becker, U. Bosch-Wicke, T. Hild, F. Meissner, R. Kirchner, E. Roeckl, and K. Rykaczewski, in *Proceedings of the 6th International Conference on Nuclei Far from Stability and 9th International Conference on Atomic Masses and Fundamental Constants, Bernkastel-Kues (Germany)*, edited by R. Neugart and A. Wöhr (Institute of Physics Pub., Bristol, Philadelphia, 1993).

[41] G. Neyens, Rep. Prog. Phys. **66**, 633 (2003).

[42] U. Bosch, W.-D. Schmidt-Ott, E. Runte, P. Tidemand-Petersson, P. Koschel, F. Meissner, R. Kirchner, O. Klepper, E. Roeckl, K. Rykaczewski, and D. Schardt, Nucl. Phys. A **477**, 89 (1988).

[43] K. Heyde, *The Nuclear Shell Model* (Springer, Berlin/Heidelberg, 1990).
[44] L. Gaffney *et al.*, arXiv:1506.06672.
[45] E. Caurier and F. Nowacki, Act. Phys. Pol. B **30**, 705 (1999).
[46] D. Steppenbeck, A. N. Deacon, S. J. Freeman, R. V. F. Janssens, S. Zhu, M. P. Carpenter, P. Chowdhury, M. Honma, T. Lauritsen, C. J. Lister, D. Seweryniak, J. F. Smith, S. L. Tabor, and B. J. Varley, Phys. Rev. C **81**, 014305 (2010).

6.4 Quadrupole moments

6.4.1 Difference in quadrupole moment between $I = 7/2^-$ and $I = 5/2^-$

While in section 6.3.1, it was discussed that the g-factor is not influenced by the spin and thus the coupling of the protons in the $f_{7/2}$ orbital, the situation is different for the quadrupole moment. Simple calculations by [Mayer and Jensen, 1955, p. 117] showed already that in the case of a quadrupole moment purely determined by the protons, the quadrupole moment of a $\pi\left(f_{7/2}^{-3}\right)_{5/2}$ configuration would be 2.8 times larger than the quadrupole moment of a $\pi\left(f_{7/2}^{-3}\right)_{7/2}$ configuration. Experimentally, a ratio of $Q_s(^{55}\mathrm{Mn})/Q_s(^{53}\mathrm{Mn}) = 0.32(2)/0.16(3) = 2.0(4)$ is found, in reasonable agreement with theoretical estimates. Although more generally also the influence of the neutrons needs to be considered, this simple estimate is able to qualitatively explain the jump in quadrupole moments observed between $N = 28$ and $N = 30$.

6.4.2 Article IV: Quadrupole Moments of odd-*A* $^{53-63}$Mn - Onset of Collectivity towards *N* = 40

Article IV focusses on the quadrupole moments of the odd-even $^{53-63}$Mn isotopes and how these could be determined using optical pumping in ISCOOL. The experimental quadrupole moments are compared to large-scale shell model calculations using three different effective interactions. The observed increase in quadrupole moments from $N = 36$ onwards can only be reproduced when both the $\nu g_{9/2}$ orbital and $\nu d_{5/2}$ orbital are included in the model space. Furthermore, the proton and neutron contributions to the quadrupole moments is investigated.

My contribution to the article consisted of participating in the experiment, performing a full data-analysis and actively contributing to the writing of the paper by numerous discussions with the main and co-authors and by performing shell model calculations using the GXPF1A interaction.

Physics Letters B 760 (2016) 387–392

Contents lists available at ScienceDirect

Physics Letters B

www.elsevier.com/locate/physletb

Quadrupole moments of odd-A $^{53-63}$Mn: Onset of collectivity towards $N = 40$

C. Babcock [a,b,*], H. Heylen [c,*], M.L. Bissell [d], K. Blaum [e], P. Campbell [d], B. Cheal [a], D. Fedorov [k], R.F. Garcia Ruiz [c], W. Geithner [g], W. Gins [c], T. Day Goodacre [d,b], L.K. Grob [i,d], M. Kowalska [b], S.M. Lenzi [h], B. Maass [i], S. Malbrunot-Ettenauer [b], B. Marsh [b], R. Neugart [e,j], G. Neyens [c], W. Nörtershäuser [i], T. Otsuka [f], R. Rossel [b], S. Rothe [b], R. Sánchez [g], Y. Tsunoda [l], C. Wraith [a], L. Xie [d], X.F. Yang [c]

[a] Oliver Lodge Laboratory, Oxford Street, University of Liverpool, L69 7ZE, UK
[b] ISOLDE, CERN, CH-1211 Geneva 23, Switzerland
[c] KU Leuven, Instituut voor Kern- en Stralingsfysica, 3001 Leuven, Belgium
[d] School of Physics and Astronomy, University of Manchester, M13 9PL, UK
[e] Max-Plank-Institut für Kernphysik, D-69117 Heidelberg, Germany
[f] Dept. of Physics, University of Tokyo, Hongo, Bunkyo-ku, Tokyo 113-0033, Japan
[g] GSI Helmholtzzentrum für Schwerionenforschung GmbH, D-64291 Darmstadt, Germany
[h] Dipartimento di Fisica e Astronomia dell'Università and INFN, Sezione di Padova, I-35131 Padova, Italy
[i] Institut für Kernphysik, TU Darmstadt, D-64289 Darmstadt, Germany
[j] Institut für Kernchemie, Johannes Gutenberg-Universität Mainz, D-55128, Germany
[k] Petersburg Nuclear Physics Institute, 188350 Gatchina, Russia
[l] Center for Nuclear Study, University of Tokyo, Hongo, Bunkyo-ku, Tokyo 113-0033, Japan

ARTICLE INFO

Article history:
Received 20 March 2016
Received in revised form 23 June 2016
Accepted 6 July 2016
Available online 12 July 2016
Editor: D.F. Geesaman

Keywords:
Quadrupole moments
Laser spectroscopy
Manganese
Deformation
Optical pumping

ABSTRACT

The spectroscopic quadrupole moments of the odd–even Mn isotopes between $N = 28$ and $N = 38$ have been measured using bunched-beam collinear laser spectroscopy at ISOLDE, CERN. In order to increase sensitivity to the quadrupole interaction, the measurements have been done using a transition in the ion rather than in the atom, with the additional advantage of better spectroscopic efficiency. Since the chosen transition is from a metastable state, optical pumping in ISOLDE's cooler and buncher (ISCOOL) was used to populate this state. The extracted quadrupole moments are compared to large-scale shell model predictions using three effective interactions, GXPF1A, LNPS and modified A3DA. The inclusion of both the $1\nu g_{9/2}$ and $2\nu d_{5/2}$ orbitals in the model space is shown to be necessary to reproduce the observed increase in the quadrupole deformation from $N = 36$ onwards. Specifically, the inclusion of the $2\nu d_{5/2}$ orbital induces an increase in neutron and proton excitations across the reduced gaps at $N = 40$ and $Z = 28$, leading to an increase in deformation above $N = 36$.

1. Introduction

The region around $N = 40$ has been extensively studied in recent years due to the sudden changes in nuclear structure observed below $^{68}_{28}$Ni$_{40}$. The neutron-rich manganese isotopes studied here ($Z = 25$) provide an opportunity to investigate shell structure evolution towards this weak subshell closure [1,2]. In the neighboring elements of Cr ($Z = 24$) and Fe ($Z = 26$), the electromagnetic transition probabilities and level structures have been studied in several works and evidence has been found for deformation in their neutron-rich isotopes. In Fe, the onset of collectivity is found at ^{64}Fe$_{38}$ [1] and this collectivity persists in more neutron-rich isotopes, as demonstrated by $B(E2)$ values [3,4], the decreased energy of the 2^+_1 state in ^{66}Fe$_{40}$ [5] and the $E(4^+)/E(2^+)$ ratio systematics [6]. From the measured $B(E2)$ values, a deformation parameter of $\beta \approx 0.28$ is found for ^{64,66}Fe$_{38,40}$ [3].

In Cr, the isotopes between ^{56}Cr$_{32}$ and ^{60}Cr$_{36}$ begin to show an enhancement in collectivity, demonstrated by an energy level structure characteristic of the transition from vibrational exci-

* Corresponding authors.
E-mail addresses: cbabcock@cern.ch (C. Babcock), hanne.heylen@fys.kuleuven.be (H. Heylen).

http://dx.doi.org/10.1016/j.physletb.2016.07.016
0370-2693/

tation to rotational collectivity [7]. From $^{62}Cr_{38}$ onwards, the $E(4^+)/E(2^+)$ ratios suggest a more rotational character, providing evidence for static prolate deformation in the heavier isotopes [6,8], and a deformation parameter of $\beta \approx 0.35$ has been reported for $^{62}Cr_{38}$ [1]. The emerging picture of increased quadrupole collectivity is further supported by the $B(E2)$ values up to $N = 40$ [4,9]. More recently however, theoretical calculations have suggested that the low-lying states of neutron-rich Cr cannot be characterized as strictly prolate rigid-rotor and should instead be understood as dominated by large amplitude shape fluctuations [10].

Mass measurements of Cr and Fe isotopes indicate a weak $N = 40$ gap [11–13], making occupation of the $\nu g_{9/2}$ and $\nu d_{5/2}$ orbitals energetically favorable. The promotion of neutrons to the $g_{9/2}$ orbital has been proposed as a driver of deformation [8,14]. Similarly, the $\nu d_{5/2}$ orbital may play an important role in the development of quadrupole collectivity for isotopes closer to $N = 40$ [1,15], however the specific role of excitations to this orbital remains ambiguous. While some calculations in this mass region are limited to the $fpg_{9/2}$ orbitals [2,16], the $\nu d_{5/2}$ has an important influence on the development of quadrupole correlations, and hence deformation, in the quasi-SU(3) picture [17].

The development of collectivity is correlated not only to the excitation of neutrons across $N = 40$, but to the dimensions of the total proton-neutron valence space of a particular isotope [3]. It is therefore not surprising that the degree of collectivity in these open $\pi f_{7/2}$ nuclei is largest for the mid-shell Cr isotopes.

The observations of Fe and Cr suggest that we may expect to see a similar increase in collectivity in their odd-proton neighbor, Mn ($Z = 25$) [7]. Indeed, a quasi-collective band may have been observed for $^{57-60}Mn_{32-35}$ [18] and the unexpectedly long beta-decay half-lives in $N \simeq 40$ Mn isotopes are suggested to be the result of the preferential filling of the positive parity $\nu g_{9/2}$ orbital which can only decay through forbidden transitions [5]. In order to investigate the degree of collectivity in the Mn isotopes and the role played by the $\nu d_{5/2}$ orbital, the spectroscopic quadrupole moment can serve as a direct probe. This observable is, in principle, directly obtainable from the hyperfine structure measured with high-resolution laser spectroscopy in a model-independent way.

Previous laser spectroscopy studies of atomic Mn were not successful in measuring precise quadrupole moments for the neutron-rich isotopes due to the small quadrupole splitting of the atomic ground state and the chosen excited levels [19,20]. An excited state in the Mn ion at 43370.51 cm^{-1} is known to have larger quadrupole splitting [21], however the transition to this level from the ionic ground state is spectroscopically weak. A more suitable transition for spectroscopy exists between a metastable ionic state and the excited state, however the natural population of the metastable state after the ion production process is too low to efficiently perform spectroscopy. Optical pumping has therefore been used to enhance the population of the metastable state [21,22].

Here, the technique of optical pumping is used in ISOLDE's cooler/buncher ion trap for the first time to enable the quadrupole moments of neutron-rich odd–even ionic manganese isotopes to be measured.

2. Experimental method

The experiment was performed at ISOLDE [23], CERN, where the manganese ions were produced by bombarding a uranium carbide target with a 1.4 GeV proton beam. After diffusing from the target, the reaction products of interest were ionized using the Resonance Ionization Laser Ion Source (RILIS) [24], then extracted and passed through the two mass-separating dipole magnets of the High Resolution Separator (HRS). They were then collected in ISCOOL, ISOLDE's radio frequency quadrupole cooler and buncher [25], which decelerates and cools the ions then traps the cooled ions in a potential well. While they were trapped in the potential well, the ions were optically pumped into the metastable state by resonant laser excitation and decay, using an additional pulsed laser from the RILIS laser lab. The optical pumping laser beam entered the second separator magnet via a quartz window, then passed through the separator magnet and the injection apertures of ISCOOL to interact with the trapped ion bunch near the extraction region, as shown in Fig. 1.

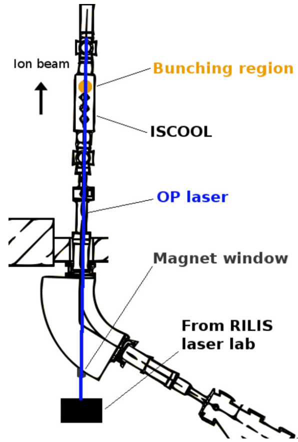

Fig. 1. Schematic for the entry of optical pumping (OP) lasers from the RILIS laser lab into the cooler/buncher (ISCOOL), where they interact with trapped ions in the bunching region (color online).

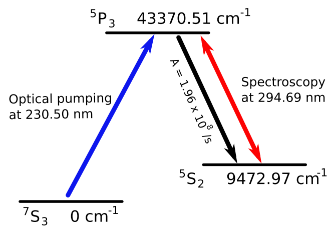

Fig. 2. Optical pumping scheme used to excite trapped manganese ions from the ground state to a low-lying metastable state at 9472.97 cm^{-1} via an intermediate excited state (color online).

The optical pumping scheme is shown in Fig. 2. A pulsed laser beam with a repetition rate of 10 kHz was produced by a frequency quadrupled titanium sapphire laser at 230.50 nm. The broadband 10 GHz laser linewidth was well matched to the Doppler broadened profile of the ions in the trap. The ions were first excited from the $^7S_3$ ground state to the $^5P_3$ state at 43 370.51 cm^{-1}. The relatively weak transition strength ($A_{ki} = 1.55 \times 10^6$ s^{-1} [26]) is offset by the extended trapping time in the cooler/buncher (200 ms), which allowed multiple laser-ion interactions to take place, even with moderate laser power. From the excited state, the ions decay with a branching ratio of 0.8 to the $^5S_2$ level at 9472.97 cm^{-1}. The decay from the $^5S_2$ metastable state to the ground state is a forbidden transition, so with increasing laser interaction time, the population of ions in the metastable state accumulates. Any effects of collisional de-excitation were balanced

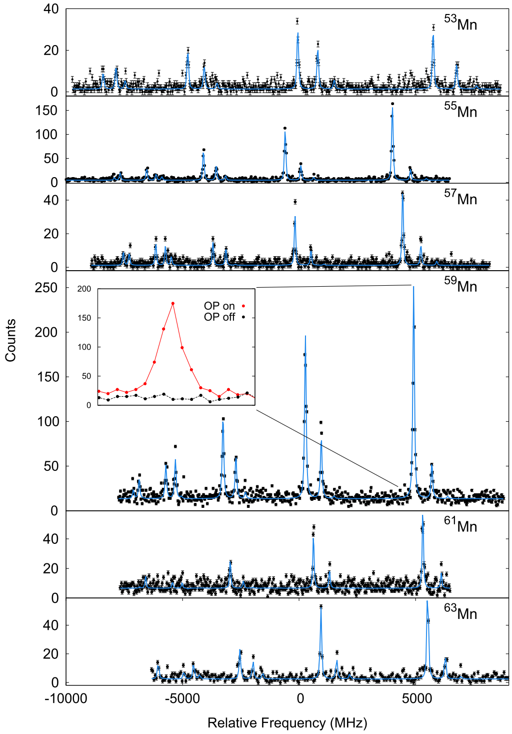

Fig. 3. Example spectra for the odd–even isotopes $^{53-63}$Mn, with the fits overlaid. The inset shows one peak of ^{59}Mn with the optical pumping (OP) laser on and off. The frequency is plotted relative to the ^{55}Mn centroid (color online).

by the repeated laser-ion interactions, and thus did not affect the population of the final state.

The optically pumped ions were subsequently released in bunches of approximately 4 μs length and directed to the COLLAPS setup [27] for investigation via collinear laser spectroscopy. The beam was overlapped with co-propagating light from a frequency-doubled narrowband dye laser that provided approximately 1 mW of power at a Doppler-shifted vacuum wavelength of 294.69 nm, in order to probe the transition from the metastable state described above. A tuning voltage applied to the interaction region modulated the energy of the bunch from its initial 30 keV, thus effectively Doppler shifting the laser frequency seen by the ions over the range of the hyperfine splitting. Four photomultiplier tubes surrounded the interaction region of the setup and detected the emitted fluorescence as the ions decayed back to the metastable state. The background due to dark counts and randomly scattered laser light was reduced by a factor of approximately 10^4 by restricting the data acquisition system to accept photomultiplier counts only during the time that the ion bunch traversed the interaction region [28–30]. In the case of ^{63}Mn, photons were only accepted within one half-life (275 ms) after the proton pulse on target (a method called proton triggering, see [20] for details) in order to further suppress the background counts. A total experimental efficiency gain of approximately an order of magnitude was observed with respect to our previous measurement using atomic manganese [19]. In addition to the increased sensitivity to

Table 1
The hyperfine A and B values of the upper ($^5P_3$) and lower ($^5S_2$) states extracted in this experiment (the $B(^5S_2)$ values were approximately 0 MHz for all isotopes). Statistical errors, which dominate the uncertainty, are shown.

Isotope	$A(^5P_3)$ (MHz)	$B(^5P_3)$ (MHz)	$A(^5S_2)$ (MHz)
^{53}Mn	−156.2(9)	+16(13)	−1239.4(13)
^{55}Mn	−150.1(2)	+86(3)	−1195.3(4)
^{57}Mn	−151.3(5)	+95(6)	−1201.1(7)
^{59}Mn	−151.2(7)	+90(9)	−1204.9(9)
^{61}Mn	−153.5(4)	+95(5)	−1218.2(6)
^{63}Mn	−149.7(5)	+124(7)	−1185.8(9)

the quadrupole interaction provided by the chosen transition, ionic transitions have the advantage that they do not suffer from the problem of populating a large number of states during the charge-exchange process, as is the case in the atom. Despite lower yields resulting from problems with the ISOLDE target, these advantages enabled a successful investigation of isotopes up to ^{63}Mn.

The hyperfine spectra collected in this way were fitted with Voigt line profiles and unconstrained intensities, using a least-squares method as outlined in [28]. The known nuclear spins [19] were used to extract the A and B coefficients of the hyperfine structure [28–30].

Fig. 3 shows example spectra for all six isotopes measured. Without the use of optical pumping, no resonant counts were seen.

3. Results

The extracted A and B coefficients of the hyperfine spectra for the $^5P_3$ and $^5S_2$ states are shown in Table 1. The A and B coefficients for ^{53,55}Mn have been measured previously in a similar optical pumping experiment for neutron-deficient isotopes [21], and the results shown here agree to within 2σ. Table 2 shows the magnetic dipole moments extracted from the $A(^5P_3)$ state and the spectroscopic quadrupole moments extracted from the $B(^5S_2)$ state using the relations [28,30],

$$\mu = \mu_{\text{ref}} \frac{IA}{I_{\text{ref}} A_{\text{ref}}} \tag{1}$$

$$Q_s = Q_{\text{ref}} \frac{B}{B_{\text{ref}}} \tag{2}$$

where the reference values are those of ^{55}Mn listed in Table 2. The hyperfine anomaly was assumed to be negligible. The dipole moments show good agreement with those previously measured for atomic Mn [19].

4. Discussion

Comparison of experimental data to theoretical calculations is a powerful method for testing our current understanding of nuclear structure and dynamics across the nuclear chart. In particular, regions of rapid structural change, such as those around $N = 40$, pose serious challenges.

Fig. 4 and Table 2 show a comparison of the experimental quadrupole moments with the results of large-scale shell model calculations, performed using three different effective interactions and model spaces. The GXPF1A effective interaction [31] uses a ^{40}Ca core and is restricted to the pf space for both protons and neutrons. For computational reasons, a maximum of 2 protons and 6 neutrons can be excited across $Z = N = 28$. The LNPS interaction [17] uses a ^{48}Ca core and considers the entire pf shell for protons, and the $p_{3/2}$, $f_{5/2}$, $p_{1/2}$, $g_{9/2}$ and $d_{5/2}$ orbitals for neutrons. A maximum of 11 excitations across $Z = 28$ and $N = 40$ are allowed. The modified A3DA interaction [32] considers the

Table 2
The magnetic dipole and electric quadrupole moments derived from the coefficients in Table 1. The spin assignments have already been confirmed [19]. Also shown are the quadrupole moments calculated using the GXPF1A [31], LNPS [17] and modified A3DA [32] effective interactions. All calculations are done with effective charges $e_\pi = 1.31$ and $e_\nu = 0.46$.

Isotope	N	I	μ (μ_N)	Q_s (b)	Q_s (b) [GXPF1A]	Q_s (b) [LNPS]	Q_s (b) [modified A3DA]
^{53}Mn	28	7/2	+5.036(5)	+0.06(5)	+0.08	–	+0.08
^{55}Mn	30	5/2	+3.46871790(9)[a]	+0.33(1)[b]	+0.33	–	+0.33
^{57}Mn	32	5/2	+3.485(2)	+0.37(3)	+0.33	+0.31	+0.35
^{59}Mn	34	5/2	+3.496(3)	+0.34(4)	+0.31	+0.32	+0.32
^{61}Mn	36	5/2	+3.535(2)	+0.36(3)	+0.30	+0.35	+0.38
^{63}Mn	38	5/2	+3.441(3)	+0.48(4)	+0.26	+0.41	+0.41

[a] Reference from [33] with corrections for diamagnetic shielding.
[b] Reference from [34].

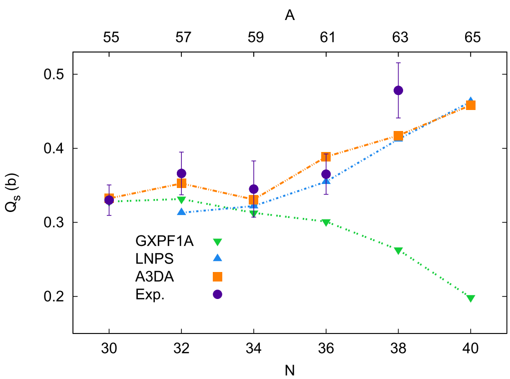

Fig. 4. Comparison of the quadrupole moments determined in this work to the results of calculations using the GXPF1A, LNPS, and modified A3DA effective interactions with $e_\pi = 1.31$ and $e_\nu = 0.46$ (color online).

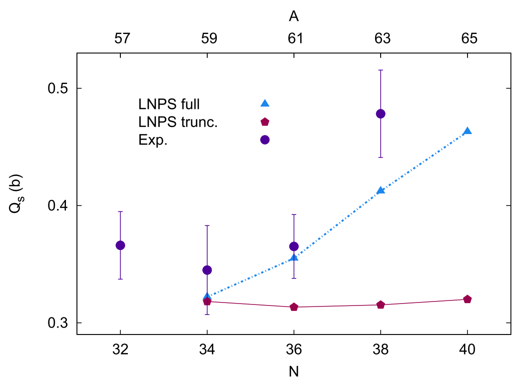

Fig. 5. The results of LNPS calculations of the quadrupole moment with neutron excitations limited to the $fpg_{9/2}$ space (labeled *trunc.*) and in the full $fpg_{9/2}d_{5/2}$ space (labeled *full*) are shown compared to experimental values (color online).

$fpg_{9/2}d_{5/2}$ space for protons and neutrons with ^{40}Ca as a core, and was able to include a larger model space by performing calculations in the Monte Carlo shell model framework [32]. Both the GXPF1A and LNPS calculations have been done using the ANTOINE shell model code [35], which imposes some computational limits on the size of the model space since a full Lanczos diagonalization is performed.

As can be seen in Fig. 4, the GXPF1A effective interaction successfully predicts the quadrupole moments up to ^{59}Mn ($N = 34$), after which the predictions and experimental data begin to diverge. The data follows an upward trend in deformation, as predicted by LNPS and modified A3DA, while the GXPF1A calculations follow a downward trend, as would be expected if there was a subshell gap at $N = 40$. Indeed, previous work on the magnetic moments [19,20] and energy levels [18] has demonstrated that the GXPF1A model space, which does not permit excitations across $N = 40$, is too limited to accurately describe the more neutron-rich Mn isotopes. Thus the larger model spaces employed by the LNPS and modified A3DA interactions are necessary to reproduce the experimental data. Both interactions have proven to be successful in this region of the nuclear chart [19,20,36,37], and LNPS has recently been used to accurately characterize a similar deformation trend in ^{58,60,62}Cr$_{34,36,38}$ [38].

Quadrupole moments are a useful tool to investigate the role of excitations across $N = 40$ because of their sensitivity to 2p-2h and 4p-4h excitations, and to the strength of the quadrupole collectivity. In particular, the quadrupole moments will be used to probe the role of the $\nu d_{5/2}$ orbital in the development of this collectivity. For this purpose, calculations of the theoretical quadrupole moments have been performed using LNPS in a truncated model space which excludes the $\nu d_{5/2}$ orbital. Fig. 5 shows the results of these calculations (labeled *trunc.*), where excitations have been limited to the $\nu g_{9/2}$ orbital. The quadrupole moments calculated this way do not reproduce the rising trend of the experimental data, but remain nearly constant from $N = 34$ onwards. The trend of the experimental data is only reproduced in the full $fpg_{9/2}d_{5/2}$ space. This demonstrates the necessity of including both the $\nu g_{9/2}$ and $\nu d_{5/2}$ orbitals in the model space – neutron excitations to $\nu g_{9/2}$ alone are not sufficient to explain the deformation in the Mn isotopes. This can be understood in terms of the pseudo and quasi SU(3) symmetry as discussed in [39].

The effect of the excitations across $N = 40$ can be seen more clearly in the occupation numbers of protons and neutrons for the upper pf and $g_{9/2}d_{5/2}$ orbitals. Fig. 6 shows a comparison of occupation numbers calculated using the LNPS interaction in the truncated $fpg_{9/2}$ space and the full $fpg_{9/2}d_{5/2}$ space.

The top panel of Fig. 6 shows that excitations to the $\nu g_{9/2}$ orbital are suppressed in the truncated $fpg_{9/2}$ space as compared to the $fpg_{9/2}d_{5/2}$ space. This illustrates the correlation between the increased occupation of the $\nu d_{5/2}$ orbital and the quadrupole collectivity, which also increases the excitations to the $\nu g_{9/2}$ orbital. The reduced neutron excitations across $N = 40$ in the $fpg_{9/2}$ space provide a possible explanation for the difference in predicted deformation, as shown in Fig. 5.

The exclusion of the $\nu d_{5/2}$ orbital also has consequences for proton excitations across $Z = 28$. The lower panel in Fig. 6 shows the proton excitations into the upper pf orbitals for both the $fpg_{9/2}$ and $fpg_{9/2}d_{5/2}$ spaces. While the total upper πpf shell oc-

C. Babcock et al. / Physics Letters B 760 (2016) 387–392 391

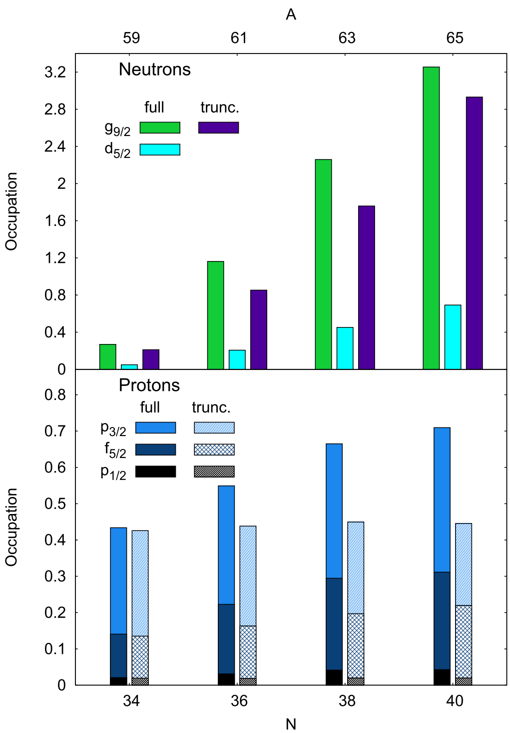

Fig. 6. Orbital occupation numbers for excitations past $N = 40$ and $Z = 28$. The labels *full* and *trunc.* refer to calculations done in the $fpg_{9/2}d_{5/2}$ and $fpg_{9/2}$ spaces respectively (color online).

cupation for the truncated $fpg_{9/2}$ space remains nearly constant, this same occupation rises in the full $fpg_{9/2}d_{5/2}$ space with increasing N.

Since the exclusion of the $\nu d_{5/2}$ orbital has a significant effect on both neutron and proton excitations, it is helpful to look at the separate neutron and proton contributions to the total quadrupole moment, by decomposing it into its components, $Q = Q_\pi + Q_\nu$. The results for both the full and truncated spaces are shown in Fig. 7. In the limited $fpg_{9/2}$ model space, both the neutron and proton contributions remain essentially constant, showing no increase in deformation towards $N = 40$. In contrast, both contributions rise with increasing N in the full model space. The contribution from neutron correlations dominates the overall increase in the quadrupole moments, although the protons also induce an increase of $\Delta Q_s = 0.035\,\text{b}$ between $N = 34$ and $N = 40$. The increase in the experimentally observed quadrupole moments between $N = 36$ and $N = 38$ is due to a combination of the rise in the neutron and proton quadrupole components. The comparison between the $fpg_{9/2}$ and $fpg_{9/2}d_{5/2}$ spaces emphasizes the trend seen in the occupation numbers.

Calculations using the modified A3DA interaction (see Fig. 4) obtain results similar to those of LNPS for the quadrupole moments, as well as the neutron and proton occupation numbers. In addition, this interaction has been used to calculate the potential energy surfaces of the Mn ground states, and the minima of these plots have shown a progression from a near spherical shape

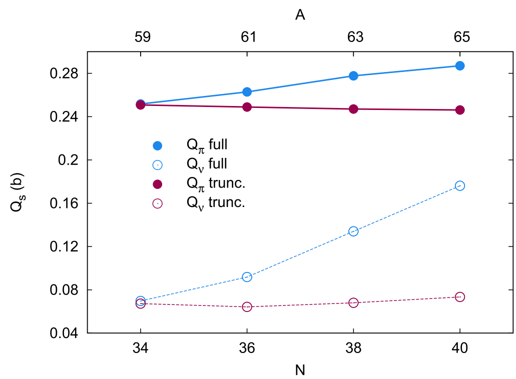

Fig. 7. Contribution of the neutrons and protons to the total quadrupole moment for both the $fpg_{9/2}$ and $fpg_{9/2}d_{5/2}$ space, where the labels *full* and *trunc.* have been used to indicate the $fpg_{9/2}d_{5/2}$ and $fpg_{9/2}$ spaces respectively (color online).

in ^{53}Mn, towards increasing prolate deformation in the more neutron rich isotopes up to ^{65}Mn [40]. This deformation is, however, not rigid and there is evidence that shape fluctuations with triaxial components play a role in the ground state structure of manganese towards $N = 40$. Though the spectroscopic quadrupole moment is not sensitive to such fluctuations, the rising deformation with neutron number predicted by the potential energy surfaces mirrors the increasing deformation observed experimentally.

5. Conclusions

Optical pumping in the ISOLDE cooler/buncher has been successfully applied in order to enhance the population of ionic Mn in a chosen metastable state, which allowed efficient collinear laser spectroscopy to be performed on the neutron-rich isotopes. Hyperfine A and B coefficients were extracted and electric quadrupole moments were determined for the odd–even $^{53-63}$Mn isotopes. The theoretically predicted quadrupole moments were calculated using three shell model effective interactions, GXPF1A, LNPS and modified A3DA. In comparing the observed moments to those calculated with the shell model interactions, the influence of the $\nu g_{9/2}$ and $\nu d_{5/2}$ orbitals on the developing collectivity can clearly be seen in the deviation of the observed values from those predicted by GXPF1A. The larger model spaces used by LNPS and modified A3DA reproduce the trend of the quadrupole moments very well in the region approaching $N = 40$. Calculations done using LNPS in a truncated $fpg_{9/2}$ space (thus excluding the $\nu d_{5/2}$ orbital) shed some light on the roles played by the individual orbitals above $N = 40$. It is found that the increase of the quadrupole moments and thus the development of collectivity towards $N = 40$ can only be reproduced if both the $g_{9/2}$ and $d_{5/2}$ orbitals are included in the calculations. By comparing the neutron and proton occupation numbers for the full and truncated LNPS calculations, it is clear that the inclusion of the $\nu d_{5/2}$ orbital leads to an increase in both neutron and proton excitations. A calculation of the individual neutron and proton contributions to the spectroscopic quadrupole moment confirmed this interpretation and demonstrated the important role of the $\nu d_{5/2}$ orbital in producing the necessary neutron and proton excitations to reproduce the observed deformation in the neutron-rich Mn isotopes.

Acknowledgements

This work was supported by the Belgian Research Initiative on Exotic Nuclei (IAP-project P7/12), the FWO-Vlaanderen, GOA grants 10/010 and 15/010 from KU Leuven, BMBF (05P15RDICA), the Max-Planck Society, the Science and Technology Facilities Council, and the European Union's Seventh Framework Programme for Research and Technological Development under Grant Agreements ENSAR (No. 262010), CATHI (No. 264330), COFUND (No. 267194) and LA^3NET (289191). We would like to thank the ISOLDE technical group for their support and assistance.

References

[1] J. Ljungvall, et al., Phys. Rev. C 81 (2010) 061301.
[2] J.J. Valiente-Dobón, et al., Phys. Rev. C 78 (2008) 024302.
[3] W. Rother, et al., Phys. Rev. Lett. 106 (2011) 022502.
[4] H.L. Crawford, et al., Phys. Rev. Lett. 110 (2013) 242701.
[5] M. Hannawald, et al., Phys. Rev. Lett. 82 (1999) 1391.
[6] C. Santamaria, et al., Phys. Rev. Lett. 115 (2015) 192501.
[7] N. Aoi, et al., Nucl. Phys. A 805 (2008) 400c, INPC 2007 Proceedings of the 23rd International Nuclear Physics Conference.
[8] N. Aoi, et al., Phys. Rev. Lett. 102 (2009) 012502.
[9] T. Baugher, et al., Phys. Rev. C 86 (2012) 011305.
[10] K. Sato, et al., Phys. Rev. C 86 (2012) 024316.
[11] S. Rahaman, et al., Eur. Phys. J. A 34 (2007) 5.
[12] S. Naimi, et al., Phys. Rev. C 86 (2012) 014325.
[13] C. Guénaut, et al., Phys. Rev. C 75 (2007) 044303.
[14] N. Hoteling, et al., Phys. Rev. C 82 (2010) 044305.
[15] E. Caurier, F. Nowacki, A. Poves, Eur. Phys. J. A 15 (2002) 145.
[16] H. Jin, Y. Sun, K. Kaneko, S. Tazaki, Phys. Rev. C 87 (2013) 044327.
[17] S.M. Lenzi, F. Nowacki, A. Poves, K. Sieja, Phys. Rev. C 82 (2010) 054301.
[18] D. Steppenbeck, et al., Phys. Rev. C 81 (2010) 014305.
[19] C. Babcock, et al., Phys. Lett. B 750 (2015) 176.
[20] H. Heylen, et al., Phys. Rev. C 92 (2015) 044311.
[21] F. Charlwood, et al., Phys. Lett. B 690 (2010) 346.
[22] B. Cheal, et al., Phys. Rev. Lett. 102 (2009) 222501.
[23] E. Kugler, Hyperfine Interact. 129 (2000) 23.
[24] B. Marsh, et al., Hyperfine Interact. 196 (2010) 129.
[25] H. Frånberg, et al., Nucl. Instrum. Methods B 266 (2008) 4502.
[26] M. McNally (Ed.), Kurucz Database, vol. XXB, Trans. IAU, Kluwer, Dordrecht, 1988.
[27] J. Papuga, et al., Phys. Rev. C 90 (2014) 034321.
[28] B. Cheal, K. Flanagan, J. Phys. G, Nucl. Part. Phys. 37 (2010) 113101.
[29] K. Blaum, J. Dilling, W. Nörtershäuser, Phys. Scr. 2013 (2013) 014017.
[30] P. Campbell, I. Moore, M. Pearson, Prog. Part. Nucl. Phys. 86 (2016) 127.
[31] M. Honma, T. Otsuka, B.A. Brown, T. Mizusaki, Eur. Phys. J. A 25 (2005) 499.
[32] T. Otsuka, et al., Prog. Part. Nucl. Phys. 47 (2001) 319.
[33] O. Lutz, W. Steinkilberg, Z. Naturforsch. 29a (1974) 1467.
[34] J. Dembczyński, et al., Z. Phys. Hadrons Nucl. 291 (1979) 207.
[35] E. Caurier, F. Nowacki, Acta Phys. Pol. B 30 (1999) 705.
[36] E. Sahin, et al., Phys. Rev. C 91 (2015) 034302.
[37] Y. Tsunoda, et al., Phys. Rev. C 89 (2014) 031301.
[38] T. Braunroth, et al., Phys. Rev. C 92 (2015) 034306.
[39] A.P. Zuker, A. Poves, F. Nowacki, S.M. Lenzi, Phys. Rev. C 92 (2015) 024320.
[40] H. Heylen, et al., 2016, submitted to Phys. Rev. C.

6.4.3 Comparison of theoretical Q_0 of neutron-rich Cr, Mn and Fe

In article IV, the proton and neutron contributions to the spectroscopic quadrupole moment are compared for the Mn isotopes. LNPS calculations were performed in the full $\nu fpg_{9/2}d_{5/2}$ and truncated $\nu fpg_{9/2}$ model space and the quadrupole moments were calculated via the $E2$ transition amplitudes A_ν and A_π which can be related to the intrinsic quadrupole moment Q_0 using

$$Q_0 = \sqrt{16\pi}(e_\pi A_\pi + e_\nu A_\nu)$$

The spectroscopic quadrupole moment can then be extracted in the strong coupling regime

$$Q_s = \frac{3K^2 - I(I+1)}{(I+1)(2I+3)} Q_0$$

A similar approach was employed by Crawford et al. [2013] which discussed the measured $B(E2)$ values of neutron-rich Fe and Cr isotopes in the LNPS framework. In this paper, the pure transition amplitudes were shown which do not include a necessary, albeit somewhat ambiguous scaling by the effective proton and neutron charges and which can be related the $B(E2)$ values via

$$B(E2 : 2_1^+ \to 0_1^+) = (e_\pi A_\pi + e_\nu A_\nu)^2$$
$$= \frac{Q_0^2}{16\pi}$$

In Fig. 6.7 the intrinsic quadrupole moments for the neighbouring Cr ($Z = 24$), Mn ($Z = 25$) and Fe ($Z = 26$) isotopes are shown calculated with the universal effective charges [Dufour and Zuker, 1996].

A large increase in neutron quadrupole moments towards $N = 40$ is seen which saturates at $N = 38$ in Cr and $N = 40$ in Fe. For Mn no calculations beyond $N = 40$ are performed but the close correspondence with Fe at the other neutron numbers suggests a similar saturation behaviour. While for the three isotopic chains, the increase in quadrupole moment is mostly due to the increase in neutron contribution, also a neutron dependence of the proton contribution is seen. In Mn and Fe the proton quadrupole moment increases towards $N = 40$, but it decreases in the Cr isotopic chain. There doesn't seem to be an immediate explanation for this different behaviour.

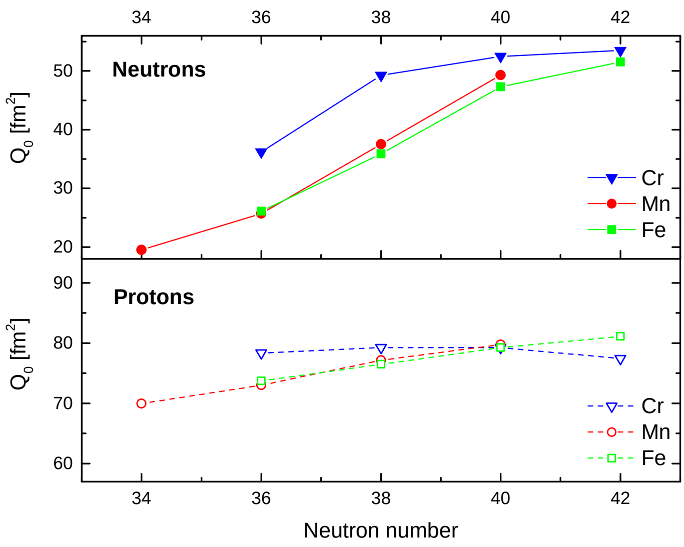

Figure 6.7: Intrinsic quadrupole moments of Cr and Fe [Crawford et al., 2013] and Mn (this work) decomposed in the proton and neutron contribution calculated using the LNPS effective interaction. The universal effective charges $e_\pi = 1.31$ and $e_\nu = 0.46$ are used in the calculations.

6.5 Mean-square charge radii

6.5.1 Article V: Changes in nuclear structure along the Mn isotopic chain studied via charge radii

In article V, the data of the first and second experiment are combined and from the measured isotope shifts on the atomic and ionic transition, two consistent sets of mean-square charge radii are extracted. As a conclusion to our studies of the Mn isotopes, the nuclear structure along the isotopic chain is discussed in light of the experimentally known ground state properties: the magnetic and quadrupole moments, mean square charge radii and masses. This discussion is not limited to the neutron-rich cases but considers the Mn isotopes from $N = 25$ up to $N = 39$.

This article is written in a large collaboration of laser spectroscopists, atomic theorists and nuclear theorists. The data analysis was performed in parallel with Carla Babcock. Afterwards I was in charge of discussing the content of the paper with the relevant collaborators, writing the manuscript and preparing it for submission.

Status: this paper is submitted Physical Review C.

APS/123-QED

Changes in nuclear structure along the Mn isotopic chain studied via charge radii

H. Heylen,[1,*] C. Babcock,[2,3,†] R. Beerwerth,[4,5] J. Billowes,[6] M.L. Bissell,[1,6] K. Blaum,[7] J. Bonnard,[8] P. Campbell,[6] B. Cheal,[2] T. Day Goodacre,[3,6] D. Fedorov,[9] S. Fritzsche,[4,5] R.F. Garcia Ruiz,[1] W. Geithner,[10] Ch. Geppert,[11,12] W. Gins,[1] L.K. Grob,[3,12] M. Kowalska,[3] K. Kreim,[7] S.M. Lenzi,[13] I.D. Moore,[14,15] B. Maass,[12] S. Malbrunot-Ettenauer,[3] B. Marsh,[3] R. Neugart,[7,11] G. Neyens,[1] W. Nörtershäuser,[12] T. Otsuka,[16] J. Papuga,[1] R. Rossel,[3] S. Rothe,[3] R. Sánchez,[10] Y. Tsunoda,[17] C. Wraith,[2] L. Xie,[6] X.F. Yang,[1] and D.T. Yordanov[7,‡]

[1]*KU Leuven, Instituut voor Kern- en Stralingsfysica, 3001 Leuven, Belgium*
[2]*Oliver Lodge Laboratory, Oxford Street, University of Liverpool, L69 7ZE, United Kingdom*
[3]*ISOLDE, Physics Department, CERN, CH-1211 Geneva 23, Switzerland*
[4]*Helmholtz Institute Jena, Fröbelstieg 3, 07743 Jena, Germany*
[5]*Theoretisch-Physikalisches Institut, Friedrich-Schiller-Universität Jena, 07743 Jena, Germany*
[6]*School of Physics and Astronomy, The University of Manchester, Manchester M13 9PL, United Kingdom*
[7]*Max-Planck-Institut für Kernphysik, D-69117 Heidelberg, Germany*
[8]*Istituto Nazionale di Fisica Nucleare, Sezione di Padova, 35131 Padova, Italy*
[9]*Petersburg Nuclear Physics Institute, 188350 Gatchina, Russia*
[10]*GSI Helmholtzzentrum für Schwerionenforschung GmbH, D-64291 Darmstadt, Germany*
[11]*Johannes Gutenberg-Universität Mainz, Institut für Kernchemie, D-55128, Germany*
[12]*Institut für Kernphysik, TU Darmstadt, D-64289 Darmstadt, Germany*
[13]*Dipartimento di Fisica e Astronomia dell'Università and INFN, Sezione di Padova, Padova, Italy*
[14]*Department of Physics, University of Jyväskylä, PB 35 (YFL) Jyväskylä, Finland*
[15]*Helsinki Institute of Physics, FI-00014, University of Helsinki, Finland*
[16]*Deptarment of Physics, University of Tokyo, Hongo, Bunkyo-ku, Tokyo 113-0033, Japan*
[17]*Center for Nuclear Study, University of Tokyo, Hongo, Bunkyo-ku, Tokyo 113-0033, Japan*

(Dated: September 16, 2016)

The hyperfine spectra of $^{51,53-64}$Mn were measured in two experimental runs using collinear laser spectroscopy at ISOLDE, CERN. Laser spectroscopy was performed on the atomic $3d^5\ 4s^2\ {}^6\mathrm{S}_{5/2} \rightarrow 3d^5\ 4s4p\ {}^6\mathrm{P}_{3/2}$ and ionic $3d^5\ 4s\ {}^5\mathrm{S}_2 \rightarrow 3d^5\ 4p\ {}^5\mathrm{P}_3$ transitions, yielding two sets of isotope shifts. The mass and field shift factors for both transitions have been calculated in the multiconfiguration Dirac-Fock framework and were combined with a King plot analysis in order to obtain a consistent set of mean-square charge radii which, together with earlier work on neutron-deficient Mn, allow the study of nuclear structure changes from $N = 25$ across $N = 28$ up to $N = 39$. A clear development of deformation is observed towards $N = 40$, confirming the conclusions of the nuclear moments studies. From a Monte Carlo Shell Model study of the shape in the Mn isotopic chain, it is suggested that the observed development of deformation is not only due to an increase in static prolate deformation but also due to shape fluctuations and triaxiality. The changes in mean-square charge radii are well reproduced using the Duflo-Zuker formula except in the case of large deformation.

PACS numbers: 21.10.Ft, 21.60.Cs, 42.62.Fi

I. INTRODUCTION

The structure of exotic nuclei exhibits many peculiarities such as halo nuclei, islands of inversion and shape coexistence. Laser spectroscopy has played a decisive role in studying these phenomena as it enables measurements of spins, nuclear moments and changes in mean-square charge radii from the valley of stability to exotic regions of the nuclear chart [1]. Due to the complementarity of the measured ground state properties, a comprehensive description of nuclear structure can be established, for example the evolution of both single-particle and collective aspects as a function of nucleon number [2, 3]. Mean-square charge radii in particular have been systematically measured across the nuclear chart. They are sensitive to the shape and size of the nucleus and can also be extracted for even-even nuclei with $I = 0$, for which the magnetic moments and spectroscopic quadrupole moments are zero.

The region between the proton-magic Ca ($Z = 20$) and Ni ($Z = 28$) isotopes has attracted much attention due to its rich variety in nuclear structure. Around calcium, early measurements revealed a remarkable behaviour of the charge radii between $N = 20$ and $N = 28$ [4–7]. Furthermore, the appearance of new magic numbers at $N = 32$ and $N = 34$ was investigated [8–12]. Adding a few protons towards the nickel isotopic chain and a few neutrons towards $N = 40$, a rapid development of collectivity is observed, bearing close resemblance to the island of inversion around $N = 20$ [13, 14]. Although nuclear

* hanne.heylen@fys.kuleuven.be
† cbabcock@triumf.ca
‡ Present address: Institut de Physique Nucléaire, CNRS-IN2P3, Univ. Paris-Sud, Université Paris-Saclay, 91406 Orsay, France

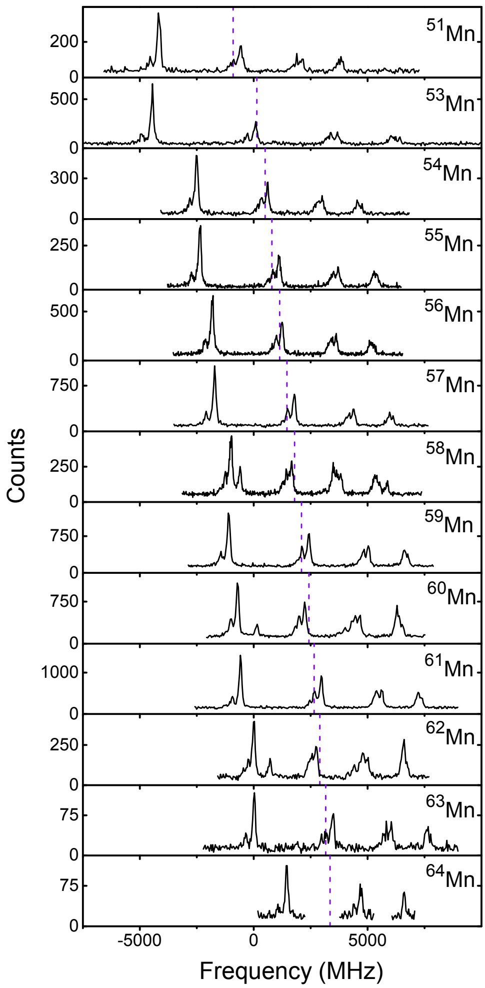

FIG. 1. Hyperfine spectra of $^{51,53-64}$Mn measured on the atomic $^6S_{5/2} \rightarrow {}^6P_{3/2}$ transition. The centroid for each spectrum is indicated with a vertical dashed line. For ^{58,60,62}Mn only the centroid frequency of the ground state is indicated (the isomer shift is too small to be visible on this scale).

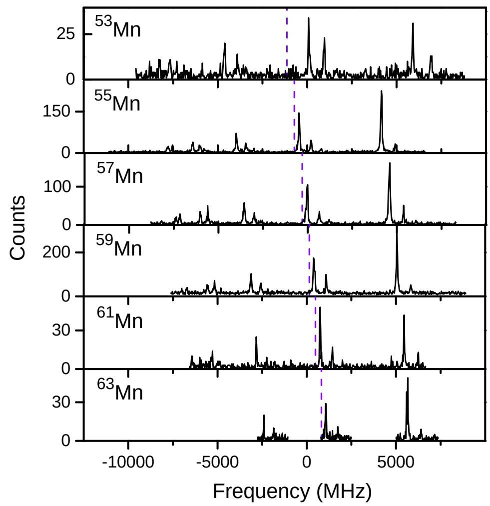

FIG. 2. Hyperfine spectra of the odd-even $^{53-63}$Mn isotopes measured on the ionic $^5S_2 \rightarrow {}^5P_3$ transition. The centroid frequency for each spectrum is indicated with a vertical dashed line. Due to the limited yield at ^{63}Mn only the 3 last multiplets in the hyperfine spectrum were measured, sufficient to extract the centroid and hyperfine parameters.

moments and mean-square charge radii have been essential in the interpretation of the nuclear structure around $N = 20$ [15–18], so far the experimental knowledge of these observables around $N = 40$ is scarce. Their measurements therefore provide necessary and complementary information.

With 25 protons, the manganese isotopes lie centrally between the Ca and Ni isotopic chains. The nuclear moments and mean-square charge radii of Mn between $N = 25$ and $N = 31$ were previously studied at the IGISOL facility, JYFL, Jyväskylä [19]. These measurements have now been extended to $N = 39$ in two collinear laser spectroscopy experiments at ISOLDE, CERN [20–22]. With the ground state properties of Mn known from $N = 25$ across $N = 28$ up to $N = 39$, a detailed picture of the changing nuclear structure emerges. The mean-square charge radii and quadrupole moments show a clear kink at $N = 28$ associated with a neutron shell closure, while the effect of $N = 28$ on the two-neutron separation energies is not immediately apparent [19]. The steeply increasing slope of the radii between $N = 28$ and $N = 32$ is found to be common to the isotopic chains in this region, indicating an almost Z-independent core-polarization by neutrons filling the upper pf-shell [23]. Going even more neutron-rich, the Mn magnetic and quadrupole moments show evidence of increased collectivity towards $N = 40$ [20–22]. Comparisons with large-scale shell model calculations have illustrated the importance of particle-hole excitations across $N = 40$ and $Z = 28$ for the description of the nuclear structure approaching $N = 40$.

In this article, the mean-square charge radii of $^{51,53-64}$Mn measured in the two previously mentioned ISOLDE experiments are presented. Mn is to date the first isotopic chain below $Z = 28$ for which the ground state properties beyond $N = 28$ can be systematically studied for such a long sequence of isotopes.

II. EXPERIMENTAL METHOD

The experimental campaign was performed at the ISOLDE radioactive ion beam facility in CERN where exotic manganese isotopes were produced via the bombardment of a thick uranium carbide target with 1.4-GeV protons. Element selective ionization was achieved using the resonance ionization laser ion source (RILIS) [24]. After mass separation in the HRS, the isotopically pure ion beam was cooled and bunched in the gas-filled RFQ ISCOOL [25] and reaccelarated to, respectively, 40 keV and 30 keV in the first and second experiment. The bunched beam was then guided to the dedicated collinear laser spectroscopy beam line COLLAPS [26–28] where it was overlapped with a co-propagating narrowband laser beam. A Doppler-tuning potential was applied to scan the laser frequency across the hyperfine structure in the reference frame of the ions/atoms. The fluorescence light from the decay following the resonant laser-induced excitations between the hyperfine levels was detected using sensitive photomultiplier tubes placed perpendicular to the beam line.

In a first experiment, laser spectroscopy was performed on an atomic transition from the $3d^5\ 4s^2\ {}^6S_{5/2}$ ground state to the $3d^5\ 4s4p\ {}^6P_{3/2}$ excited state at a wavelength of 280.1907 nm (in vacuum). Hyperfine spectra of $^{51,53-64}$Mn were obtained. The details of the experiment and data analysis are described in [20, 21]. To improve the sensitivity to quadrupole moments, a second experiment was performed on an ionic transition at 295.0066 nm (in vacuum) from the $3d^5\ 4s\ {}^5S_2$ metastable state at 9472.97 cm^{-1} to the $3d^5\ 4p\ {}^5P_3$ state at 43370.51 cm^{-1}. The population of the ionic metastable state was enhanced using the technique of optical pumping in the ISCOOL cooler/buncher, as outlined in [22]. In this second experiment, only hyperfine spectra of the odd-even $^{53-63}$Mn isotopes were measured.

III. RESULTS

Typical hyperfine spectra measured on the atomic and ionic transition are shown in Fig. 1 and 2, respectively. The centroid frequency ν_0^A for each spectrum is indicated with a vertical dashed line. The isotope shifts relative to ^{55}Mn

$$\delta\nu^{55,A} = \nu_0^A - \nu_0^{55}$$

extracted from these hyperfine spectra are presented in Table I, the hyperfine A and B parameters were reported earlier in [20–22]. Statistical errors obtained in the fit procedure are indicated with round brackets while a systematic error due to a ±15 V uncertainty in the acceleration voltage calibration is assumed for both experiments,

TABLE I. Mn isotope shifts relative to ^{55}Mn measured on the atomic $3d^5\ 4s^2\ {}^6S_{5/2} \rightarrow 3d^5\ 4s4p\ {}^6P_{3/2}$ transition and the ionic $3d^5\ 4s\ {}^5S_2 \rightarrow 3d^5\ 4p\ {}^5P_3$ transition. Additional to the statistical uncertainty in round brackets, the systematic uncertainty on the isotope shifts due to a ±15V uncertainty on the calibration of the acceleration voltage is indicated in square brackets.

A	N	$\delta\nu^{55,A}_{\text{atom}}$ (MHz)	$\delta\nu^{55,A}_{\text{ion}}$ (MHz)
50g	25	-	−1573(2)[27][a]
50m	25	-	−1514(8)[27][a]
51	26	−1698(7)[20]	−1201(26)[21][a]
52g	27	-	−745(7)[16][a]
52m	27	-	−782(3)[16][a]
53	28	−669(6)[9]	−418(3)[10] −418(2)[10][a]
54	29	−307(6)[5]	−192(4)[5][a]
55	30	0	0
56	31	340(7)[5]	240(6)[5][a]
57	32	655(7)[9]	422(5)[10]
58g	33	983(4)[13]	-
58m	33	990(4)[13]	-
59	34	1284(5)[17]	863(11)[19]
60g	35	1607(10)[21]	-
60m	35	1594(4)[21]	-
61	36	1843(7)[25]	1215(2)[27]
62g	37	2099(8)[28]	-
62m	37	2088(5)[28]	-
63	38	2355(6)[32]	1542(5)[35]
64	39	2566(6)[35]	-

[a] Isotope shift measured in [19] including a systematic error arising from a ±15V uncertainty of the calibration in the acceleration voltage.

indicated in square brackets. For completeness, also the isotope shifts measured previously at the IGISOL facility JYFL in Jyväskylä [19] using the same ionic transition are reported in Table I.

The measured isotope shifts can be related to the changes in mean-square charge radii $\delta\langle r^2\rangle$ using (see e.g. [3])

$$\delta\nu_j^{55,A} = M_j \frac{m_A - m_{55}}{m_A m_{55}} + F_j \delta\langle r^2\rangle^{55,A}. \quad (1)$$

Here m_A is the mass of an isotope A and M_j and F_j are the mass and field shift parameters specific to the electronic transition j. The first term (mass shift) is due to the recoil kinetic energy of a nucleus with finite mass while the second term (field shift) originates from the changes in nuclear charge distribution and hence contains the charge radius dependence. To reliably extract the changes in mean-square charge radii, an accurate knowledge of both electronic parameters is required. In first-order perturbation theory, these parameters are constant along an isotopic chain but they need to be determined for each electronic transition separately.

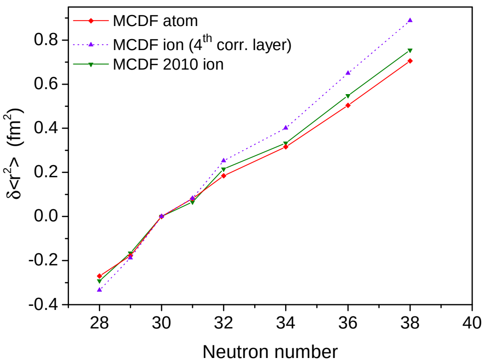

FIG. 3. (Color online) Comparison between the changes in mean-square charge radii between $N = 28$ and $N = 39$ calculated using the mass and field shift factors obtained in three different MCDF calculations. Only the statistical experimental uncertainties are shown.

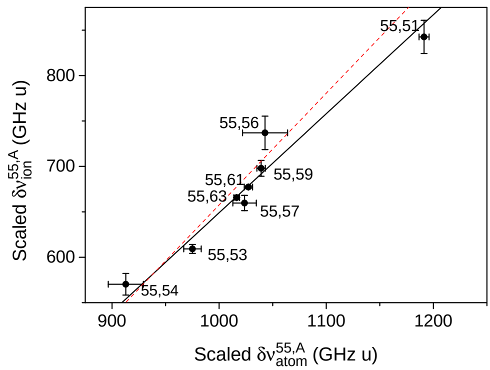

FIG. 4. (Color online) King plot using the isotope shifts of the atomic and ionic transitions, shown in Table I. The best linear fit (black solid line) is shown together with the linear relation obtained by filling in the atomic MCDF and the ionic MCDF 2010 factors in eq. (2) (dashed red line).

A. Electronic factor calculations

For Mn, the mass and field shift factors cannot be determined by a direct comparison between the measured isotope shifts and the independently known charge radii since only the absolute charge radius of one isotope is known from non-optical methods. Therefore, one has to rely on theoretical calculations to obtain the electronic M and F factors, using e.g. the multiconfiguration Dirac-Fock (MCDF) method [29].

The MCDF method, implemented in the GRASP2K code [30], is applied to generate the orbitals for the atomic $3d^5 4s^2\ ^6S_{5/2}$ and $3d^5 4s4p\ ^6P_{3/2}$ configurations as well as the ionic $3d^5 4s\ ^5S_2$ and $3d^5 4p\ ^5P_3$ levels. In a subsequent step, the Breit interaction is included by first-order perturbation theory in the configuration-interaction method [31]. The resulting wave functions are then used to compute the mass shift parameters by utilizing the RIS3 module [32] and the field shift parameter is computed using the RATIP tools [33]. This distinguishes the current results from the previous computations on the same ionic transition reported in [19], where the relativistic correction to the mass shift operator was neglected. However, these corrections do not exceed the uncertainty due to the complex electronic structure. The open $3d$ shell makes theoretical calculations on atomic and singly ionized manganese very challenging and extensive in terms of required computational power.

In the MCDF approach, the wave function is represented as a superposition of configuration state functions (CSFs). Each CSF represents a specific electronic configuration and the choice of this basis set is crucial for the quality of the obtained results. In the lowest-order approximation, the model space consists of the $3d$, $4s$ and $4p$ valence shells. This space is then extended by adding a set of correlation orbitals nl, which are populated by virtual excitations from the reference configurations. Due to computational restrictions, the correlation orbitals are limited to orbitals with angular momentum up to f. In subsequent steps, the model space is systematically extended by further layers with a new principal quantum number n. The virtue of this model is that it allows convergence of the desired quantities to be monitored as the model space is expanded. For all computations performed in this work, single and double excitations from the valence shells, as well as single excitations from all

TABLE II. Overview of the electronic mass and field shift factors for the atomic $3d^5\ 4s^2\ ^6S_{5/2} \rightarrow 3d^5\ 4s4p\ ^6P_{3/2}$ transition and the ionic $3d^5\ 4s\ ^5S_2 \rightarrow 3d^5\ 4p\ ^5P_3$ transition calculated in the multiconfiguration Dirac-Fock framework. Also the atomic factors calculated with respect to (wrt) the ionic factors using the King plot analysis are shown and vice versa. The estimated theoretical uncertainties on the parameters are indicated in square brackets, and where applicable, the fit errors from the King plot are indicated in round brackets. For details about the empirically modified parameters, see section IV.

Transition	Method	M (GHz u)	F (MHz/fm^2)
Atom:	**MCDF**	**+1158**[81]	**−465**[70]
$^6S_{5/2} \rightarrow {}^6P_{3/2}$	King plot wrt MCDF 2010	+1188(108)[65]	−525(39)[93]
	Emp. Mod.	+1215	−465
Ion:	MCDF 4th	+875[131]	−546[82]
$^5S_2 \rightarrow {}^5P_3$	MCDF 2010 [19]	+852[60]	−572[86]
	King plot wrt MCDF atom	**+819**(125)[88]	**−506**(38)[76]
	Emp. Mod.	+881(129)	−506(38)

TABLE III. Changes in mean-square charge radii of $^{50-64}$Mn relative to ^{55}Mn extracted from the isotope shifts measured on the atomic $^6S_{5/2} \to {}^6P_{3/2}$ and the ionic $^5S_2 \to {}^5P_3$ transition. On the lefthand side of the table, the charge radii are obtained with the electronic parameters shown in bold in Table II. On the righthand side of the table, the charge radii are obtained with the empirically modified electronic parameters, as explained in section IV A. The statistical uncertainties and the systematic uncertainties due to the uncertainty on the acceleration voltage are shown in round and square brackets, respectively. No theoretical uncertainties due to the uncertainty on the calculated mass and field shift factors are shown, as explained in section III B.

A	N	$\delta\langle r^2\rangle^{55,A}$ (fm^2)		$\delta\langle r^2\rangle^{55,A}_{\text{emp. mod.}}$ (fm^2)	
		atom	ion	atom	ion
50g	25	-	0.168(4)[53]	-	−0.055(4)
50m	25	-	0.051(16)[53]	-	−0.171(16)
51	26	0.102(14)[42]	0.065(53)[41]	−0.073(14)	−0.11(5)
52g	27	-	−0.226(14)[31]	-	−0.354(14)
52m	27	-	−0.153(6)[31]	-	−0.281(6)
53	28	−0.270(12)[20]	−0.285(7)[20]	−0.354(12)	−0.369(7)
54	29	−0.177(12)[10]	−0.166(8)[10]	−0.219(12)	−0.207(8)
55	30	0	0	0	0
56	31	0.081(15)[10]	0.053(12)[10]	0.121(15)	0.093(12)
57	32	0.185(15)[19]	0.202(11)[19]	0.263(15)	0.280(11)
58g	33	0.234(8)[28]	-	0.350(8)	-
58m	33	0.220(8)[28]	-	0.336(8)	-
59	34	0.316(10)[37]	0.297(21)[37]	0.467(10)	0.448(21)
60g	35	0.329(14)[45]	-	0.515(14)	-
60m	35	0.357(9)[45]	-	0.544(9)	-
61	36	0.504(15)[53]	0.504(5)[54]	0.724(15)	0.724(5)
62g	37	0.615(18)[61]	-	0.868(18)	-
62m	37	0.640(9)[61]	-	0.893(9)	-
63	38	0.706(13)[69]	0.704(10)[69]	0.990(13)	0.988(10)
64	39	0.873(14)[76]	-	1.188(14)	-

core shells, are taken into account. All calculations are performed with common core orbitals, while the correlation orbitals are separately optimized for the upper and lower level.

For the atomic calculations, the reference configurations $3d^54(s^2+p^2)$ for the ground state and the excited state configurations $3d^54s4p$ and $3d^64s$ are used to generate five correlation layers. This choice of the reference configurations yields a well-balanced basis-expansion such that the transition energy as well as the M and F parameters converge well. The main source of error comes from omitted electronic correlations. Because these contributions are difficult to quantify, a conservative theoretical uncertainty of 15% on M and F is assumed.

The computations on the ionic transitions show much more complex electron correlations. It is found that the two levels of interest significantly correlate with configurations where at least one electron is excited to the $4f$ or $4d$ shell. A complete treatment of this kind of correlations is not possible due to the extremely large basis expansions. Therefore, an alternative approach is used where the zeroth-order approximation is computed with a space spanned by the $3d^54s$, $3d^44p^2$ and $3d^34s4d^2$ configurations for the lower level and $3d^54p$, $3d^44s4p$ and $3d^34p4d^2$ for the upper level. The correlation layers were then generated by using only the $3d^5(4s+4p)$ configurations as a reference. This approach yields good convergence for the first four layers, however, convergence fails for the fifth layer, possibly due to neglected electronic correlations.

An overview of the different electronic factors obtained from the computations described above and in [19] (labeled MCDF 2010) can be found in Table II and a comparison of the changes in charge radii evaluated with those factors is shown in Fig. 3. There is good agreement between the charge radii obtained with the electronic factors for the atomic transition calculated in this work and the previously published calculations on the ionic transition. The computation on the ionic transition including up to four correlation layers (this work) yields slightly larger differences in charge radii, but the agreement is still better than the above estimated uncertainty. Due to the aforementioned convergence problems of the ionic calculations and the limited treatment of electronic correlations, the atomic calculations are considered to be more reliable. Therefore, the atomic results are used in the following King plot analysis.

An additional consistency check of the calculations is performed via the King plot method [34]

$$\mu^{55,A}\delta\nu^{55,A}_{\text{ion}} = \frac{F_{\text{ion}}}{F_{\text{atom}}}\mu^{55,A}\delta\nu^{55,A}_{\text{atom}} + M_{\text{ion}} - \frac{F_{\text{ion}}}{F_{\text{atom}}}M_{\text{atom}} \quad (2)$$

where $\mu^{55,A} = m^{55}m^A/(m^A - m^{55})$ is used as a scaling factor for the isotope shifts. In Fig. 4 the scaled isotope shifts of the ionic transition are plotted against those of the atomic transition. A linear fit then gives the slope $\frac{F_{\rm ion}}{F_{\rm atom}} = 1.09(8)$ and intercept $M_{\rm ion} - \frac{F_{\rm ion}}{F_{\rm atom}} M_{\rm atom} = -44(8) \cdot 10^4$ MHz u from which the mass and field shift parameters of the atomic transition can be determined from the ionic computation and vice versa (see Table II).

Comparison with the independently computed values then permits the estimation of the uncertainty of the computations. This suggests that the above quoted uncertainty of 15% on F is realistic while a 15% uncertainty on M seems overestimated. From the comparison to regional systematics in section IV and the agreement of the King plot analysis, an uncertainty of 7% on M seems to be more appropriate.

B. Changes in mean-square charge radii

The changes in mean-square charge radii relative to ^{55}Mn are determined using the experimental isotope shifts in Table I and the electronic factors shown in bold in Table II. Because a King plot is used to link the mass and field shift factors of the ionic transition to the atomic transition, the charge radii extracted from the two transitions are consistent with each other, as can be seen in Table III. Nevertheless, since the charge radii are obtained by using only two parameters for each transition, the one-by-one agreement between the two transitions provides an independent cross check of the consistency of the isotope shift measurements.

In Table III no theoretical uncertainties are shown. This is justified because although the theoretical uncertainty on the electronic factors gives a large uncertainty on the exact $\delta\langle r^2\rangle$ value, it does not alter the discussion in section IV. Indeed, a variation of M and F causes a general pivot about the reference point but does not change the local trends. Since nuclear structure effects manifest themselves as local irregularities in the course of the charge radii, the interpretation is not affected by the theoretical uncertainty.

Details on the empirically modified charge radii shown on the righthand side of Table III will be given in the next section. Note that in this case only statistical uncertainties are shown because the systematic uncertainty on the isotope shifts is incorporated effectively in the modified mass shift parameter [35].

IV. DISCUSSION

A. Mn radii systematics

In Fig. 5 the mean-square charge radii $\langle r^2\rangle$ of the $^{50-64}$Mn isotopes ($N = 25 - 39$) are plotted along with the charge radii of the neighboring isotopes between $_{19}$K and $_{29}$Cu. For Mn the results from the atomic transition are shown except for ^{50,51,52,54,56}Mn for which only ionic data is available. The $\langle r^2\rangle$ values are obtained with the reference radii of Fricke and Heilig [36] and the published changes in mean-square charge radii [12, 23, 37–40].

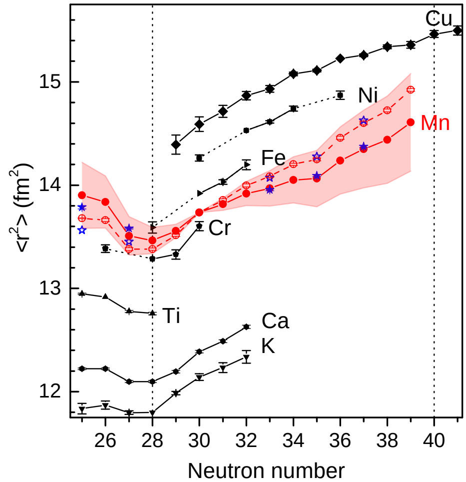

FIG. 5. (Color online) The experimental mean-square charge radii known in the Mn region between $N = 25$ and $N = 39$. The Mn isotopes are highlighted in red with the isomers in ^{50,52,58,60,64}Mn indicated by a blue star. The Mn charge radii obtained using the MCDF atomic parameters and King plot ionic parameters are indicated by full symbols connected by a solid line. The shaded area represents the systematic uncertainty assuming 15% uncertainty on F and 7% on M. The empirically modified Mn charge radii are shown by open symbols connected with a dashed line (see text).

A first observation is that the mean-square charge radii of the 4^+ isomers in neutron-rich ^{58,60,62}Mn are very close to the 1^+ ground state radii, as indicated by the blue stars in Fig. 5. This suggests similar degrees of deformation and no sizable shape coexistence. Although the absolute difference in charge radii of the two states is small, the charge radius of the isomer in ^{58}Mn is slightly smaller than that of the ground state, while it is slightly larger in ^{60}Mn and ^{62}Mn. Note that the difference in isomer and ground state charge radii is much larger on the neutron-deficient side. In the self-conjugate $N = Z = 25$ nucleus ^{50}Mn this can be understood in terms of the difference in isospin ($T = 0$ and $T = 1$), as was discussed previously for $^{38}_{19}K_{19}$ [41].

A strong effect of the $N = 28$ shell closure is seen in all isotopic chains. Moreover, beyond $N = 28$ the increase in charge radii is strikingly independent of Z, as pointed out in a study of the neutron-rich K isotopes [23]. Also the recently published radii of the Cu isotopes [40], with 10 protons more than K, precisely follow this systematic trend. The slope of the Mn radii determined in this work on the other hand, appears to be

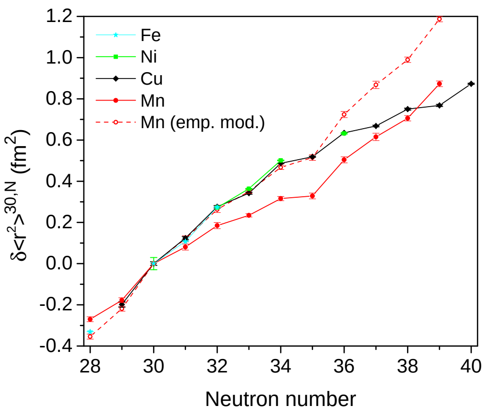

FIG. 6. (Color online) Changes in mean-square charge radii of Mn, Fe, Ni and Cu with respect to $N = 30$. The Mn radii obtained using the MCDF parameters are indicated by full symbols and full lines while the empirically modified ones are shown with open symbols and dashed lines. Only statistical errors are shown.

slightly too low. This becomes especially evident in Fig. 6 which plots the changes in mean-square charge radii of $_{26}$Fe [38], $_{28}$Ni [39] and $_{29}$Cu [40] relative to $N = 30$ together with the changes in mean-square charge radii of Mn determined in this work. Although nuclear structure effects appear as local features in $\delta\langle r^2\rangle$, irrespective of the general slope, the similarities and differences with other isotopic chains become more clear when the Mn radii are empirically modified to reproduce the regional trend. This is achieved by increasing M_{atom} by 5% and keeping F_{atom} constant. The corresponding F_{ion} and M_{ion} are calculated from the King plot results. This modification causes a tilt of the charge radii about the ^{55}Mn reference point but keeps the local features unaltered as shown by the open symbols connected by a dashed line in Figs. 5 and 6. Note that although the charge radius at $N = 35$ might seem anomalous at first, the use of the modified M and F shows that the apparent dip is rather due to a combination of odd-even staggering and a sudden increase in charge radii at $N = 36$, as will be discussed next.

As shown in Fig. 6, the modified Mn radii follow the Fe, Ni and Cu trend up to $N = 35$ while beyond $N = 35$ a clear divergence between the Mn and Cu isotopes is seen. Whereas in Cu the mean-square charge radii exhibit a weakly parabolic behavior between $N = 28$ and $N = 40$ [40], in Mn a rapid increase in charge radii is observed from $N = 36$ onwards. This observation is consistent with the increase in the spectroscopic quadrupole moments [22] and the behaviour of the magnetic moments [20, 21], interpreted as arising from particle-hole excitations across $Z = 28$ and $N = 40$. From $N = 36$ onwards, these magnetic and quadrupole moments can be described by large-scale shell model calculations only if excitations of neutrons from the pf shell into the $g_{9/2}$ and $d_{5/2}$ orbits are included, as well as proton excitations across $Z = 28$.

A good reproduction of the experimental magnetic and quadrupole moments is achieved in the Monte Carlo Shell Model (MCSM) framework using the modified A3DA interaction [42, 43] which includes the full pf shell and $g_{9/2}d_{5/2}$ orbitals in the model space for both protons and neutrons [22]. This gives confidence in the predictive power of these calculations to discuss the shape of the Mn ground states. A constrained Hartree-Fock calculation using this A3DA shell model Hamiltonian provides the potential energy surface on which the distribution of the MCSM basis states (deformed slater determinants) as a function of the intrinsic quadrupole moments $Q_0 \propto \langle 2z^2 - x^2 - y^2\rangle$ and $Q_2 \propto \langle x^2 - y^2\rangle$ is plotted. Fig. 7 presents these potential energy surfaces for the ground states of the odd-even $^{53-65}$Mn isotopes, showing the evolution of intrinsic shape between $N = 28$ and $N = 40$. At the $N = 28$ shell closure the distribution of intrinsic shapes is centered around the spherical minimum. This changes towards moderately deformed prolate structures between $N = 30$ and 34, then an additional increase in prolate deformation is seen in $N = 36$ and 38 and a maximum is reached at $N = 40$. However, a picture in which only axial symmetric deformation is considered too simple since from $N = 34$ onwards a triaxial minimum appears and becomes dominant in $N = 36, 38$ and $N = 40$. Moreover, the observed spread in the distribution of intrinsic shapes points to considerable shape fluctuations in the ground states of the neutron-rich Mn isotopes. Such shape fluctuations were already suggested to be important in the low-energy structure of the neutron-rich $_{24}$Cr isotopes from a constrained Hartree-Fock-Bogoliubov plus local quasiparticle random-phase approximation study [44].

The sudden increase in experimental charge radii is in accordance with the predicted change in nuclear shape at $N = 36$ although these calculations indicate that the change in the radii cannot be solely attributed to a change in static prolate deformation.

B. Charge radii and masses

In this section, the connection between the trend in mean-square charge radii and the masses of the Mn isotopes is examined. Across the nuclear chart, trends in charge radii are in general closely reflected in the course of the two-neutron separation energies, with clear examples in the $A \sim 100$ and rare-earth regions [48, 49]. However, this correspondence is not always straightforward, as shown in [19] for the light mass region. For example, the prominent $N = 28$ shell closure effect in the Mn charge radii is almost not visible in the two-neutron separation energies. Such discrepancies are not

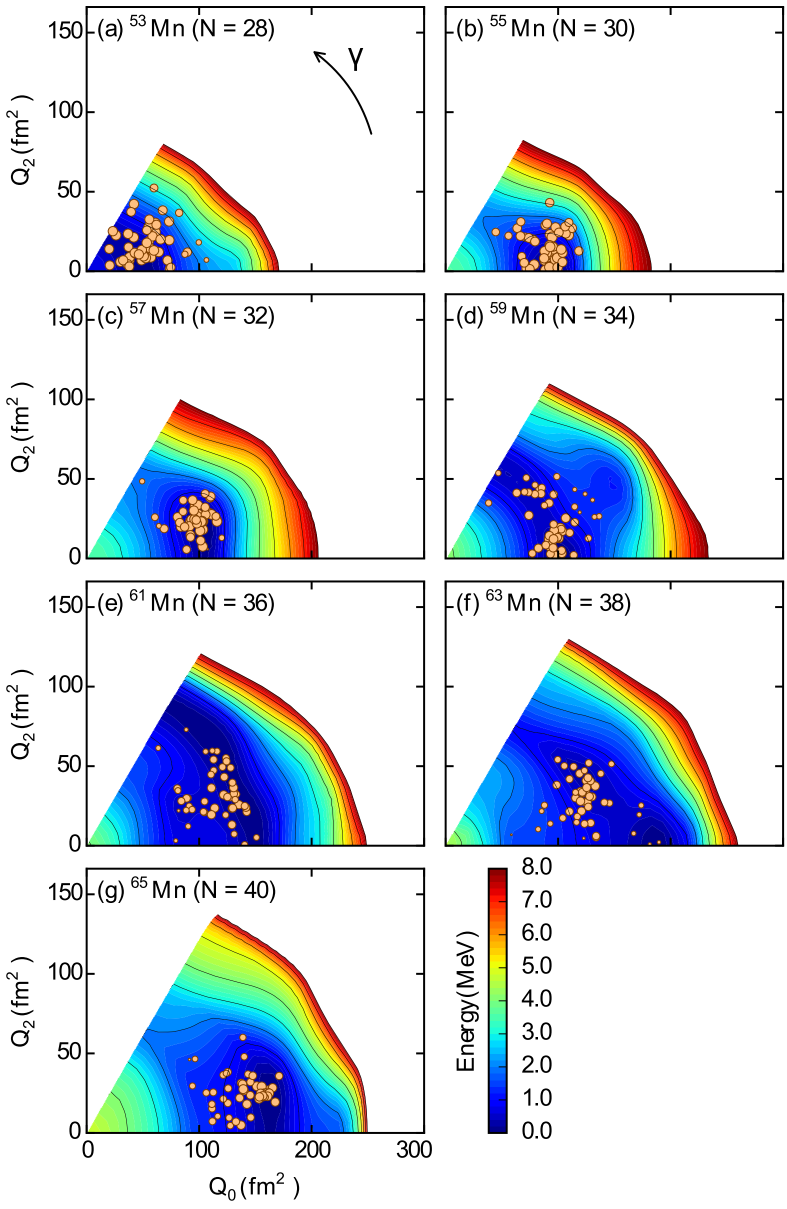

FIG. 7. (Color online) Potential energy surfaces of odd-even $^{53-63}$Mn isotopes including the distribution of the MCSM basis states, depicted by the circles. The locations of the circles indicate the intrinsic shapes of the MCSM basis states and the sizes denote their importance in the total wave function, see reference [42] for more information. The energy scale is relative to the minimum of each potential energy surface, and the contour plots are shown up to a cut-off energy of 8 MeV.

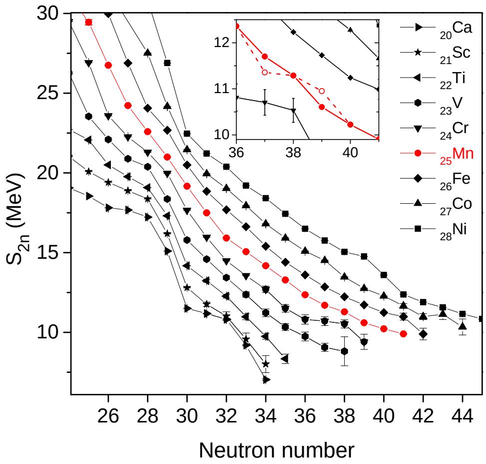

FIG. 8. (Color online) Two-neutron separation energies plotted from $_{20}$Ca to $_{28}$Ni. Data taken from the AME2012 atomic-mass evaluation [45] complemented with data from [10, 46]. The ^{62}Mn binding energy is recalculated with the tentative Coulomb excitation information [47] which influences the S_{2n} at ^{62}Mn and ^{64}Mn. The inset shows the difference between the recalculated values (full line) and the original publication [46] (dashed line).

unexpected, since the charge radii and binding energies reflect different aspects of the nuclear wave function. In the context of shape coexistence for example, it becomes clear that states with very different quantum-mechanical structure can be almost degenerate in energy, thus a huge effect in nuclear size can be accompanied by a small change in nuclear binding. In particular, for the Mn isotopes the $Z \approx N \approx 25$ (also known as the Wigner effect [50]) plays an important role in modifying the trend of the two-neutron separation energies close to $N = 28$. Furthermore, a change of ground-state structure when crossing $N = 28$ might also bring an additional energy contribution to the trend close to the semi-magic ^{53}Mn$_{28}$. Indeed, the spin changes from $5/2^-$ to $7/2^-$ and back to $5/2^-$ in ^{51,53,55}Mn, along with a significant increase of their quadrupole moments going from $Q_s(^{53}\text{Mn})=+0.16(3)$ fm^2 at the shell closure to $Q_s = +0.42(7)$ fm^2 and $Q_s = +0.33(1)$ fm^2 in ^{51,55}Mn, respectively [19, 22].
Precise mass measurements of the neutron-rich Mn were presented by Naimi *et al.* [46] noting that it was unclear whether the observed 4^+ state in ^{62}Mn was the ground or isomeric state, with a tentative assignment to the isomer. In the mean time, a Coulomb excitation experiment has been performed in which the 4^+ state was proposed to lie 346 keV above the 1^+ ground state [47]. With this new information, the ground state two-neutron separation energies can be recalculated, as shown in Fig. 8. The inset highlights the difference between the original (dashed line) and recalculated (solid line) values. While in the original publication a sudden increase in two-neutron separation energies at $N = 38$ was observed using the measured ^{62}Mn mass, this effect is washed out using the recalculated ground state mass. Instead, the two-neutron separation energies gradually curve up towards $N = 40$, which would rather be linked to a gradual onset of collectivity [51]. So although the onset of deformation seems to occur suddenly at $N = 36$ in the charge radii, this is accompanied by a smooth change of the ground state binding energies.
Similar to Mn, a smooth upwards curvature is also seen in the $_{26}$Fe isotopic chain while an abrupt discontinuity at $N = 36$ is observed in the AME2012 evaluation of $_{24}$Cr isotopes. However, new measurements show a much smoother behavior [52] although the reported errors are relatively large. High-precision mass measurements are required to clarify the issue. To complete the picture, mean-square charge radii measurements for the Cr and Fe isotopes would be highly desirable.

C. Duflo-Zuker analysis

To conclude the discussion, the changes in mean-square charge radii of the Mn isotopes are compared to theoretical calculations using the Duflo-Zuker [53] formalism, shown in Fig. 9. It is based on the fact that radii are single particle operators that depend on orbital occupancies and their sizes. A recent study [54] has shown that it accounts for shell effects due to anomalously large orbits ($s_{1/2}$, $p_{3/2}$ and $p_{1/2}$ in the neutron sd and pf shells, re-

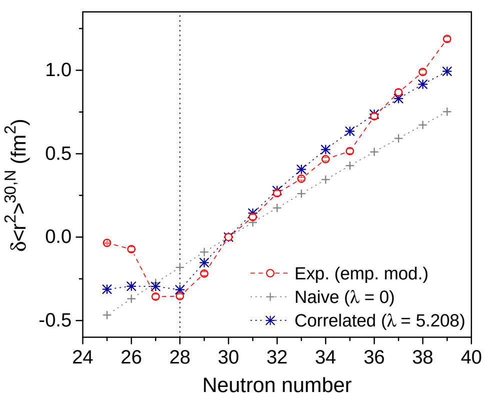

FIG. 9. (Color online) Empirically modified changes in mean-square charge radii of Mn compared to the naive (eq. 3a) and correlated (eq. 3a+3b) predictions using the Duflo-Zuker expression.

spectively), and leads to the first successful reproduction of the experimental changes in root mean-square charge radii in K and Ca.
The Duflo-Zuker expression consists of two terms

$$\sqrt{\langle r_\pi^2 \rangle} = A^{1/3}\left[\rho_0 - \frac{\zeta}{2}\frac{t}{A^{4/3}} - \frac{\upsilon}{2}\left(\frac{t}{A}\right)^2\right] e^{(g/A)} \quad \text{(3a)}$$

$$+ \frac{\lambda}{A^{1/3}}\left[\frac{z(D_\pi - z)}{D_\pi^2}\frac{n(D_\nu - n)}{D_\nu^2}\right] \quad \text{(3b)}$$

where $t = N - Z$. Considering the terms 3a and 3b separately, the first term (eq. 3a) is derived by noting that r_π is an isospin vector. Therefore, its square contains a scalar, a vector and a tensor, associated with coefficients ρ_0, ζ and υ, respectively. The expression for neutrons, is obtained by reversing the sign of t, so the difference in neutron and proton charge radius, the neutron skin, is given by

$$\Delta r_{\nu\pi} = \sqrt{\langle r_\nu^2 \rangle} - \sqrt{\langle r_\pi^2 \rangle} = \frac{\zeta t e^{g/A}}{A}. \quad (4)$$

Here $e^{g/A}$ is a phenomenological correction factor which accounts for the larger radii in light nuclei. By a four-parameter fit to the known radii of isotopes with $A \leq 60$, $g = 1.37$, $\rho_0 = 0.947$ fm, $\upsilon = 0.295$ fm and $\zeta = 0.8$ fm are found giving a rms deviation of 0.04 fm. Using this first term as a naive approach which only depends on t and A, a smooth variation of the charge radii is obtained as shown in Fig. 9. The necessary shell effects are introduced by adding a second term (eq. 3b) which depends on the orbital occupancies of the extruder-intruder (EI) valence spaces, delimited by N, $Z = 6, 14, 28, 50, \ldots$ [55, Sec. IC]. The degeneracy of each valence shell is then given by $D_{\pi,\nu} = 8, 14, 22, \ldots$ and the number of active particles is indicated by n, z. For the Mn isotopes this becomes: $z = 11$ and $D_\pi = 14$ for the protons and $n = N - 14$, $D_\nu = 14$ for $N \leq 28$ or $n = N - 28$ and $D_\nu = 22$ for $N > 28$. Note that this second term becomes zero at the extruder-intruder shell closures.
Once the second term (eq. 3b) is included in the fit, slightly adapted fit parameters ($g = 1.14$, $\rho_0 = 0.94$ fm, $\upsilon = 0.334$ fm, $\zeta = 0.8$ fm and λ=5.208) are extracted and a good reproduction of the charge radii below $Z = 30$ is obtained. This reduces the rms deviation is to 0.02 fm.
The changes in mean-square charge radii obtained using the full Duflo-Zuker expression applied to the Mn isotopic chain (blue stars) are compared to the experimental values (red circles) in Fig. 9. Between $N = 28$ and $N = 37$, the agreement is particularly good and similar to K and Ca, the strong increase in charge radii beyond $N = 28$ is suggested to be associated with the large size of the (halo) neutron $p_{3/2}$ orbital [54]. Due to isovector polarizability [54], an increase of neutron radii causes larger charge (proton) radii as well. Nevertheless, above $N = 37$ and below $N = 28$ there are clear deviations between theory and experiment. This indicates that the large deformations, shown to be important for the Mn isotopes in this and previous work [19–22], are not fully taken into account in eq. 3. Since in the K and Ca isotopes no similar large onset of deformation below $N = 28$ is observed, the mean-square charge radii are well reproduced [54].

V. CONCLUSION

The $^{51,53-64}$Mn isotopes have been studied in two collinear laser spectroscopy experiments at the COLLAPS beam line at ISOLDE, CERN. In this article, the isotope shifts and extracted mean-square charge radii were presented.
The electronic mass shift and field shift factors for the atomic $3d^54s^2\ ^6S_{5/2} \rightarrow 3d^54s4p\ ^6P_{3/2}$ and the ionic $3d^54s\ ^5S_2 \rightarrow 3d^54p\ ^5P_3$ transitions have been calculated in the multi-configurational Dirac-Fock framework. Because of the open $3d$ electron shell, these calculations are particularly complex and relatively large uncertainties on M and F are assumed. Alternatively, results are also presented in which M is increased by 5% in order to obtain a better agreement with the regional trend. Whether or not this modification is warranted will only become clear when more independently determined charge radii information in the region becomes available. It needs to be stressed once more that although the empirical modification causes a global tilt about the reference point, it does not affect the local irregularities in the charge radii. Since these local irregularities reveal the nuclear structure phenomena we are interested in, the physics discussion remains valid irrespective of the final choice of F and M (within the presented uncertainty).
The nuclear structure along the Mn isotopic chain is discussed based on the available ground state properties. A clear connection between the moments and charge radii is observed, pointing to a good $N = 28$ shell closure and a rapid onset of deformation towards $N = 40$. The variation of the two-neutron separation energies on the other hand is rather smooth showing that these effects do not necessarily lead to discontinuities in the mass surface.
Furthermore, the evolution of the intrinsic shapes in the Mn isotopic chain was investigated in the Monte Carlo Shell Model framework using the modified A3DA effective interaction. This suggests that the increase in charge radii from $N = 35$ is not only due to a static increase in prolate deformation, but that also triaxiality and shape fluctuations are important.
Finally, the changes in mean-square charge radii were discussed using the Duflo-Zuker model. The sharp increase in charge radii beyond $N = 28$, common to all isotopes studied in the region so far, has been related to the occupancy of the neutron (halo) orbitals. However, below $N = 28$ and above $N = 37$ the experimental values depart from the theoretical predictions, which is explained as due to deformation.

ACKNOWLEDGEMENTS

We would like to thank the ISOLDE technical group for their support and assistance. H. H. thanks V. Manea for the interesting discussions and the insightful suggestions related to the separation energies.
This work was supported by the Belgian Research Initiative on Exotic Nuclei (IAP-project P7/12), the FWO-Vlaanderen, GOA grant 10/010 and 10/015 from KU Leuven, the German Ministry for Education and Research (BMBF) under contract 05P15RDICA and 05P15SJCIA, the Max-Planck Society, the Science and Technology Facilities Council. This project has received funding through the European Union's Seventh Framework Programme for Research and Technological Development under Grant Agreements: 262010 (ENSAR), 267194 (COFUND), and 289191 (LA^{3}NET).

[1] P. Campbell, I. D. Moore, and M. R. Pearson, Prog. Part. Nucl. Phys. **86**, 127 (2016).
[2] G. Neyens, Rep. Progr. Phys. **66**, 633 (2003).
[3] K. Blaum, J. Dilling, and W. Nörtershäuser, Phys. Scr. **T152**, 014017 (2013).
[4] F. Touchard, P. Guimbal, S. Büttgenbach, R. Klapisch, M. D. S. Simon, J. Serre, C. Thibault, H. Duong, P. Juncar, S. Liberman, J. Pinard, and J. Vialle, Phys. Lett. B **108**, 169 (1982).
[5] C. W. P. Palmer, P. E. G. Baird, S. A. Blundell, J. R. Brandenberger, C. J. Foot, D. N. Stacey, and G. K. Woodgate, Journal of Physics B: Atomic and Molecular Physics **17**, 2197 (1984).
[6] K. Blaum, W. Geithner, J. Lassen, P. Lievens, K. Marinova, and R. Neugart, Nucl. Phys. A **799**, 30 (2008).
[7] M. Avgoulea, Y. P. Gangrsky, K. P. Marinova, S. G. Zemlyanoi, S. Fritzsche, D. Iablonskyi, C. Barbieri, E. C. Simpson, P. D. Stevenson, J. Billowes, P. Campbell, B. Cheal, B. Tordoff, M. L. Bissell, D. H. Forest, M. D. Gardner, G. Tungate, J. Huikari, A. Nieminen, H. Penttilä, and J. Äystö, J. Phys. G **38**, 025104 (2011).
[8] A. Huck, G. Klotz, A. Knipper, C. Miehé, C. Richard-Serre, G. Walter, A. Poves, H. L. Ravn, and G. Marguier, Phys. Rev. C **31**, 2226 (1985).
[9] D. Steppenbeck, S. Takeuchi, N. Aoi, P. Doornenbal, M. Matsushita, H. Wang, H. Baba, N. Fukuda, S. Go, M. Honma, J. Lee, K. Matsui, S. Michimasa, T. Motobayashi, D. Nishimura, T. Otsuka, H. Sakurai, Y. Shiga, P.-A. Soderstrom, T. Sumikama, H. Suzuki, R. Taniuchi, Y. Utsuno, J. J. Valiente-Dobon, and K. Yoneda, Nature **502**, 207 (2013).
[10] F. Wienholtz, D. Beck, K. Blaum, C. Borgmann, M. Breitenfeldt, R. B. Cakirli, S. George, F. Herfurth, J. D. Holt, M. Kowalska, S. Kreim, D. Lunney, V. Manea, J. Menéndez, D. Neidherr, M. Rosenbusch, L. Schweikhard, A. Schwenk, J. Simonis, J. Stanja, R. N. Wolf, and K. Zuber, Nature **498**, 346 (2013).
[11] R. F. Garcia Ruiz, M. L. Bissell, K. Blaum, N. Frömmgen, M. Hammen, J. D. Holt, M. Kowalska, K. Kreim, J. Menéndez, R. Neugart, G. Neyens, W. Nörtershäuser, F. Nowacki, J. Papuga, A. Poves, A. Schwenk, J. Simonis, and D. T. Yordanov, Phys. Rev. C **91**, 041304 (2015).
[12] R. F. Garcia Ruiz, M. L. Bissell, K. Blaum, A. Ekstrom, N. Frommgen, G. Hagen, M. Hammen, K. Hebeler, J. D. Holt, G. R. Jansen, M. Kowalska, K. Kreim, W. Nazarewicz, R. Neugart, G. Neyens, W. Nortershauser, T. Papenbrock, J. Papuga, A. Schwenk, J. Simonis, K. A. Wendt, and D. T. Yordanov, Nature Physics **12**, 594 (2016).
[13] J. Ljungvall, A. Görgen, A. Obertelli, W. Korten, E. Clément, G. de France, A. Bürger, J.-P. Delaroche, A. Dewald, A. Gadea, L. Gaudefroy, M. Girod, M. Hackstein, J. Libert, D. Mengoni, F. Nowacki, T. Pissulla, A. Poves, F. Recchia, M. Rejmund, W. Rother, E. Sahin, C. Schmitt, A. Shrivastava, K. Sieja, J. J. Valiente-Dobón, K. O. Zell, and M. Zielińska, Phys. Rev. C **81**, 061301 (2010).
[14] S. M. Lenzi, F. Nowacki, A. Poves, and K. Sieja, Phys. Rev. C **82**, 054301 (2010).
[15] Y. Utsuno, T. Otsuka, T. Glasmacher, T. Mizusaki, and M. Honma, Phys. Rev. C **70**, 044307 (2004).
[16] P. Himpe, G. Neyens, D. L. Balabanski, G. Bélier, J. M. Daugas, F. de Oliveira Santos, M. De Rydt, K. T. Flanagan, I. Matea, P. Morel, Y. E. Penionzhkevich, L. Perrot, N. A. Smirnova, C. Stodel, J. C. Thomas, N. Vermeulen, D. T. Yordanov, Y. Utsuno, and T. Otsuka, Phys. Lett. B **658**, 203 (2008).
[17] G. Neyens, Phys. Rev. C **84**, 064310 (2011).
[18] D. T. Yordanov, M. L. Bissell, K. Blaum, M. De Rydt, C. Geppert, M. Kowalska, J. Krämer, K. Kreim, A. Krieger, P. Lievens, T. Neff, R. Neugart, G. Neyens, W. Nörtershäuser, R. Sánchez, and P. Vingerhoets, Phys. Rev. Lett. **108**, 042504 (2012).
[19] F. C. Charlwood, J. Billowes, P. Campbell, B. Cheal, T. Eronen, D. Forest, S. Fritzsche, M. Honma, A. Jokinen, I. D. Moore, H. Penttilä, R. Powis, A. Saastamoinen, G. Tungate, and J. Aystö, Phys. Lett. B **690**, 346 (2010).
[20] C. Babcock, H. Heylen, J. Billowes, M. L. Bissell, K. Blaum, P. Campbell, B. Cheal, R. F. Garcia Ruiz, C. Geppert, W. Gins, M. Kowalska, K. Kreim, S. M. Lenzi, I. D. Moore, R. Neugart, G. Neyens, W. Nörtershäuser, J. Papuga, and D. T. Yordanov, Phys. Lett. B **750**, 176 (2015).
[21] H. Heylen, C. Babcock, J. Billowes, M. L. Bissell, K. Blaum, P. Campbell, B. Cheal, R. F. Garcia Ruiz, C. Geppert, W. Gins, M. Kowalska, K. Kreim, S. M. Lenzi, I. D. Moore, R. Neugart, G. Neyens, W. Nörtershäuser, J. Papuga, and D. T. Yordanov, Phys. Rev. C **92**, 044311 (2015).
[22] C. Babcock, H. Heylen, M. Bissell, K. Blaum, P. Campbell, B. Cheal, D. Fedorov, R. Garcia Ruiz, W. Geithner, W. Gins, T. Goodacre, L. Grob, M. Kowalska, S. Lenzi, B. Maass, S. Malbrunot-Ettenauer, B. Marsh, R. Neugart, G. Neyens, W. Nörtershäuser, T. Otsuka, R. Rossel, S. Rothe, R. Sánchez, Y. Tsunoda, C. Wraith, L. Xie, and X. F. Yang, Physics Letters B **760**, 387 (2016).

[23] K. Kreim, M. L. Bissell, J. Papuga, K. Blaum, M. De Rydt, R. G. Ruiz, S. Goriely, H. Heylen, M. Kowalska, R. Neugart, G. Neyens, W. Nörtershäuser, M. Rajabali, R. S. Alarcón, H. H. Stroke, and D. T. Yordanov, Phys. Lett. B **731**, 97 (2014).

[24] S. Rothe, T. D. Goodacre, D. Fedorov, V. Fedosseev, B. Marsh, P. Molkanov, R. Rossel, M. Seliverstov, M. Veinhard, and K. Wendt, Nuclear Instruments and Methods in Physics Research Section B: Beam Interactions with Materials and Atoms **376**, 91 (2016), proceedings of the {XVIIth} International Conference on Electromagnetic Isotope Separators and Related Topics (EMIS2015), Grand Rapids, MI, U.S.A., 11-15 May 2015.

[25] E. Mané, J. Billowes, K. Blaum, P. Campbell, B. Cheal, P. Delahaye, K. Flanagan, D. Forest, H. Franberg, C. Geppert, T. Giles, A. Jokinen, M. Kowalska, R. Neugart, G. Neyens, W. Nörtershäuser, I. Podadera, G. Tungate, P. Vingerhoets, and D. T. Yordanov, EPJ A **42**, 503 (2009).

[26] A. Mueller, F. Buchinger, W. Klempt, E. Otten, R. Neugart, C. Ekström, and J. Heinemeier, Nucl. Phys. A **403**, 234 (1983).

[27] W. Nörtershäuser, Hyperfine Interact. **198**, 73 (2010).

[28] J. Papuga, M. L. Bissell, K. Kreim, C. Barbieri, K. Blaum, M. De Rydt, T. Duguet, R. F. Garcia Ruiz, H. Heylen, M. Kowalska, R. Neugart, G. Neyens, W. Nörtershäuser, M. M. Rajabali, R. Sánchez, N. Smirnova, V. Somà, and D. T. Yordanov, Phys. Rev. C **90**, 034321 (2014).

[29] B. Cheal, T. E. Cocolios, and S. Fritzsche, Phys. Rev. A **86**, 042501 (2012).

[30] P. Jönsson, G. Gaigalas, J. Bieroń, C. F. Fischer, and I. Grant, Computer Physics Communications **184**, 2197 (2013).

[31] S. Fritzsche, C. Fischer, and G. Gaigalas, Computer Physics Communications **148**, 103 (2002).

[32] C. Nazé, E. Gaidamauskas, G. Gaigalas, M. Godefroid, and P. Jönsson, Computer Physics Communications **184**, 2187 (2013).

[33] S. Fritzsche, Computer Physics Communications **183**, 1525 (2012).

[34] W. King, *Isotope shifts in atomic spectra* (Plenum, New York, 1984).

[35] K. Marinova, W. Geithner, M. Kowalska, K. Blaum, S. Kappertz, M. Keim, S. Kloos, G. Kotrotsios, P. Lievens, R. Neugart, H. Simon, and S. Wilbert, Phys. Rev. C **84**, 034313 (2011).

[36] G. Fricke and K. Heilig, *Nuclear Charge Radii* (Springer Berlin Heidelberg, 2004).

[37] Y. P. Gangrsky, K. P. Marinova, S. G. Zemlyanoi, I. D. Moore, J. Billowes, P. Campbell, K. T. Flanagan, D. H. Forest, J. A. R. Griffith, J. Huikari, R. Moore, A. Nieminen, H. Thayer, G. Tungate, and J. Äystö, J. Phys. G: Nuclear and Particle Physics **30**, 1089 (2004).

[38] D. M. Benton, E. C. A. Cochrane, and J. A. R. Griffith, Journal of Physics B: Atomic, Molecular and Optical Physics **30**, 5359 (1997).

[39] A. Steudel, U. Triebe, and D. Wendlandt, Z. Phys. A **296**, 189 (1980).

[40] M. L. Bissell, T. Carette, K. T. Flanagan, P. Vingerhoets, J. Billowes, K. Blaum, B. Cheal, S. Fritzsche, M. Godefroid, M. Kowalska, J. Krämer, R. Neugart, G. Neyens, W. Nörtershäuser, and D. T. Yordanov, Phys. Rev. C **93**, 064318 (2016).

[41] M. L. Bissell, J. Papuga, H. Naïdja, K. Kreim, K. Blaum, M. De Rydt, R. F. Garcia Ruiz, H. Heylen, M. Kowalska, R. Neugart, G. Neyens, W. Nörtershäuser, F. Nowacki, M. M. Rajabali, R. Sanchez, K. Sieja, and D. T. Yordanov, Phys. Rev. Lett. **113**, 052502 (2014).

[42] Y. Tsunoda, T. Otsuka, N. Shimizu, M. Honma, and Y. Utsuno, Phys. Rev. C **89**, 031301 (2014).

[43] N. Shimizu, T. Abe, Y. Tsunoda, Y. Utsuno, T. Yoshida, T. Mizusaki, M. Honma, and T. Otsuka, Progress of Theoretical and Experimental Physics **2012**, 01A205 (2012).

[44] K. Sato, N. Hinohara, K. Yoshida, T. Nakatsukasa, M. Matsuo, and K. Matsuyanagi, Phys. Rev. C **86**, 024316 (2012).

[45] M. Wang, G. Audi, A. Wapstra, F. Kondev, M. MacCormick, X. Xu, and B. Pfeiffer, Chin. Phys. C **36**, 1603 (2012).

[46] S. Naimi, G. Audi, D. Beck, K. Blaum, C. Böhm, C. Borgmann, M. Breitenfeldt, S. George, F. Herfurth, A. Herlert, A. Kellerbauer, M. Kowalska, D. Lunney, E. Minaya Ramirez, D. Neidherr, M. Rosenbusch, L. Schweikhard, R. N. Wolf, and K. Zuber, Phys. Rev. C **86**, 014325 (2012).

[47] L. P. Gaffney, J. Walle, B. Bastin, V. Bildstein, A. Blazhev, N. Bree, J. Cederkäll, I. Darby, H. Witte, D. DiJulio, J. Diriken, V. N. Fedosseev, C. Fransen, R. Gernhäuser, A. Gustafsson, H. Hess, M. Huyse, N. Kesteloot, T. Kröll, R. Lutter, B. A. Marsh, P. Reiter, M. Seidlitz, P. Duppen, D. Voulot, N. Warr, F. Wenander, K. Wimmer, and K. Wrzosek-Lipska, EPJ A **51**, 1 (2015).

[48] F. C. Charlwood, K. Baczynska, J. Billowes, P. Campbell, B. Cheal, T. Eronen, D. H. Forest, A. Jokinen, T. Kessler, I. D. Moore, H. Penttilä, R. Powis, M. Rffer, A. Saastamoinen, G. Tungate, and J. Äystö, Phys. Lett. B **674**, 23 (2009).

[49] R. B. Cakirli, R. F. Casten, and K. Blaum, Phys. Rev. C **82**, 061306 (2010).

[50] P. Van Isacker, D. D. Warner, and D. S. Brenner, Phys. Rev. Lett. **74**, 4607 (1995).

[51] R. Fossion, C. D. Coster, J. García-Ramos, T. Werner, and K. Heyde, Nucl. Phys. A **697**, 703 (2002).

[52] Z. Meisel, S. George, S. Ahn, D. Bazin, B. A. Brown, J. Browne, J. F. Carpino, H. Chung, R. H. Cyburt, A. Estradé, M. Famiano, A. Gade, C. Langer, M. Matoš, W. Mittig, F. Montes, D. J. Morrissey, J. Pereira, H. Schatz, J. Schatz, M. Scott, D. Shapira, K. Sieja, K. Smith, J. Stevens, W. Tan, O. Tarasov, S. Towers, K. Wimmer, J. R. Winkelbauer, J. Yurkon, and R. G. T. Zegers, Phys. Rev. C **93**, 035805 (2016).

[53] J. Duflo and A. P. Zuker, Phys. Rev. C **66**, 051304 (2002).

[54] J. Bonnard, S. M. Lenzi, and A. P. Zuker, Phys. Rev. Lett. **116**, 212501 (2016).

[55] E. Caurier, G. Martínez-Pinedo, F. Nowacki, A. Poves, and A. P. Zuker, Rev. Mod. Phys. **77**, 427 (2005).

7 Conclusion

Unraveling the structure of exotic nuclei is one of the major challenges in nuclear physics research. In particular, considerable effort is dedicated to identifying the driving mechanisms behind the rapid structural changes observed in these exotic regions of the nuclear chart.
A prototypical example of such rapid structural change can be found in the island of inversion around $N = 20$. While the $N = 20$ shell gap prevents the development of collective effects near the valley of stability, at exotic proton-to-neutron ratios, the energy cost of exciting neutrons across $N = 20$ can be compensated by the large gain in energy associated with proton-neutron correlations, and quadrupole deformation can develop. This same delicate balance between stabilising shell gaps and quadrupole collectivity also dictates the observed nuclear dynamics in the island of inversion around $N = 40$.
The goal of this thesis was to explore the nuclear structure in these islands of inversion via the measurements of nuclear spins, magnetic dipole moments, electric quadrupole moments and changes in the mean-square charge radii.

Results

At the border of the island of inversion around $N = 20$, the transitional character of the neutron-rich Al ($Z = 13$) isotopes was investigated. Via a high-precision quadrupole moment measurement of ^{33}Al, a significant amount of intruder configurations in its ground state wave function could be established. This settles the long-standing issue about its intruder nature. Maybe more importantly, isotopes such as ^{33}Al, on the edge between normal and intruder states, provide the most sensitive tests for state-of-the-art models as their predictions depend critically on the parametrisation of the shell gaps and correlations. For example, while the SDPF-U-MIX interaction (the most recent interaction developed for this region) generally gives a good description of the properties in and near the island of inversion, it cannot reproduce the observed

rise in quadrupole moment of ^{33}Al.
Furthermore, the g-factor and electric quadrupole moment of the 1^+ state in ^{34}Al provide a unique opportunity to study the potential increase in deformation due to its proposed 1p-1h intruder nature. Experimentally, these measurements are however very challenging. Analysis of the data is still ongoing and no firm conclusions can be drawn yet. Preliminary results from the online analysis point to a significant increase in quadrupole moment of the 1^+ state in ^{34}Al, as compared to that of the normal 1^+ ground state in ^{32}Al. A more detailed analysis will be performed in the next months.

In the region below $^{68}_{28}$Ni$_{40}$, the nuclear structure of the Mn ($Z = 25$) isotopes between $N = 26$ and $N = 39$ is studied.
The previously tentatively assigned ground state spins in ^{61,63}Mn, ^{58,60,62,64}Mn and isomeric state spins in ^{58,60,62}Mn are firmly established to be $I = 5/2$, $I = 1$ and $I = 4$, respectively. Furthermore, the experimental magnetic dipole moments and electric quadrupole moments have been compared to shell model calculations using different interactions and model spaces. Only when neutron excitations across $N = 40$ are allowed, can the observed values be reproduced. From an analysis of the calculated wave functions, the increasing significance of neutron excitations across $N = 40$ and proton excitations across $Z = 28$ towards $N = 40$ is shown. Special attention is given to the important role of the $\nu d_{5/2}$ orbital, in combination with the $\nu g_{9/2}$ orbital, for the development of quadrupole collectivity. The onset of this quadrupole collectivity is also manifested in the changes in mean-square charge radii which show a clear increase from $N = 36$ onwards. Hence, from the nuclear moments and charge radii a consistent picture of the Mn structure emerges. These results provide a benchmark for future studies on the neutron-rich nuclei between $Z = 20$ and $Z = 28$ for which currently the ground state property information is scarce.

Comparison between collinear laser spectroscopy and β-NMR

In this thesis, two different experimental techniques were employed at two different radioactive beam facilities.
The ground state properties of Mn were determined via bunched-beam, fluorescence detected collinear laser spectroscopy at ISOLDE. Collinear laser spectroscopy is a versatile technique which allows the extraction of four observables (spins, magnetic dipole moments, electric quadrupole moments and changes mean-square charge radii) from a single hyperfine spectrum. It is particularly suitable for systematic studies along an isotopic chain as it can be used for stable species as well as isotopes with half-lives down to a

few ms[1]. Although there are limitations on which transitions are suitable for laser spectroscopy, for example because some wavelengths are not efficiently produced by narrowband lasers or because particular electronic transitions are not sensitive to all nuclear observables, the development of methods like optical pumping into a metastable ionic state in a cooler/buncher helps to overcome these limitations. Additionally, the inherent inefficiency of fluorescence detection hinders the measurement of the most exotic cases where the yields are very low (typically less than a few 1000 ions/s). However, the use of resonance ionization spectroscopy in a collinear geometry (CRIS) has recently been proven to be very promising, showing a high sensitivity in combination with a high resolution. Finally, the range of isotopes which can be studied with collinear laser spectroscopy at ISOLDE is limited by the chemistry-dependent production process. In this context, a considerable effort is dedicated to the development of methods to slow down and cool radioactive beams at in-flight facilities, in order to produce low-energy, low-emittance beams suitable for high-precision laser spectroscopy.

In-flight beams are now already regularly used for nuclear moment measurements of isotopes or isomers inaccessible with laser spectroscopy at ISOL-facilities. In this thesis, the magnetic and quadrupole moments of the very neutron-rich Al isotopes were measured via continuous-beam β-NMR/NQR at the LISE3 fragment separator at GANIL. Although the increased sensitivity of β-detection and universality of (spin-polarized) beam production at in-flight facilities are a big advantage, there are also many disadvantages compared to collinear laser spectroscopy. First of all, less information can be extracted for more effort. From a measured spectrum only the g-factor or the electric quadrupole moment can be obtained, depending on the used crystal. Furthermore, these spectra only yield the absolute value of g and Q_s, not the sign, nor any direct information on the spin or the mean-square charge radius. Additionally, the maximal half-lives of the isotopes which can be studied is limited due to spin-lattice relaxation effects (typically up to a few seconds). From a technical point of view, finding a suitable implantation crystal is in general less straightforward than finding a suitable laser transition. Nevertheless, in particular cases β-NMR/NQR offers the only possibility to study the structure of interesting isotopes which would otherwise be out of reach.

Outlook

The results on the neutron-rich Al and Mn isotopes obtained in this work provide valuable information on the nuclear structure in the islands of inversion

[1] In practice, the lower limit on the half-life is set by the release from the ISOL-target. In the specific case of bunched-beam collinear laser spectroscopy, also the accumulation time in the cooler/buncher needs to be taken into account.

around $N = 20$ and $N = 40$. Nevertheless, there are still many open questions and interesting physics cases which deserve a closer investigation in the future. A few examples are discussed below[2].

A clear piece of missing information in the Al isotopic chain is the electric quadrupole moment of the 4^- ground state in ^{34}Al. While a β-NQR experiment in GANIL would in principle be feasible[3], this experiment would suffer from the same challenges as those encountered in the ^{34m}Al case. Additional complications arise due to the uncertainty on the predicted quadrupole moment, which means that a large range of frequencies needs to be scanned. With the observed count rates, this would take very long such that at the moment, the experiment is deemed to be extremely difficult in practice.
Also the determination of the Al mean-square charge radii would provide interesting complementary information on the transition into the island of inversion. This summer, a COLLAPS experiment has shown that fluorescence detected collinear laser spectroscopy at ISOLDE can be performed up to $^{32}Al_{19}$. In order to go more neutron-rich, to the isotopes in which intruder configurations become important, a more sensitive technique such as CRIS would be required. However, since the field shift contribution to the total isotope shift is calculated to be small in aluminium, the uncertainty on the extracted isotope shifts would need to be around 1 MHz or less. Although this level of precision is envisioned for future experiments at CRIS, it has not yet been demonstrated experimentally.
After 40 years of research in the island of inversion around $N = 20$, a wide range of experimental data exist. The current ambition should therefore be to achieve a consistent theoretical description of all this available data, and in particular, if discrepancies show up such as in the calculations of the quadrupole moment of ^{33}Al, to understand where these discrepancies come from and what can be learned from them.

The Mn data measured in this work end at $N = 39$, but with the experimental efficiencies obtained in the second experiment on the ionic transition, it could realistically be expected to go one isotope more neutron-rich, up to $N = 40$. Although this would nicely complete the systematics between $N = 28$ and $N = 40$, the physics case seems to be answered with the current data and little new insight is expected to be gained with one new isotope. Similarly, the quadrupole moments of the odd-odd Mn isotopes are not a high priority due to the limited new information they are expected to bring.
On the other hand, there is still much work to do on the isotopic chains close to Mn. It would be very interesting to extend the information on the mean-square

[2] Although these examples focus on the nuclear moments and mean-square charge radii, a more complete picture also requires other observables such as level schemes, transition probabilities, spectroscopic factors etc.

[3] The lack of success of a previous attempt is at least partly explained by the lower efficiency of the used β-NQR set-up at that time.

charge radii in the region. In that respect, Cr seems to be a very promising case for a laser spectroscopy experiment at ISOLDE, since a significant enhancement in yield is achieved as a result of the recent development of an ionization scheme by RILIS. With the observed yields, measurements up to $N = 37$ should be possible, extending into the region where the effects of the onset of deformation are expected to be visible.

Furthermore, a detailed study of the (ground state properties of the) Co-isotopes would also be very useful. With one proton outside of the closed $Z = 28$ core, their structure is supposed to be relatively simple, facilitating an interpretation in the shell model framework. As such they are very suitable to investigate how the single-particle structure and collectivity evolves towards $N = 40$. However, these measurements are not foreseen in the near-future due to the technical challenges related to do them. Indeed, laser spectroscopic studies at ISOLDE are not straightforward due to the refractory nature of Co and a first attempt to measure the nuclear moments of $^{64-67}$Co via β-NMR at GANIL was unfortunately not successful.

A Appendix

A.1 Experimental asymmetry

The experimental asymmetry is defined as the difference between the asymmetry on and off resonance

$$\mathcal{A}_{\text{exp}} = \mathcal{A}_{\text{on}} - \mathcal{A}_{\text{off}}. \tag{A.1}$$

Including the β's originating from ^{34m}Al, ^{34g}Al and the daughters (d), this becomes

$$\mathcal{A}_{\text{exp}} = \frac{\left(N^{34m}_{\text{up,on}} + N^{34g}_{\text{up,on}} + N^{d}_{\text{up,on}}\right) - \left(N^{34m}_{\text{do,on}} + N^{34g}_{\text{do,on}} + N^{d}_{\text{do,on}}\right)}{N^{34m}_{\text{tot,on}} + N^{34g}_{\text{tot,on}} + N^{d}_{\text{tot,on}}}$$
$$- \frac{\left(N^{34m}_{\text{up,off}} + N^{34g}_{\text{up,off}} + N^{d}_{\text{up,off}}\right) - \left(N^{34m}_{\text{do,off}} + N^{34g}_{\text{do,off}} + N^{d}_{\text{do,off}}\right)}{N^{34m}_{\text{tot,off}} + N^{34g}_{\text{tot,off}} + N^{d}_{\text{tot,off}}}. \tag{A.2}$$

where $N_{\text{up}} + N_{\text{do}} = N_{\text{tot}}$. To roughly estimate the effect of the β-decay of the ^{34g}Al isotopes and the daughters on the measured asymmetry, a few assumptions and approximations are made:

- No asymmetry is present in the set-up such that on resonance $N^{34m}_{\text{up,on}} - N^{34m}_{\text{down,on}} = 0$.
- The total number of isomeric decays doesn't change between on resonance and off resonance $N^{34m}_{\text{tot}} = N^{34m}_{\text{up,on}} + N^{34m}_{\text{do,on}} = N^{34m}_{\text{up,off}} + N^{34m}_{\text{do,off}}$.
- The β-decay from the daughters as well as from the ground state is not changed between on resonance and off resonance ($N_{\text{on}} - N_{\text{off}} = 0$). The total background decay, the sum of the daughter and the ground state decay, is therefore unchanged as well $N^{bg}_{\text{tot}} = N^{bg}_{\text{up}} + N^{bg}_{\text{do}} = N^{d}_{\text{tot}} + N^{34g}_{\text{tot}}$

This gives

$$
\begin{aligned}
\mathcal{A}_{\text{exp}} &= \frac{N^{34m}_{\text{up,on}} - N^{34m}_{\text{do,on}}}{N^{34m}_{\text{tot}} + N^{bg}_{\text{tot}}} + \frac{N^{34g}_{\text{up,on}} - N^{34g}_{\text{do,on}}}{N^{34m}_{\text{tot}} + N^{bg}_{\text{tot}}} + \frac{N^{d}_{\text{up,on}} - N^{d}_{\text{do,on}}}{N^{34m}_{\text{tot}} + N^{bg}_{\text{tot}}} \\
&\quad - \left(\frac{N^{34m}_{\text{up,off}} - N^{34m}_{\text{do,off}}}{N^{34m}_{\text{tot}} + N^{bg}_{\text{tot}}} + \frac{N^{34g}_{\text{up,off}} - N^{34g}_{\text{do,off}}}{N^{34m}_{\text{tot}} + N^{bg}_{\text{tot}}} + \frac{N^{d}_{\text{up,off}} - N^{d}_{\text{do,off}}}{N^{34m}_{\text{tot}} + N^{bg}_{\text{tot}}} \right) \\
&= \left(\frac{(N^{34m}_{\text{up,on}} - N^{34m}_{\text{do,on}}) - (N^{34m}_{\text{up,off}} - N^{34m}_{\text{do,off}})}{N^{34m}_{\text{tot}} + N^{bg}_{\text{tot}}} \right) \\
&\quad - \left(\frac{(N^{34g}_{\text{up,on}} - N^{34g}_{\text{up,off}}) - (N^{34g}_{\text{do,on}} - N^{34g}_{\text{do,off}})}{N^{34m}_{\text{tot}} + N^{bg}_{\text{tot}}} \right) \\
&\quad - \left(\frac{(N^{b}_{\text{up,on}} - N^{b}_{\text{up,off}}) - (N^{b}_{\text{do,on}} - N^{b}_{\text{do,off}})}{N^{34m}_{\text{tot}} + N^{bg}_{\text{tot}}} \right) \\
&= -\frac{N^{34m}_{\text{up,off}} - N^{34m}_{\text{do,off}}}{N^{34m}_{\text{tot}} + N^{bg}_{\text{tot}}} \qquad \text{(A.3)}
\end{aligned}
$$

Compared with a situation in which only the isomer ^{34m}Al would be present, the asymmetry is therefore reduced by a factor

$$
\begin{aligned}
\frac{\mathcal{A}_{\text{exp}}}{\mathcal{A}^{34m}} &= \frac{\dfrac{N^{34m}_{\text{up,off}} - N^{34m}_{\text{do,off}}}{N^{34m}_{\text{tot}} + N^{bg}_{\text{tot}}}}{\dfrac{N^{34m}_{\text{up,off}} - N^{34m}_{\text{do,off}}}{N^{34m}_{\text{tot}}}} \\
&= \frac{N^{34m}_{\text{tot}}}{N^{34m}_{\text{tot}} + N^{bg}_{\text{tot}}} \qquad \text{(A.4)}
\end{aligned}
$$

Bibliography

Angeli, I., Y. P. Gangrsky, K. P. Marinova, I. N. Boboshin, S. Y. Komarov, B. S. Ishkhanov, and V. V. Varlamov (2009). *N and Z dependence of nuclear charge radii.* Journal of Phys. G 36(8), 085102. pages

Anne, R., D. Bazin, A. Mueller, J. Jacmart, and M. Langevin (1987). *The achromatic spectrometer LISE at GANIL.* NIM A 257(2), 215 – 232. pages

Aoi, N., E. Takeshita, H. Suzuki, S. Takeuchi, S. Ota, H. Baba, S. Bishop, T. Fukui, Y. Hashimoto, H. J. Ong, E. Ideguchi, K. Ieki, N. Imai, M. Ishihara, H. Iwasaki, S. Kanno, Y. Kondo, T. Kubo, K. Kurita, K. Kusaka, T. Minemura, T. Motobayashi, T. Nakabayashi, T. Nakamura, T. Nakao, M. Niikura, T. Okumura, T. K. Ohnishi, H. Sakurai, S. Shimoura, R. Sugo, D. Suzuki, M. K. Suzuki, M. Tamaki, K. Tanaka, Y. Togano, and K. Yamada (2009). *Development of Large Deformation in* ^{62}Cr. Phys. Rev. Lett. *102*, 012502. pages

Arima, A. and H. Horie (1954). *Configuration Mixing and Magnetic Moments of Odd Nuclei.* Progress of Theoretical Physics 12(5), 623–641. pages

Asahi, K., M. Ishihara, N. Inabe, T. Ichihara, T. Kubo, M. Adachi, H. Takanashi, M. Kouguchi, M. Fukuda, D. Mikolas, D. Morrissey, D. Beaumel, T. Shimoda, H. Miyatake, and N. Takahashi (1990). *New aspect of intermediate energy heavy ion reactions. Large spin polarization of fragments.* Phys. Lett. B 251(4), 488 – 492. pages

Asahi, K. and K. Matsuta (2001). *Nuclear electromagnetic moments. β-NMR and its applications.* Nucl. Phys. A 693(1-2), 63 – 76. pages

Ascher, P., D. Atanasov, B. Blank, K. Blaum, C. Borgmann, M. Breitenfeld, S. George, M. Gerbaux, S. Grevy, F. Herfurth, A. Herlert, M. Kowalska, S. Kreim, R. Lica, D. Lunney, V. Manea, N. Marginean, S. Naimi, F. Negoita, D. Neidherr, M. Rosenbusch, F. Rotaru, L. Schweikhard, F. Wienholtz,

R. Wolf, and K. Zuber (2013). *Energy of the 2p1h intruder state in* ^{34}Al*: an extension of the island of inversion?* Proposal to the ISOLDE and Neutron Time-of-Flight Committee. pages

Babcock, C. (2015). *Collinear laser spectroscopy of manganese isotopes using the radio frequency quadrupole cooler and buncher at ISOLDE.* Ph. D. thesis, University of Liverpool. pages

Baugher, T., A. Gade, R. V. F. Janssens, S. M. Lenzi, D. Bazin, B. A. Brown, M. P. Carpenter, A. N. Deacon, S. J. Freeman, T. Glasmacher, G. F. Grinyer, F. G. Kondev, S. McDaniel, A. Poves, A. Ratkiewicz, E. A. McCutchan, D. K. Sharp, I. Stefanescu, K. A. Walsh, D. Weisshaar, and S. Zhu (2012). *Intermediate-energy Coulomb excitation of* ^{58,60,62}Cr*: The onset of collectivity toward* $N = 40$. Phys. Rev. C *86*, 011305. pages

Bazin, D., O. Tarasov, M. Lewitowicz, and O. Sorlin (2002). *The program LISE: a simulation of fragment separators.* NIM A 482(1–2), 307 – 327. pages

Berdichevsky, D. and F. Tondeur (1985). *Nuclear core densities, isotope shifts, and the parametrization of the droplet model.* Z. Phys. A 322(1), 141–147. pages

Bernas, M., P. Dessagne, M. Langevin, J. Payet, F. Pougheon, and P. Roussel (1982). *Magic features of* ^{68}Ni. Phys. Lett. B 113(4), 279 – 282. pages

Block, M., C. Bachelet, G. Bollen, M. Facina, C. M. Folden, C. Guénaut, A. A. Kwiatkowski, D. J. Morrissey, G. K. Pang, A. Prinke, R. Ringle, J. Savory, P. Schury, and S. Schwarz (2008). *Discovery of a Nuclear Isomer in* ^{65}Fe *with Penning Trap Mass Spectrometry.* Phys. Rev. Lett. *100*, 132501. pages

Blumenfeld, Y., T. Nilsson, and P. Van Duppen (2013). *Facilities and methods for radioactive ion beam production.* Phys. Scripta 2013(T152), 014023. pages

Borremans, D., D. L. Balabanski, K. Blaum, W. Geithner, S. Gheysen, P. Himpe, M. Kowalska, J. Lassen, P. Lievens, S. Mallion, R. Neugart, G. Neyens, N. Vermeulen, and D. Yordanov (2005). *New measurement and reevaluation of the nuclear magnetic and quadrupole moments of* ^{8}Li *and* ^{9}Li. Phys. Rev. C *72*, 044309. pages

Borremans, D., J. M. Daugas, S. Teughels, D. L. Balabanski, N. Coulier, F. de Oliveira Santos, G. Georgiev, M. Hass, M. Lewitowicz, I. Matea, Y. E. Penionzhkevich, W.-D. Schmidt-Ott, Y. E. Sobolev, M. Stanoiu, K. Vyvey, and G. Neyens (2002). *Spin polarization of* ^{27}Na *and* ^{31}Al *in intermediate energy projectile fragmentation of* ^{36}S. Phys. Rev. C *66*, 054601. pages

Bosch, U., W.-D. Schmidt-Ott, E. Runte, P. Tidemand-Petersson, P. Koschel, F. Meissner, R. Kirchner, O. Klepper, E. Roeckl, K. Rykaczewski, and D. Schardt (1988). *Beta- and gamma-decay studies of neutron-rich chromium, manganese, cobalt and nickel isotopes including the new isotopes* ^{60}Cr *and* ^{60g}Mn. Nucl. Phys. A 477(1), 89 – 104. pages

Broda, R., B. Fornal, W. Królas, T. Pawłat, D. Bazzacco, S. Lunardi, C. Rossi-Alvarez, R. Menegazzo, G. de Angelis, P. Bednarczyk, J. Rico, D. De Acuña, P. J. Daly, R. H. Mayer, M. Sferrazza, H. Grawe, K. H. Maier, and R. Schubart (1995). $N = 40$ *Neutron Subshell Closure in the* ^{68}Ni *Nucleus.* Phys. Rev. Lett. *74*, 868–871. pages

Brown, B. A. and B. H. Wildenthal (1988). *Status of the Nuclear Shell Model.* Annu. Rev. Nucl. Part. Sci. 38(1), 29–66. pages

Budinčević, I., J. Billowes, M. L. Bissell, T. E. Cocolios, R. P. de Groote, S. De Schepper, V. N. Fedosseev, K. T. Flanagan, S. Franchoo, R. F. Garcia Ruiz, H. Heylen, K. M. Lynch, B. A. Marsh, G. Neyens, T. J. Procter, R. E. Rossel, S. Rothe, I. Strashnov, H. H. Stroke, and K. D. A. Wendt (2014). *Laser spectroscopy of francium isotopes at the borders of the region of reflection asymmetry.* Phys. Rev. C *90*, 014317. pages

Campbell, P., I. D. Moore, and M. R. Pearson (2016). *Laser spectroscopy for nuclear structure physics.* Prog. Part. Nucl. Phys. *86*, 127 – 180. pages

Campi, X., H. Flocard, A. Kerman, and S. Koonin (1975). *Shape transition in the neutron rich sodium isotopes.* Nucl. Phys. A 251(2), 193 – 205. pages

Castel, B. and I. S. Towner (1990). *Modern theories of nuclear moments.* Oxford : Clarendon Press ; New York : Oxford University Press. pages

Casten, R. F. (2000). *Nuclear Structure from a Simple Perspective.* New York, NY: Oxford Univ. Press. pages

Caurier, E., G. Martínez-Pinedo, F. Nowacki, A. Poves, and A. P. Zuker (2005). *The shell model as a unified view of nuclear structure.* Rev. Mod. Phys. *77*, 427–488. pages

Caurier, E. and F. Nowacki (1999). *Present Status of Shell Model Techniques.* Act. Phys. Pol. B *30*, 705. pages

Caurier, E., F. Nowacki, and A. Poves (2014). *Merging of the islands of inversion at* $N = 20$ *and* $N = 28$*.* Phys. Rev. C *90*, 014302. pages

Charlwood, F. C., J. Billowes, P. Campbell, B. Cheal, T. Eronen, D. Forest, S. Fritzsche, M. Honma, A. Jokinen, I. D. Moore, H. Penttilä, R. Powis,

A. Saastamoinen, G. Tungate, and J. Aystö (2010). *Ground state properties of manganese isotopes across the shell closure*. Phys. Lett. B 690(4), 346 – 351. pages

Cheal, B., J. Billowes, M. Bissell, P. Campbell, T. Cocolios, K. Flanagan, D. Forest, K. Lynch, B. Marsh, I. Moore, G. Neyens, T. Procter, M. Rajabali, M. Reponen, and G. Tungate (2010). *Collinear laser spectroscopy of manganese isotopes using optical pumping in ISCOOL*. Proposal to the 38th meeting of the INTC. pages

Cheal, B., T. E. Cocolios, and S. Fritzsche (2012). *Laser spectroscopy of radioactive isotopes: Role and limitations of accurate isotope-shift calculations*. Phys. Rev. A *86*, 042501. pages

Cheal, B., E. Mané, J. Billowes, M. L. Bissell, K. Blaum, B. A. Brown, F. C. Charlwood, K. T. Flanagan, D. H. Forest, C. Geppert, M. Honma, A. Jokinen, M. Kowalska, A. Krieger, J. Krämer, I. D. Moore, R. Neugart, G. Neyens, W. Nörtershäuser, M. Schug, H. H. Stroke, P. Vingerhoets, D. T. Yordanov, and M. Žáková (2010). *Nuclear Spins and Moments of Ga Isotopes Reveal Sudden Structural Changes between* $N = 40$ *and* $N = 50$. Phys. Rev. Lett. *104*, 252502. pages

Chiara, C. J., I. Stefanescu, N. Hoteling, W. B. Walters, R. V. F. Janssens, R. Broda, M. P. Carpenter, B. Fornal, A. A. Hecht, W. Królas, T. Lauritsen, T. Pawłat, D. Seweryniak, X. Wang, A. Wöhr, J. Wrzesiński, and S. Zhu (2010). *Influence of the* $\nu g_{9/2}$ *orbital on level structures of neutron-rich* $^{61,62}Mn_{36,37}$. Phys. Rev. C *82*, 054313. pages

Cottenier, S. and M. Rots (2005). *Hyperfine Interactions and their Applications in Nuclear Condensed Matter Physics: a microscopic introduction*. Course text *Hyperfine interactions*, KU Leuven 2011. pages

Crawford, H. L., R. M. Clark, P. Fallon, A. O. Macchiavelli, T. Baugher, D. Bazin, C. W. Beausang, J. S. Berryman, D. L. Bleuel, C. M. Campbell, M. Cromaz, G. de Angelis, A. Gade, R. O. Hughes, I. Y. Lee, S. M. Lenzi, F. Nowacki, S. Paschalis, M. Petri, A. Poves, A. Ratkiewicz, T. J. Ross, E. Sahin, D. Weisshaar, K. Wimmer, and R. Winkler (2013). *Quadrupole Collectivity in Neutron-Rich Fe and Cr Isotopes*. Phys. Rev. Lett. *110*, 242701. pages

Davis, S. J., J. J. Wright, and L. C. Balling (1971). *Hyperfine Structure of the Ground State of* ^{55}Mn. Phys. Rev. A *3*, 1220–1223. pages

De Rydt, M. (2010). *A dedicated β-NMR/ β-NQR setup for LISE-GANIL and study of the nuclear moments of the neutron-rich Al and Cl isotopes*. Ph. D. thesis, KU Leuven. pages

De Rydt, M., R. Lozeva, N. Vermeulen, F. de Oliveira Santos, S. Grévy, P. Himpe, C. Stödel, J. C. Thomas, P. Vingerhoets, and G. Neyens (2009). *A new dedicated β-NMR/ β-NQR setup for LISE-GANIL.* NIM A 612(1), 112 – 121. pages

De Rydt, M., G. Neyens, K. Asahi, D. L. Balabanski, J. M. Daugas, M. Depuydt, L. Gaudefroy, S. Grévy, Y. Hasama, Y. Ichikawa, P. Morel, T. Nagatomo, T. Otsuka, L. Perrot, K. Shimada, C. Stodel, J. Thomas, H. Ueno, Y. Utsuno, W. Vanderheijden, N. Vermeulen, P. Vingerhoets, and A. Yoshimi (2009). *Precision measurement of the electric quadrupole moment of* ^{31}Al *and determination of the effective proton charge in the sd-shell.* Phys. Lett. B 678(4), 344 – 349. pages

Détraz, C., D. Guillemaud, G. Huber, R. Klapisch, M. Langevin, F. Naulin, C. Thibault, L. C. Carraz, and F. Touchard (1979). *Beta decay of* $^{27-32}$Na *and their descendants.* Phys. Rev. C *19*, 164–176. pages

Duflo, J. and A. P. Zuker (2002). *Mirror displacement energies and neutron skins.* Phys. Rev. C *66*, 051304. pages

Dufour, M. and A. P. Zuker (1996). *Realistic collective nuclear Hamiltonian.* Phys. Rev. C *54*, 1641–1660. pages

Elliott, J. P. (1958a). *Collective Motion in the Nuclear Shell Model. I. Classification Schemes for States of Mixed Configurations.* Proc. R. Soc. A 245(1240), 128–145. pages

Elliott, J. P. (1958b). *Collective Motion in the Nuclear Shell Model. II. The Introduction of Intrinsic Wave-Functions.* Proc. R. Soc. A 245(1243), 562–581. pages

Flanagan, K. T., K. M. Lynch, J. Billowes, M. L. Bissell, I. Budinčević, T. E. Cocolios, R. P. de Groote, S. De Schepper, V. N. Fedosseev, S. Franchoo, R. F. Garcia Ruiz, H. Heylen, B. A. Marsh, G. Neyens, T. J. Procter, R. E. Rossel, S. Rothe, I. Strashnov, H. H. Stroke, and K. D. A. Wendt (2013). *Collinear Resonance Ionization Spectroscopy of Neutron-Deficient Francium Isotopes.* Phys. Rev. Lett. *111*, 212501. pages

Flanagan, K. T., P. Vingerhoets, M. Avgoulea, J. Billowes, M. L. Bissell, K. Blaum, B. Cheal, M. De Rydt, V. N. Fedosseev, D. H. Forest, C. Geppert, U. Köster, M. Kowalska, J. Krämer, K. L. Kratz, A. Krieger, E. Mané, B. A. Marsh, T. Materna, L. Mathieu, P. L. Molkanov, R. Neugart, G. Neyens, W. Nörtershäuser, M. D. Seliverstov, O. Serot, M. Schug, M. A. Sjoedin, J. R. Stone, N. J. Stone, H. H. Stroke, G. Tungate, D. T. Yordanov, and Y. M. Volkov (2009). *Nuclear Spins and Magnetic Moments of* ^{71,73,75}Cu*: Inversion of* $\pi 2p_{3/2}$ *and* $\pi 1f_{5/2}$ *Levels in* ^{75}Cu. Phys. Rev. Lett. *103*, 142501. pages

Flynn, E., O. Hansen, R. Casten, J. Garrett, and F. Ajzenberg-Selove (1975). *The (t, p) reaction on* ^{36,38,40}Ar. Nucl. Phys. A 246(1), 117 – 140. pages

Fritzsche, S. (2002). *Large-Scale Accurate Structure Calculations for Open-Shell Atoms and Ions.* Phys. Scripta 2002(T100), 37. pages

Gade, A. (2015). *Excitation energies in neutron-rich rare isotopes as indicators of changing shell structure.* EPJ A 51(9), 1–22. pages

Gade, A., R. V. F. Janssens, T. Baugher, D. Bazin, B. A. Brown, M. P. Carpenter, C. J. Chiara, A. N. Deacon, S. J. Freeman, G. F. Grinyer, C. R. Hoffman, B. P. Kay, F. G. Kondev, T. Lauritsen, S. McDaniel, K. Meierbachtol, A. Ratkiewicz, S. R. Stroberg, K. A. Walsh, D. Weisshaar, R. Winkler, and S. Zhu (2010). *Collectivity at* $N = 40$ *in neutron-rich* ^{64}Cr. Phys. Rev. C *81*, 051304. pages

Gade, A. and S. N. Liddick (2016). *Shape coexistence in neutron-rich nuclei.* J. Phys. G 43(2), 024001. pages

Gaffney, L. P., J. Walle, B. Bastin, V. Bildstein, A. Blazhev, N. Bree, J. Cederkäll, I. Darby, H. Witte, D. DiJulio, J. Diriken, V. N. Fedosseev, C. Fransen, R. Gernhäuser, A. Gustafsson, H. Hess, M. Huyse, N. Kesteloot, T. Kröll, R. Lutter, B. A. Marsh, P. Reiter, M. Seidlitz, P. Duppen, D. Voulot, N. Warr, F. Wenander, K. Wimmer, and K. Wrzosek-Lipska (2015). *Low-energy Coulomb excitation of* ^{62}Fe *and* ^{62}Mn *following in-beam decay of* ^{62}Mn. EPJ A 51(10), 1–9. pages

Garcia Ruiz, R. F. (2015). *Collinear Laser Spectroscopy on exotic Ca Isotopes towards new magic numbers* $N = 32$ *and* $N = 34$. Ph. D. thesis, KU Leuven. pages

Garcia Ruiz, R. F., M. L. Bissell, K. Blaum, N. Frömmgen, M. Hammen, J. D. Holt, M. Kowalska, K. Kreim, J. Menéndez, R. Neugart, G. Neyens, W. Nörtershäuser, F. Nowacki, J. Papuga, A. Poves, A. Schwenk, J. Simonis, and D. T. Yordanov (2015). *Ground-state electromagnetic moments of calcium isotopes.* Phys. Rev. C *91*, 041304. pages

Garrett, P. E. and J. L. Wood (2010). *On the robustness of surface vibrational modes: case studies in the Cd region.* Journal of Physics G: Nuclear and Particle Physics 37(6), 064028. pages

Gaudefroy, L. (2005). *Etude de la fermeture de couche N=28 autour du noyau* $^{46}_{18}$Ar$_{28}$ *par reaction de transfert d'un neutron : application l'astrophysique et Spectroscopie* $\beta\gamma$ *de noyaux riches en neutrons autour de* $N = 32/34$ *et* $N = 40$. Ph. D. thesis, Université de Paris XI. pages

Gaudefroy, L., O. Sorlin, C. Donzaud, J. Angélique, F. Azaiez, C. Bourgeois, V. Chiste, Z. Dlouhy, S. Grévy, D. Guillemaud-Mueller, F. Ibrahim, K.-L. Kratz, M. Lewitowicz, S. Lukyanov, I. Matea, J. Mrasek, F. Nowacki, F. de Oliveira Santos, Y.-E. Penionzhkevich, B. Pfeiffer, F. Pougheon, M. Saint-Laurent, and M. Stanoiu (2005). *Beta-decay studies of neutron-rich Sc- Cr nuclei.* EPJ A 23(1), 41–48. pages

Goeppert-Mayer, M. (1949). *On Closed Shells in Nuclei. II.* Phys. Rev. *75*, 1969–1970. pages

Guénaut, C., G. Audi, D. Beck, K. Blaum, G. Bollen, P. Delahaye, F. Herfurth, A. Kellerbauer, H.-J. Kluge, J. Libert, D. Lunney, S. Schwarz, L. Schweikhard, and C. Yazidjian (2007). *High-precision mass measurements of nickel, copper, and gallium isotopes and the purported shell closure at* $N = 40$. Phys. Rev. C *75*, 044303. pages

Hammer, H.-W., A. Nogga, and A. Schwenk (2013). *Colloquium : Three-body forces: From cold atoms to nuclei.* Rev. Mod. Phys. *85*, 197–217. pages

Hannawald, M., T. Kautzsch, A. Wöhr, W. B. Walters, K.-L. Kratz, V. N. Fedoseyev, V. I. Mishin, W. Böhmer, B. Pfeiffer, V. Sebastian, Y. Jading, U. Köster, J. Lettry, H. L. Ravn, and the ISOLDE Collaboration (1999). *Decay of Neutron-Rich Mn Nuclides and Deformation of Heavy Fe Isotopes.* Phys. Rev. Lett. *82*, 1391–1394. pages

Haxel, O., J. H. D. Jensen, and H. E. Suess (1949). *On the "Magic Numbers" in Nuclear Structure.* Phys. Rev. *75*, 1766–1766. pages

Heyde, K. (1990). *The Nuclear Shell Model.* Springer Berlin Heidelberg. pages

Heyde, K. (2013). *The Atomic Nucleus: a Bound System of Interacting Nucleons.* Lecture notes from the ISOLDE lecture series. pages

Heyde, K. and J. L. Wood (2011). *Shape coexistence in atomic nuclei.* Rev. Mod. Phys. *83*, 1467–1521. pages

Himpe, P. (2006). *Nuclear g-factors of neutron rich* $^{31-34}$Al *and* ^{35}Si*: probes for changing shell structure.* Ph. D. thesis, KU Leuven. pages

Himpe, P., G. Neyens, D. L. Balabanski, G. Bélier, D. Borremans, J. M. Daugas, F. de Oliveira Santos, M. De Rydt, K. Flanagan, G. Georgiev, M. Kowalska, S. Mallion, I. Matea, P. Morel, Y. E. Penionzhkevich, N. A. Smirnova, C. Stodel, K. Turzó, N. Vermeulen, and D. T. Yordanov (2006). *g factors of* ^{31,32,33}Al*: Indication for intruder configurations in the* ^{33}Al *ground state.* Phys. Lett. B 643(5), 257 – 262. pages

Himpe, P., G. Neyens, D. L. Balabanski, G. Bélier, J. M. Daugas, F. de Oliveira Santos, M. De Rydt, K. T. Flanagan, I. Matea, P. Morel, Y. E. Penionzhkevich, L. Perrot, N. A. Smirnova, C. Stodel, J. C. Thomas, N. Vermeulen, D. T. Yordanov, Y. Utsuno, and T. Otsuka (2008). *g factor of the exotic isotope* ^{34}Al*: probing the and shell gaps at the border of the "island of inversion".* Phys. Lett. B 658(5), 203 – 208. pages

Hogenbirk, A., H. Blok, M. Brand, A. V. Hees, J. V. Hienen, and F. Jansen (1990). *A study of* ^{36}S *by high-resolution inelastic proton and alpha scattering.* Nucl. Phys. A 516(2), 205 – 254. pages

Honma, M., T. Mizusaki, and T. Otsuka (1995). *Diagonalization of Hamiltonians for Many-Body Systems by Auxiliary Field Quantum Monte Carlo Technique.* Phys. Rev. Lett. *75*, 1284–1287. pages

Hossain, M. D., Z. Salman, D. Wang, K. H. Chow, S. Kreitzman, T. A. Keeler, C. D. P. Levy, W. A. MacFarlane, R. I. Miller, G. D. Morris, T. J. Parolin, M. Pearson, H. Saadaoui, and R. F. Kiefl (2009). *Low-field cross spin relaxation of* ^{8}Li *in superconducting* $NbSe_2$. Phys. Rev. B *79*, 144518. pages

Huber, G., F. Touchard, S. Büttgenbach, C. Thibault, R. Klapisch, H. T. Duong, S. Liberman, J. Pinard, J. L. Vialle, P. Juncar, and P. Jacquinot (1978). *Spins, magnetic moments, and isotope shifts of* $^{21-31}$Na *by high resolution laser spectroscopy of the atomic* D_1 *line.* Phys. Rev. C *18*, 2342–2354. pages

Kameda, D., H. Ueno, K. Asahi, M. Takemura, A. Yoshimi, T. Haseyama, M. Uchida, K. Shimada, D. Nagae, G. Kijima, T. Arai, K. Takase, S. Suda, T. Inoue, J. Murata, H. Kawamura, Y. Kobayashi, H. Watanabe, and M. Ishihara (2007). *Measurement of the electric quadrupole moment of* ^{32}Al. Phys. Lett. B 647(2–3), 93 – 97. pages

King, W. (1984). *Isotope shifts in atomic spectra.* Plenum, New York. pages

Korringa, J. (1950). *Nuclear magnetic relaxation and resonance line shifts in metals.* Physica *16*, 601010. pages

Krane, K. (1987). *Introductory Nuclear Physics, 3rd Edition.* Wiley. pages

Krücken, R. (2011). *Introduction to shell structure in exotic nuclei.* Contemp. Phys. 52(2), 101–120. pages

Kwiatkowski, A. A., C. Andreoiu, J. C. Bale, A. Chaudhuri, U. Chowdhury, S. Malbrunot-Ettenauer, A. T. Gallant, A. Grossheim, G. Gwinner, A. Lennarz, T. D. Macdonald, T. J. M. Rauch, B. E. Schultz, S. Seeraji, M. C. Simon, V. V. Simon, D. Lunney, A. Poves, and J. Dilling (2015). *Observation of a crossover of* S_{2n} *in the island of inversion from precision mass spectrometry.* Phys. Rev. C *92*, 061301. pages

Lenzi, S. M., F. Nowacki, A. Poves, and K. Sieja (2010). *Island of inversion around* ^{64}Cr. Phys. Rev. C *82*, 054301. pages

Liddick, S. N., P. F. Mantica, B. A. Brown, M. P. Carpenter, A. D. Davies, M. Horoi, R. V. F. Janssens, A. C. Morton, W. F. Mueller, J. Pavan, H. Schatz, A. Stolz, S. L. Tabor, B. E. Tomlin, and M. Wiedeking (2006). *Half-life and spin of* ^{60}Mn^{g}. Phys. Rev. C *73*, 044322. pages

Liddick, S. N., S. Suchyta, B. Abromeit, A. Ayres, A. Bey, C. R. Bingham, M. Bolla, M. P. Carpenter, L. Cartegni, C. J. Chiara, H. L. Crawford, I. G. Darby, R. Grzywacz, G. Gürdal, S. Ilyushkin, N. Larson, M. Madurga, E. A. McCutchan, D. Miller, S. Padgett, S. V. Paulauskas, J. Pereira, M. M. Rajabali, K. Rykaczewski, S. Vinnikova, W. B. Walters, and S. Zhu (2011). *Shape coexistence along* $N = 40$. Phys. Rev. C *84*, 061305. pages

Lievens, P., E. Arnold, W. Borchers, U. Georg, M. Keim, A. Klein, R. Neugart, L. Vermeeren, and R. E. Silverans (1996). *On the odd-even staggering of mean-square charge radii in the light krypton and strontium region.* EPL 33(1), 11. pages

Ljungvall, J., A. Görgen, A. Obertelli, W. Korten, E. Clément, G. de France, A. Bürger, J.-P. Delaroche, A. Dewald, A. Gadea, L. Gaudefroy, M. Girod, M. Hackstein, J. Libert, D. Mengoni, F. Nowacki, T. Pissulla, A. Poves, F. Recchia, M. Rejmund, W. Rother, E. Sahin, C. Schmitt, A. Shrivastava, K. Sieja, J. J. Valiente-Dobón, K. O. Zell, and M. Zielińska (2010). *Onset of collectivity in neutron-rich Fe isotopes: Toward a new island of inversion?* Phys. Rev. C *81*, 061301. pages

Lutter, R., O. H. usser, D. Donahue, R. Hershberger, F. Riess, H. Bohn, T. Faestermann, F. Feilitzsch, and K. L. bner (1974). *Negative-parity states in Pb isotopes: g-factor of the 480 ns, J = 9 isomer in* ^{200}Pb. Nucl. Phys. A 229(2), 230 – 240. pages

Machleidt, R. and D. Entem (2011). *Chiral effective field theory and nuclear forces.* Phys. Rep. 503(1), 1 – 75. pages

Magnante, P. C. and H. H. Stroke (1969). *Isotope Shift between* ^{209}Bi *and 6.3-day* ^{206}Bi. J. Opt. Soc. Am. 59(7), 836–841. pages

Mané, E., J. Billowes, K. Blaum, P. Campbell, B. Cheal, P. Delahaye, K. Flanagan, D. Forest, H. Franberg, C. Geppert, T. Giles, A. Jokinen, M. Kowalska, R. Neugart, G. Neyens, W. Nörtershäuser, I. Podadera, G. Tungate, P. Vingerhoets, and D. T. Yordanov (2009). *An ion cooler-buncher for high-sensitivity collinear laser spectroscopy at ISOLDE.* EPJ A 42(3), 503–507. pages

Marsh, B. A., L.-E. Berg, D. V. Fedorov, V. N. Fedosseev, O. J. Launila, M. Lindroos, R. Losito, F. K. Österdahl, T. Pauchard, I. T. Pohjalainen, U. Sassenberg, M. D. Seliverstov, A. M. Sjödin, and G. Tranströmer (2010). *The ISOLDE RILIS pump laser upgrade and the LARIS Laboratory.* Hyperfine Interact. 196(1), 129–141. pages

Mayer, M.-G. and J. H. D. Jensen (1955). *Elementary theory of nuclear shell structure.* New York : Wiley. pages

Mieher, R. L. (1960). *Nuclear Relaxation via Quadrupole Coupling.* Phys. Rev. Lett. *4*, 57–59. pages

Mizusaki, T. (2000). *MShell.* RIKEN accelerator progress report *33*, 14. pages

Moller, P., J. Nix, W. Myers, and W. Swiatecki (1995). *Nuclear Ground-State Masses and Deformations.* At. Data Nucl. Data Tables 59(2), 185 – 381. pages

Myers, W. D. and K.-H. Schmidt (1983). *An update on droplet-model charge distributions.* Nucl. Phys. A 410(1), 61 – 73. pages

Nagae, D., H. Ueno, D. Kameda, M. Takemura, K. Asahi, K. Takase, A. Yoshimi, T. Sugimoto, K. Shimada, T. Nagatomo, M. Uchida, T. Arai, T. Inoue, S. Kagami, N. Hatakeyama, H. Kawamura, K. Narita, and J. Murata (2009). *Ground-state electric quadrupole moment of* ^{31}Al. Phys. Rev. C *79*, 027301. pages

Naimi, S., G. Audi, D. Beck, K. Blaum, C. Böhm, C. Borgmann, M. Breitenfeldt, S. George, F. Herfurth, A. Herlert, A. Kellerbauer, M. Kowalska, D. Lunney, E. Minaya Ramirez, D. Neidherr, M. Rosenbusch, L. Schweikhard, R. N. Wolf, and K. Zuber (2012). *Surveying the* $N = 40$ *island of inversion with new manganese masses.* Phys. Rev. C *86*, 014325. pages

Neugart, R. (1981). *Laser spectroscopy on mass-separated radioactive beams.* NIM 186(1–2), 165 – 175. pages

Neyens, G. (2003). *Nuclear magnetic and quadrupole moments for nuclear structure research on exotic nuclei.* Rep. Progr. Phys. 66(4), 633. pages

Neyens, G. (2011). *Multiparticle-multihole states in* ^{31}Mg *and* ^{33}Mg*: A critical evaluation.* Phys. Rev. C *84*, 064310. pages

Neyens, G. (2016). *Shape coexistence in the N = 19 and N = 21 isotones.* J. Phys. G 43(2), 024007. pages

NIST (2016). *Digital Library of Mathematical Functions Version 1.0.11: Voigt function.* `http://dlmf.nist.gov/7.19`. pages

NNDC (2016). *National Nuclear Data Center - Chart of nuclides.* `http://www.nndc.bnl.gov/chart`. pages

Nörtershäuser, W. and C. Geppert (2014). *The Euroschool on Exotic Beams, Vol. IV*, Chapter Nuclear Charge Radii of Light Elements and Recent Developments in Collinear Laser Spectroscopy, pp. 233–292. Berlin, Heidelberg: Springer Berlin Heidelberg. pages

Nowacki, F. and A. Poves (2009). *New effective interaction for $0\hbar\omega$ shell model calculations in the sd-pf valence space.* Phys. Rev. C *79*, 014310. pages

Noya, H., A. Arima, and H. Horie (1958). *Nuclear Moments and Configuration Mixing.* Progr. Theor. Exp. Phys. Suppl. *8*, 33–112. pages

Nummela, S., P. Baumann, E. Caurier, P. Dessagne, A. Jokinen, A. Knipper, G. Le Scornet, C. Miehé, F. Nowacki, M. Oinonen, Z. Radivojevic, M. Ramdhane, G. Walter, and J. Äystö (2001). *Spectroscopy of* ^{34,35}Si *by β decay: $sd - fp$ shell gap and single-particle states.* Phys. Rev. C *63*, 044316. pages

Oinonen, M., Y. Jading, U. Köster, J. Lettry, H. Ravn, J. Äystö, P. Dendooven, J. Huikari, A. Jokinen, P. Lipas, A. Nieminen, K. Peräjärvi, T. Siiskonen, P. Baumann, A. Huck, A. Knipper, M. Ramdhane, G. Walter, F. Didierjean, V. Fedoseyev, V. Mishin, M. Koizumi, W. Liu, E. Roeckl, and V. Sebastian (2000). *Laser ionization in beta-decay studies of Zn and Mn nuclei.* Hyperfine Interact. 127(1), 431–436. pages

Okuno, H., K. Asahi, H. Sato, H. Ueno, J. Kura, M. Adachi, T. Nakamura, T. Kubo, N. Inabe, A. Yoshida, T. Ichihara, Y. Kobayashi, Y. Ohkubo, M. Iwamoto, F. Ambe, T. Shimoda, H. Miyatake, N. Takahashi, J. Nakamura, D. Beaumel, D. Morrissey, W.-D. Schmidt-Ott, and M. Ishihara (1994). *Systematic behavior of ejectile spin polarization in the projectile fragmentation reaction.* Phys. Lett. B 335(1), 29 – 34. pages

Olaizola, B., L. M. Fraile, H. Mach, A. Aprahamian, J. A. Briz, J. Cal-González, D. Ghiţa, U. Köster, W. Kurcewicz, S. R. Lesher, D. Pauwels, E. Picado, A. Poves, D. Radulov, G. S. Simpson, and J. M. Udías (2013). *β^- decay of* ^{65}Mn *to* ^{65}Fe. Phys. Rev. C *88*, 044306. pages

Otsuka, T. (2001). *Radioactive Nuclear Beams Monte Carlo shell model.* Nucl. Phys. A 693(1), 383 – 393. pages

Otsuka, T. (2009). *The Euroschool Lectures on Physics with Exotic Beams, Vol. III*, Chapter Shell Structure of Exotic Nuclei, pp. 1–25. Berlin, Heidelberg: Springer Berlin Heidelberg. pages

Otsuka, T., R. Fujimoto, Y. Utsuno, B. A. Brown, M. Honma, and T. Mizusaki (2001). *Magic Numbers in Exotic Nuclei and Spin-Isospin Properties of the NN Interaction.* Phys. Rev. Lett. *87*, 082502. pages

Otsuka, T., T. Suzuki, R. Fujimoto, H. Grawe, and Y. Akaishi (2005). *Evolution of Nuclear Shells due to the Tensor Force.* Phys. Rev. Lett. *95*, 232502. pages

Otsuka, T. and Y. Tsunoda (2016). *The role of shell evolution in shape coexistence.* J. Phys. G 43(2), 024009. pages

Ouellet, C. and B. Singh (2011). *Nuclear Data Sheets for $A = 32$.* Nuclear Data Sheets 112(9), 2199 – 2355. pages

Paar, V. (1973). *Coupling of a three-particle (hole) valence-shell cluster to quadrupole vibrations (Alaga model): The $Z = 50$ region: odd Ag and I isotopes; and the $Z = 28$ region: odd Mn and Ga isotopes.* Nucl. Phys. A 211(1), 29 – 76. pages

Paar, V. (1979). *A parabolic rule for the energy dependence on $x = I(I + 1)$ for proton-neutron multiplets in odd-odd nuclei.* Nucl. Phys. A 331(1), 16 – 28. pages

Papuga, J., M. L. Bissell, K. Kreim, K. Blaum, B. A. Brown, M. De Rydt, R. F. Garcia Ruiz, H. Heylen, M. Kowalska, R. Neugart, G. Neyens, W. Nörtershäuser, T. Otsuka, M. M. Rajabali, R. Sánchez, Y. Utsuno, and D. T. Yordanov (2013). *Spins and Magnetic Moments of* ^{49}K *and* ^{51}K *Establishing the* $1/2^+$ *and* $3/2^+$ *Level Ordering Beyond* $N = 28$. Phys. Rev. Lett. *110*, 172503. pages

Pauwels, D., O. Ivanov, N. Bree, J. Büscher, T. E. Cocolios, J. Gentens, M. Huyse, A. Korgul, Y. Kudryavtsev, R. Raabe, M. Sawicka, I. Stefanescu, J. Van de Walle, P. Van den Bergh, P. Van Duppen, and W. B. Walters (2008). *Shape isomerism at* $N = 40$*: Discovery of a proton intruder state in* ^{67}Co. Phys. Rev. C *78*, 041307. pages

Persson, J. (2013). *Table of hyperfine anomaly in atomic systems.* At. Data Nucl. Data Tables 99(1), 62 – 68. pages

Poves, A. (2011). *The Nuclear Shell Model: Past, Present and Future.* Lecture notes of the 2011 International Joliot-Curie school. pages

Poves, A. (2016). *Shape coexistence: the shell model view.* Journal of Physics G: Nuclear and Particle Physics 43(2), 024010. pages

Poves, A. and F. Nowacki (2001). *An Advanced Course in Modern Nuclear Physics*, Chapter The nuclear shell model, pp. 70–101. Berlin, Heidelberg: Springer Berlin Heidelberg. pages

Pritychenko, B., M. Birch, B. Singh, and M. Horoi (2016). *Tables of E2 transition probabilities from the first states in even even nuclei.* At. Data Nucl. Data Tables *107*, 1 – 139. pages

Raju, R., J. Draayer, and K. Hecht (1973). *Search for a coupling scheme in heavy deformed nuclei: The pseudo SU(3) model.* Nucl. Phys. A 202(3), 433 – 466. pages

Recchia, F., S. M. Lenzi, S. Lunardi, E. Farnea, A. Gadea, N. Mărginean, D. R. Napoli, F. Nowacki, A. Poves, J. J. Valiente-Dobón, M. Axiotis, S. Aydin, D. Bazzacco, G. Benzoni, P. G. Bizzeti, A. M. Bizzeti-Sona, A. Bracco, D. Bucurescu, E. Caurier, L. Corradi, G. de Angelis, F. Della Vedova, E. Fioretto, A. Gottardo, M. Ionescu-Bujor, A. Iordachescu, S. Leoni, R. Mărginean, P. Mason, R. Menegazzo, D. Mengoni, B. Million, G. Montagnoli, R. Orlandi, G. Pollarolo, E. Sahin, F. Scarlassara, R. P. Singh, A. M. Stefanini, S. Szilner, C. A. Ur, and O. Wieland (2012). *Spectroscopy of odd-mass cobalt isotopes toward the $N = 40$ subshell closure and shell-model description of spherical and deformed states.* Phys. Rev. C *85*, 064305. pages

Rotaru, F., F. Negoita, S. Grévy, J. Mrazek, S. Lukyanov, F. Nowacki, A. Poves, O. Sorlin, C. Borcea, R. Borcea, A. Buta, L. Cáceres, S. Calinescu, R. Chevrier, Z. Dombrádi, J. M. Daugas, D. Lebhertz, Y. Penionzhkevich, C. Petrone, D. Sohler, M. Stanoiu, and J. C. Thomas (2012). *Unveiling the Intruder Deformed 0_2^+ State in ^{34}Si.* Phys. Rev. Lett. *109*, 092503. pages

Rothe, S., T. D. Goodacre, D. Fedorov, V. Fedosseev, B. Marsh, P. Molkanov, R. Rossel, M. Seliverstov, M. Veinhard, and K. Wendt (2016). *Laser ion beam production at CERN-ISOLDE: New features – More possibilities.* NIM B *376*, 91 – 96. Proceedings of the XVIIth International Conference on Electromagnetic Isotope Separators and Related Topics (EMIS2015), Grand Rapids, MI, U.S.A., 11-15 May 2015. pages

Runte, E., K. Gippert, W. Schmidt-Ott, P. Tidemand-Petersson, L. Ziegeler, R. Kirchner, O. Klepper, P. Larsson, E. Roeckl, D. Schardt, N. Kaffrell, P. Peuser, M. Bernas, P. Dessagne, M. Langevin, and K. Rykaczewski (1985). *Decay studies of neutron-rich isotopes of manganese, iron, cobalt, nickel, copper and zinc.* Nucl. Phys. A 441(2), 237 – 260. pages

Runte, E., W.-D. Schmidt-Ott, P. Tidemand-Petersson, R. Kirchner, O. Klepper, W. Kurcewicz, E. Roeckl, N. Kaffrell, P. Peuser, K. Rykaczewski, M. Bernas, P. Dessagne, and M. Langevin (1983). *Decay studies of neutron-rich products from ^{76}Ge induced multinucleon transfer reactions including the new isotopes ^{62}Mn, ^{63}Fe and ^{71,72,73}Cu.* Nucl. Phys. A 399(1), 163 – 180. pages

Schmidt-Ott, W.-D., K. Becker, U. Bosch-Wicke, T. Hild, F. Meissner, R. Kirchner, E. Roeckl, and K. Rykaczewski (1993). *Conversion measurements in odd-odd isotopes* ^{58}*Mn and* ^{60}*Mn.* Proceedings 6th International Conference on Nuclei Far from Stability and 9th International Conference on Atomic Masses and Fundamental Constants, Bernkastel-Kues (Germany), edited by R. Neugart and A. Wöhr. pages

Schwerdtfeger, W., P. G. Thirolf, K. Wimmer, D. Habs, H. Mach, T. R. Rodriguez, V. Bildstein, J. L. Egido, L. M. Fraile, R. Gernhäuser, R. Hertenberger, K. Heyde, P. Hoff, H. Hübel, U. Köster, T. Kröll, R. Krücken, R. Lutter, T. Morgan, and P. Ring (2009). *Shape Coexistence Near Neutron Number* $N = 20$*: First Identification of the* $E0$ *Decay from the Deformed First Excited* $J^\pi = 0^+$ *State in* ^{30}Mg. Phys. Rev. Lett. *103*, 012501. pages

Seltzer, E. C. (1969). *K X-Ray Isotope Shifts.* Phys. Rev. *188*, 1916–1919. pages

Shimada, K., H. Ueno, G. Neyens, K. Asahi, D. L. Balabanski, J. M. Daugas, M. Depuydt, M. De Rydt, L. Gaudefroy, S. Grévy, Y. Hasama, Y. Ichikawa, D. Kameda, P. Morel, T. Nagatomo, L. Perrot, C. Stodel, T. J. C., Y. Utsuno, W. Vanderheijden, N. Vermeulen, P. Vingerhoets, E. Yagi, K. Yoshida, and A. Yoshimi (2012). *Erosion of shell in investigated through the ground-state electric quadrupole moment.* Phys. Lett. B 714(2-5), 246 – 250. pages

Shimizu, N., T. Otsuka, Y. Utsuno, T. Mizusaki, M. Honma, and T. Abe (2013). *History and future perspectives of the Monte Carlo shell model -from Alphleet to K computer-.* Journal of Physics: Conference Series 445(1), 012004. pages

Sood, D. (1978). *Empirical rules for substitutionality in metastable surface alloys produced by ion implantation.* Phys. Lett. A 68(5), 469 – 472. pages

Sorlin, O. (2009). *Shell closures, magic and exotic nuclei.* Lecture notes of the 2009 International Joliot-Curie school. pages

Sorlin, O. (2014). *Shell Evolutions and Nuclear Forces.* EPJ Web of Conferences *66*, 01016. pages

Sorlin, O., S. Leenhardt, C. Donzaud, J. Duprat, F. Azaiez, F. Nowacki, H. Grawe, Z. Dombrádi, F. Amorini, A. Astier, D. Baiborodin, M. Belleguic, C. Borcea, C. Bourgeois, D. M. Cullen, Z. Dlouhy, E. Dragulescu, M. Górska, S. Grévy, D. Guillemaud-Mueller, G. Hagemann, B. Herskind, J. Kiener, R. Lemmon, M. Lewitowicz, S. M. Lukyanov, P. Mayet, F. de Oliveira Santos, D. Pantalica, Y.-E. Penionzhkevich, F. Pougheon, A. Poves, N. Redon, M. G. Saint-Laurent, J. A. Scarpaci, G. Sletten, M. Stanoiu, O. Tarasov, and C. Theisen (2002). $^{68}_{28}$Ni$_{40}$*: Magicity versus Superfluidity.* Phys. Rev. Lett. *88*, 092501. pages

Steppenbeck, D., A. N. Deacon, S. J. Freeman, R. V. F. Janssens, S. Zhu, M. P. Carpenter, P. Chowdhury, M. Honma, T. Lauritsen, C. J. Lister, D. Seweryniak, J. F. Smith, S. L. Tabor, and B. J. Varley (2010). *High-spin structures in the neutron-rich isotopes* $^{57-60}$Mn. Phys. Rev. C *81*, 014305. pages

Tarasov, O. B. and D. Bazin (2008). *LISE++: Radioactive beam production with in-flight separators.* NIM B 266(19 20), 4657 – 4664. Proceedings of the XVth International Conference on Electromagnetic Isotope Separators and Techniques Related to their Applications. pages

Thibault, C., R. Klapisch, C. Rigaud, A. M. Poskanzer, R. Prieels, L. Lessard, and W. Reisdorf (1975). *Direct measurement of the masses of* ^{11}Li *and* $^{26-32}$Na *with an on-line mass spectrometer.* Phys. Rev. C *12*, 644–657. pages

Torbohm, G., B. Fricke, and A. Rosén (1985). *State-dependent volume isotope shifts of low-lying states of group-II a and -II b elements.* Phys. Rev. A *31*, 2038–2053. pages

Tripathi, V., S. L. Tabor, P. F. Mantica, Y. Utsuno, P. Bender, J. Cook, C. R. Hoffman, S. Lee, T. Otsuka, J. Pereira, M. Perry, K. Pepper, J. S. Pinter, J. Stoker, A. Volya, and D. Weisshaar (2008). *Intruder Configurations in the* $A = 33$ *Isobars:* ^{33}Mg *and* ^{33}Al. Phys. Rev. Lett. *101*, 142504. pages

Tsunoda, N. and T. Otsuka (2016). *Exotic neutron-rich medium-mass nuclei with realistic nuclear forces.* arXiv:1601.06442. pages

Turzó, K., P. Himpe, D. L. Balabanski, G. Bélier, D. Borremans, J. M. Daugas, G. Georgiev, F. d. O. Santos, S. Mallion, I. Matea, G. Neyens, Y. E. Penionzhkevich, C. Stodel, N. Vermeulen, and D. Yordanov (2006). *Spin polarization of* ^{34}Al *fragments produced by nucleon pickup at intermediate energies.* Phys. Rev. C *73*, 044313. pages

Utsuno, Y., T. Otsuka, T. Glasmacher, T. Mizusaki, and M. Honma (2004). *Onset of intruder ground state in exotic* Na *isotopes and evolution of the* $N = 20$ *shell gap.* Phys. Rev. C *70*, 044307. pages

Utsuno, Y., T. Otsuka, T. Mizusaki, and M. Honma (1999). *Varying shell gap and deformation in* $N \sim 20$ *unstable nuclei studied by the Monte Carlo shell model.* Phys. Rev. C *60*, 054315. pages

Valiente-Dobón, J. J., S. M. Lenzi, S. J. Freeman, S. Lunardi, J. F. Smith, A. Gottardo, F. D. Vedova, E. Farnea, A. Gadea, D. R. Napoli, M. Axiotis, S. Aydin, D. Bazzacco, P. G. Bizzeti, A. M. Bizzeti-Sona, G. Benzoni, D. Bucurescu, L. Corradi, A. N. Deacon, G. De Angelis, E. Fioretto, B. Guiot, M. Ionescu-Bujor, A. Iordachescu, S. Leoni, N. Mărginean, R. Mărginean,

P. Mason, R. Menegazzo, D. Mengoni, B. Million, G. Montagnoli, R. Orlandi, F. Recchia, E. Sahin, F. Scarlassara, R. P. Singh, A. M. Stefanini, D. Steppenbeck, S. Szilner, C. A. Ur, B. J. Varley, and O. Wieland (2008). *Spectroscopy of neutron-rich* $^{59-63}$Mn *isotopes.* Phys. Rev. C *78*, 024302. pages

Van Duppen, P. and K. Riisager (2011). *Physics with REX-ISOLDE: from experiment to facility.* J. Phys. G 38(2), 024005. pages

Van Isacker, P. and S. Pittel (2016). *Symmetries and deformations in the spherical shell model.* Phys. Scripta 91(2), 023009. pages

Vermeeren, L., R. E. Silverans, P. Lievens, A. Klein, R. Neugart, C. Schulz, and F. Buchinger (1992). *Ultrasensitive radioactive detection of collinear-laser optical pumping: Measurement of the nuclear charge radius of* ^{52}Ca. Phys. Rev. Lett. *68*, 1679–1682. pages

Villars, F. (1957). *The collective model of nuclei.* Ann. Rev. Nucl. Sci. *7*, 185. pages

Vingerhoets, P., K. T. Flanagan, M. Avgoulea, J. Billowes, M. L. Bissell, K. Blaum, B. A. Brown, B. Cheal, M. De Rydt, D. H. Forest, C. Geppert, M. Honma, M. Kowalska, J. Krämer, A. Krieger, E. Mané, R. Neugart, G. Neyens, W. Nörtershäuser, T. Otsuka, M. Schug, H. H. Stroke, G. Tungate, and D. T. Yordanov (2010). *Nuclear spins, magnetic moments, and quadrupole moments of Cu isotopes from* $N = 28$ *to* $N = 46$*: Probes for core polarization effects.* Phys. Rev. C *82*, 064311. pages

Vyvey, K., G. Neyens, N. Coulier, R. Coussement, G. Georgiev, S. Ternier, S. Teughels, A. Lépine-Szily, and D. L. Balabanski (2000). *Preservation of orientation of fusion-evaporation reaction residues recoiling into vacuum in a level mixing spectroscopy experiment.* Phys. Rev. C *62*, 034317. pages

Wang, M., G. Audi, A. Wapstra, F. Kondev, M. MacCormick, X. Xu, and B. Pfeiffer (2012). *The Ame2012 atomic mass evaluation.* Chin. Phys. C 36(12), 1603. pages

Warburton, E. K., J. A. Becker, and B. A. Brown (1990). *Mass systematics for A =29–44 nuclei: The deformed A ∼32 region.* Phys. Rev. C *41*, 1147–1166. pages

Watt, A., R. P. Singhal, M. H. Storm, and R. R. Whitehead (1981). *A shell-model investigation of the binding energies of some exotic isotopes of sodium and magnesium.* J. Phys. G 7(7), L145. pages

Wildenthal, B. H. and W. Chung (1980). *Collapse of the conventional shell-model ordering in the very-neutron-rich isotopes of Na and Mg.* Phys. Rev. C *22*, 2260–2262. pages

Wimmer, K., T. Kröll, R. Krücken, V. Bildstein, R. Gernhäuser, B. Bastin, N. Bree, J. Diriken, P. Van Duppen, M. Huyse, N. Patronis, P. Vermaelen, D. Voulot, J. Van de Walle, F. Wenander, L. M. Fraile, R. Chapman, B. Hadinia, R. Orlandi, J. F. Smith, R. Lutter, P. G. Thirolf, M. Labiche, A. Blazhev, M. Kalkühler, P. Reiter, M. Seidlitz, N. Warr, A. O. Macchiavelli, H. B. Jeppesen, E. Fiori, G. Georgiev, G. Schrieder, S. Das Gupta, G. Lo Bianco, S. Nardelli, J. Butterworth, J. Johansen, and K. Riisager (2010). *Discovery of the Shape Coexisting* 0^+ *State in* ^{32}Mg *by a Two Neutron Transfer Reaction.* Phys. Rev. Lett. *105*, 252501. pages

Zuker, A. P., A. Poves, F. Nowacki, and S. M. Lenzi (2015). *Nilsson-SU3 self-consistency in heavy* $N = Z$ *nuclei.* Phys. Rev. C *92*, 024320. pages

Zuker, A. P., J. Retamosa, A. Poves, and E. Caurier (1995). *Spherical shell model description of rotational motion.* Phys. Rev. C *52*, R1741–R1745. pages

FACULTY OF SCIENCE
DEPARTMENT OF PHYSICS AND ASTRONOMY
INSTITUUT VOOR KERN- EN STRALINGSFYSICA
Celestijnenlaan 200D
B-3001 Leuven